



Norwegian University of
Science and Technology

Cold impact performance of polypropylene (PP)

Oppførsel av støtpåkjent PP ved lav
temperatur

Anders Engebakken

Jørgen Gudbrand Frøyland Skjennum

Master of Science in Mechanical Engineering

Submission date: June 2018

Supervisor: Arild Holm Clausen, KT

Co-supervisor: Einar Schwenke, KT

David Morin, KT

Lodewijk Coevert, Toyota Motor Europe ñ R&D centre Zaventem,

Norwegian University of Science and Technology

Department of Structural Engineering



MASTER THESIS 2018

SUBJECT AREA: Polymer Engineering	DATE: 11 th of June 2018	NO. OF PAGES: 22 + 198 + 97
--------------------------------------	--	--------------------------------

TITLE:

Cold impact performance of polypropylene (PP)

Oppførsel av støtpåkjent PP ved lav temperatur

BY:

Anders Engebakken, Jørgen Skjennum



SUMMARY:

When Toyota develop new polymer components for their vehicles, experimental drop tests are conducted at -30 °C to evaluate the cold impact performance of the parts. The objective of this thesis is to replicate the behaviour found in a drop test conducted on a Toyota Yaris polypropylene (PP) door trim, using the finite element method.

The material characterisation involved a series of uniaxial tensile tests in three different strain rate regimes. Specimens from two sources were tested to expose any difference in properties due to process effects associated with the component. Small-scale impact tests were conducted in a drop tower, in an attempt to validate the calibrated material model under controlled conditions. Experimental full-scale drop tests were performed and compared to numerical simulations employing the validated material model.

Ductile behaviour was found in the uniaxial tensile test campaign in the quasi-static and meso-dynamic regimes. The mechanical properties of the two material sources were nearly identical, with the exception of strain at fracture. A Split-Hopkinson tension bar test rig enabled testing in the dynamic regime, where entirely brittle material response was obtained. In addition, a log-bilinear strain rate sensitivity was observed for the material.

The first material characterisation produced accurate results in the numerical representation of the small-scale impact test. In contrast, the ductility was clearly overestimated for the brittle failure mode observed for the second characterisation. A recalibration was performed to accommodate these discrepancies, also involving an inverse modelling procedure of the fracture parameters according to the results from the drop tower. However, the numerical model still demonstrated overly ductile behaviour when the full-scale component drop test was simulated.

RESPONSIBLE TEACHER: Professor Arild H. Clausen

SUPERVISOR(S): Arild H. Clausen, Einar Schwenke, Lodewijk Coevert, David Morin

CARRIED OUT AT: CASA, Department of Structural Engineering, NTNU and Toyota Motor Europe – R&D centre Zaventem, Belgium

MASTER THESIS 2018

Anders Engebakken and Jørgen Skjennum

Cold impact performance of polypropylene (PP)

(Oppførsel av støtpåkjent PP ved lav temperatur)

When designing components made of polymers, Toyota evaluates the impact properties of such parts at low temperatures. They do this through a set of standardized tests at $-30\text{ }^{\circ}\text{C}$. On the other hand, the finite element method (FEM) is an important design tool, and the material models do also have to cover the cold impact performance. The main task of the thesis is to reproduce the behavior observed in cold impact tests on polypropylene (PP) parts in numerical FEM simulations. This thesis is thus a cooperation between Toyota and the research centre CASA at NTNU.

The thesis work will involve a typical door trim applied in cars produced by Toyota. The impact tests on these parts at low temperatures will be carried out in Toyota's laboratory in Brussels. The tension tests required for the calibration of the material model in the non-linear FE program LS-DYNA are to be performed in the laboratory at NTNU in Trondheim. NTNU can also facilitate other tests relevant for gaining more knowledge on the material's response, for instance a drop tower. Special attention should be paid to the failure mode. Toyota provides the geometrical part of the FEM model. The polymer model of CASA will be employed to describe the material behaviour.

Possible keywords for activities in this master thesis research work may include:

- Literature review: Polymeric materials, material models, energy absorption, low temperature.
- Experimental work: Material and component tests at low temperature. Presentation of test results.
- Numerical work: Calibration of material model. Modelling and simulation of experimental tests. Optimization of the model.
- Validation: Comparison of experimental and numerical results. Evaluation of the model. Presentation of results at Toyota.

The candidates may agree with the supervisors to pay particular attention to specific parts of the investigation, or include other aspects than those already mentioned.

The thesis is to be organized as a research report, recognising the guidelines provided by Department of Structural Engineering.

Supervisors at NTNU: Einar Schwenke, David Morin and Arild Holm Clausen
Supervisor at Toyota: Lodewijk Coevert

The report is to be handed in not later than 11 June 2018.

NTNU, 15 January 2018

Arild Holm Clausen

Abstract

Polymeric materials are notorious for being highly sensitive to conditions such as temperature and strain rate. When Toyota develop new polymer components for their vehicles, experimental drop tests are conducted at $-30\text{ }^{\circ}\text{C}$ to evaluate the cold impact performance of the parts. The objective of this thesis is to replicate the behaviour found in a drop test conducted on a Toyota Yaris polypropylene (PP) door trim, using the finite element method (FEM). A comprehensive material model, developed for ductile thermoplastics such as PP, was utilised. Enabling accurate estimation of the properties for newly designed components prior to production, has the potential to reduce the design costs for Toyota.

This thesis investigates how the highly sensitive behaviour of the PP material can be replicated in numerical FEM simulations. Two sources of PP were utilised; the actual door trim, and material sample plates. The material characterisation involved a series of uniaxial tensile tests in three different strain rate regimes. Specimens from the two sources were tested to expose any difference in properties due to process effects associated with the component. Small-scale impact tests were conducted in a drop tower, in an attempt to validate the calibrated material model under controlled conditions. Experimental full-scale drop tests were performed and compared to numerical simulations employing the validated material model.

Exclusively ductile behaviour was found in the uniaxial tensile test campaign, in addition to a log-linear strain rate dependence in the quasi-static and meso-dynamic regimes, even at low temperature. The mechanical properties of the two respective material sources were nearly identical, with the exception of strain at fracture. Based on these findings, an initial calibration was conducted accommodating the adiabatic heating effects at higher strain rates. A Split-Hopkinson tension bar test rig enabled testing in the dynamic regime, where entirely brittle material response was found. The brittle-ductile transition was confirmed in scanning electron microscopy analyses of the through-thickness fracture surfaces. In addition, a log-bilinear strain rate sensitivity was observed for the material. Hence, a recalibration of the material model was attempted in order to account for the embrittlement.

The first material characterisation, calibrated from ductile tensile tests, produced accurate results in the numerical representation of the small-scale impact test for the material sample plates. In contrast, the ductility was clearly overestimated for the brittle failure mode observed for the door trim material. A recalibration was performed to accommodate these discrepancies, also involving an inverse modelling procedure of the fracture parameters according to the results from the drop tower.

However, the numerical model still demonstrated overly ductile behaviour when the full-scale component drop test was simulated. It is suggested that the differences in failure mode resulting from the small- and full-scale drop tests could account for some of this discrepancy.

Further work is recommended in order to investigate the strain rates associated with the brittle-ductile transition. By use of a higher strain rate in the electromechanical test machine, more accurate strain measurements in the meso-dynamic regime could allow for calibration of fracture parameters based on brittle behaviour.

Sammendrag

Polymerers mekaniske egenskaper er svært avhengige av både temperatur og tøyingsrate. Når Toyota utvikler nye polymerdeler til sine biler, utføres eksperimentelle kuleslipptester ved $-30\text{ }^{\circ}\text{C}$. Testene utføres for å undersøke hvordan polymerdelene oppfører seg under disse forholdene. Målet med denne oppgaven er å reprodusere oppførselen til et Toyota Yaris dørpanel, laget av polypropylen, i en slik test ved bruk av elementmetoden. En omfattende materialmodell, utviklet for duktile termoplaste som polypropylen, ble brukt. Et presist estimat av dørpanelets oppførsel, allerede før det er produsert, vil kunne redusere kostandene knyttet opp mot utviklingsprosessen.

Denne oppgaven tar for seg hvordan den sensitive materialoppførselen til polypropylen kan gjenskapes ved bruk av numeriske simuleringer. En rekke enaksielle strekktester ble utført ved forskjellige tøyingsrater, for å sikre nøyaktig karakterisering av materialet. To materialkilder ble undersøkt. Den primære materialkilden var prøvestykker tatt fra selve dørpanelet. I tillegg ble materialprøver undersøkt for å avdekke eventuelle prosesseffekter som kan påvirke oppførselen til dørpanelet. Resultatet fra disse testene ble brukt til å kalibrere materialmodellen. Småskala støttester ble gjennomført i et fallverk for å validere materialparameterne under kontrollerte forhold, før eksperimentelle kuleslipptester ble utført på dørpanelet. Resultatene ble sammenlignet med tilsvarende numeriske resultater, oppnådd gjennom bruk av den validerte materialmodellen.

De enaksielle strekktestene viste at materialoppførselen var duktil, og en log-lineær tøyingsrate-avhengighet ble funnet i de kvasistatiske og mesodynamiske regimene, selv ved lav temperatur. De mekaniske egenskapene for de to respektive kildene var tilnærmet identiske, med unntak av tøyning ved brudd. Den adiabatisk oppvarmingen som ble funnet for de mesodynamiske tøyingsratene ble også tatt hensyn til i kalibreringen. Et Split-Hopkinson strekkstag ble brukt for materialtesting i det dynamiske tøyingsrateregimet. Resultatene viste at materialet oppførte seg sprøtt. Analyser med skanningelektronmikroskop av prøvestykkens bruddoverflater bekreftet overgangen fra duktil- til sprøtt brudd. I tillegg ble en log-bilineær tøyingsrate-avhengighet funnet for materialet. En omkalibrering av materialmodellen ble gjennomført på bakgrunn av disse resultatene.

Den første materialkalibreringen, basert på duktil oppførsel, resulterte i en presis numerisk representasjon av de småskala støttestene gjennomført på materialprøvene. Duktiliteten var derimot overestimert for sprøbruddsoppførselen som ble funnet for dørpanelene i fallverket. Omkalibreringen, som ble gjennomført for å ta hensyn til den sprø materialoppførselen, involverte også inversmodellering av modellens brud-

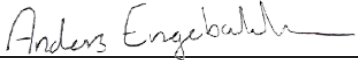
dparametere. Dette ble utført for å oppnå overensstemmelse med de eksperimentelle resultatene fra fallverket. Den numeriske modellen av kuleslipptesten overestimerte duktiliteten til dørpanelet, til tross for flere forsøk på å gjenscape den sprø responsen. Det ble foreslått at forskjellen i bruddmoder mellom de små- og fullskala støttestene kunne forårsake disse avvikene.

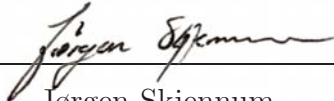
I det videre arbeidet er det anbefalt å undersøke hvordan overgangen fra duktil- til sprø materialoppførsel påvirkes av tøyningraten. Ved bruk av en elektromekanisk testmaskin og høyhastighetskameraer, kan man muliggjøre kalibrering av bruddkriterieparametere for den sprø oppførselen i det mesodynamiske tøyningrateregimet.

Preface

This master thesis was written during the spring of 2018 at the Department of Structural Engineering (DSE) at the Norwegian University of Science and Technology (NTNU) under the supervision of Professor Arild H. Clausen. It concludes two degrees of Master of Science in Mechanical Engineering, Applied Mechanics. The project was initiated by Toyota Motors Europe (TME) and has been completed in cooperation with the Centre for Advanced Structural Analysis (CASA).

Trondheim, 11th of June 2018


Anders Engebakken


Jørgen Skjennum

Acknowledgement

We would like to use this opportunity to thank everyone who has helped us during our master project. Special thanks to PhD Candidate Einar Schwenke, whom is not only our predecessor, but also provided useful knowledge and served as an excellent discussion partner throughout the entire project.

We wish to express our sincere gratitude to the main supervisor of this project, Professor Arild H. Clausen, for valuable and constructive guidance during our research. His ability to show special interest in our project and the problems we faced along the way, has been highly educational.

We would like to thank everyone at TME and to offer a special thanks to Senior Engineer Lodewijk Coevert, for involving us in this project. Being able to visit the R&D centre in Zaventem, Belgium, is something we will remember for the rest of our lives.

Many thanks to Senior Engineer Trond Auestad, for all assistance and guidance during the testing at NTNU, and to Technician Hendrik Serré, for helping us perform the experimental campaign at TME. Thanks to Senior Engineer Sergey Khromov, for supplying all scanning electron micrographs, and to Senior Engineer Tore Wisth, for arrangement of test specimen machining.

Advices given by Researcher Torodd Berstad and Associate Professor David Morin have been of great value. Finally, we would like to acknowledge the support provided by Research Scientist T erence Coudert at SINTEF, during the calibration of the material model.

Contents

Abstract	v
Sammendrag	vii
Preface	ix
Acknowledgement	x
Table of Contents	xvi
Nomenclature	xxi
1 Introduction	1
1.1 Problem definition	1
1.2 Previous work	3
1.2.1 Uniaxial tensile and compression tests	3
1.2.2 Charpy V-notch tests	4
1.2.3 Component drop tests	5
1.2.4 Priorities and focus areas	6
2 Theoretical Background	9
2.1 Material	9
2.1.1 Polypropylene	10
2.1.2 Mechanical behaviour	11
2.1.3 Yielding and fracture behaviour	12
2.1.4 Brittle-ductile behaviour	14
2.1.5 Production process	16
2.2 Analytic background	18
2.2.1 Material properties	18
2.2.2 Digital image correlation	21
2.3 Material model	22
2.3.1 Rheological model	22
2.3.2 Hypoelasticity	23
2.3.3 Yielding and plastic flow	24

2.3.4	Viscoplasticity	26
2.3.5	Hardening and softening	27
2.3.6	Adiabatic heating	28
2.3.7	Damage	29
2.4	Finite element analysis	30
2.4.1	Solution methods	30
2.4.2	Mass scaling	31
2.4.3	Full- and reduced integration	31
2.4.4	Spurious modes	33
2.5	Scanning electron microscopy	34
2.5.1	Scanning process and image formation	34
2.5.2	Sample preparation	35
2.5.3	Resolution	35
3	Quasi-Static and Meso-Dynamic Material Testing	37
3.1	Introduction	37
3.2	Uniaxial tensile test procedure	40
3.2.1	Test specimens	40
3.2.2	Setup	41
3.2.3	Post processing	44
3.3	Results - Material sample plates	46
3.3.1	Visual results	47
3.3.2	Measured results	48
3.3.3	SEM results	53
3.4	Results - Door trim cutouts	54
3.4.1	Visual results	56
3.4.2	Measured results	57
3.4.3	SEM results	63
3.5	Summary	64
4	Calibration of Material Model	67
4.1	MatPrePost	67
4.2	Material tests	68
4.3	Elasticity	69
4.4	Hardening and softening	70
4.5	Pressure sensitivity	72
4.6	Plastic dilatation	73
4.7	Strain rate dependence	74
4.8	Damage	74

4.9	Calibrated material parameters	76
5	Verification of Material Model	79
5.1	Introduction	79
5.2	Numerical model	80
5.3	Results	82
5.3.1	Refinement of numerical model	82
5.3.2	Verification	84
6	Drop Tower Impact Testing	87
6.1	Experiment	87
6.1.1	Test specimens	88
6.1.2	Setup	90
6.1.3	Post processing	93
6.1.4	Results - Material sample plates	94
6.1.5	Results - Door trim cutouts	100
6.2	Numerical analysis	107
6.2.1	Numerical model	108
6.2.2	Results - Material sample plates	109
6.2.3	Results - Door trim cutouts	112
6.3	Sensitivity study	113
6.3.1	Material parameters	114
6.3.2	Plate thickness	116
6.3.3	Mesh size	117
6.3.4	Element formulation	119
6.3.5	Coefficient of friction	120
6.4	Discussion	122
7	Dynamic Material Testing	125
7.1	Introduction	125
7.2	Split-Hopkinson tension bar testing	126
7.2.1	Test specimens	127
7.2.2	Setup	128
7.2.3	Post processing	130
7.2.4	Results	132
7.3	Recalibration of material model	140
7.3.1	Alternative material model	140
7.3.2	Calibration procedure	142
7.4	Verification of material models	144
7.4.1	Split-Hopkinson tension bar test	144

7.4.2	Drop tower impact test	145
7.4.3	Calibrated material parameters	148
7.5	Discussion	150
8	Component Impact Testing	153
8.1	Experiment	153
8.1.1	Test components	154
8.1.2	Setup	155
8.1.3	Results	157
8.2	Numerical analysis	161
8.2.1	Numerical model	162
8.2.2	Results	168
8.3	Discussion	180
9	Conclusion	187
10	Suggestions for Further Work	189
	Bibliography	197
A	Mathematical Derivation	A1
A.1	Plastic dilatation parameter	A1
A.2	Force correction factor	A4
B	Material Tests	B1
B.1	Material sample plates	B2
B.1.1	UT_S_00_H-30_01	B2
B.1.2	UT_S_00_H-30_02	B3
B.1.3	UT_S_00_L-30_02	B4
B.1.4	UT_S_00_L-30_03	B5
B.1.5	UT_S_00_M-30_01	B6
B.1.6	UT_S_00_M-30_02	B7
B.1.7	UT_S_00_VL-30_02	B8
B.1.8	UT_S_00_VL-30_03	B9
B.1.9	UT_S_00_VL-30_01	B10
B.2	Door trim cutouts	B11
B.2.1	UT_A-10.00_H-30	B12
B.2.2	UT_A-10.00_L-30	B13
B.2.3	UT_A-10.00_M-30	B14
B.2.4	UT_A-1.00_VL-30	B15
B.2.5	UT_A-2.00_L-30	B16

B.2.6	UT_A-2.45_L-30	B17
B.2.7	UT_A-2.90_L-30	B18
B.2.8	UT_A-3.00_H-30	B19
B.2.9	UT_A-3.00_M-30	B20
B.2.10	UT_A-3.00_VL-30	B21
B.2.11	UT_B-10.00_VL-30	B22
B.2.12	UT_B-11.00_H-30	B23
B.2.13	UT_B-11.00_VL-30	B24
B.2.14	UT_B-11.00_M-30	B25
B.2.15	UT_B-2.00_L-30	B26
B.2.16	UT_B-2.45_L-30	B27
B.2.17	UT_B-2.90_L-30	B28
B.2.18	UT_CS-12.90_L-30	B29
B.2.19	UT_CS-12.90_VL-30	B30
B.2.20	UT_CR-1.00_VL-30	B31
B.2.21	UT_CR-2.00_L-30	B32
B.2.22	UT_CR-2.45_L-30	B33
B.2.23	UT_CR-2.90_L-30	B34
B.2.24	UT_CR-3.00_VL-30	B35
B.2.25	UT_CL-1.00_VL-30	B36
B.2.26	UT_CL-2.00_L-30	B37
B.2.27	UT_CL-2.45_L-30	B38
B.2.28	UT_CL-2.90_L-30	B39
B.2.29	UT_CL-3.00_VL-30	B40
C	Drop Tower Tests	C1
C.1	Dimensionless results	C2
C.2	Material sample plates	C3
C.2.1	DT_S-30_07	C3
C.2.2	DT_S-30_08	C4
C.2.3	DT_S-30_01	C5
C.2.4	DT_S-30_03	C6
C.2.5	DT_S-30_04	C7
C.2.6	DT_S-30_05	C8
C.2.7	DT_S-30_06	C9
C.3	Door trim cutouts	C10
C.3.1	DT_C-4-30	C10
C.3.2	DT_C-5-30	C11
C.3.3	DT_C-7-30	C12

C.3.4	DT_C-8_-30	C13
C.3.5	DT_C-9_-30	C14
C.3.6	DT_CS-10_-30	C15
C.3.7	DT_CS-11_-30	C16
D	Split-Hopkinson Tension Bar Tests	D1
D.1	Strain and stress waves	D1
D.2	Door trim cutouts	D4
D.2.1	SH_B-3_02	D5
D.2.2	SH_B-10_02	D6
D.2.3	SH_B-4_01	D7
D.2.4	SH_B-4_02	D8
D.2.5	SH_B-5_01	D9
E	Component Tests	E1
E.1	Door trims	E2
E.1.1	Door trim 3	E3
E.1.2	Door trim 6	E4
E.1.3	Door trim 7	E5
E.1.4	Door trim 8	E6
E.1.5	Door trim 9	E7
E.1.6	Door trim 10	E8
E.1.7	Door trim 11	E9
E.1.8	Door trim 12	E10
E.1.9	Door trim 13	E11
E.1.10	Door trim 15	E12
E.1.11	Door trim 16	E13
E.1.12	Door trim 17	E14
E.1.13	Door trim 18	E15
E.1.14	Door trim 19	E16
E.1.15	Door trim 20	E17
F	Material Cards	F1
F.1	Abaqus	F1
F.2	LS-DYNA	F2
G	Friction Coefficient Test	G1

Nomenclature

Abbreviations

AFM Atomic force microscopy

CASA Centre for Advanced Structural Analysis

DIC Digital image correlation

DSE Department of structural engineering

EM Electromechanical

EPR Ethylene-propylene rubber

FE Finite element

FEA Finite element analysis

FEM Finite element method

H High

L Low

M Medium

NTNU Norwegian University of Science and Technology

PC Polycarbonate

PE Polyethylene

PP Polypropylene

R&D Research and development

RP Reference point

SEM Scanning electron microscopy

SHTB Split-Hopkinson tension bar

SIMLab Structural Impact Laboratory

SPM SIMLab polymer model

TEM Transmission electron microscopy

TME Toyota Motor Europe

TS Toyota Standards

VL Very low

Symbols

α Pressure sensitivity parameter

β Plastic dilatation parameter

$\boldsymbol{\sigma}$ Cauchy stress tensor

$\boldsymbol{\sigma}'$ Deviatoric stress tensor

\boldsymbol{C}^σ Isotropic tensor of elastic moduli

\boldsymbol{D} Rate-of-deformation tensor

\boldsymbol{I} Identity matrix

ΔT Temperature change

Contents

Δt	Sampling time	ε_f^p	Equivalent plastic strain at fracture
Δt_{cr}	Critical time step	ε_I	Incident strain wave
$\dot{\varepsilon}^p$	Equivalent plastic strain rate tensor	ε_R	Reflected strain wave
$\dot{\lambda}$	Plastic parameter	ε_T	Transmitted strain wave
$\dot{\varepsilon}$	Strain rate	ε_V	Volumetric strain
$\dot{\varepsilon}_0^p$	Reference plastic strain rate	φ, σ_{eq}	Equivalent stress
$\dot{\varepsilon}_s$	Analytic specimen strain rate	A	Cross-sectional area
\dot{T}	Temperature rate	C	Strain rate sensitivity
$\hat{\sigma}_{eff}$	Effective stress tensor	c_0	Specimen wave propagation velocity
\mathfrak{D}	Dissipation energy	c_b	Bar wave propagation velocity
μ	Coefficient of friction	c_d	Dilatation wave speed
ν	Poisson's ratio	c_T	Specific heat capacity
Φ	von Mises norm	D	Damage variable
ρ	Material density	d	Diameter
σ	True stress	D_C	Critical damage
σ^*	Stress triaxiality	D_I	Initial damage
σ_B	Brittle fracture stress	D_v	Cowper-Symonds viscoplastic parameter
σ_C	Yield strength in compression	E	Young's modulus
σ_H	Hydrostatic stress	e	Nominal strain
σ_T	Yield strength in tension	E_t	Tangent stiffness
σ_v	Viscous stress	F	Force
σ_Y	Yield stress	f	Yield function
θ	Inclined plane angle	g	Flow potential
θ_{Ri}	Initial hardening parameters	g_a	Gravitational acceleration
ε	Logarithmic strain	h	Height
ε^e	Elastic logarithmic strain		
ε^p	Plastic logarithmic strain		

I_1	First stress invariant	R	Isotropic hardening variable
J_2	Second deviatoric stress invariant	R_r	Retraction ratio
L	Specimen gauge length	s	Nominal stress
l	Inclined plane length	t	Time
L^e	Characteristic length of the smallest element	T_g	Glass transition temperature
m	Mass	u	Displacement
N_0	Pre-tension force	v	Velocity
P	Measured force	v_{bl}	Ballistic limit velocity
q	Cowper-Symonds viscoplastic parameter	v_i	Initial velocity
Q_{Ri}	Saturation hardening parameters	v_r	Residual velocity
		h	Specimen height
		t	Specimen thickness
		w	Specimen width

Introduction

1.1 Problem definition

When new plastic components are developed by Toyota, they are evaluated in a series of tests before a final design can be fixed. These tests are intended to replicate conditions that may arise in the everyday life of the part. The design procedure involves several choices related to cost, weight, appearance, durability and strength. Hence, it offers a complicated balancing act, where strength is the most challenging property to determine during the design of the component. In this thesis, one such test will be reproduced using the finite element method (FEM), where several material representations have been developed in order to model polymers.

The test replicated in this thesis is intended to evaluate the performance of a polypropylene (PP) Toyota Yaris door trim in cold impact conditions. The car and associated door trim are shown in Figure 1.1. In order to standardise the test conditions, a steel ball of 1 kg is dropped onto the surface of the component at -30°C . Different requirements are specified in the Toyota Standards (TS) with respect to allowable drop heights for particular sections of the part. A challenge related to the development of a new part is that the test can not be conducted before the design is set, i.e. the material and geometry are chosen, and the tools are produced such that a prototype can be made. At this time, however, failing to satisfy the requirements would mean that the entire process was wasted. Thus, an accurate estimate of the part's performance before the final design is fixed, i.e. without the need of a physical component, could potentially lead to large reductions in design costs for Toyota.

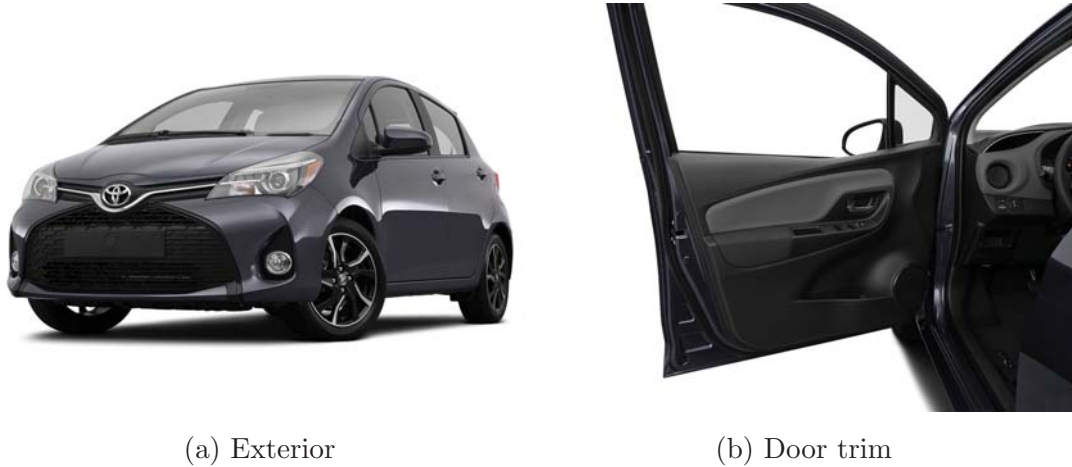


Figure 1.1: 2017 Toyota Yaris 5-door [1]

By use of the FEM during the design of the component, its mechanical performance could be evaluated, and any problems solved before the part is produced. However, large uncertainties are related to replicating the behaviour of the polymer, due to the high strain rates and low temperatures associated with a cold impact. Under such conditions, the brittle-ductile transition is of special interest since it could severely affect the properties of the material. This thesis aims to investigate how to model the behaviour found in the component accurately, by employing the SIMLab polymer model (SPM) in finite element analyses (FEA). Although the SPM is developed and validated for ductile thermoplastics, such as the one used in the door trim, the main concern is whether the behaviour associated with the extreme conditions of a cold impact can be reproduced precisely. The outline of the thesis, as well as a brief description of each chapter, is given below:

Chapter 2 - Theoretical Background: Initially, a theoretical foundation for this thesis is provided. Special emphasis is placed on the understanding of the mechanical behaviour observed for injection moulded PP, and how this is reproduced by the SPM through a series of constitutive relations.

Chapter 3 - Quasi-Static and Meso-Dynamic Material Testing: An extensive tensile test programme on two different material sources is described. Accurate representation of the behaviour in the numerical model requires a thorough characterisation of the material.

Chapter 4 - Calibration of Material Model: The different stages related to the calibration procedure of the material model are outlined in this chapter.

Chapter 5 - Validation of Material Model: To allow for the material characterisation to be extrapolated to other load cases, validation of the material model

in a uniaxial stress state was a requirement.

Chapter 6 - Drop Tower Impact Testing: Two experimental test campaigns conducted in a drop tower are provided here. This allowed for further validation of the calibrated material model, in a load case resembling the full-scale component drop test.

Chapter 7 - Dynamic Material Testing: To better represent the dynamic material response of the PP, an experimental campaign was conducted in a Split-Hopkinson tension bar (SHTB). Based on the findings, a recalibration of the material model was attempted to accommodate the dynamic behaviour.

Chapter 8 - Component Impact Testing: The experimental door trim drop tests and associated numerical representation are described here. In order to evaluate the quality of the finite element (FE) model, these results were compared and discrepancies discussed.

Chapters 9 and 10 - Conclusion and Suggestions for Further Work: A brief summary of the most important findings in this thesis is provided, in addition to suggestions for further work.

1.2 Previous work

Relevant work completed prior to this thesis was performed by Einar Schwenke during the spring of 2017. Through his master thesis [2], the SPM's ability to represent the cold impact properties of PP door trims was investigated. Since this thesis is a continuation of Schwenke's work, a brief review of his most important findings is provided here. Based on this summary, a short discussion regarding the focus areas of this thesis is also given.

1.2.1 Uniaxial tensile and compression tests

The main material source utilised in the uniaxial tensile- and compression tests of Schwenke's work [2] was PP material sample plates, provided by Toyota. A total of 33 tests were performed on specimens extracted from such material sample plates. However, only 11 are relevant for this thesis, as three different PP materials were investigated. The results revealed that the material is ductile, even at -30 °C. A selection of the results are shown in Figure 1.2 in terms of nominal stress-logarithmic strain curves. Furthermore, the material showed uniform- and isotropic behaviour.

A second material source was an actual door trim, provided by Toyota, from which a total of nine tensile specimens were extracted. From these experimental results it was evident that the door trim cutouts and the material sample plates behaved identically with the exception of strain at fracture, which varied to some extent. It must be noted that these tests were performed at room temperature, i.e. at 20 °C.

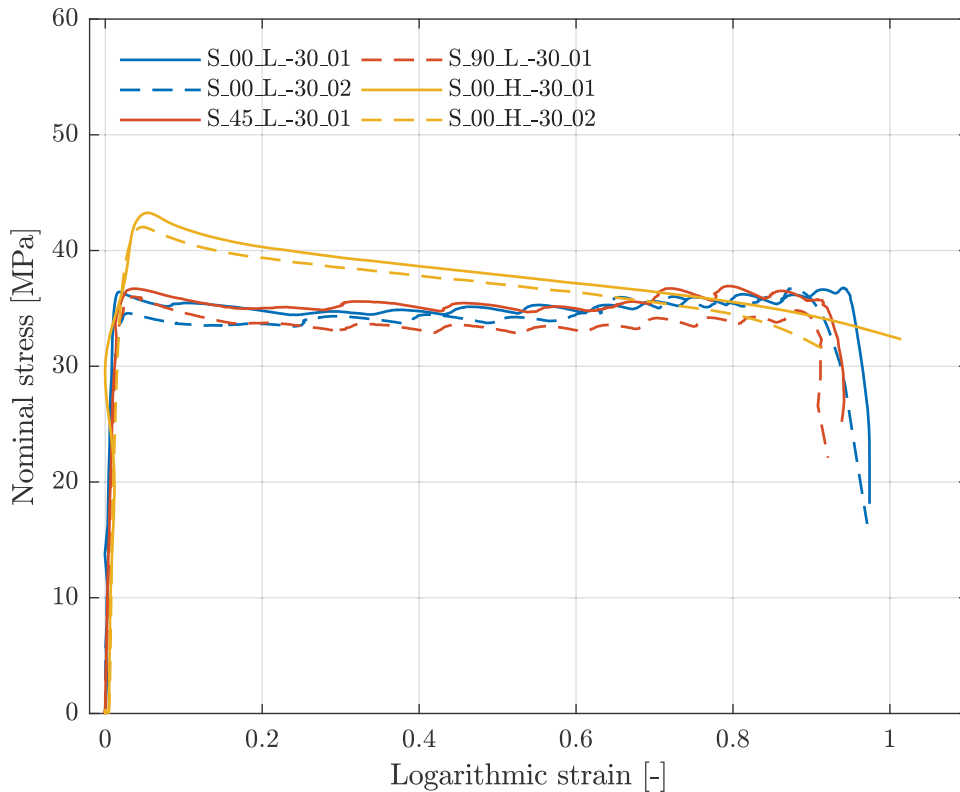


Figure 1.2: Tensile test results for material sample plates [2]

1.2.2 Charpy V-notch tests

In order to make sure that the material model was able to represent the correct behaviour, also in impact situations, Charpy V-notch tests were performed. Through these tests, experimental results for which the material experienced both elevated strain rates and higher triaxiality, were achieved. It was believed that such conditions would promote brittle fracture.

For the Charpy V-notch tests, the specimens were extracted from equivalent PP material sample plates as those utilised for the tensile specimens. The assumption of material embrittlement under such conditions was confirmed. Hence, it was concluded that the initial choice of fracture criterion was not capable of properly

representing the appearing brittle-ductile transition. To accommodate this brittle material behaviour, inverse modelling of the fracture parameter was performed, enabling coinciding results from the experiments and the numerical simulations.

1.2.3 Component drop tests

The full-scale drop tests on door trims were conducted in order to evaluate their cold impact performance according Toyota's standards and requirements. Seven distinct locations on the door trim were utilised in these drop tests. However, only one location was chosen for numerical investigation. This location was selected due to the planar geometry of the surface and the consistency of the experimental data, as seen in Figure 1.3.

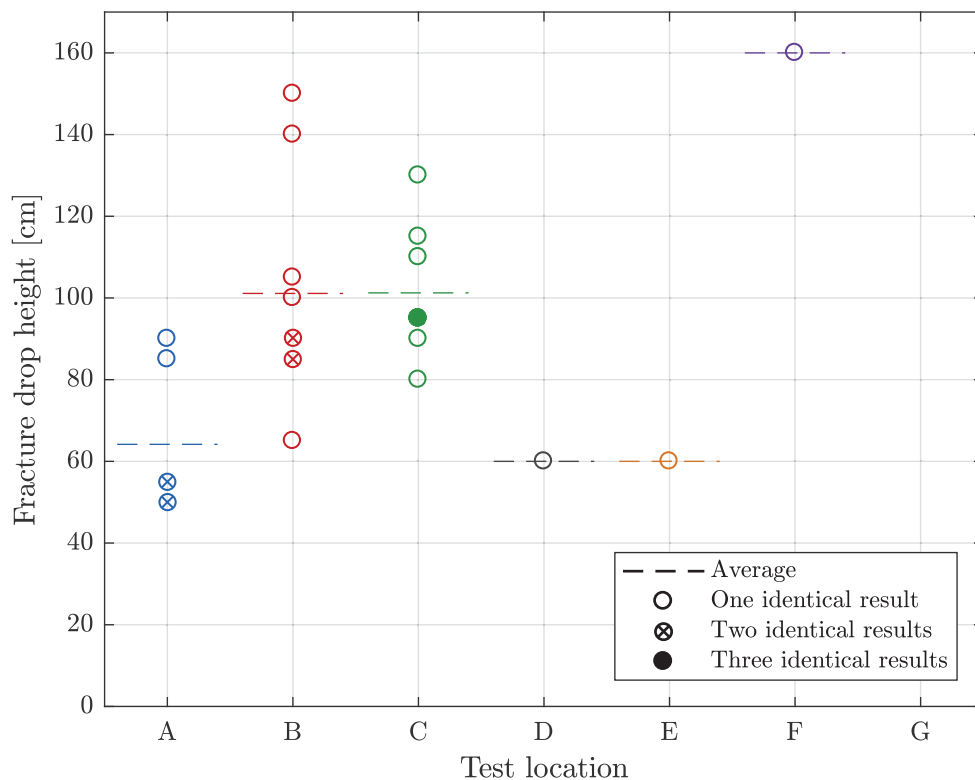


Figure 1.3: Full-scale component drop test results [2]

The results obtained from these full-scale drop tests implied that the material calibration estimated an overly ductile behaviour. Hence, two different attempts were made in order to better represent the material response. One attempt was the inverse modelling of the Charpy V-notch test. The second attempt included introduction of an alternative criterion, causing fracture at a certain critical stress,

found from the tensile test results. As there were several uncertainties related to the numerical representation of the door trim, a basis model was defined such that these could be further investigated in a comprehensive sensitivity study. The most crucial outcome of the study was the model's sensitivity with respect to the choice of fracture parameter.

1.2.4 Priorities and focus areas

Experimental testing of door trim cutouts

During Schwenke's work [2], the majority of material tests were performed using PP sample plates. However, it is obvious that there are some differences between these plates and the actual door trims. Some of these differences are due to additives such as, colour pigments, i.e. *carbon black* and *blue*, and UV stabilising pigments, i.e. *hindered amine light stabilisers*. In total, these additives constitute an amount of approximately 1-2 % of the volume of the door trim. Additionally, there are clear differences with respect to geometry of the material sources, which could possibly influence the specimens due to process effects. The differences between the actual door trims and the material sample plates, suggest that their mechanical behaviour may deviate considerably. Thus, more focus will be placed on testing of door trim cutouts instead of the material sample plates. Furthermore, large variations were found in strain at fracture for both specimen orientation and -cutout location. These effects will be investigated further in this thesis. All considered locations are shown in Figure 1.4.

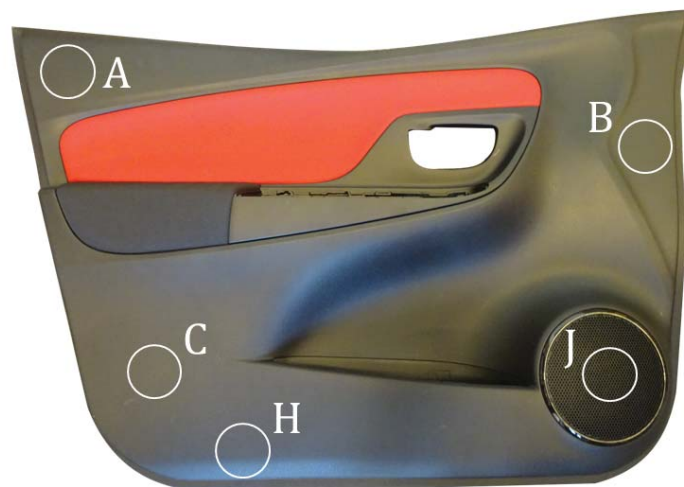


Figure 1.4: Considered locations on the door trims

Brittle-ductile transition

Through comprehensive material testing at elevated strain rates and different triaxialities, the brittle-ductile transition is believed to influence the mechanical properties. Since Schwenke's work [2] recommended that the material should be further characterised under such conditions, emphasis will be placed on an increased number of material tests at several strain rates in three different regimes. Furthermore, small-scale impact tests in a drop tower can provide more knowledge of the material's response in a stress state similar to that of the component drop test. This can enable a more precise determination of a fracture parameter that better suits brittle material behaviour.

Adiabatic heating and strain rate dependence

Previously, thermal softening effects were found in uniaxial tensile tests with strain rates above quasi-static conditions. For brittle behaviour, however, the plastic strains, and subsequent internal energy dissipated as heat, are relatively small. As the experimental tensile tests proved to be rather ductile even at $-30\text{ }^{\circ}\text{C}$, the door trim may also be susceptible to some ductile deformation due to adiabatic conditions causing local softening in the material. On these grounds, thorough investigation of the potential thermal softening of the material will be conducted throughout this thesis. Utilisation of both high speed and thermal cameras enable monitoring of actual heat generation and material behaviour in each experiment. The SPM can calculate the heat generation, but it is not yet capable of implementing feedback of the adiabatic heating effects through temperature dependent material parameters. Hence, an approach using experimental data taken from material tests where such conditions are evident will be adopted in order to circumvent this modelling challenge.

Failure mode

It is of utmost interest to investigate the brittle-ductile transition and the behaviour of the PP material. By provoking various material responses through change of load conditions, different failure modes can be triggered. Furthermore, utilisation of a scanning electron microscope (SEM) can relate these failure modes to microscopic phenomena governing the fracture characteristics of the PP. Such information is extremely important in the further development and selection of material composition of PP parts for Toyota.

Theoretical Background

To accomplish the main objective of this thesis, the material behaviour of the component in question must be fully understood. As the topic of this project involves the impact performance of PP at $-30\text{ }^{\circ}\text{C}$, an accurate material representation is essential for obtaining valid numerical results. In this chapter, a thorough introduction of the mechanical behaviour observed in injection moulded PP will be given. Important tools for understanding and analysing this material are also presented. In order to reproduce the mechanical behaviour in numerical simulations, a material model must be utilised. The model outlined in this chapter enables the complex material characteristics to be replicated through several constitutive relations. By implementing this material model into FEM simulations, accurate predictions of the component behaviour can be obtained. Hence, a brief discussion regarding some important aspects of the FEM, that were utilised in this thesis, is also given here. To gain a better understanding of the fracture properties of the material, SEM analyses were also performed. This allowed for the microscopic failure mechanisms to be related to the macroscopic response. Hence, the SEM technology is briefly presented herein.

2.1 Material

An increasing amount of lighter metallic- and polymer materials are exploited in the automotive industry today. For actors within this industry, components meeting given regulations and standards are of utmost importance. Therefore, research and development (R&D) of continually stronger, lighter, more robust and cheaper

materials, enhancing their products is of special interest. One such material class is the so-called *high performance plastics*. In addition to their light weight, and thus the subsequent reduction in fuel usage, the high performance plastics incorporate advantages like; minimal corrosion allowing for longer vehicle lifetime, substantial design freedom facilitating more advanced creativity and innovation, flexibility with respect to integration of components, safety-, comfort- and economic aspects, and of course recyclability. Within the automotive industry, PP stands out as the most widely used material among several other high performance plastics because of its robustness and resistance to a multitude of chemical solvents, bases and acids. At Toyota, PP is supplied in different grades, depending on requirements and applications. These different compositions of the same basic material are so-called *high crystalline copolymers*, designed for injection moulding of parts in the automotive industry. Such material grades have improved thermal stability, stiffness and impact resistance.

2.1.1 Polypropylene

PP is a polymer and consists of long molecular chains. Polymers are created from small molecules called monomers, in a process called polymerisation. For PP, the process involves formation of an active site in form of an unpaired electron, denoted as \cdot , created in a reaction between an initiator, $R\cdot$, and the hydrocarbon propene, C_3H_6 . This active site further creates a single covalent bond with a similar monomeric unit. The mechanism is shown in Figure 2.1 and is repeated creating long chains of several thousands to hundred thousands repeated units [3]. Solid PP contains a great number of such chains, with large variation in lengths.

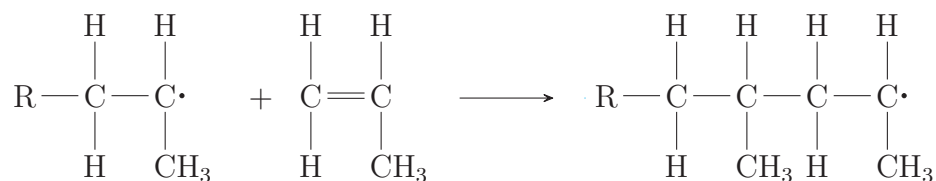


Figure 2.1: Polymerisation of polypropylene

In polymers, the intermolecular bonds are of great importance. Depending on the bonding between the chains, polymers can be divided into two groups, thermoplastic- and thermosetting polymers. Thermoplastic, or linear polymers, have weak hydrogen- or *van der Waals* intermolecular bonding, while thermosetting, or crosslinked, polymers also contain some covalent bonds between the chains in addition to the weaker bonds. Due to the linear shape of the PP backbone, only weak bonds are present between the molecules. Therefore it is a thermoplastic polymer. Even though the

van der Waals bonds are weaker than the covalent bonds, they have a significant impact on the mechanical properties of the material, due to the length of the molecular chains.

Although the molecular structure of PP is referred to as linear, the backbone atoms are arranged in a zigzag fashion. This is a result of the equilibrium angle between alternating carbon atoms being 109° [3]. Additionally, the carbon atoms in the chains can rotate about the intermolecular bonds in a spatial arrangement referred to as *molecular conformation*. Therefore, an individual PP chain will form in a seemingly random manner during polymerisation, causing extensive intertwining and entanglement with neighbouring chains. Straightening of these entanglements is responsible for the elastic behaviour of PP.

PP is a semicrystalline material, containing both crystalline and amorphous regions. In the crystalline regions, the molecular chains are folded back and forth in a regular fashion called lamellae, while in the amorphous regions, the molecules are randomly oriented. Folded-chain lamellae tend to grow in a spherical shape from the nucleation site, creating so-called spherulite structures. The degree of crystallinity has a great effect on the mechanical properties of polymers. Due to the close packing of molecular chains in the crystalline regions, it is associated with an extensive amount of secondary van der Waals bonding. In the amorphous regions, the lack of ordered molecular chains result in a smaller amount of secondary bonds. Therefore, the strength of the polymer increases with the degree of crystallinity, but at the cost of ductility. Since the amorphous regions lack order, the molecular chains are allowed to disentangle and align before the chains start sliding with respect to each other. This process is associated with relatively large deformations. The crystalline regions have a higher strength, but will separate and break suddenly, with little warning in form of deformation [4].

2.1.2 Mechanical behaviour

In order to get a better understanding of the mechanical behaviour of semicrystalline polymers, a section describing their underlying microscopic deformation mechanisms might be useful. The deformation can be divided into five stages, as shown in the generic tensile stress-strain curve in Figure 2.2. Initial elastic deformation is caused by straightening of the molecular chains. Weak van der Waals bonds between molecular chain segments govern the mechanical behaviour in this region. The upper yield point corresponds to the formation of a small neck in the gauge area of the specimen, as the stress reaches a local maximum. Inside the neck, the molecular chains

are aligned parallel to the loading axis. Once the neck is created, some polymers experience strain softening, where an increasing strain results in a reduction in the stress. This effect is, however, not present in all polymers, and seems to be related to the ability of the molecular chains to reorganise [5].

As the deformation continues, the neck region propagates along the gauge length and the chain reorientation phenomenon continues. This process is called cold drawing, and is completed once the neck has reached the ends of the gauge area. At this stage, the mechanical behaviour is controlled by stretching of the covalent bonds between carbon atoms. Finally, fracture results from severing of the now aligned molecular chains. There are two main mechanisms that might cause yielding and fracture in polymers. These will be introduced in the following section.

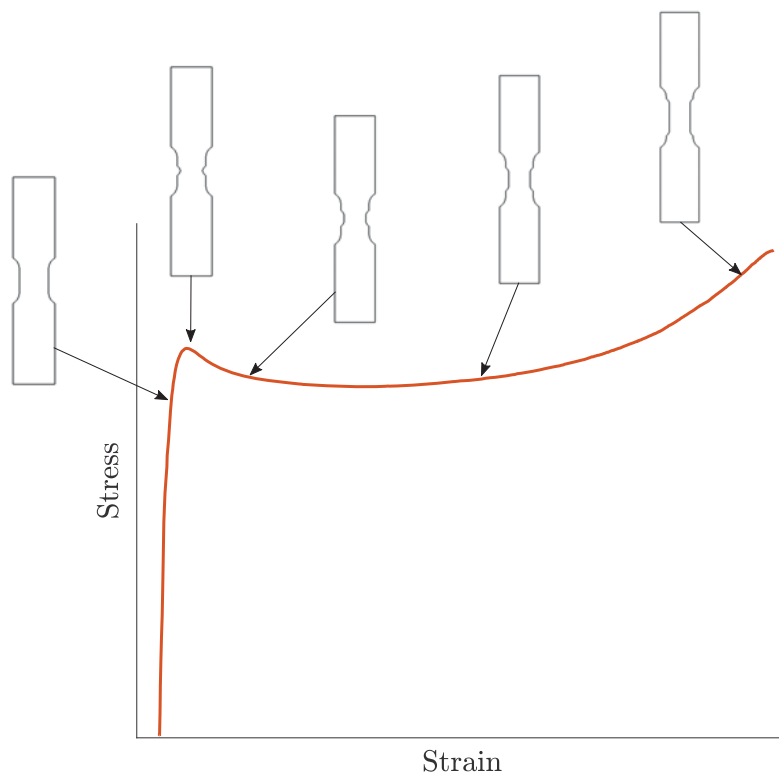


Figure 2.2: Schematic tensile stress-strain curve for a semicrystalline polymer

2.1.3 Yielding and fracture behaviour

There are two mechanisms that can cause yielding in polymers, *shear banding* and *crazing*. Both mechanisms are associated with inhomogeneous plastic deformation of the specimen. Shear banding occurs when the molecular chains slide with respect

to each other when subjected to a critical shear stress [6]. Crazing, however, corresponds to growth of microvoids where the stress concentration is high, illustrated in Figure 2.3. Such stress concentrations often initiate at surface scratches, mineral particles or even small voids that were introduced to the polymer matrix during manufacturing.

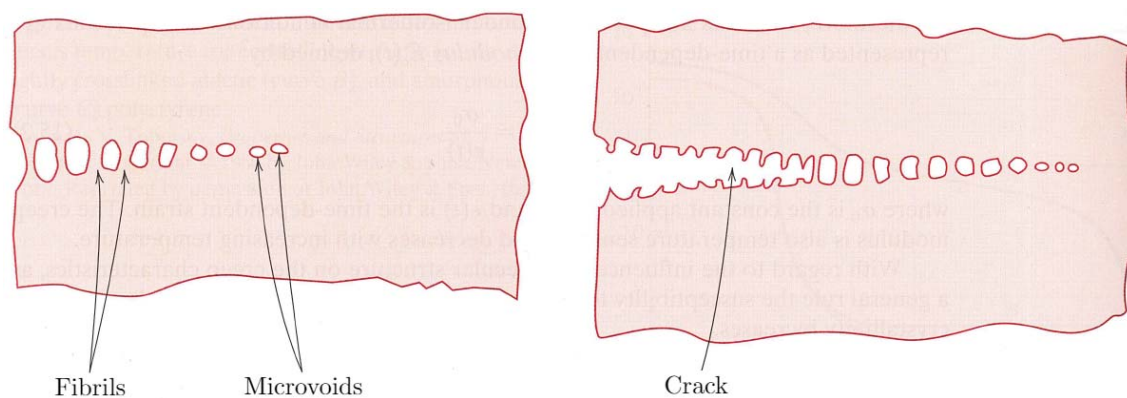


Figure 2.3: Schematic illustration of the crazing mechanism leading to fracture [4]

Due to the growth of microvoids, crazing is associated with an increasing volume, whereas the volume remains essentially constant during shear banding [5]. Hence, crazing is a *dilatation process*, i.e. one that causes changes in volume, and is greatly enhanced by the hydrostatic stress, while shear banding favors a large deviatoric stress component. Crazing can be identified on a macroscopic level, as a region of a low refraction index. This effect is often referred to as *stress-whitening*. The orientation of the fracture surface resulting from the two mechanisms is also different. While the crazes are formed perpendicular to the maximum principle stress direction, the shear bands coincide with the angle of the octahedral shear stress, which is based on von Mises yield criterion. The angle, however, depends on the ductility of the material [3].

Fracture in polymers is caused by a process called *chain scission* on a microscopic level, where the covalent bonding between chain segments are broken. Although the theoretical strength of these molecular chains may be several orders of magnitude higher than the strength at fracture, defects such as crazes in the material can create significant stress concentrations. Also, unevenly stressed molecular chains in the polymer might facilitate chain scission [6]. Once the strain becomes sufficiently high, *fibrils* of aligned molecular chains are created between the microvoids. The reduction in effective cross-sectional area causes one or more of these molecular chains to break. This process subsequently leads to chain scission in the neighbouring molecules and is repeated until the entire fibril ruptures. A similar stress redistribution effect causes the surrounding fibrils to fail, leading to fracture on a macroscopic level, as

shown in Figure 2.3. Another microscopic failure mechanism in polymers is called *chain disentanglement*. The process involves separation of molecular chains, while each chain remain intact. Both the degree of chain entanglement and length of molecules will effect whether chain disentanglement occurs or not.

In order to enhance the ductility of polymers, low-modulus, rubber particles are often added to the matrix. These particles provide nucleation sites for voids, such that rupture occurs in the second phase prior to the fibrils. Absorption of energy during rupture of the rubber particles increases the ductility of the polymer. However, this comes at the expense of yield strength, which is reduced by the addition of these particles [6]. For the PP grade studied in this thesis, a secondary phase of elastomeric particles is finely dispersed in the PP matrix. This is achieved by adding a ethylene monomer during the final stage of the polymerisation, resulting in spherical particles of *ethylene-propylene copolymer rubber* (EPR) [7, 8]. The ultimate goal of this process is to increase the fracture toughness and impact resistance [9]. The presence of these rubber particles and how they affect crack growth can be revealed in a microscope, hence SEM analyses were be performed in this project.

2.1.4 Brittle-ductile behaviour

Due to the extreme conditions that the door trim is exposed to during a cold impact, the brittle-ductile behaviour of PP is of particular interest in this thesis. The mechanical behaviour of thermoplastic polymers is highly sensitive to temperature, strain rate and stress state. Depending on these conditions, either brittle or ductile behaviour is possible. An interesting property of polymers, is the time-temperature superposition effect, meaning that an increase in strain rate has an equivalent effect as a decrease in temperature [10]. The transition from brittle to ductile can result from small changes in the previously stated conditions, but has a significant impact on the mechanical properties. In order to distinguish between the brittle- and ductile failure mode, both the energy absorption before fracture, and the appearance of the fracture surface can be examined.

Temperature dependence

The temperature dependence of the brittle-ductile transition is a well-researched topic. A phenomenological hypothesis by Ludwig-Davidenkov-Orowan [11] predicted that brittle fracture and plastic flow are independent processes [12]. Once the flow stress reaches a critical value, the material fractures, as shown in Figure 2.4a. This suggests that the brittle fracture stress, σ_B , and the yield stress, σ_Y , are given by

separate curves with respect to the temperature, as seen in 2.4b. The brittle stress curve is much less affected by the temperature than the yield stress curve, although both curves decrease with increasing temperature.

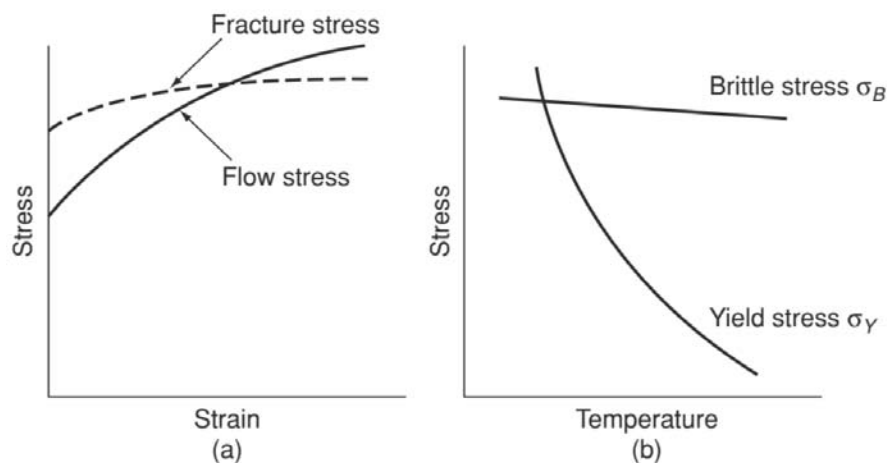


Figure 2.4: Phenomenological brittle-ductile transitions [12]

Although the brittle-ductile transition in polymers is, in general, believed to be related to the enhanced motion of the molecular chains with increasing temperature, this is not the case for most thermoplastics [12]. However, the *glass transition temperature*, T_g , is still used to describe the abrupt transition from rigid to rubbery state with increasing temperature. The temperature is also found to cause other changes in the mechanical properties of polymers, such as stiffness, heat capacity and coefficient of thermal expansion [4].

Strain rate dependence

An increase in the strain rate will typically increase the brittle-ductile transition temperature. The process can be represented by a shift to the right of the curves shown in Figure 2.4a. Similar to what is seen with temperature, the σ_Y -curve is more sensitive to changes in strain rate than the σ_B -curve.

As the strain rate is increased, there is another effect that plays an important role in the fracture of the material. When the loading rate is high, the heat generated by plastic work is unable to diffuse, and the temperature increases. This effect is referred to as *adiabatic heating*. For low strain rates, however, the heat has time to transfer from the specimen and isothermal conditions are achieved. Since the isothermal-adiabatic transition does not affect the yield stress, it does not affect the ductile-brittle transition either. However, due to the considerable reduction in energy at fracture, the isothermal-adiabatic transition should be considered at

elevated strain rates such as impacts, even if brittle fracture does not occur [12]. Although the transition is dependent on material properties and specimen size, strain rates in the order of 10^{-2} to 10^0 s $^{-1}$ may experience adiabatic heating [13].

Stress triaxiality

The stress triaxiality ratio has also been found to have a significant effect on the brittle-ductile transition of thermoplastic polymers [14]. The stress triaxiality, σ^* , is defined as stress in all three spatial direction, and is given by

$$\sigma^* = \frac{\sigma_H}{\sigma_{eq}}, \quad (2.1)$$

where σ_H is the hydrostatic stress and σ_{eq} is the equivalent von Mises stress, which will be introduced later. Increasing the triaxiality has shown to promote brittle fracture of polymers [15, 16]. In many cases, the introduction of a notch in the test specimen is used to obtain a higher stress triaxiality. A stress triaxiality of $\sigma^* = -\frac{1}{3}$ corresponds to uniaxial compression, $\sigma^* = 0$ is pure shear, $\sigma^* = \frac{1}{3}$ corresponds to uniaxial tension while $\sigma^* = \frac{2}{3}$ is a biaxial stress state, all of which are relevant for this thesis.

2.1.5 Production process

The door trim investigated in this thesis is created in a process called injection moulding. Injection moulding utilises heat and pressure along with a mould cavity in order to form the part. The manufacturing process allows for complex geometries at a low production-cycle time, resulting in components of near net shape. Hence, little or no subsequent machining is required to complete the geometry of the part [17]. Due to the cost related to fabrication of moulds for complex parts, the process is only economical for large production quantities, making it well suited for the production of door trims.

A diagram of the injection moulding machine is shown in Figure 2.5, with its two main components; the plastic injection unit and the mould clamping unit. In the injection unit, plastic pellets are supplied from the feed hopper and fed down the barrel by the reciprocating screw. The rotating motion of the screw allows for mixing and uniform heating of the polymer, in addition to driving the molten material into the mould. To allow for quick injection into the mould, the screw not only rotates, it also rapidly moves forwards, acting as a ram. Backwards flow of the

material is prevented by a nonreturn valve, mounted on the tip of the screw. The molten polymer is further injected into the mould, operated by the clamping unit. It consists of two platens, one stationary and one movable, each holding one section of the mould. To achieve easy access of the finished part, while still obtaining an appropriate clamping force, the movable platen is operated by a hydraulic cylinder.

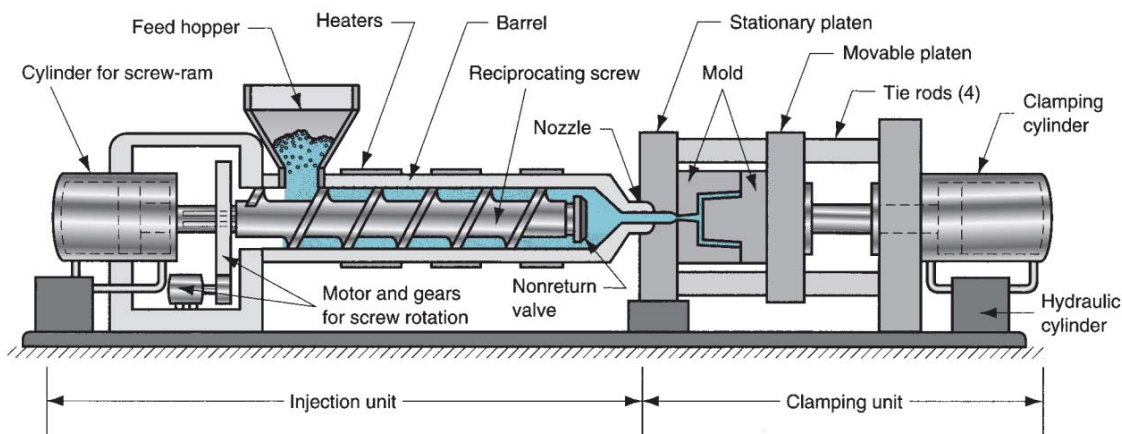


Figure 2.5: Schematic diagram of an injection moulding machine [17]

A brief description of some common defects in injection moulded parts might be appropriate at this point, since such defects can affect the performance of the finished parts. Due to the high thermal expansion coefficient of polymers, shrinkage may occur in the mould during cooling. This effect is greater in semicrystalline- than in amorphous polymers [17]. As a result of the different cooling rates between the skin and the core of the section, the skin solidifies before the core. As the core material solidifies, the shrinkage manifests itself as voids or warpage inside the component. In addition, the flow direction of molten material can cause heterogeneous crystallisation of the polymer. Research done by Kantz et al. [18] suggested that three distinct crystalline zones often can be observed in injection moulded polypropylene parts: A nonspherulitic skin of highly oriented molecules along the flow direction and a spherulitic core, separated by an intermediate shear zone. Another defect that is common in injection moulding of complex parts, is weld lines. These are formed when opposing polymer melt fronts meet and join in the mould. Due to the incomplete diffusion between these melt fronts, weld lines are associated with significant loss in strength [19]. Hence, highly anisotropic mechanical behaviour is often found in injection moulded parts.

2.2 Analytic background

In order to study the behaviour of polymers when subjected to mechanical stress, some important characteristics will be presented. The definitions of stress and strain will be introduced as well as some important mechanical properties of materials. Figure 2.6 will be used to visualise the following discussion. To measure the strains that occur in the test specimen when subjected to certain loads, a technique called *digital image correlation* (DIC) was employed. This method will be introduced in this section.

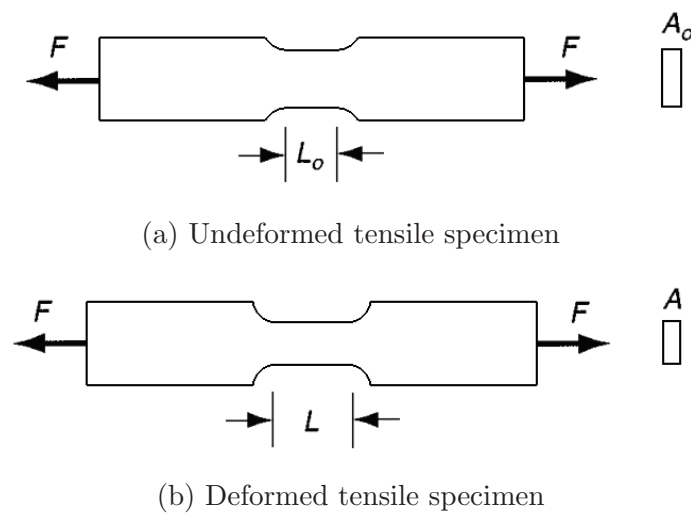


Figure 2.6: Tensile specimen in uniaxial stress state

2.2.1 Material properties

The classic approach, used to to define stress and strain, is relative to the original cross-sectional area and gauge length. These measures are called nominal stress and strain and are based on the assumption of small deformations. The nominal stress, s , is given by

$$s = \frac{F}{A_0}, \quad (2.2)$$

where F is the applied force normal to the original cross-sectional area of the specimen, A_0 , as shown in Figure 2.6a. Furthermore, the nominal strain, e , is expressed by

$$e = \frac{\Delta L}{L_0} = \frac{L - L_0}{L_0}, \quad (2.3)$$

where L is the current gauge length at any point during deformation while L_0 refers to the original gauge length.

Since polymers often are associated with significant amounts of elongation prior to fracture, logarithmic strain measures might be more appropriate. The logarithmic strain is defined relative to the current cross-sectional area and gauge length. Hence, the logarithmic strain, ε , is defined by

$$\varepsilon = \ln \left(\frac{L}{L_0} \right), \quad (2.4)$$

where L and L_0 are the current- and original gauge length, respectively. Similarly, true stress, σ , is also defined relative to the current cross-sectional area

$$\sigma = \frac{F}{A}, \quad (2.5)$$

where A is the actual cross-sectional area resisting the applied force, F .

A uniaxial representation of the strains is, however, only sufficient up to a certain point during a tensile test, for which this assumption no longer holds. Additionally, uniaxial stress is not guaranteed for an arbitrary stress state. The strain must therefore be decomposed into three directions once the deformation becomes inhomogeneous. Hence, the logarithmic strain in x-, y- and z-direction are introduced as ε_{xx} , ε_{yy} and ε_{zz} , respectively. The sum of these three strain components now corresponds to the volumetric strain, ε_V , in the specimen

$$\varepsilon_V = \varepsilon_{xx} + \varepsilon_{yy} + \varepsilon_{zz}. \quad (2.6)$$

This can be described as the amount of volume change a material experiences during deformation. A material that experiences no volume change when it is deformed, is called incompressible, while a material for which deformation also results in a change in volume is compressible. Hence, for an incompressible material, the longitudinal strain component can be expressed as

$$\varepsilon_V = 0, \quad \Rightarrow \quad \varepsilon_{xx} = -\varepsilon_{yy} - \varepsilon_{zz}. \quad (2.7)$$

It should, however, be noted that many materials experience some volume change when deformed, but are still assumed to be incompressible. The decomposition of

the logarithmic strain also enables the true strain to be expressed in terms of the nominal stress. Since the change in cross-sectional area can be expressed using the lateral strain components, the general relation is obtained

$$\sigma = s \cdot \exp(-\varepsilon_{yy} - \varepsilon_{zz}). \quad (2.8)$$

Employing the relation given in Eq. (2.7), the equation above can be simplified for incompressible materials. The true stress can now be calculated by

$$\sigma = s \cdot \exp(\varepsilon_{xx}). \quad (2.9)$$

Although the deformation is reversible in the elastic domain, the plastic domain is associated with irreversible deformation. Hence, when a material is plastically deformed, it does not fully recover once it is unloaded. It can therefore be useful to divide the strains into an elastic and a plastic part

$$\varepsilon = \varepsilon^e + \varepsilon^p, \quad (2.10)$$

where ε^e and ε^p correspond to the elastic- and plastic logarithmic strain, respectively. In this case, it is assumed that the elastic region is approximately linear. This assumption holds for metallic materials, while many polymers experience nonlinear elastic behaviour. Such effects will not be considered in this thesis. The logarithmic elastic strain can therefore be expressed using Hooke's law

$$\sigma = E\varepsilon^e \quad \Leftrightarrow \quad \varepsilon^e = \frac{\sigma}{E}, \quad (2.11)$$

where E is the Young's modulus of the material. Young's modulus can be regarded as the slope of the stress-strain curve of the material in the elastic domain and is an important material property. This relation can be used in order to obtain the plastic strain by substituting into Eq. (2.10), and solving for the logarithmic plastic strain

$$\varepsilon^p = \varepsilon - \frac{\sigma}{E}. \quad (2.12)$$

Another important property of materials is the Poisson's ratio. It describes the relation between the longitudinal- and transverse logarithmic strain components in the elastic domain,

$$\nu_y = -\frac{\varepsilon_{yy}^e}{\varepsilon_{xx}^e}, \quad \nu_z = -\frac{\varepsilon_{zz}^e}{\varepsilon_{xx}^e}, \quad (2.13)$$

where ν_y and ν_z correspond to the Poisson's ratios in y- and z-directions, respectively. The negative signs are included in the expressions since the two strain components normally have opposite signs. For isotropic materials, the strains in the lateral directions, perpendicular to the direction of the applied load, are equal, i.e. $\varepsilon_{yy}^e = \varepsilon_{zz}^e$. Hence, the Poisson's ratios in the two directions are also equal, i.e. $\nu_y = \nu_z$. Similarly, strain ratios are defined for the plastic domain as well

$$R_y = -\frac{\varepsilon_{yy}^p}{\varepsilon_{xx}^p}, \quad R_z = -\frac{\varepsilon_{zz}^p}{\varepsilon_{xx}^p}, \quad (2.14)$$

where R_y and R_z are the retraction ratios in y- and z-directions, respectively. As for Poisson's ratios, the retraction ratios in the two lateral directions are also equal for isotropic materials, i.e. $R_r = R_y = R_z$.

2.2.2 Digital image correlation

In order to measure the strain field that occurs within the test specimens during deformation, an optical measuring technique called DIC will be used. An extensometer is conventionally used to obtain the strains during uniaxial tensile testing. The strains can be calculated from the measurements assuming the deformation is homogeneous. This approach is generally satisfactory for metallic materials until necking, for which deformation becomes inhomogeneous. For polymeric materials, however, early necking and possible dilatation means that an extensometer is generally not applicable. High local strains also support the use of alternative measurement techniques. Hence, DIC is a good substitute that allows for determination of the strain fields during uniaxial tensile testing.

DIC has a range of applications including tracking of grayscale patterns, point tracking and edge tracing [20]. The former will be used in this thesis. The technique is not only limited to 2D, in-plane deformation measurements, but can also be extended to out-of-plane measurements in 3D analyses. The technique involves comparing digital images of the test specimen that are obtained throughout the deformation. A random speckle pattern is created on the surface prior to testing in order to produce a grayscale pattern that easily can be traced by the algorithm. In the DIC software, a virtual grid, or mesh, is placed over a reference image of the undeformed specimen. The pattern within each element of the mesh can then be traced during the entire test, allowing the software to calculate the surface deformations of the

specimen. This can, in turn, be used to determine the full-field 2D- or 3D strain maps.

2.3 Material model

In order to obtain an accurate representation of the behaviour of PP in numerical simulations, a material model is needed. Although most commercial FEM softwares provide material models that describe the behaviour of polymers, these are often simplified due to the complexity of such materials. A constitutive model for thermoplastics was proposed by Polanco-Loria et al. [21]. It has been refined since 2010, and will be referred to as the SPM. The model has been validated through several master theses [22, 23, 24, 2] and will be used in this thesis as well. The SPM is based on the following assumptions:

- Small elastic deformations and finite plastic deformations and rotations.
- Isotropic elastic behaviour.
- Isotropic viscoplastic behaviour.
- Pressure-dependent yielding.
- Isothermal conditions.
- Plastic dilatation.

A brief theoretical description of some important elements of the SPM [25] will be given in the following section.

2.3.1 Rheological model

A rheological model displaying the most important features of the SPM [25] is shown in Figure 2.7 for a uniaxial stress state. Rheological models employ basic elastic and viscous elements in order to describe the physical behaviour of the material. The model is divided into two parts, an elastic part to the left and a plastic part to the right. A linear viscoelastic model is used to describe the elastic behaviour of the material. This implies that the material's elastic properties are strain rate dependent and therefore, by increasing the strain rate, the elastic stiffness also increases. Such effects must be considered in creep and relaxation processes, where the time scale is significantly greater than a drop test. Also, the plastic deformations are considered

the most important in this case. Hence, the viscoelastic effects of the PP are assumed to be small and will not be included in this thesis.

A nonlinear viscoplastic model is used to describe the mechanical behaviour of the material in the plastic domain. It is comprised of a viscous element, a nonlinear spring and a frictional element, representing the viscous stress, kinematic hardening and isotropic hardening or softening, respectively. Kinematic hardening is an effect which causes a material to have a lower strength in compression after being plastically deformed in tension, or vice versa. Since no changed loading directions are expected in a drop test, kinematic hardening will not be employed. Although the rheological model illustrates the main features of the SPM in a uniaxial stress state, introduction of some relevant mathematical formulations in a more general multiaxial stress state is appropriate.

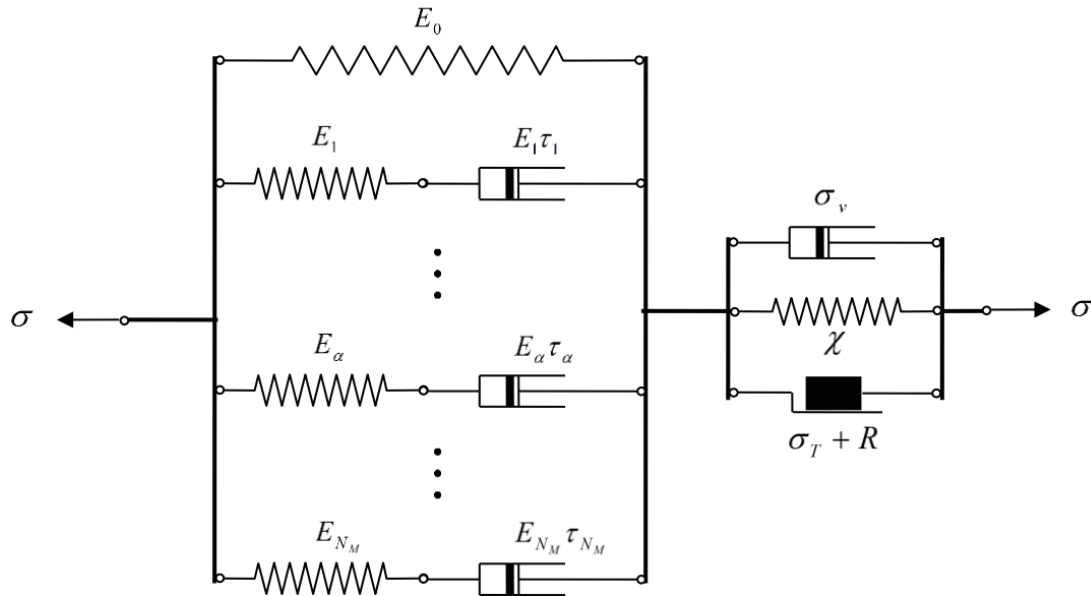


Figure 2.7: Illustration of the rheological model used in the SPM [25]

2.3.2 Hypoelasticity

A hypoelastic formulation is employed in the material model, as opposed to the initial proposal [21], where a hyperelastic formulation was used. This implies that the stress tensor no longer is obtained from strain energy functions, but rather that a rate form is used. Hence, the elastic constitutive equations are derived as functions of the elastic rate-of-deformation tensor, the result being that elastic deformations might also lead to energy dissipation. Since the elastic strains are assumed to be small compared to the finite plastic strains and rotations, it is reasonable to adopt

such a formulation [26]. In addition, a corotational stress approach is used to avoid the introduction of stresses resulting from rigid body motions. Hence, the linear hypoelastic relation is given by

$$\dot{\hat{\boldsymbol{\sigma}}} = \hat{\mathbf{C}}^\sigma : \hat{\mathbf{D}}^e, \quad (2.15)$$

where $\dot{\hat{\boldsymbol{\sigma}}}$ is the time derivative of the corotational stress tensor, $\hat{\mathbf{C}}^\sigma$ is the isotropic tensor of the elastic moduli while $\hat{\mathbf{D}}^e$ is the corotational elastic rate-of-deformation tensor. The hat-notation will be used to denote corotational variables throughout this thesis.

2.3.3 Yielding and plastic flow

Yield function

The yield function f is given by

$$f(\hat{\boldsymbol{\sigma}}, R) = \varphi(\hat{\boldsymbol{\sigma}}) - (\sigma_T + R), \quad (2.16)$$

where $\hat{\boldsymbol{\sigma}}$ is the corotational Cauchy stress tensor, $\sigma_{eq} = \varphi(\hat{\boldsymbol{\sigma}})$ is the equivalent stress, σ_T is the yield stress in uniaxial tension and R is the variable controlling isotropic hardening. Mathematically, the yield limit is reached when $f = 0$ for which plastic flow is allowed in the material. When $f < 0$, the material is in the elastic domain, while $f > 0$ is inadmissible.

The Raghava yield criterion

In order to capture the pressure-dependent behaviour of ductile polymers, the SPM utilizes the Raghava yield criterion proposed by Raghava et al. [27]. The relation is a modified version of the von Mises criterion and accommodates the difference between yield strength in tension and compression observed in polymers. Additionally, any dependence of the hydrostatic stress component in the stress state is accounted for. The yield criterion is given by

$$\varphi(\hat{\boldsymbol{\sigma}}) = \frac{(\alpha - 1) \text{tr } \hat{\boldsymbol{\sigma}} + \sqrt{(\alpha - 1)^2 (\text{tr } \hat{\boldsymbol{\sigma}})^2 + 4\alpha \Phi^2(\hat{\boldsymbol{\sigma}}')}}{2\alpha}, \quad (2.17)$$

where the pressure sensitivity in the material is described by the parameter $\alpha = \sigma_C/\sigma_T \geq 1$ for which σ_C is the yield strength in uniaxial compression. The von Mises norm for deviatoric stress tensors, Φ , is given by

$$\Phi(\hat{\boldsymbol{\sigma}}') = \sqrt{\frac{3}{2}\hat{\boldsymbol{\sigma}}' : \hat{\boldsymbol{\sigma}}'}, \quad (2.18)$$

where $\hat{\boldsymbol{\sigma}}'$ is the deviatoric stress tensor. These expressions are based on the stress tensor being decomposed into a deviatoric and a hydrostatic part, $\boldsymbol{\sigma} = \hat{\boldsymbol{\sigma}}' + \sigma_H \mathbf{I}$. Here, \mathbf{I} represents the identity matrix. Since classic plasticity theory is based on the assumption that yielding and plastic flow is only affected by the deviatoric stress component, such a separation is often convenient [28]. However, this is not the case for polymers, requiring that the pressure sensitivity is included in the correction of the yield criterion in Eq. (2.17). It should be noted that for $\alpha = 1$, the Raghava criterion reduces to the von Mises criterion given in Eq. (2.18).

The Raghava yield surface in principal plane stress is shown in Figure 2.8. Here, the yield criterion forms an ellipse. Different values of the pressure sensitivity, α , are plotted to demonstrate that the yield strength in uniaxial compression increases with increasing α . The yield strength in uniaxial tension, however, remains the same. The figure also shows the special case where $\alpha = 1$, i.e. the von Mises yield surface. In a more general principal stress state, the Raghava yield surface is represented by an elliptic cone oriented around the hydrostatic axis.

Flow potential

Since plastic deformations are irreversible, the following inequality must hold for the plastic dissipation, \mathfrak{D}_p , in order for the second law of thermodynamics to be satisfied

$$\mathfrak{D}_p = \hat{\sigma}_{ij} \hat{D}_{ij}^p \geq 0, \quad (2.19)$$

where \hat{D}_{ij}^p is the plastic rate-of-deformation tensor. The second law of thermodynamics states that the transformation of mechanical energy into heat must be zero or positive [26]. In order to satisfy this condition, the flow rule is defined by

$$\hat{D}^p = \dot{\lambda} \frac{\partial g}{\partial \hat{\boldsymbol{\sigma}}}, \quad (2.20)$$

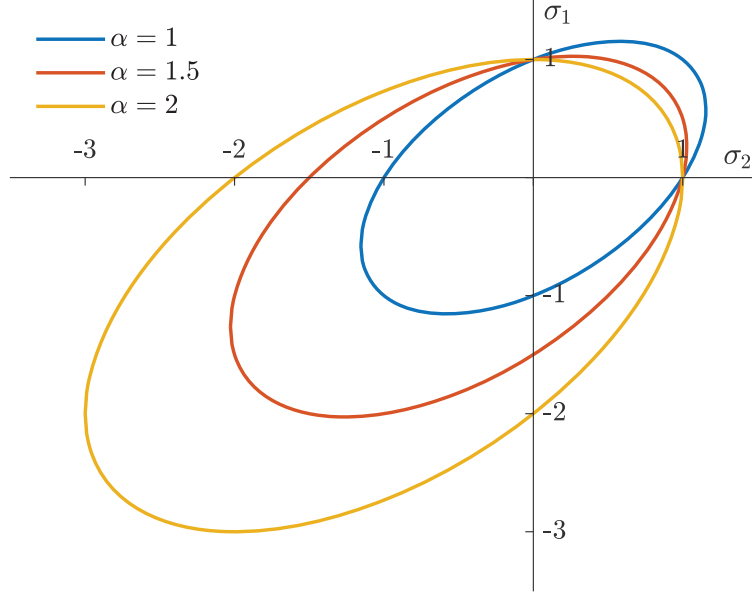


Figure 2.8: Raghava yield surface in plane stress

where $\dot{\lambda} \geq 0$ is the plastic parameter. Note that in the elastic domain $\dot{\lambda} = 0$, for which no plastic dissipation occurs. The plastic parameter is introduced in order to satisfy the yield condition, i.e. $f = 0$, in Eq. (2.16) for plastic loading and elastic unloading. The function defined by $g = g(\hat{\boldsymbol{\sigma}})$ is the flow potential, given by

$$g(\hat{\boldsymbol{\sigma}}) = \frac{(\beta - 1) \text{tr} \hat{\boldsymbol{\sigma}} + \sqrt{(\beta - 1)^2 (\text{tr} \hat{\boldsymbol{\sigma}})^2 + 4\beta \Phi^2(\hat{\boldsymbol{\sigma}}')}}{2\beta} \geq 0, \quad (2.21)$$

where the volumetric plastic strain is controlled by the material parameter $\beta \geq 1$. An isochoric, i.e. volume preserving, flow potential can be obtained by $\beta = 1$ while an associated flow rule is obtained by $\beta = \alpha$. Due to the dilatation observed for polymers during plastic flow, the Raghava yield function itself was originally suggested to act as the plastic potential. This approach did, however, turn out to overestimate the plastic strains. Hence, a non-associated flow potential given on a similar form as Eq. (2.17) is used in the constitutive model.

2.3.4 Viscoplasticity

For the material model to be able to account for the strain rate dependent plastic behaviour, viscoplasticity is included. Due to the dynamic nature of an impact re-

sulting from a drop test, this is an important feature in this thesis. When increasing the strain rate, the material becomes stiffer and the flow stress increases. Hence, the stress must be allowed to move outside the yield surface for which $f = 0$. The value of f greater than zero, must therefore correspond to the viscous stress. Substituting this condition into Eq. (2.16), the viscous stress, σ_v , is defined by

$$\sigma_v = \varphi(\hat{\boldsymbol{\sigma}}) - (\sigma_T + R). \quad (2.22)$$

By solving for the equivalent stress, the constitutive relation for rate dependency can be obtained by

$$\sigma_{eq} \equiv \varphi(\hat{\boldsymbol{\sigma}}) = \sigma_T + R + \sigma_v \quad \text{for } f > 0. \quad (2.23)$$

The following constitutive relation for the equivalent plastic strain rate, $\dot{\varepsilon}^p$, can now be adopted to model the rate-dependent plastic behaviour of the material

$$\dot{\varepsilon}^p = \begin{cases} 0 & \text{if } f \leq 0 \\ \dot{\varepsilon}_0^p \left\{ \exp \left[\frac{1}{C} \left(\frac{\varphi(\hat{\boldsymbol{\sigma}})}{\sigma_T + R} - 1 \right) \right] - 1 \right\} & \text{if } f > 0, \end{cases} \quad (2.24)$$

where the coefficient $\dot{\varepsilon}_0^p$ is the reference plastic strain rate and C is a constant governing the rate sensitivity of the material. Solving the expression with respect to the equivalent stress, the constitutive relation can now be expressed by

$$\sigma_{eq} \equiv \varphi(\hat{\boldsymbol{\sigma}}) = (\sigma_T + R) \left[1 + C \ln \left(1 + \frac{\dot{\varepsilon}^p}{\dot{\varepsilon}_0^p} \right) \right] \quad \text{if } f > 0. \quad (2.25)$$

2.3.5 Hardening and softening

For metallic materials, work hardening is associated with dislocation movement and -generation inside the crystal lattice. These dislocations interact, causing them to become pinned or entangled. The result is that dislocation movement becomes more constrained, and the material is strengthened. For polymers, however, work hardening is caused by the molecular chains becoming increasingly aligned. Once the chains are aligned, further deformation is opposed by the covalent bonding between atoms in the molecular chains. Due to the large variety of hardening behaviour for different polymers, an extended Voce rule with three isotropic hardening terms is used in the SPM. The hardening rule is given by

$$R = \sum_{i=1}^3 Q_{Ri} \left(1 - \exp \left(- \frac{\theta_{Ri}}{Q_{Ri}} \varepsilon^p \right) \right), \quad (2.26)$$

where θ_{Ri} and Q_{Ri} are model parameters controlling initial hardening and saturation for each hardening term i , respectively. The three hardening terms can be combined such that the appropriate behaviour of the material can be modelled. Depending on the desired material behaviour, different degrees of hardening, softening or re-hardening can be obtained.

2.3.6 Adiabatic heating

The mechanical behaviour of polymers is often highly sensitive to adiabatic heating during load conditions with high strain rates. Adiabatic conditions imply that the heat generation due to plastic dissipation has no time to diffuse, resulting in a temperature increase in the material. This phenomenon is considered an important effect in impact loading and can cause large local temperature increases. Polymers are particularly sensitive to adiabatic heating, since a small change in temperature has a significant effect on their mechanical behaviour. Additionally, the poor heat conduction properties of polymers means that the heat diffusion is slow, causing even larger local increases in temperature. In adiabatic processes, this might eventually lead to strain softening for which increasing plastic strain causes the stress to decrease. The temperature rate, \dot{T} , is calculated by the following expression

$$\dot{T} = \frac{\mathfrak{D}_p}{\rho c_T}, \quad (2.27)$$

where ρ is the material density and c_T is the specific heat capacity. By time integration of the expression above, the temperature increase, ΔT , can be obtained by

$$\Delta T = \int_0^t \frac{\mathfrak{D}_p}{\rho c_T} dt. \quad (2.28)$$

Although polymers are notorious for being highly sensitive to changes in temperature, adiabatic heating is not included in the SPM. The model does, however, allow for the temperature increase to be calculated, but no feedback is implemented. Care must therefore be taken in simulations of transient-dynamic load cases, as any softening effects due to adiabatic heating are not accounted for.

2.3.7 Damage

Damage coupling

Since ductile damage in polymers is often caused by growth of microvoids, which eventually coalesce, the load carrying capacity of the material is reduced as deformation progresses. This effect is recreated in the material model through damage coupling. Hence, the evolution of damage also leads to softening in the material. This is implemented in the material model by substituting the stress tensor $\hat{\boldsymbol{\sigma}}$ with an effective alternative in all constitutive equations that are used in the SPM. The effective stress tensor, $\hat{\boldsymbol{\sigma}}_{eff}$, is given by

$$\hat{\boldsymbol{\sigma}}_{eff} = \frac{\hat{\boldsymbol{\sigma}}}{1 - D}, \quad (2.29)$$

where $0 \leq D < 1$ is the damage variable. Note that as D approaches unity, the effective stress tensor tends to infinity. Failure is therefore introduced by a critical damage value $D_C < 1$. It should also be noted that uncoupled damage can be obtained, for which the relation above is not utilised. In that case, the damage evolves normally, but has no influence on the constitutive relations in the model before fracture occurs.

Damage evolution

Damage evolution is implemented in the SPM by the following relation

$$\dot{D} = (1 - D) \text{tr} \hat{\mathbf{D}}^p, \quad (2.30)$$

where \dot{D} is the time derivative of the damage variable. By integrating the relation above, the damage evolution can be expressed on the form

$$D = 1 - (1 - D_I) \exp(-\varepsilon_V^p), \quad (2.31)$$

where D_I is the initial damage and ε_V^p is the volumetric plastic strain. The initial damage parameter can be used to introduce possible defects which might be present in the material prior to deformation.

Fracture

Finally, fracture occurs once the damage variable reaches the critical value $D = D_C$, resulting in the failure of an integration point. The number of integration points that must fail before the element is eroded, depends of the FEM software being used. Element erosion is used to model fracture and crack propagation in the SPM. When critical damage is reached, the stress tensor of the element is set to zero, and it can no longer carry any load.

2.4 Finite element analysis

In order to ensure realistic numerical representations of physical problems in FEA, selection of appropriate options for the designated problem must be emphasised. Additionally, the efficiency of the models with respect to computational time is of importance. Hence, different alternatives regarding solution methods, mesh and element formulation, as well as control algorithms with respect to undesirable deformation modes should be chosen carefully. The following section provides a brief discussion regarding some of these matters with emphasis on the most important options.

2.4.1 Solution methods

In general, the time integration scheme in FEA is selected based on the test duration, as well as level of nonlinearity of the problem at hand. When protracted test times are modelled, and the level of nonlinearity is distributed over the whole simulated test duration, *implicit methods* are often the preferred choice [29, 30]. An implicit solution method involves solving equations simultaneously for the entire model during every time step. Furthermore, implicit methods imply indirect solving of the equilibrium equations using iterations, which subsequently leads to convergence, or undesired divergence. This method is rather computationally demanding, but allows for larger time steps and superior stability compared to the *explicit method*.

Explicit methods imply direct solving of the equilibrium equations using values already known from previous time steps. A single equation is used to evaluate new nodal variables for each time step. This may give a huge advantage in computational efficiency since no iterations are required for the equation solving. However, explicit methods are known for being only conditionally stable. This is one of the main drawbacks of the method. To avoid information propagating further than the

distance between neighbouring nodes, Δt must be chosen sufficiently small [29]. For an undamped material, this critical time step, Δt_{cr} , can be determined by

$$\Delta t_{cr} \leq \frac{L^e}{c_d} = \frac{L^e}{\sqrt{E/\rho}}, \quad (2.32)$$

where L^e is the characteristic length of the smallest element in the FE mesh and c_d is the dilatational wave speed in a particular medium. Without going into further detail, explicit solution methods have shown great promises in solving highly nonlinear dynamic problems, like crashworthiness and structural impacts [30, 31, 32].

2.4.2 Mass scaling

Due to the small time step required in explicit solution methods, *mass scaling* provides a solution to reduce the computational cost [30, 32]. This is feasible since the critical time step depends on the density, as discussed in the preceding section. Thus, by increasing the size of the time step in each cycle, reduced computational cost and improved performance can be attained.

The physical interpretation of mass scaling in numerical modelling involves assigning an artificially large mass to the material by increasing its density. From Eq. (2.32), it is evident that the critical time increment, Δt_{cr} , increases with the material density, ρ . Hence, numerical stability is achieved for larger time steps, and the duration of the simulation is greatly reduced. However, a consequence of dynamic problems, introducing higher strain rates, is possible inertial effects. Hence, care must be taken such that the associated kinetic energy, and thus the simulation results, does not get overly affected by the mass scaling. If the mass is increased excessively, it may produce substantial dynamic effects possibly leading to inaccurate results. Therefore, the ratio between the internal- and kinetic energy in the system should be monitored carefully.

2.4.3 Full- and reduced integration

In FEA, the most common method for numerical integration of matrices is through the use of *Gauss quadrature*. This is due to the accuracy for a given number of sampling points, which is better for the Gauss quadrature compared to other quadrature rules [29]. The method approximates the definite integral of a given polynomial and locates sampling points. These points are traditionally called *Gauss points*, which

are further assigned an individual weighting factor in order to minimise the numerical error. The quadrature rule is designed to yield exact integration for polynomials of order $2n - 1$, if n sampling points are used.

The expressions *full-* and *reduced integration* are often employed in FEA, and refer to the order of the integration scheme. The former implies a Gauss quadrature scheme, where the number of quadrature points is sufficient to provide exact integration of all stiffness coefficients incorporated in the element stiffness matrix. This is, however, only true when the element exerts its regular shape, i.e. when it is geometrically undistorted. The latter term is, on the other hand, a similar integration scheme, but of lower order than what is required for the full integration. Hence, reduced integration elements provide less accurate estimates of the integrated polynomials than the full integration counterpart.

In general, the reduced integration elements are the preferred formulation, primarily due to two reasons; they are more computationally efficient since the number of integration points is one order lower, and they tend to soften the FE model. This is favourable, since FE modes are generally too stiff, due to the shear- and volumetric locking that is associated with some elements. Hence, the reduced integration element is favoured in explicit FEA, since many time steps are required. The softening effect introduced by the reduced integration is due to so-called parasitic polynomial terms, that do not contribute to the element stiffness in the Gauss points, for which they become zero [29]. In addition, reduced integration elements may experience *spurious modes*.

Figures 2.9a and 2.9b render two general quadrilateral shell elements employing reduced- and full integration, respectively. The positioning of the nodes and the Gauss quadrature points within the element are illustrated in the figures. Here, the blue dots represent the four nodes of the element, while the red dots represent the integration points through the shell thickness. Additionally, the figures display the local degrees of freedom for one of the nodes.

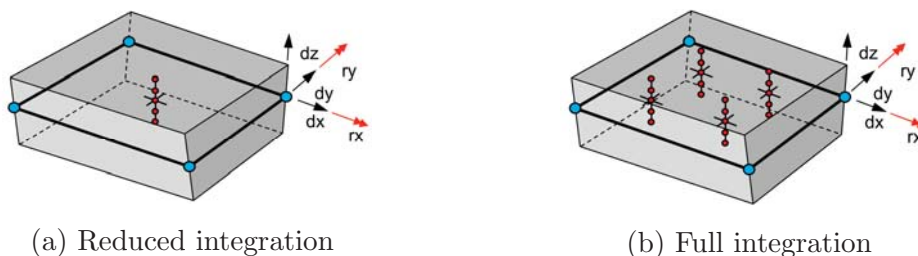


Figure 2.9: Two different quadrature rules possible in the quadrilateral shell element [33]

2.4.4 Spurious modes

Spurious modes of deformation may occur in reduced integration elements due to rank deficiency of the stiffness matrix [29]. Rank deficiency, or mathematical instability, imposes so-called matrix defects which could lead to a singular stiffness matrix caused by the numerical integration. Another common expression for these spurious modes is *hourglassing*. Hourglassing is an undesirable phenomenon where the element exhibits a zero energy mode, i.e. a deformation mode that do not occupy strain energy [34]. This nonphysical mode of artificial deformation does not produce strains or stresses, or forces from which these arise. Hence, no energy is present in spite of noteworthy deformation. This may eventually lead to nonphysical and large deformations of the numerical model. Such modes tend to emerge through oscillatory patterns which often need to be stabilised [29]. The associated frequencies usually deviate from the component's global structural response which results in distorted elements. Occurrence of such undesirable modes could produce inaccurate results and should be minimised. In FEM softwares, the typical characteristics regarding hourglassing are no stiffness and a zigzag deformation pattern in the mesh.

These spurious deformations occur without provoking energy growth. To account for this, *hourglass control* is introduced, which implements an artificial energy into the solution without excessive constraints on the physical response [35]. Two common methods for avoiding these zero energy modes are either adjustment of the bulk viscosity of the numerical model, or addition of a small elastic stiffness. For highly dynamic explicit analyses, the viscosity based type is recommended, while the stiffness based type serve as a multipurpose control algorithm for quasi-static implicit- and explicit analyses [36].

Spurious modes are difficult to detect in nonlinear explicit dynamic analyses. This is primarily due to the fact that they may diminish through energy-dissipating material behaviour as e.g. plastic work. Thus, the artificial energy introduced by the hourglass control algorithm is often hard to detect because the solution may appear reasonable. For explicit dynamic problems, inspection of the energy balance of the numerical model throughout the analysis is important, as this may alarm if numerical instability is present. Nevertheless, to completely eliminate the concerns regarding the artificial energy that emerges when hourglass control is implemented, quadrature rules employing full integration can be utilised.

2.5 Scanning electron microscopy

In order to relate the macroscopic behaviour of PP to the microscopic failure mechanisms, SEM analyses will be performed on a selection of test specimens. The effect of adiabatic heating on the fracture surface is of special interest, as well as exposing any differences between the microstructure of material sample plates compared to the door trim cutouts. The technique involves a highly focused electron beam which is used to scan the surface that is analysed. SEM is considered the best method of evaluating the structural properties of polymers, providing a better resolution than ordinary optical microscopes [37].

2.5.1 Scanning process and image formation

The main components of a SEM are an electron column, a sample stage and one or more detectors. A schematic representation of a SEM is provided in Figure 2.10. Due to the short life of the electron beam in air, a vacuum is required for the microscope to operate. The electron beam is emitted from its source, scanning the sample surface in a raster pattern, i.e. from side to side in lines from top to bottom. On the sample surface, secondary electrons are emitted before being detected and amplified by the microscope. In the secondary electron detector, the electrons are simply counted. Hence, no determination of the position of which the secondary electrons have, can be provided by the detector. The image projection is exclusively obtained due to the electron beam raster and image raster being synchronised [38]. Furthermore, no understanding for the chemical composition of the polymer or second phase particles can be obtained using SEM. It is merely used to provide micrographs of the surface.

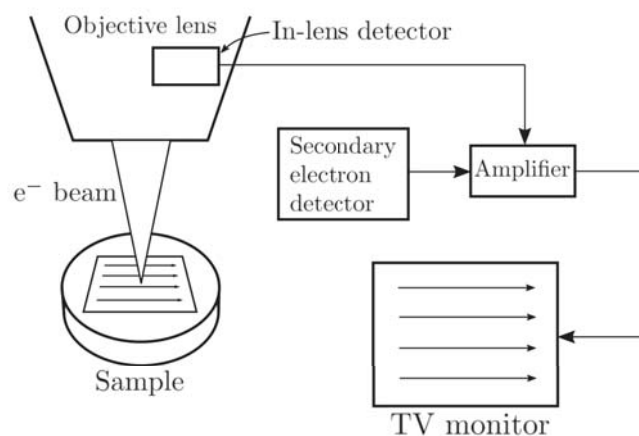


Figure 2.10: Block diagram of a scanning electron microscope [38]

2.5.2 Sample preparation

The complexity of the SEM analysis increases drastically due to the low electrical conductivity of thermoplastic materials. For such materials, accumulation of negative charge of the sample surface may lead to a serious reduction in image resolution. At worst, such an accumulation might damage the surface. Care must therefore be taken during the preparation of the sample. In order to increase the conductivity of the test specimens, a thin gold film is sputter coated onto their surface prior to the SEM analysis. This allows the charge to be dispersed during the analysis.

2.5.3 Resolution

In the right conditions, a resolution of 1 nm can be achieved with SEM. This is close to other microscopy techniques such as transmission electron microscopy (TEM) and atomic force microscopy (AFM). These techniques, however, demand a much more comprehensive sample preparation. Traditionally, the resolution obtained with SEM is related to the electron beam spot size, which can be altered with the acceleration voltage. The electron beam spot size decreases with increasing acceleration voltage [37]. No resolution smaller than 1 μm will, however, be used in this thesis.

Quasi-Static and Meso-Dynamic Material Testing

To allow for an accurate representation of the door trim in numerical FEM simulations, the PP material must be characterised. This was achieved through an extensive tensile test programme, where particular emphasis was placed on investigating the strain rate sensitivity of the material. The experimental data would later serve as a basis from which the material model could be calibrated. Additionally, revealing any material behaviour that could not be replicated by the SPM was of special interest. Discovering such material properties could provide a better understanding of the numerical discrepancies associated with the door trim simulation conducted during Schwenke's work [2]. The test procedures and -results are presented in the following sections.

3.1 Introduction

To investigate the rate sensitivity of the material, several tests in the quasi-static and meso-dynamic strain rate regimes were conducted. These regimes, with respective strain rates, are shown in Figure 3.1 below, in addition to the test device. The quasi-static regime is associated with slow deformation, where the material is assumed to be in internal equilibrium. Higher rates are termed meso-dynamic and, in turn, dynamic. In these regimes, adiabatic heating effects are important. In the latter, inertia effects should be considered. Additionally, possible inhomogeneous material behaviour of the door trim, and comparison with the material sample plates, were

3.1. Introduction

of special interest. Schwenke’s work [2], summarised in Section 1.2, suggested that this variation could account for some, if not all of the discrepancy in the numerical simulation. Hence, Toyota arranged for shipment of 12 Toyota Yaris door trims that were used for material testing. These acted as a primary material source, in addition to the material sample plates, supplied during Schwenke’s project. The material from the two separate sources are supposedly the same, except for a small amount of additives, as discussed in Section 1.2.

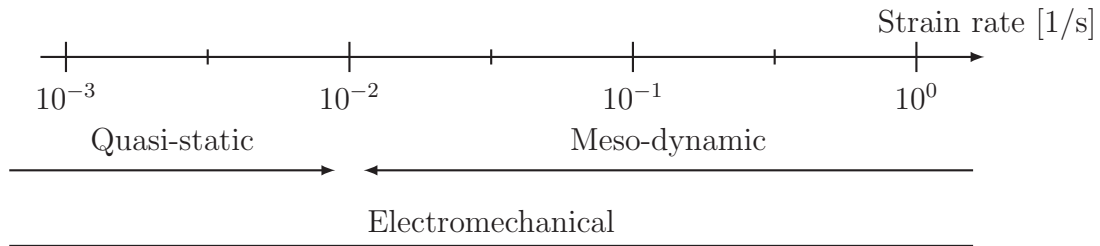


Figure 3.1: Schematic drawing of different strain rate regimes and test device

In this chapter, two different uniaxial tensile test campaigns are presented. Initially, tensile tests on the material sample plates were performed at different strain rates in the quasi-static and meso-dynamic regime. This was mainly done to examine the strain rate sensitivity of the sample plates, and to investigate any difference in material behaviour compared to what was found during Schwenke’s project [2]. A more comprehensive test campaign was, however, based on door trim cutouts, in the same strain rate regimes used for the material sample plates. Additionally, different cutout locations and orientations were tested to identify any inhomogeneity, which might be present in the door trim. The fracture surfaces for different material sources and in the different strain rate regimes were investigated using SEM. This was done in order to relate the different failure mechanisms observed for the PP material, to the microscopic behaviour.

Table 3.1 contains a detailed description of the two tensile test campaigns with respective material sources, divided by horizontal lines in the table. An electromechanical (EM) test machine was used for quasi-static and meso-dynamic testing. As previously explained, the material behaviour of the sample plates was found to be isotropic [2], and no variation of specimen orientation was therefore investigated for this material source. The table also includes the strain rates and number of successful replicates for each specific test. The ID shown in the rightmost column of Table 3.1 will be used to identify each test throughout this thesis. The structure of the ID is given as: Type of test - Material source - Orientation - Strain rate - Temperature - Replicate number.

The four different strain rates; very low (VL), low (L), medium (M) and high (H)

Table 3.1: Material test program

Material source	Test machine	Orientation	Strain rate	Replicates	ID*
Sample plate	EM	0°	VL	2	UT_S_00_VL_-30_#
Sample plate	EM	0°	L	2	UT_S_00_L_-30_#
Sample plate	EM	0°	M	2	UT_S_00_M_-30_#
Sample plate	EM	0°	H	2	UT_S_00_H_-30_#
Door trim	EM	0°	VL	7	UT_X-□_00_VL_-30
Door trim	EM	0°	L	4	UT_X-□_00_L_-30
Door trim	EM	45°	L	4	UT_X-□_45_L_-30
Door trim	EM	90°	L	6	UT_X-□_90_L_-30
Door trim	EM	0°	M	3	UT_X-□_00_M_-30
Door trim	EM	0°	H	3	UT_X-□_00_H_-30

Material sample plates: # is a placeholder for the replicate number of each individual test.

Door trim cutouts: X and □ are placeholders for the location and door trim number from which the specimen was extracted.

from Table 3.1, are defined in Table 3.2. The two former are in the quasi-static regime, while the two latter are in the meso-dynamic regime. Half decades were employed in order to investigate the viscoplastic properties of the polymer. Since the behaviour was assumed to be log-linear, two strain rates are sufficient in order to characterise the rate dependence. However, to ensure better accuracy, four different strain rates were tested here. For each abbreviation, the initial strain rate and corresponding constant crosshead displacement rate are given. The latter was assigned to the test machine prior to testing of each specimen.

Table 3.2: Strain rate regimes

Strain rate regime	Initial strain rate [1/s]	Crosshead displacement rate [mm/min]
VL	$10^{-2.0}$	3.60
L	$10^{-1.5}$	11.4
M	$10^{-1.0}$	36.0
H	$10^{-0.5}$	114

The strain rate can be derived from the logarithmic strain, which is given by

$$\varepsilon = \ln \left(\frac{L}{L_0} \right) = \ln \left(\frac{L_0 + \Delta L}{L_0} \right), \quad (3.1)$$

where L_0 and ΔL is the initial and change in gauge length, respectively. By differentiating this expression with respect to the time, the strain rate, $\dot{\varepsilon}$, can be expressed by

$$\dot{\varepsilon} = \frac{\Delta \dot{L}}{L_0 + \Delta L}, \quad (3.2)$$

where $\Delta \dot{L}$ is the displacement rate. From the expression above, it is obvious that although the crosshead displacement rate is constant during the tensile test, the strain rate is not. The gauge length changes as the specimen is deformed, causing a reduction in the strain rate. Hence, the initial strain rate referred to in Table 3.2, only arises at the beginning of the test for which the change in gauge length is zero, i.e. $\Delta L = 0$.

3.2 Uniaxial tensile test procedure

The uniaxial tensile test is by far the most well-known experiment for determination of mechanical properties of materials. This experimental technique is fundamental in material science and -engineering, and involves stretching of the subjected specimen in a controlled fashion until fracture occurs. Such experiments are performed in somewhat universal testing machines, often categorised into two classes; servo-hydraulic and EM. The servo-hydraulic testing machines are usually capable of carrying higher forces at higher speeds, while both speed and position of the crosshead can be controlled more accurately using an EM test machine. In this thesis, however, an EM *Instron 5944 single column* test machine was utilised. More details concerning the uniaxial tensile testing are described in the following sections.

3.2.1 Test specimens

During Schwenke's work, tensile specimens were water jet cut in order to save time with respect to machining. However, former PhD candidate Jon E. Pettersen found that strain at fracture of milled PP specimens were notably larger than similar specimens that were water jet cut. It was concluded that the PP material is very sensitive to notches, since water jet cutting could result in somewhat fringed cutting surfaces and subsequent premature fracture [39]. Hence, all specimens considered in

this project were milled. Furthermore, since the material sample plates and the door trims are fairly thin and relatively flat, planar dog-bone shaped specimens proved to be the most suitable. A dimensional drawing of the specimen geometry can be seen from Figure 3.2.

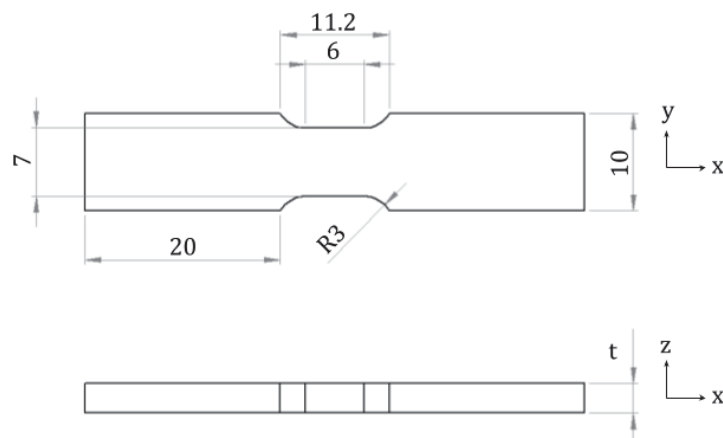


Figure 3.2: Tensile specimen geometry [mm]

To avoid protracted test times due to the ductility of polymers, the dimensions of the tensile specimens were chosen sufficiently small [2]. Additionally, to enhance a basis of comparison with the previous work described in Section 1.2, identical test specimens as those found in Schwenke's work were employed. The thickness deviated slightly with respect to the different material source, particularly for the door trim cutouts. The averaged thicknesses are given in Table 3.3 for the two respective material sources.

Table 3.3: Average test specimen thicknesses

Dimension	Material sample plates	Door trim cutouts
t	3.15 mm	2.45 mm

3.2.2 Setup

The Instron 5944 testing machine, as shown in Figure 3.3, was instrumented such that measurements of both displacement and loading could be obtained. This

is possible by logging of the crosshead displacement and the corresponding load-measurements through a fitted load cell. The maximal capacity of this load cell is 2 kN, which is adequate for polymers of the relevant specimen dimensions. Mounting of the test specimens involved clamping by use of flat shouldered fixations with serrated grips. Since this thesis considers cold impact performance of PP, all tests were performed at $-30\text{ }^{\circ}\text{C}$, and a similar procedure as that of Johnsen et al. [40] was adopted.

The setup utilised for the low temperature testing is shown in Figure 3.3. A fitted polycarbonate (PC) environmental cooling chamber enabled a relatively stable and low temperature during the testing. However, the PC chamber is neither air tight nor particularly thermally insulated. Hence, the temperature was controlled by a thermocouple sensor connected to the nitrogen injection valve controller. Cooling of the interior of the PC chamber was achieved through a valve releasing bursts of the liquid nitrogen into the chamber until the desired temperature was achieved. As the nitrogen was released from its high pressure container, it instantaneously expanded when entering the chamber. A suited hose was utilised leading the cold gas through a small hole in one of the narrower side walls. To ensure the desired temperature in the most critical portion of the specimen, the sensor was placed close to the gauge section. This method, however, introduced noticeable variations in temperature. By taking temperature readings just before and subsequent to the release of the liquid nitrogen, the temperature was found to fluctuate by $6\text{ }^{\circ}\text{C}$, i.e. from -28 to $-33\text{ }^{\circ}\text{C}$. Even though the fitted thermometer displayed such variation within the cooling chamber, identical variations are not necessarily evident within the test specimens. However, some temperature fluctuation is nonetheless expected.

Due to the substantial temperature difference between the inside- and outside of the PC chamber, problems involving condensation and consecutive icing would occur. However, this was avoided through continuous airflow over the chamber walls, provided by a fan. The test machine was cooled approximately one hour prior to the experiment with the purpose of preventing any significant thermal disturbance on the test specimens. For the same reason, the specimens were also cooled prior to testing. Their size was fairly small, it was reckoned that 30 minutes of cooling would provide satisfactory results. To be confident that the temperature was correct prior to testing, the specimens were nonetheless kept inside the cooling chamber for an additional 10 minutes after being mounted.

To enable measurements of both longitudinal- and transverse strain, two cameras at a frame rate of up to 15 Hz were utilised. Hence, two Prosilica GC2450 cameras, both equipped with Samyang 100 mm macrolenses, allowed for DIC measurements.

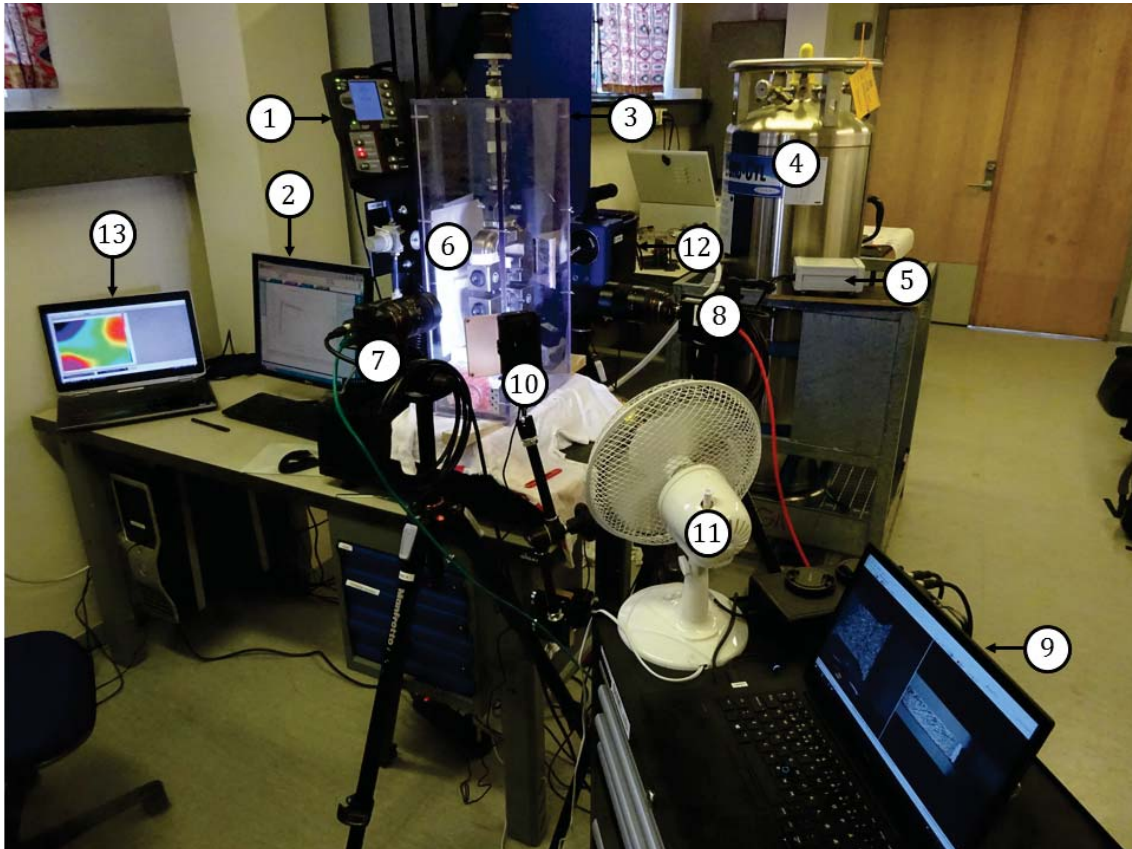


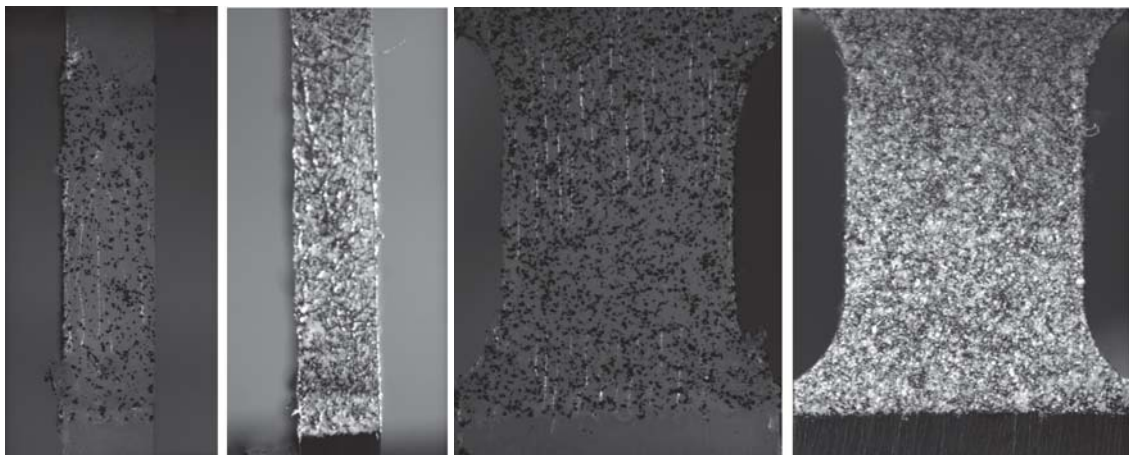
Figure 3.3: Uniaxial tensile test setup at low temperature

① Test machine controller, ② Test data recording, ③ Polycarbonate chamber, ④ Liquid nitrogen container, ⑤ Nitrogen injection valve controller, ⑥ Test specimen mount, ⑦ DIC camera 1, ⑧ DIC camera 2, ⑨ DIC data recording, ⑩ Additional light source, ⑪ Fan preventing condensation, ⑫ IR camera, ⑬ IR camera recording

Both were positioned at a distance of approximately 300 mm from the tested specimen. Furthermore, a FLIR SC7000 thermal camera was utilised such that adiabatic heating within the specimens could be measured during the tests. For the thermal camera to accurately monitor the temperature, a free line-of-sight is needed relative to the test specimen. This was achieved by placing the thermal camera such that its monitoring sector operated within a rectangular slit in the side wall of the PC chamber, as shown in Figure 3.3. It should, however, be noted that the FLIR camera provides accurate measurements for temperatures above $-20\text{ }^{\circ}\text{C}$ only.

By capturing pictures of the experimental test at a sufficient frame rate, a DIC software could be utilised to monitor the specimen deformation, as discussed in Section 2.2.2. To enable the DIC measurements, aerosol spray paint is traditionally used to obtain a random black and white speckle pattern deforming along with the specimen. However, this conventional method fails at lower temperatures as the

spray paint becomes brittle and cracks, even at relatively small strains. To circumvent this problem, and due to colour differences between the two material sources, separate methods were utilised for the specimens originating from the material sample plates and the door trim cutouts. For the material sample plates, a neutrally coloured grease, i.e. white or black, was smeared on the specimen gauge area before a contrasting powder was dispersed onto the grease layer through a sieve. For the door trim cutouts, the same neutrally coloured grease was smeared on the specimen gauge area before aerosol spray paint was employed to obtain the speckle pattern. Since the paint was added on top of the grease layer, it deformed along with the specimen and only small cracks occurred. Figure 3.4 shows the separate speckle patterns from both side- and front views, obtained from DIC camera 1 and 2, respectively. By employing this method, little cracking of the speckle pattern was found, even at larger strains. However, this method introduces some complexity in the DIC analysis. Although a fairly even distribution of the powder was obtained, the grease created a relatively thick layer on the outside of the specimen, hiding its actual geometry.



(a) DIC camera 1: Side view

(b) DIC camera 2: Front view

Figure 3.4: Speckle patterned specimens originating from the material sample plates and the door trim cutouts

3.2.3 Post processing

Post processing of the experimental data was mainly done through DIC. A brief introduction of the general procedure used to obtain the strains during tensile testing was given in Section 2.2.2. All DIC analyses were performed using the software, *eCorr*, developed by the NTNU researcher Egil Fagerholt [41]. The force applied

to the specimen was, however, obtained directly from the tensile test machine. Although the displacements were also recorded by the test machine, they could not be used for analyses. This is due to slipping of the grips, the stiffness of the crosshead and deformation outside the gauge part of the sample, possibly affecting the results.

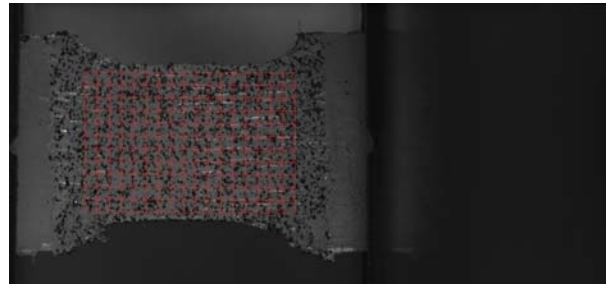
Strain measurements

In order for the strains to be measured using DIC, the sequence of images obtained through the test was imported into eCorr. A mesh of quadrilateral, structured elements was placed over a reference image of the undeformed specimen as shown in Figure 3.5a. Furthermore, it was manually positioned over the area desired for strain calculations. Care was taken such that each element contained a sufficient amount of speckles and associated grayscale pattern, enabling easy tracking of the deformation. An element size of 50×50 pixels was used, as a compromise between large elements that are less susceptible to grayscale noise, and small elements that give a better representation of the displacement field [42]. This procedure was done for the images obtained from both side and front views of the specimen. The DIC analysis could then be conducted, for which the software calculates the surface deformations, as shown in Figure 3.5.

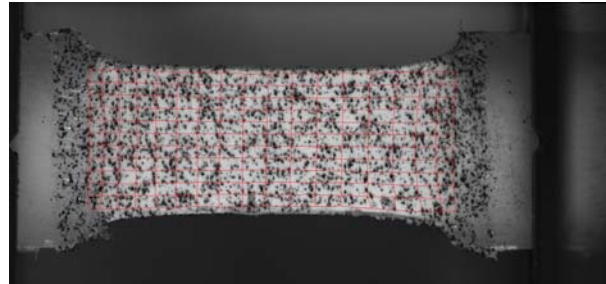
By tracking of the grayscale pattern within each element, eCorr is able to calculate the displacements at each respective node. Hence, the deformation of each element can be used to determine how the material deforms. Once the DIC analysis was completed, the column of elements experiencing the largest amount of logarithmic strains was selected for use in material calibration. Emphasis was placed on positioning the mesh such that the crack propagated through the middle of these elements, allowing the largest strains to be used. An averaged value of the logarithmic strain components in all spatial directions were extracted from this column.

Stress measurements

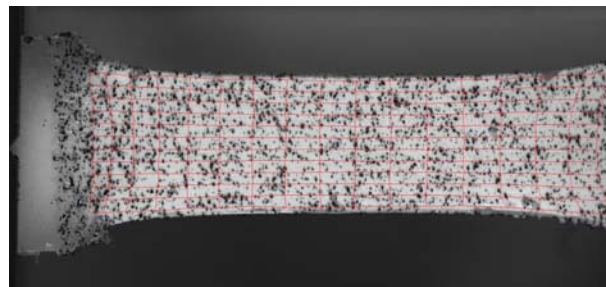
To accurately represent the stresses that occurred in the test specimens, both the applied force recorded by the test machine, and the strain values obtained from DIC were used. The recordings from the test machine and the DIC cameras were synchronised, such that each data point from the two measurements corresponded to one another. For some of the tests, however, one of the images in the sequence was missing. Care was therefore taken such that the two recordings matched. Both the nominal- and true stress could then be calculated using the approach described in Section 2.2.1. In uniaxial tensile tests, the stress in the material is assumed to act in



(a) Undeformed



(b) Intermediately deformed



(c) Fully deformed

Figure 3.5: DIC analysis at low temperature

the load direction only. In general, this is true until necking occurs in the specimen, for which the stress triaxiality increases. For a dog-bone specimen, however, these effects are assumed to be small. Therefore, no such effects were accounted for in the process stated above.

3.3 Results - Material sample plates

For the material sample plates, a simple mould requiring one injection gate is employed during production, leaving the flow pattern of the PP melt relatively uncomplicated. Furthermore, a clear gate mark stretching was present on one edge of every sample plate. Hence, the flow direction of the part was easily identified. All specimens were, however, extracted in the same orientation in this cases, since the material was assumed to be isotropic.

3.3.1 Visual results

Figure 3.6 shows the deformation just before fracture of two tensile tests conducted at different strain rates. Both were captured using DIC camera 2. The specimens exposed to VL and H strain rates are shown to the left and right, respectively. Stress-whitening effects are present in both specimens. For the VL strain rate in Figure 3.6a, significant elongation of the specimen was observed before fracture. No signs of a clear neck can be seen in the figure, suggesting that stable necking was present during the test. Hence, a small neck was created early and propagated along the gauge area of the specimen until it reached the ends, as discussed in Section 2.1.2. This process is often associated with large strains. For the test at H strain rate, shown in Figure 3.6b, a considerable reduction in ductility was found before fracture. Comparing the two specimens, it is obvious that the presence of a neck is much more pronounced at H strain rate. In this case, however, the neck was not stable and a phenomenon called *localisation* occurred. During localisation, all subsequent deformation develops within this neck, resulting in high local strains. Additionally, localisation leads to the introduction of triaxial stresses, which also promotes a reduction in ductility.

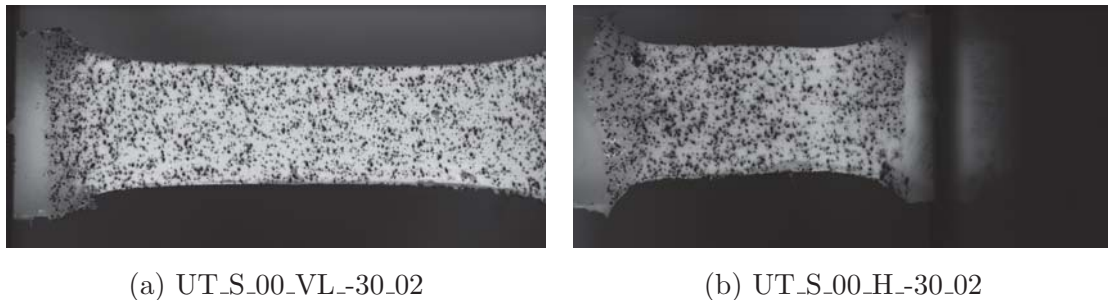


Figure 3.6: Deformation just before fracture for specimens at VL and H strain rates

For the test specimen experiencing a VL strain rate, a magnification of the area for which the crack initiates is shown in Figure 3.7. The figure shows the process of crack propagation and fracture of the specimen. The crack propagates from the surface, suggesting that initiation is caused by some sort of surface defect. At first, the crack propagation is slow, before fracture suddenly takes place. A severed fibril can be observed before fracture occurs. Both stress-whitening and the presence of fibrils suggest that crazing is the main yield mechanism in this particular case.

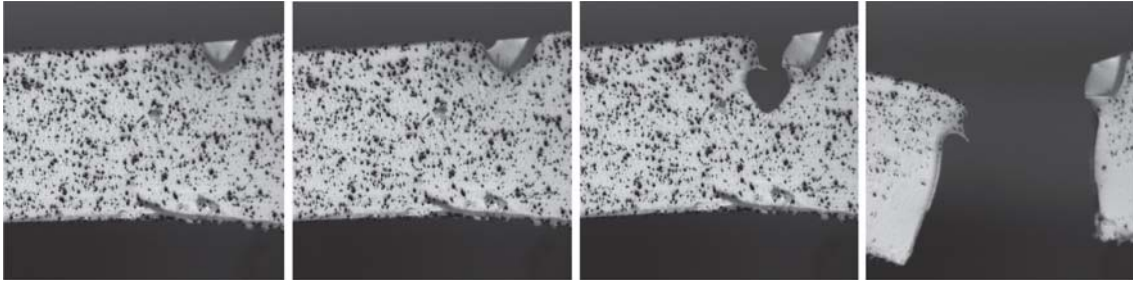


Figure 3.7: Failure of test specimen UT_S.00_VL.-30.02

3.3.2 Measured results

The strain fields just before fracture of two tensile specimens exposed to VL and H strain rates are shown in Figure 3.8a and 3.8b, respectively. The strain fields display the logarithmic strain components in the longitudinal direction of the specimens and were determined from a DIC analysis in eCorr. The difference between stable necking and localisation is clarified by these figures. In Figure 3.8a, stable necking occurs and the strain is uniformly distributed over the gauge area. For Figure 3.8b, however, the strain is highly localised in a small region of the gauge area, corresponding to the neck. The dark red fields in the right sections of both specimens, indicates where the crack initiated. Hence, the strains from these columns of elements were used for further calibration, and are presented in the results below.

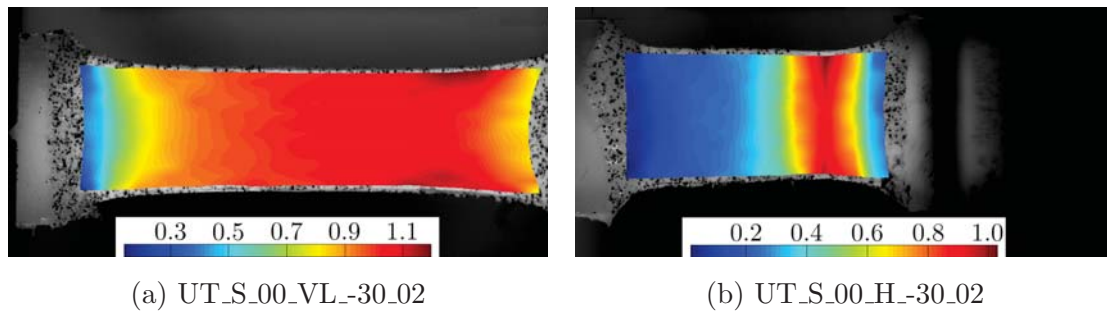


Figure 3.8: Longitudinal strain fields just before fracture for specimens at VL and H strain rates, obtained from DIC

Figure 3.9 shows eight tensile test results for the material sample plates at different strain rates. All tests were performed at $-30\text{ }^{\circ}\text{C}$ and extracted from the material source with the same orientation. The figure shows the relation between the nominal stress and the logarithmic strain in the longitudinal direction. The nominal stress is plotted instead of the force in order to compensate for the difference in initial cross-sectional area. A summary of the test data from every tested specimen can be found in Appendix B.

The test results indicate good repeatability, and no large variations were found between the two replicates for each strain rate. Although all tests were performed at low temperature, the material was still ductile, with elongations from 96 to 137 % for H and M strain rates, respectively. This suggests that the glass transition temperature is below $-30\text{ }^{\circ}\text{C}$. The greatest variations between different strain rates were related to yield strength and the strain at fracture. Additionally, the slope in the plastic domain was found to vary between the different strain rates. The tests conducted at a VL strain rate show a clear hardening effect. For increasing strain rates, however, the thermal softening becomes predominant.

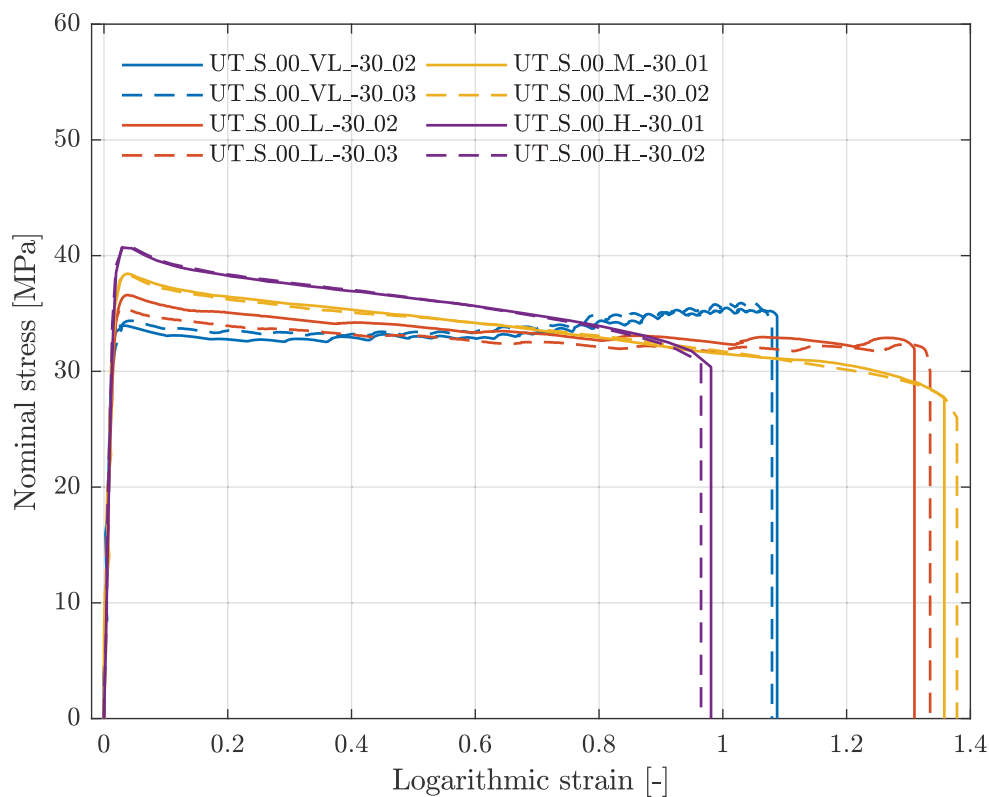


Figure 3.9: Tensile test results for material sample plates

For the nominal stress-logarithmic strain curves at VL and L strain rates, a wave-pattern is evident in the plastic domain. However, the curves related to M and H strain rates are smooth. This effect is artificially caused by the temperature fluctuations in the environmental chamber, and is not directly related to the mechanical behaviour of PP. Once the nitrogen is injected, the temperature in the chamber drops, causing the material to stiffen, i.e. the stress increases. As the temperature rises, due to the ambient temperature surrounding the chamber, the material softens, causing the stress to drop. This results in a wave-pattern in the stress-strain

curves. Due to the duration of the tests performed at VL and L strain rates, several such injections occurred during the respective tests. For the M and H strain rates, however, the test durations were much shorter. Hence, no such effects can be seen in the nominal stress-logarithmic strain curves for these strain rates.

An interesting observation is the strain at fracture, which was found to increase as the strain rate was elevated by half a decade from VL to L. By further raising the strain rate from L to M, the increase in strain at fracture was practically negligible. Finally, an additional half decade increase from M to H caused a drastic reduction in fracture strain. This effect might be caused by two competing effects, adiabatic heating and localisation. Adiabatic heating is projected onto the stress-strain curves through an increased softening with strain rate. The localisation effect shown in Figure 3.6b for the test at H strain rate, is also apparent in Figure 3.9. For the tests at elevated strain rates, M and H, an additional reduction in stress is observed immediately before fracture. To summarise, an increase in strain rate from VL to L, causes a small heating effect in the material, making it more ductile. For the M strain rate, the increased ductility is nullified by the localisation, which becomes more dominant. At H strain rate, the localisation is the governing failure mechanism, and the increased ductility due to adiabatic heating has less of an influence on the strain at fracture.

Compared to Schwenke's results [2], a similar mechanical behaviour was found for the PP sample plates. The associated nominal stress-logarithmic strain curves are shown in Figure 1.2. A clear increase in strain at fracture was, however, observed in the more recent results. Previously, an average fracture strain of approximately 93 % was found at VL strain rate, compared to 108 % in this section. This outcome could be caused by several effects, such as the machining of the test specimens discussed in Section 1.2. Additionally, a much less distinct wave-pattern was obtained during the recent tensile testing at low temperature. This was due to the liquid nitrogen injection valve controller, being improved since Schwenke's project. Hence, a more consistent, low temperature could be obtained as a result of an increased nitrogen injection rate.

The logarithmic strain components and the volumetric strain for UT_S.00_VL_-30_02 are shown in Figure 3.10. Here, the directions of the strain components refer to the coordinate system shown in Figure 3.2. Hence, ε_{xx} refers to the logarithmic strain in the longitudinal direction, while ε_{yy} and ε_{zz} correspond to the two transverse directions. The two former were obtained through DIC camera 2 while the latter was obtained from DIC camera 1. The figure shows that ε_{yy} and ε_{zz} are similar in size, and small compared to ε_{xx} . This confirms that the material is truly isotropic.

Furthermore, the size difference between the longitudinal and transverse strain components, results in a significant volumetric strain, defined in Eq. (2.6). Hence, the material must be considered compressible.

Figure 3.11 shows three different stress measures plotted as functions of the logarithmic strain, all of which were derived in Section 2.2.1. The incompressible true stress is computed based on the assumption of incompressible material behaviour, i.e. zero volumetric strain, as defined in Eq. (2.9). From Figure 3.10, the volumetric strain component is clearly not zero, meaning that such an assumption cannot be adopted in this case. This is also evident in Figure 3.11, where the incompressible true stress is more than twice as high as the compressible true stress at fracture. The nominal- and compressible true stress, defined in Eq. (2.8), and nominal stress are, however, quite similar. Since the nominal stress does not take the change in cross-sectional area into account, this suggests that such effects are small. A compressible true stress definition will therefore be employed in this thesis.

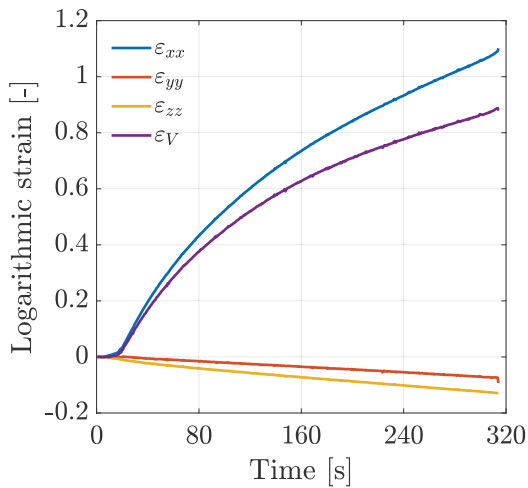


Figure 3.10: Logarithmic strain components and volumetric strain

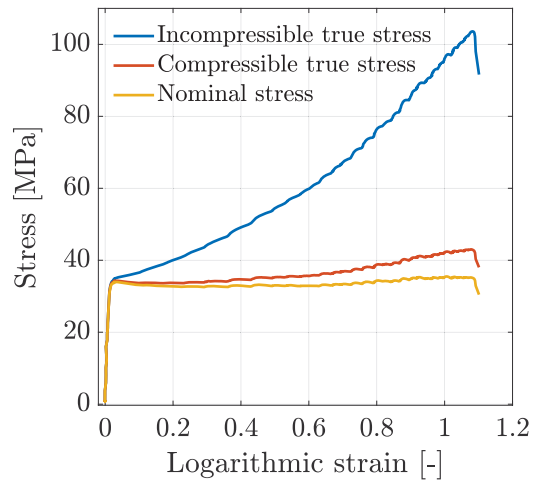


Figure 3.11: Comparison of different stress measures

The consistency of the strain measurements for the tensile tests performed at low temperature is evident in Figure 3.12. Here, the volumetric strain and retraction ratio, R_r , are plotted as functions of the longitudinal strain for three replications in Figure 3.12a and 3.12b, respectively. A near linear relationship was found for the volumetric strain and the longitudinal strain component. The development of the volumetric plastic strain in the material model is controlled by the parameter β , introduced in Section 2.3.3. This β is calibrated using the retraction ratio which relates the longitudinal and transverse plastic strain components. In order to determine β , the retraction ratio must be constant. Figure 3.12b shows that the

assumption of a constant retraction ratio only holds for intermediate to large plastic strains. The small variations between the three repetitions in Figure 3.12 confirms a very consistent material behaviour with respect to the volumetric strain.

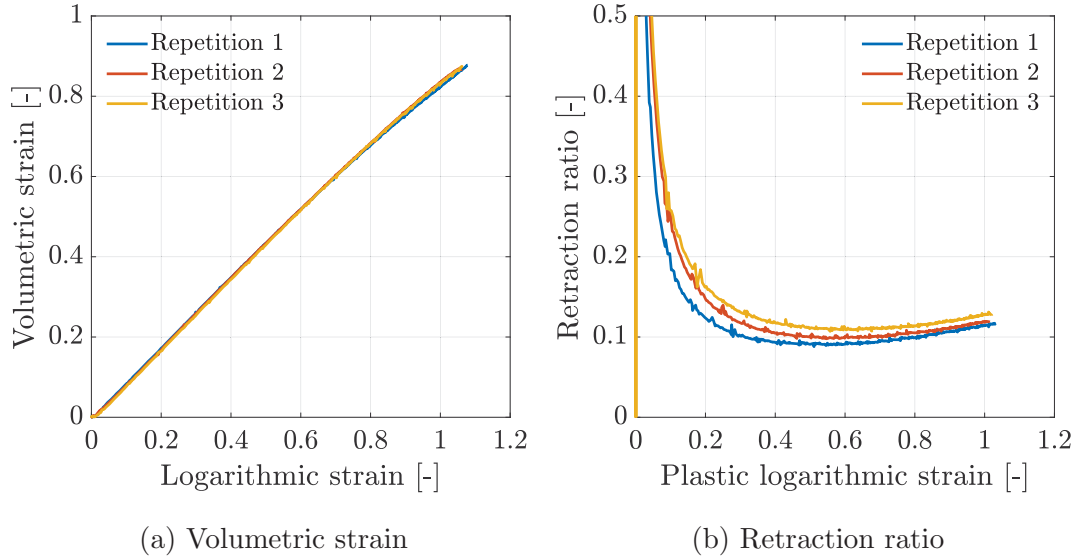


Figure 3.12: Consistent strain measures for UT_S_00_VL_#

The peak nominal stress for different strain rates are plotted in Figure 3.13. A clear positive correlation between the peak nominal stress and strain rate was found. This suggests that employing a viscoplastic constitutive relation, is suitable in the material model. Although the relation may seem log-linear, since the points correspond to an increase in strain rate of $10^{0.5} \text{ s}^{-1}$, this may not be the case for larger strain rates. This will be investigated further at a later stage. The figure also confirms that the test results obtained for each replication was highly consistent.

Figure 3.14 shows how the volumetric plastic strain at fracture changes with respect to the strain rate in the tensile tests. The volumetric plastic strain at fracture is the only mechanical property used for calibration of the fracture parameters in the numerical model. A better understanding of the factors affecting this property is therefore essential in this thesis. Initially, a positive correlation between the volumetric plastic strain at fracture and the strain rate was found. However, when increasing the strain rate from M to H, the softening due to adiabatic heating could no longer compensate for the localisation effect. Hence, the strain at fracture is reduced, which corresponds to what is seen in Figure 3.9.

An interesting observation is the clear increase in volumetric plastic strain at fracture that can be seen in Figure 3.14, when the strain rates are increased from L to M. In Figure 3.9, however, the increased longitudinal strain at fracture was seemingly

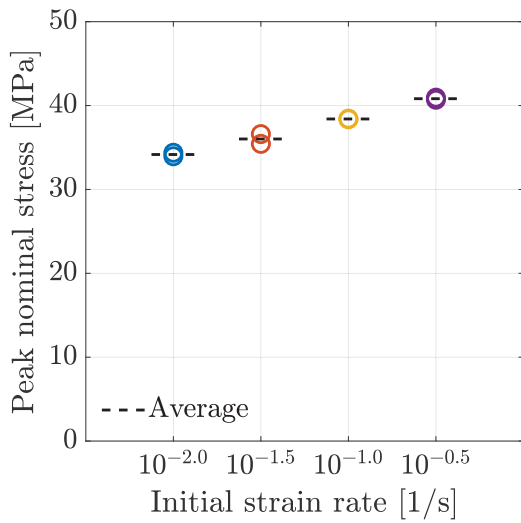


Figure 3.13: Peak nominal stress for different strain rates and replications

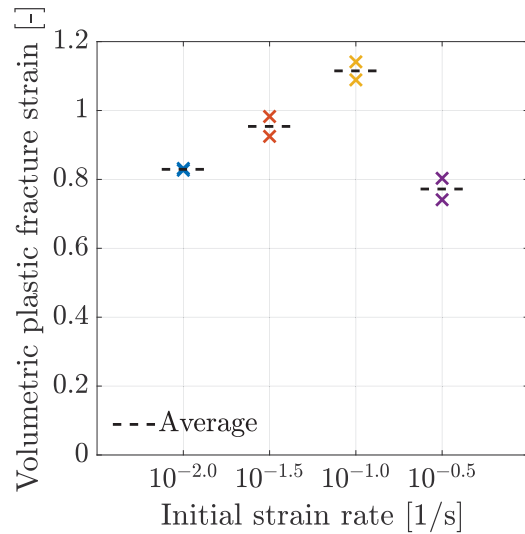


Figure 3.14: Plastic volumetric strain at fracture for different strain rates and replications

negligible for such strain rates. This is most likely due to larger transverse strains and subsequently lower volumetric strains in the specimens at L strain rate for which localisation is not present. This may seem counterintuitive, since localisation is characterised by a retraction in the cross-sectional area. For the L strain rate, however, stable necking led to a significant amount of elongation and corresponding retraction before fracture occurred, thereby lowering the volumetric plastic strain at fracture. Additionally, the figure gives an indication of the variance between the two repetitions at each strain rate. Although some difference in volumetric plastic strain at fracture was found, the deviations are fairly small.

3.3.3 SEM results

For the material sample plates, the through-thickness fracture surface of specimen UT_S_00_H_-30_2 is shown with two different magnifications in Figure 3.15. Some cavities of varying size and shape can be seen at the highest magnification. Their size suggests that the cavities had some time to grow prior to fracture. They are most likely a result of debonding of the second phase particles from the PP matrix. Some particles with spherical shape and an approximate size of $0.5 \mu\text{m}$ can be seen in the micrograph with the highest magnification. Since the material is a copolymer with ethylene, the particles are most likely an EPR, added to enhance the toughness. This was discussed in Section 2.2.1. Both rubber particles and cavities are

indicated by the encircled areas in the figure below. Furthermore, the morphology of the material surrounding the cavities contain predominantly rounded edges. This indicates the presence of adiabatic heating effects, due to the significant amount of plastic deformation occurring in a short period of time. A similar observation was found in the measured results.

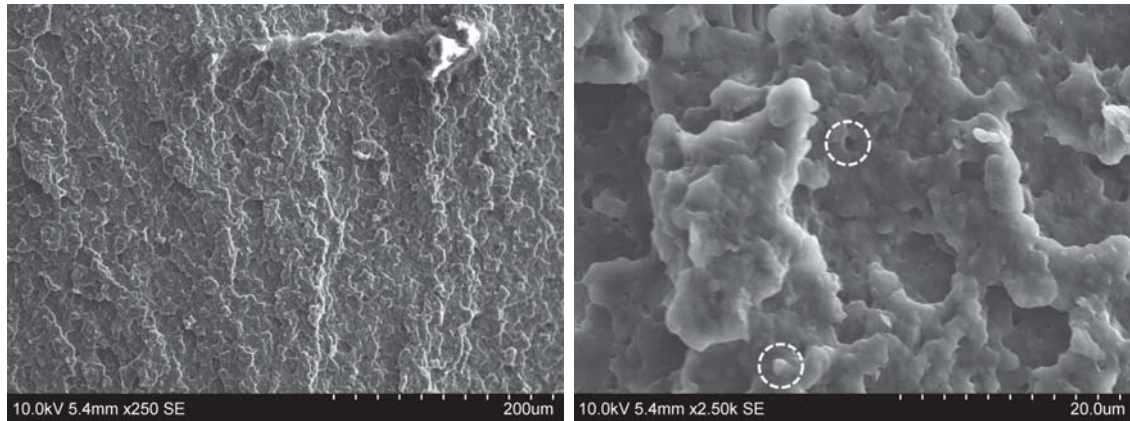


Figure 3.15: SEM micrographs of test specimen UT_S_00_H_-30_2

3.4 Results - Door trim cutouts

In order to verify that the material characterisation is able to represent the door trim behaviour precisely during impact tests, material testing of the actual component is essential. There are several factors influencing the material behaviour of the door trim, as opposed to the material sample plates. Some examples of such factors are production method and impurities in the material. The production process, which is described in Section 2.1.5, is the cause of emerging weld lines and possible inhomogeneity in the material due to the flow direction of the polymer melt when injected into the mould.

As for the quasi-static and meso-dynamic tensile testing, specimens of varying orientation and from different locations were extracted for the purpose of confirming or disproving material anisotropy and inhomogeneity of the component material. Figure 3.16 displays a representative door trim, and the associated outlined tensile specimen. Here, the left and right side of location C is denoted CL and CR, respectively. It must be noted that several other configurations with respect to orientations and locations were utilised. However, only one of the 12 door trims is shown here.

Although the manufacturing process of the material sample plates and door trims is the same, there are large differences in both the size and complexity of the two



Figure 3.16: Representative tensile specimen outline from which the door trim cutouts were extracted

material sources. For the door trims, several injection gates at different locations with respect to the part, are required in production. Hence, large variations in the orientation of the molecular chains are expected. In addition, the flow properties of the material are related to the distance from the injection gates. As a result, the mechanical behaviour is believed to differ across the door trim. The orientations chosen when extracting tensile specimens, shown in Figure 3.16, are not related to the material flow, but rather to the mounted configuration of the door trim in the vehicle.

For the sample plates, the effects described above are not present to the same extent. This is due to the small size and uniform geometry of this material source, requiring a single injection gate only. The size difference between the two also suggests that their thermal history might be different. The thermal history of thermoplastic polymers is believed to be closely related to the crystallinity and molecular conformation [10], and could therefore have a large influence on the mechanical properties of the material. Furthermore, variations in thickness and differences in surface properties could affect the test results for the door trim material.

3.4.1 Visual results

The main visual difference between the two material sources was the substantial reduction in elongation before crack initiation, observed for the door trim material at lower strain rates. Whereas clear signs of stable necking were observed for the material sample plates, this was generally not the case for the door trim material. A much more localised behaviour was found, where the deformation only developed within a small section of the total gauge length of the specimen. This effect could be explained by the fact that the thickness of the specimens often varied considerably, even over the small gauge area. However, the localised effect was only found in the section closest to the moving crosshead of the test machine. For the higher strain rates, a much more evident neck was observed, suggesting that localisation was indeed the governing failure initiator. Hence, no visual differences were indicated between the two material sources at these rates.

Stable crack propagation was a more dominant failure mechanism in the door trim material. This effect was especially present at the two lower strain rates, where large amounts of elongation was found after crack formation. In many cases, the crack propagated through the entire specimen at a seemingly constant speed. Figure 3.17 shows crack growth from both sides of the specimen in test UT_A-10_00_L_-30. Only once the two cracks met in the centre, fracture occurred. For the sample plate material, however, a much more rapid failure mode was discovered. Large amounts of stress-whitening were also found in the door trim material, and can be observed in the figure. This suggests that crazing was the main yield mechanism, also for the door trim cutouts.

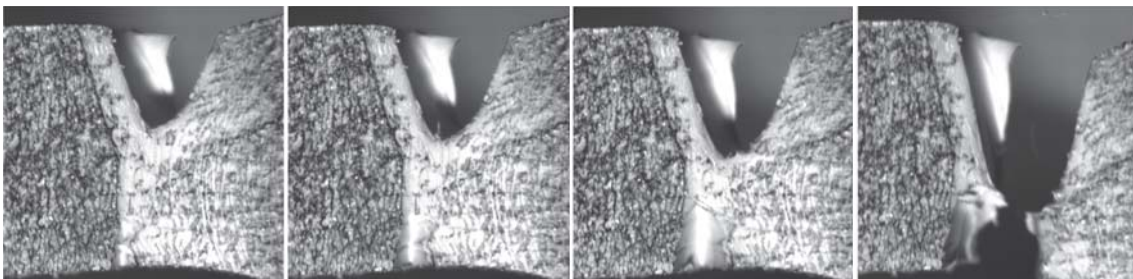


Figure 3.17: Failure of test specimen at low temperature and L strain rate (UT_A-10_00_L_-30)

3.4.2 Measured results

The measurement techniques that were utilised for the material sample plates, were also used for the door trim cutouts. Hence, the strains in all spatial directions were determined using DIC analyses in eCorr. Figure 3.18 shows the resulting longitudinal strain fields for two samples at VL strain rate just before crack initiation. Although the specimen in Figure 3.18a experienced more elongation before fracture than the specimen in Figure 3.18b, they both display the same localised strain field. By comparison with the strain field found for the material sample plates in Figure 3.8a, the tendency becomes even clearer. Hence, the small neck that occurs early at low strain rates, is not allowed to propagate along the full gauge length of the specimens. The deformation proceeds within this smaller, effective gauge length. As a result, a significant reduction in elongation was found prior to fracture.

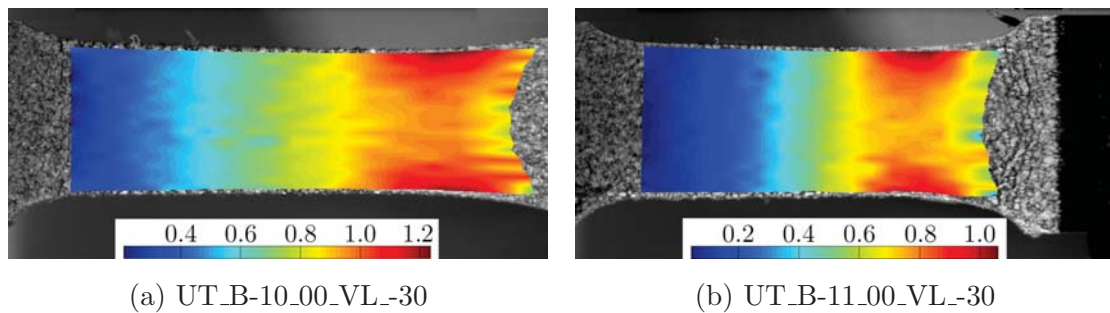


Figure 3.18: Longitudinal strain fields just before crack initiation for door trim material specimens at VL strain rate, obtained from DIC

The tensile test results in terms of nominal stress-logarithmic strain curves from the two locations CL and CR, are shown in Figure 3.19. These specimens were all extracted at 0° orientation and tested at VL strain rate at low temperature. From the figure, it is clear that mechanical properties such as elasticity, yielding, hardening and plastic flow are highly consistent at location C, regardless of which door trim is tested. However, a large difference is apparent in strain at fracture, both between the two locations, but also between door trims. This illustrates the significant variations which may be present, even for specimens extracted only a short distance apart.

Figure 3.20 presents how the mechanical properties of the door trim material changes with respect to strain rate. The nominal stress-logarithmic strain curves for VL, M and H strain rates are plotted for specimens extracted from location A and B. The same tendencies that are present in Figure 3.19, can also be observed here. Properties such as elasticity, yield stress, hardening or softening and plastic flow are comparable for the two locations at each respective strain rate. The strain at

fracture, is found to vary with respect to the location of the door trim also here. An interesting result can, however, be observed as the strain rate is increased. The difference between strain at fracture is clearly diminishing with increasing strain rate. This effect could be explained by the localisation observed at higher rates. Once localisation occurs, the difference in material properties across the door trim no longer governs the onset of fracture.

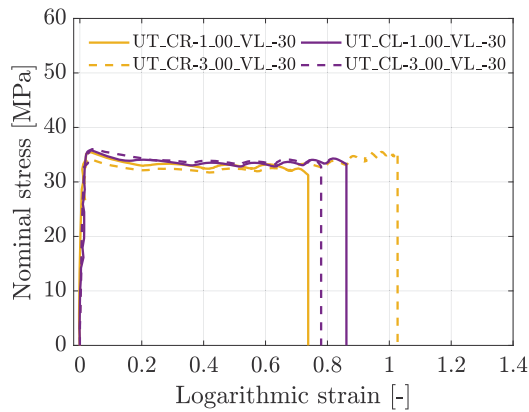


Figure 3.19: Comparison of two different door trims at location CR and CL

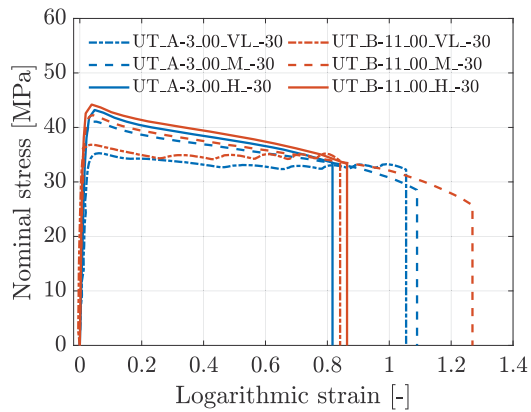


Figure 3.20: Comparison of strain rate properties at locations A and B

By raising the strain rate from VL to M, i.e. one entire decade, a clear softening effect is evident in Figure 3.20. Furthermore, the elongation before fracture is increased by a substantial amount, at least for location B in door trim 11. For location A in door trim 3, on the other hand, this increase in elongation is not as significant. The same exact effects are found in the results obtained from the material sample plates in Figure 3.9. However, the difference in fracture strain between VL and M strain rates is more conspicuous with respect to the material sample plates.

The variations in fracture strain between the different locations and door trims are clearly evident, while high consistency was observed for each replicate of the sample plate material, as shown in Figure 3.9. As the strain rate is raised to H, a similar reduction in fracture strain was found for the two material sources. It should, however, be noted that the general trend of shorter strains before fracture for the door trim cutouts compared to the material sample plates indicate behavioural differences for the two material sources.

In Figure 3.21, the true stress-logarithmic strain curves for specimens extracted from different orientations are compared for each location of door trim 2. For all figures, one replicate from the sample plate material, UT_S.00_L-30.02, is included as a reference. The figures confirm that mechanical behaviour such as elasticity and hardening is comparable for each location and orientation, as well as for the two

material sources. Some variance was, however, found in yield stress and plastic flow between different orientations within each location. The figure also suggests that these properties were found to be slightly higher for the door trim cutouts than for the sample plates. The most significant variation was, however, related to the strain at fracture. In most tests, a considerable reduction in elongation was found for the door trim cutouts, compared to the sample plate material. Although such an effect was also reported by Schwenke [2] at room temperature, a more substantial reduction in fracture strain was found at $-30\text{ }^{\circ}\text{C}$.

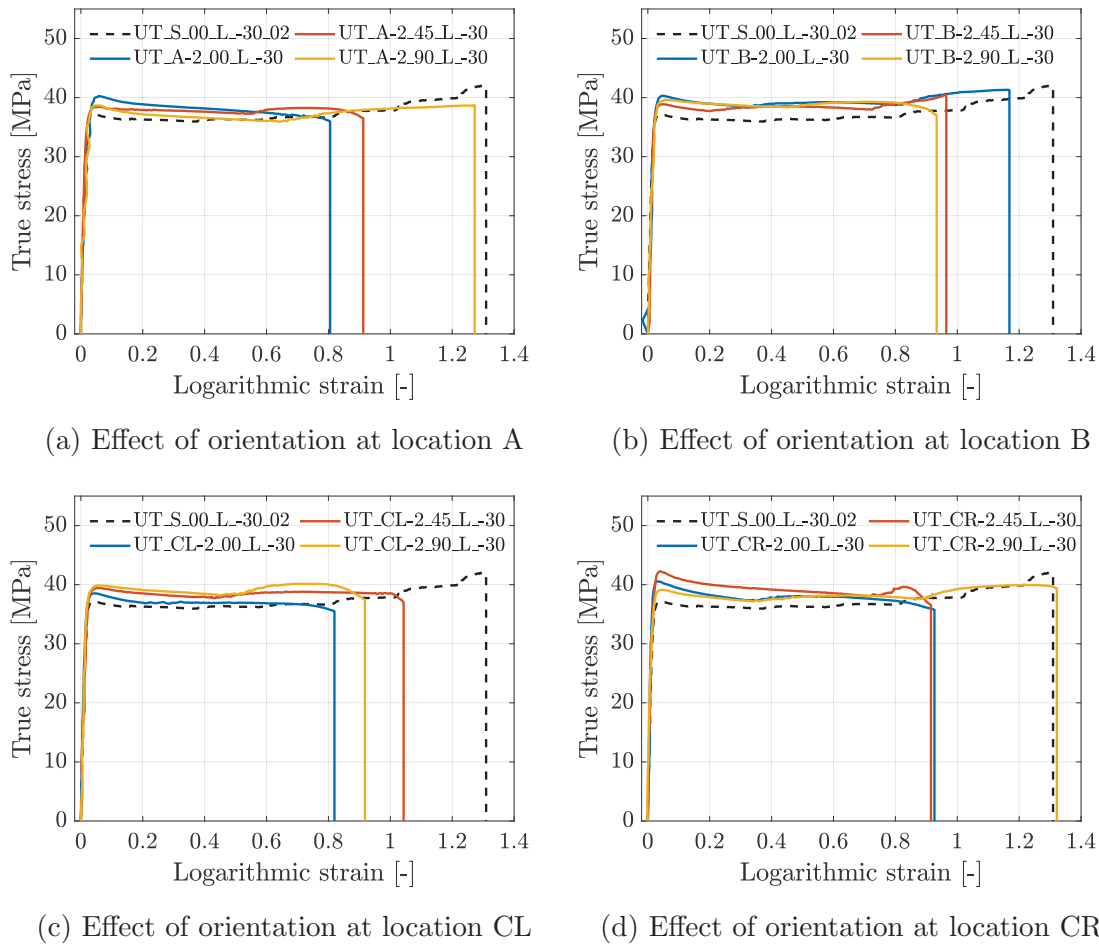


Figure 3.21: Comparing the effect of orientation at different locations of the door trim

The different logarithmic strain components and volumetric strain for the door trim cutouts are compared to the material sample plates in Figure 3.22. Considerable differences can be observed in the test duration for the door trims and sample plates at both VL and H strain rates. The general shape of the curves obtained from the two material sources are, however, similar. This discrepancy could be explained by the visual results state above. Since deformation of the door trim material was

3.4. Results - Door trim cutouts

found to be much more localised, the neck was only allowed to propagate along a fraction of the total gauge length of the specimen. Therefore, a significant reduction in the test duration resulted at VL strain rate, as shown in Figure 3.22a. For the H strain rate, however, localisation was observed also for the sample plate material. Hence, compensating for some of the effect described at VL strain rate. The test durations at H strain rate are therefore more alike, as shown in Figure 3.22b.

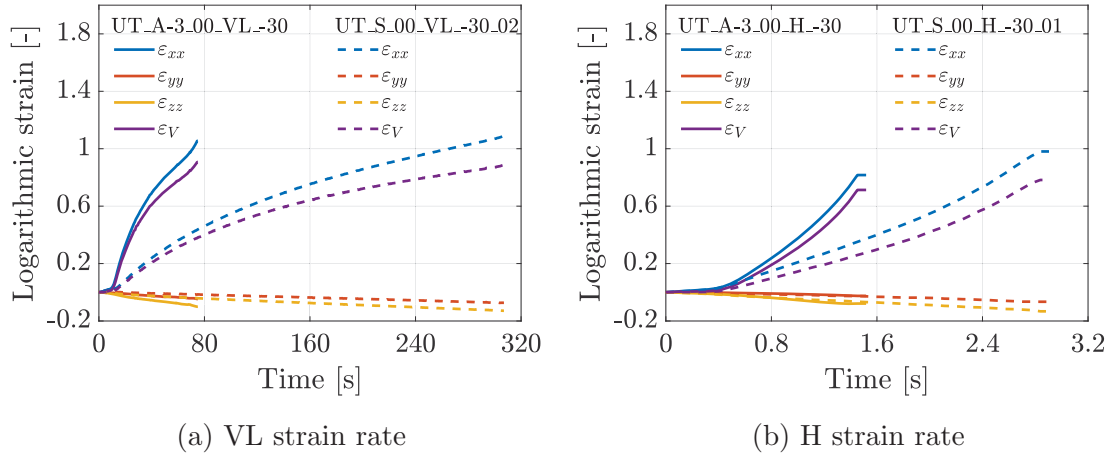


Figure 3.22: Comparing logarithmic strain components and volumetric strain for door trim and sample plates

In order to confirm that the localisation effect results in a shorter test duration, the strain rates were estimated for a selection of specimens at VL and H strain rates. A higher order polynomial was fitted to each respective longitudinal strain-time curve, and differentiated such that any noise associated with the strain measurements could be eliminated. The resulting curves are plotted in Figures 3.23a and 3.23b for VL and H strain rates, respectively. In each figure, two replicates from the door trim material are plotted in addition to one replicate obtained from the sample plates. The initial strain rate, based on the constant crosshead velocity and gauge length of the specimen is also indicated in the figures. For both figures, the strain rate in the door trim tests are clearly higher than for the sample plate material. This makes sense, since a larger amount of the strain develops in a smaller area of the specimen, due to the localised deformation. An interesting observation is that this could account for some of the difference between the yield- and flow stress of the sample plates and door trim material. Since the material is highly viscoplastic, even a small increase in strain rate could result in an increased yield strength, and subsequently higher flow stress. Yielding occurred after approximately 15 s and 1.4 s for the tests at VL and H strain rates, respectively. From Figure 3.23, significant differences in the actual strain rate can be seen for the two material sources, already

at these respective points in time. This suggests that the differences in effective gauge length for the two material sources is the cause of the discrepancy in yield strength and flow stress between the separate material sources, and not the material properties.

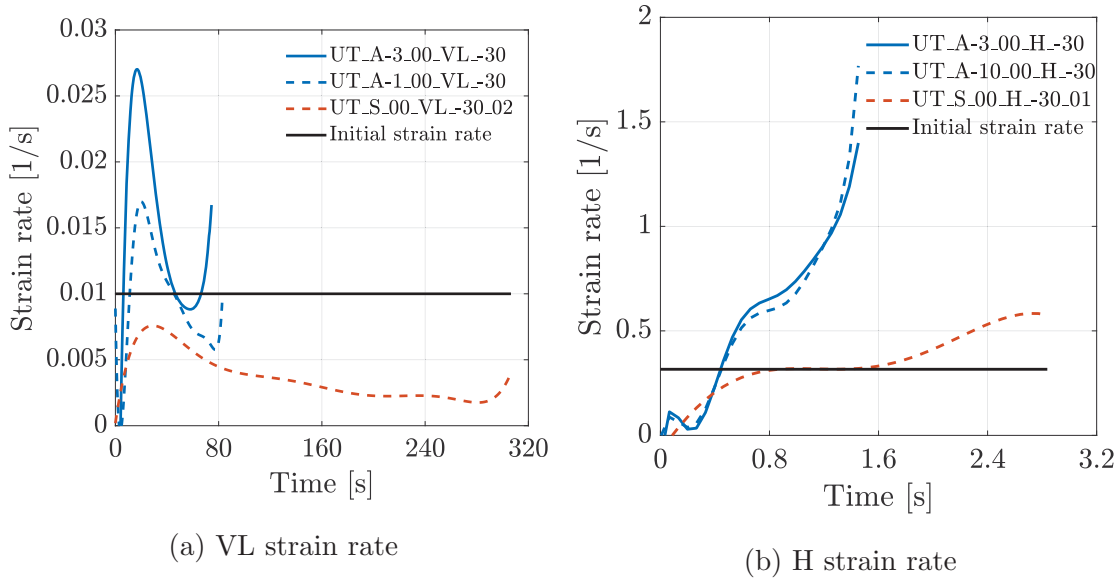


Figure 3.23: Comparing the strain rates for door trim and sample plates

The peak nominal stress obtained in the 20 tensile tests conducted on door trim cutouts in 0° orientation, are plotted according to their respective strain rates in Figure 3.24. Every location is given its individual colour, and the average peak nominal stress for each strain rate is also indicated. Compared to the results obtained for the material sample plates, seen in Figure 3.13, slightly higher peak nominal stresses were found for the specimens extracted from the door trims. Additionally, the variance is significantly larger for the door trim. This could, however, be related to the number of tests conducted for each of the two material sources. The clear positive correlation between peak nominal stress and the strain rate observed for the material sample plates, is also apparent for door trim cutout specimens. Once again, this result confirms that adopting a material model with a viscoplastic constitutive relation is reasonable.

Figure 3.25 shows the volumetric plastic strain at fracture for the same specimens plotted in Figure 3.24. An average plastic volumetric strain is also shown for each of the four different strain rates. By comparison with the sample plate material in Figure 3.14, a small reduction in volumetric strain at fracture was found for the door trims. Additionally, a less evident positive correlation between the strain rate and volumetric plastic fracture strain is indicated for the door trim cutouts. The figure

shows that large variations were present, both between the different locations, but also internally. The most significant variances were associated with the two lower strain rates. Similarly to the peak nominal stress, this result could be partially explained by the fact that a larger amount of tests were conducted at lower strain rates. However, the variance seems to diminish for higher rates, since the localisation effect is more pronounced for increasing strain rate.

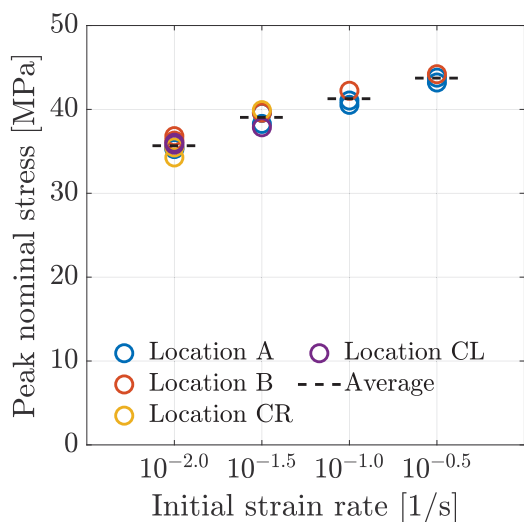


Figure 3.24: Peak nominal stress for different strain rates

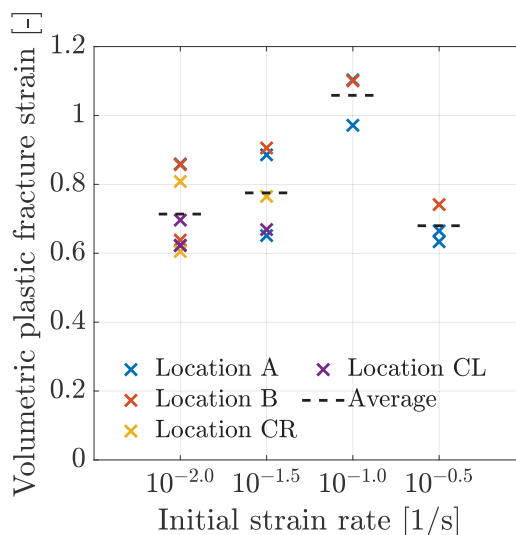


Figure 3.25: Plastic volumetric strain at fracture for different strain rates

The increased temperature due to adiabatic heating was recorded for tensile tests conducted in the meso-dynamic strain rate regime. Figure 3.26a and 3.26b shows the changes in temperature for the replicates tested at M and H strain rates, respectively. Since the thermal camera that was utilised had a lower temperature limit of $-20\text{ }^{\circ}\text{C}$, small changes in temperature could not be studied. In addition, the temperature changes were estimated using Eq. (2.28) and are shown as dashed lines in the figures. A generic specific heat capacity for PP was used here. This was done in order to evaluate the accuracy of the change in temperature estimated in the numerical model. From both figures, the final temperatures are clearly underestimated by Eq. (2.28). It is also evident that the changes in temperature are generally larger at M than at H strain rate. This is likely due to the magnitude of plastic strain and subsequent work prior fracture, being larger at M strain rate. Since PP has a low thermal conductivity, the heat is unable to diffuse from the specimen, also at M strain rate. It should be noted that the temperature increase associated with the creation of a new surface during crack propagation and fracture, is much larger than the temperature change resulting from adiabatic heating. This could affect the measured results and the final temperature readings might be invalid.

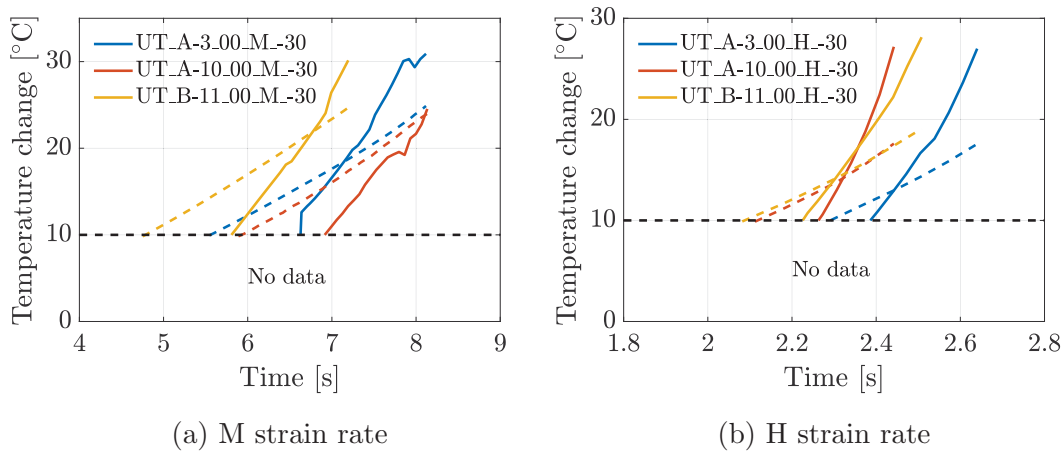


Figure 3.26: Comparing measured and estimated temperature change due to adiabatic heating for two strain rates

3.4.3 SEM results

SEM micrographs of the fracture surface found in test specimen UT_B-10_00_VL-30, are shown in Figure 3.27. The test was conducted at a quasi-static strain rate and the ductile nature of the polymer can be recognised by the presences of long pulling filaments observed at the highest magnification. From the lower magnification micrograph, the ductile failure morphology can be seen in most of the fracture surface. No signs of second phase particles were found, although some cavities are present. The cavities are indicated by an encircled area in the figure. This suggests that the filament structure is caused by interaction between cavities and the PP matrix. Such an interactin could lead to the formation of micro-necks as suggested by Peterlin [43], leading to large strain deformation. According to Galeski [44], these micro-necks are formed due to the presence of cavities in the material matrix. The could explain the large amounts of filaments that were found in this case.

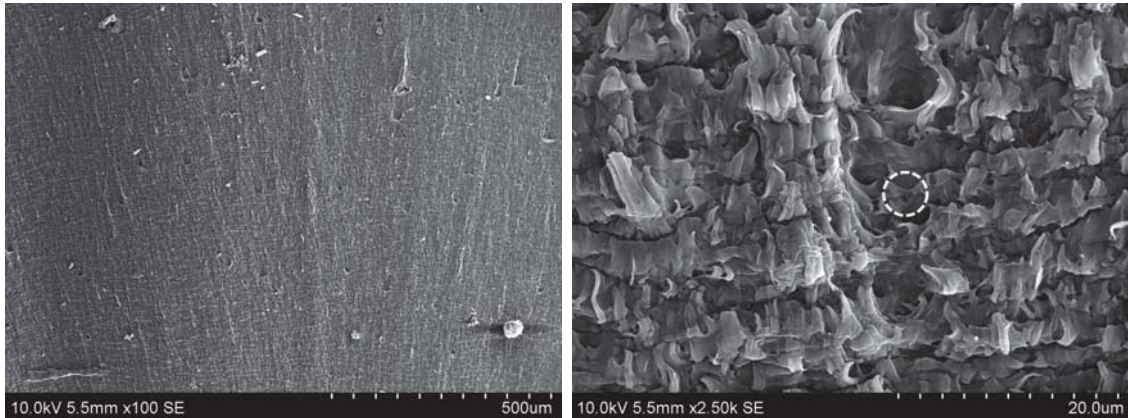


Figure 3.27: SEM micrographs of test specimen UT_B-10.00_VL_-30

3.5 Summary

In this chapter, two different uniaxial tensile test campaigns were conducted. Initially, the assumptions of the SPM were examined with respect to the material investigated in this thesis. Emphasis was, however, placed on characterising the viscoplastic properties of the material, as well as exposing any differences in mechanical behaviour between the sample plate- and door trim materials. The most important findings are summarised below:

- Both sample plate- and door trim materials showed isotropic behaviour.
- Large volumetric strains were found during deformation, suggesting that a dilatational flow potential is suitable. The retraction ratio was constant for intermediate to large plastic strains.
- A clear log-linear relation between peak stress and strain rate was evident in both sample plate- and door trim materials. Hence, a viscoplastic constitutive relation is applicable in the material model.
- Isothermal conditions were only found for the quasi-static strain rates. Large amounts of adiabatic heating and subsequent thermal softening occurred at strain rates of $10^{-1.0}$ and $10^{-0.5} \text{ s}^{-1}$.
- The material in the sample plates and door trims were found to be identical with respect to elasticity, yield strength, hardening or softening, and plastic flow. However, the volumetric plastic strain at fracture was significantly lower for the door trim material.
- The only location- and orientation-dependent mechanical property of the door trim was the strain at fracture.

- A ductile failure mode was observed at $-30\text{ }^{\circ}\text{C}$, for both sample plate- and door trim materials at strain rates between $10^{-2.0}$ and $10^{-0.5}\text{ s}^{-1}$.
- The SEM analyses conducted on specimens at strain rates of $10^{-2.0}$ and $10^{-0.5}\text{ s}^{-1}$ indicated different microscopic failure mechanisms, possibly related to the difference between stable necking and localisation. Long pulling filaments were observed at the lower strain rate, while elastometric second phase particles could be seen in the fracture surface for the highest strain rate.

Calibration of Material Model

The SPM was employed in order to replicate the mechanical behaviour observed in the experiments for the material used in the door trim, and thus the material sample plates. The material model is composed of different constitutive equations used to describe the general response of ductile thermoplastic polymers. The fact that different polymers exhibit distinctive material behaviour is incorporated in SPM through the material parameters. Calibration of the material model is a process that involves determination of these parameters and was conducted in the calibration software *MatPrePost*. This was performed using experimental data from uniaxial tensile- and compression tests at different strain rates and temperatures. As described in Chapter 3, special emphasis was placed on characterising the behaviour observed at high strain rates during this project. The hardening found at lower strain rates developed into softening as a result of the adiabatic heating that arose in the PP. Since adiabatic heating effects are not implemented in the SPM, as discussed in Section 2.3.6, an unconventional method was utilised in this project. *MatPrePost* and the associated calibration procedure are described in the following sections.

4.1 MatPrePost

Material calibration was mainly conducted in the software *MatPrePost*, which greatly simplifies the calibration process. The necessary experimental data is imported into the software along with some of the important dimensions of the specimen. In this thesis, the force, time, and logarithmic strain components obtained from the

DIC analyses, were imported as text-files into MatPrePost. Furthermore, measured cross-sectional dimensions of the gauge area and the associated initial strain rate of every test were specified. This enabled MatPrePost to compute the respective stress-strain curves. Calibration could then be conducted merely by choosing representative values from the curve related to each part of the constitutive model. The pressure sensitivity, viscoplastic behaviour and damage parameters were, however, calibrated manually. Once all model parameters had been fitted, a material card containing all calibrated values along with so-called flags controlling different features of the SPM [25] was exported. Such material cards for two different FEA softwares are shown in F.

4.2 Material tests

As discussed throughout Chapter 3, the results from both the material sample plates and the door trim cutouts were virtually identical with the exception of strain at fracture. Furthermore, since negligible variance between replicates of different tests was found for similar strain rates, only one replication of every rate in the quasi-static and meso-dynamic regimes was employed. Hence, the separate tests selected for material model calibration are listed in Table 4.1. To account for the adiabatic heating effects, the calibration procedure was mainly based on a test at H strain rate. It should be noted that these separate tests were carefully selected on the basis of being the most representative for each of the given test conditions.

Table 4.1: Tests of the sample plate material selected for calibration

ID	Initial strain rate	Calibrated parameters
UT_S_00_VL_-30_02	VL	ε_0^p, C
UT_S_00_L_-30_02	L	ε_0^p, C
UT_S_00_M_-30_02	M	ε_0^p, C
UT_S_00_H_-30_02	H	$E, \nu, R, \sigma_T, \beta, \varepsilon_0^p, C, D_I, D_C$

The first step in MatPrePost, after importing the mentioned text-files, is limitation of the valid data for every test. This is necessary because some initial inaccuracies in the machine logging, e.g. play in the mounting grips, is evident prior to stretching of the specimen. Additionally, since the data is invalid subsequent to fracture, the curve was cut at the commencement of cracking represented by an abrupt drop in stress. Since the sample plate- and door trim material was found be virtually identical, only the former were used for calibration of the material model. However, to compensate for the difference in strain at fracture for the two material sources,

the damage parameters were calibrated for both the sample plate- and door trim material.

4.3 Elasticity

The elastic material parameters, i.e. the Young's modulus, E , and the Poisson's ratio, ν , were the first parameters to be calibrated in MatPrePost. By selecting two distinct points in the assumed linear elastic region of the nominal stress-strain curve, respectively shown as two red circles in Figure 4.1, MatPrePost creates a linear curve between these points and extrapolate it along the nominal stress-strain curve. The gradient of this linear curve corresponds to the calibrated Young's modulus of the material.

A linear curve at 0.2 % offset strain is plotted by MatPrePost in order to give an estimate of the yield stress of the material. This curve intersects the nominal stress-strain curve at the point of the estimated yield stress. However, the viscoplastic material behaviour requires an effective yield stress varying with strain rate to enable accurate modelling. Hence, a constant yield stress is not calibrated for the material model. Furthermore, the calibration of the Poisson's ratio was conducted through comparison of the strains in the transverse and longitudinal direction of the selected test data. The values of both the Young's modulus and the Poisson's ratio are listed in Table 4.2.

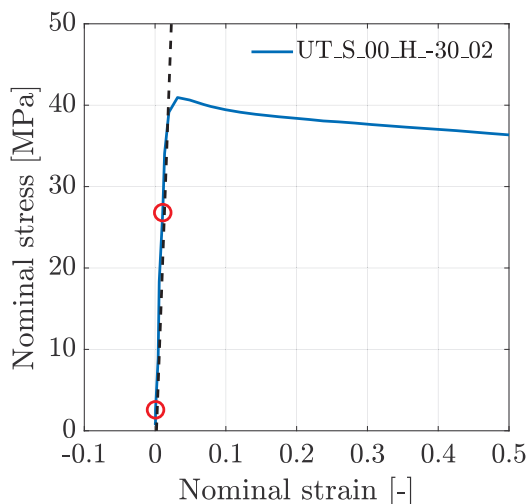


Figure 4.1: Calibration of Young's modulus, E

Table 4.2: Elastic parameters

Parameter	Value	Unit
E	2696	MPa
ν	0.267	-

In Figure 4.1, it is evident that the elastic region is substantially smaller than the

plastic region of the nominal stress-strain curve. This implies a considerable difference in number of data points between the two domains. Moreover, no pronounced transition is obvious in the curve between the elastic and plastic domains. Ultimately, this means that the calibrated elastic parameters may contain some inaccuracy. Nevertheless, by comparing the obtained test data from the separate specimens, the resulting values in Table 4.2 are reasonable.

4.4 Hardening and softening

The unconventional method of indirectly implementing the softening behaviour from the experimental results obtained at H strain rate, was utilised in order to account for the adiabatic heating effects. For sufficiently high strain rates, the softening characteristics are more pronounced than that of the hardening. Furthermore, the H strain rate has been given the most concern in order to achieve a more realistic material characterisation regarding the full-scale component behaviour undergoing impact loading. To be able to sufficiently describe the plastic domain of the material, its softening characteristics must be calibrated. The elastic domain, as well as any viscoplastic effects, are both omitted in the calibration of the softening parameters. The yield stress in tension, σ_T , was calibrated in addition to the softening term, R , constituted by three terms, i.e. R_i for $i = 1, 2, 3$. These terms are incorporated in the Voce hardening rule employed by the SPM, which is given in Eq. (2.26). Each term is dependent on both parameters, Q_{Ri} and θ_{Ri} , affecting the initial saturation value and slope of the softening, respectively. Table 4.3 lists the calibrated values of the yield stress and the six separate softening parameters.

Table 4.3: Softening parameters

Parameter	Value	Unit
σ_T	26.8	MPa
θ_{R1}	254	MPa
Q_{R1}	2.74	MPa
θ_{R2}	-45.2	MPa
Q_{R2}	-62.4	MPa
θ_{R3}	-2.56	MPa
Q_{R3}	26.8	MPa

As discussed in Section 2.3.7, the constitutive relations for damage evolution are based on volumetric strains. This means that if the material exerts incompressible

material behaviour, i.e. if $\varepsilon_V = 0$, no damage will accumulate. In order for the softening parameters to be valid in load cases other than uniaxial tension, the coupled damage evolution given in Eq. (2.29) was implemented. Hence, if the softening parameters are calibrated from a compressible material behaviour, the damage will be applied to the material twice. Therefore, the hardening parameters were calibrated from the incompressible material behaviour which is not affected by any damage, such that the coupled damage evolution could be implemented at a later stage.

In MatPrePost, the procedure of calibrating the relevant material parameters was automatically conducted by the software. The curve from the experimental data and the associated calibrated fit, employing the parameters in Table 4.3, are both plotted in Figure 4.2. It should be noted that the final drop in the curve obtained from the experimental data is due to localisation in the specimen. This effect will be included through the numerical simulation without the need of further calibration. The resulting softening term, R , and the associated components, R_1 , R_2 and R_3 , are plotted in Figure 4.3. All three components are necessary to enable an accurate fit of the whole curve. To precisely follow the experimental data at lower strains, the combination of the hardening effect incorporated by R_1 and the softening effect implemented by R_3 plays a major role. For larger strains, however, it is evident that R_2 dominates the behaviour of the resulting softening term R . Due to the chosen stress measure, Figures 4.2 and 4.3 displays a behaviour that resembles hardening and not softening. However, it is nonetheless evident from Figure 3.9 that the softening effect is dominating for the H and M strain rates.

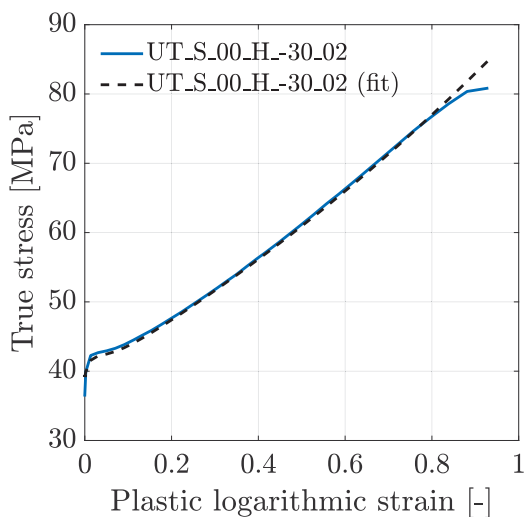


Figure 4.2: Calibration of softening parameters

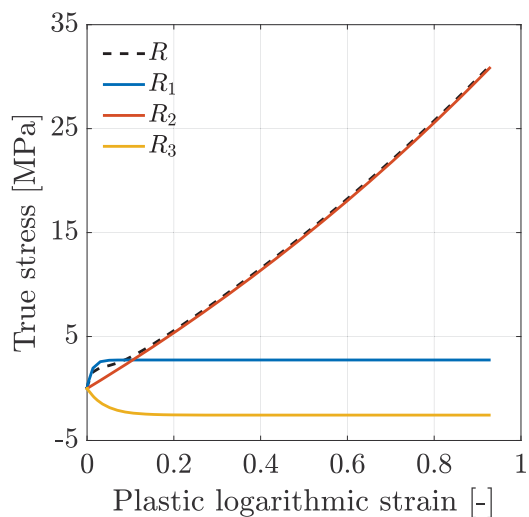


Figure 4.3: Comparison of separate softening terms

4.5 Pressure sensitivity

The pressure sensitivity of the model concerns the difference in the yield and plastic flow observed for compression and tension in ductile polymers. Hence, the yield stress from both a compression- and a tensile test at 20 °C are needed for calibration of the pressure sensitivity. In this project, no such tests were performed. However, since no significant changes in the mechanical behaviour of the sample plates were found compared to the previous work, the experimental data and procedure described by Schwenke [2] was utilised. Thus, the respective yield stresses were found from the true stress-logarithmic strain curves obtained at room temperature. A Considère construction was employed to determine the yield stress for both tests, as shown in Figure 4.4. This was done since the material exhibits some nonlinear behaviour in the elastic domain, making determination of an exact yield stress more complicated. The technique employs a tangent line, constructed from $\varepsilon = -1$, onto the stress-strain curves. Yielding is defined by the point where the slope of this tangent correspond to the slope of the stress-strain curve, as seen in Figure 4.4. In this case, the points corresponded to 26.4 MPa and 21.6 MPa for compression and tension, respectively. Hence, the resulting pressure sensitivity, α , is shown in Table 4.4. A similar pressure sensitivity of 1.24 was found for PP by Donato and Bianchi [45].

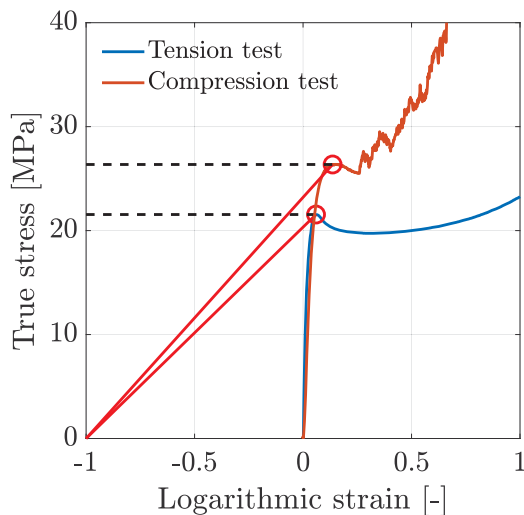


Figure 4.4: Calibration of pressure sensitivity, α

Table 4.4: Pressure dependency

Parameter	Value	Unit
α	1.22	-

4.6 Plastic dilatation

In order to model the development of volumetric strains in the material which was observed during material testing, the plastic dilatation parameter β was calibrated. Since the material was found to be isotropic in Section 3.1, i.e. the two transverse strain components were similar, they can be related to the longitudinal strain component through the retraction ratio. The SPM assumes a constant retraction ratio, which was confirmed for intermediate to large logarithmic strains, as shown in Figure 3.12b. The plastic dilatation parameter can further be derived from the retraction ratio through the following expression

$$\beta = \frac{2 - R_r}{R_r + 1}, \quad (4.1)$$

where R_r is the retraction ratio. A mathematical derivation of the expression above is provided in Appendix A. Two points corresponding to logarithmic strains of 0.4 and 0.8 were chosen in order to calibrate the plastic dilatation parameter, shown in Figure 4.5. Employing the respective retraction ratios, β could be calculated using the equation above. The result is found in Table 4.5.

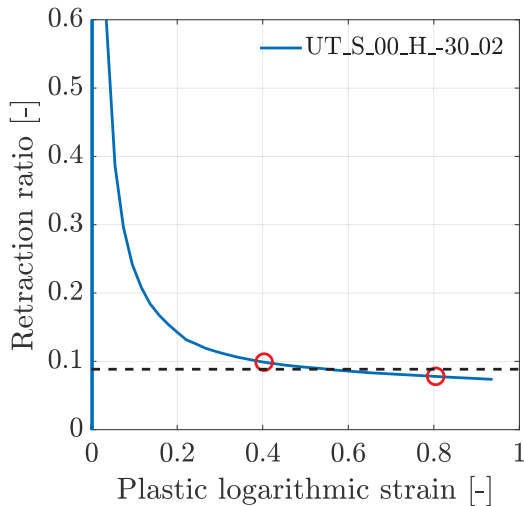


Table 4.5: Development of plastic volumetric strains

Parameter	Value	Unit
β	1.88	-

Figure 4.5: Calibration of plastic dilatation parameter, β

4.7 Strain rate dependence

The strain rate dependent behaviour of the material is modelled by calibration of two parameters, the strain rate parameter C and reference strain rate $\dot{\epsilon}_0^p$. Hence, only two tests at different strain rates are needed in order to calibrate the viscoplastic behaviour of the model. In general, these parameters allow for the plastic portion of the stress-strain curve to be vertically translated, according to the arising strain rates. The viscoplastic parameters will, however, not affect the slope of the plastic domain, resulting from the already calibrated hardening parameters.

Due to the unconventional approach for calibration of the softening parameters in this thesis, an equivalent approach was adopted when calibrating the viscous parameters. To allow for the behaviour at higher strain rates to be accurately modelled, the strain ranges included during calibration of the viscoplastic parameters were determined correspondingly. Thus, the curves at VL and L strain rates were limited to strains of 0.4 and 0.5, respectively. The softening effect observed at M and H strain rates were taken into account by including a larger portion of these curves, i.e. strains of 0.6 and 0.7. The result is seen in Figure 4.6, and shows that the curves at higher strain rates are more accurately reproduced by the calibrated parameters. The resulting strain rate parameters shown in Table 4.6 were fitted by a supplied Python-script, in addition to the softening parameters. The script was provided by SINTEF researcher, T erence Coudert, developer of MatPrePost.

Table 4.6: Strain rate dependence in material

Parameter	Value	Unit
C	0.0546	-
$\dot{\epsilon}_0^p$	6.25e-05	1/s

4.8 Damage

The evolution of damage is controlled by the plastic dilatation parameter, determining the amount of volumetric plastic strain occurring in the model. Fracture is, however, governed by the two damage parameters, D_I and D_C . As discussed in Section 2.3.7, the damage evolution, D , is expressed on the form

$$D = 1 - (1 - D_I) \exp(-\epsilon_V^p) \quad (4.2)$$

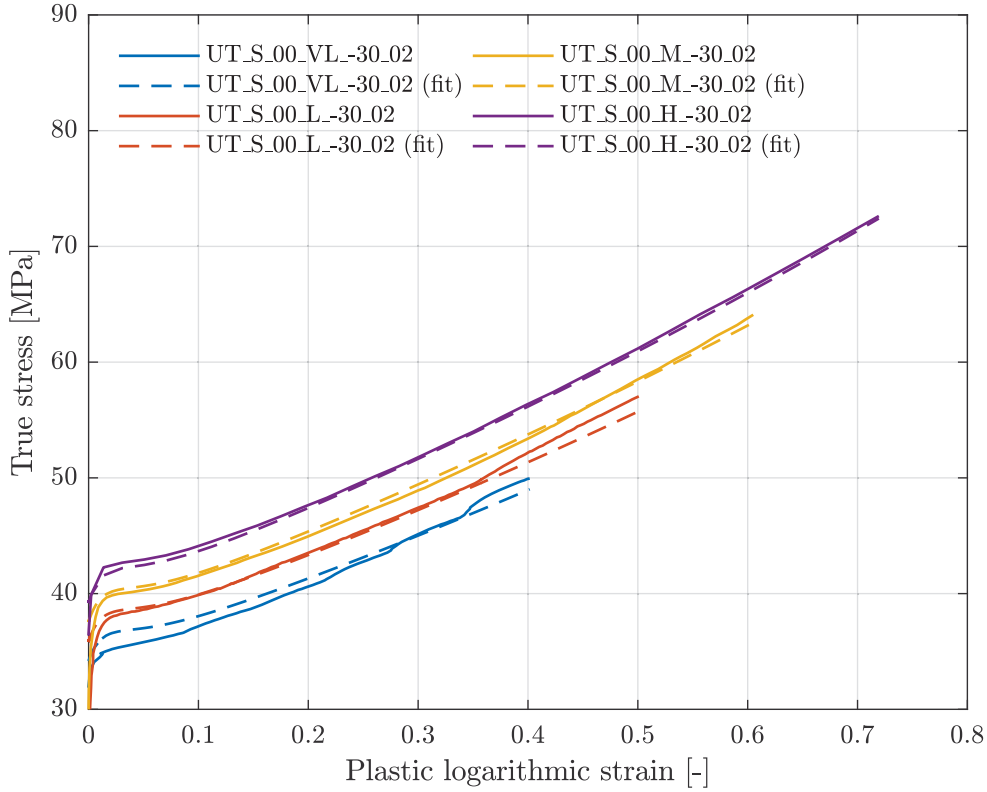


Figure 4.6: Calibration of the strain rate dependency, C and ε_0^p

were D_I is the initial damage and ε_V^p is the volumetric plastic strain. Since the material is assumed to be flawless prior to testing, the initial damage is assumed to be zero. Thus, the critical damage D_C for which fracture occurs in the material can be determined from the plastic volumetric strain at fracture, $\varepsilon_{V,f}^p$, using the following equation

$$D_C = 1 - \exp(-\varepsilon_{V,f}^p). \quad (4.3)$$

The plastic volumetric strain at fracture is plotted for a single representative test at H strain rate for the sample plate- and door trim material in Figure 4.7 and 4.8, respectively. Since the only difference between the two material sources was related to the strain at fracture, only the critical damage was altered between the two calibrations. The resulting parameters are shown in Table 4.7 and 4.8 for the sample plate- and door trim material, respectively.

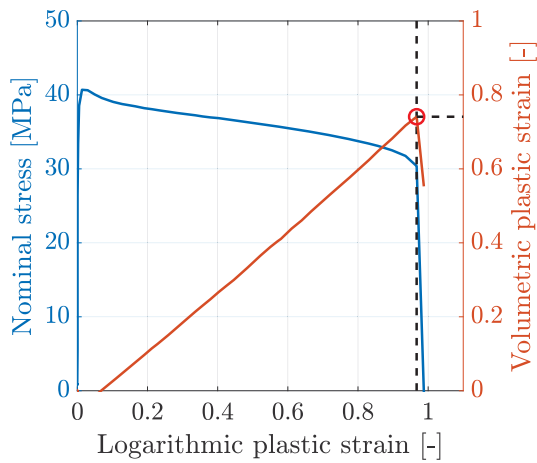


Table 4.7: Damage parameters for sample plate material

Parameter	Value	Unit
D_I	0.0	-
D_C	0.529	-

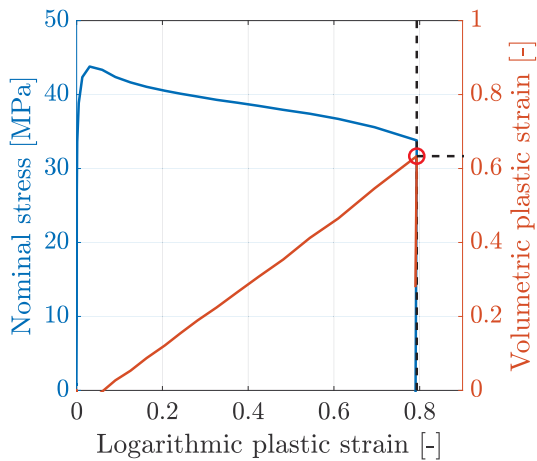
Figure 4.7: Calibration of damage parameters for sample plate material, D_I and D_C 

Table 4.8: Damage parameters for door trim material

Parameter	Value	Unit
D_I	0.0	-
D_C	0.469	-

Figure 4.8: Calibration of damage parameters for door trim material, D_I and D_C

4.9 Calibrated material parameters

All calibrated material parameters for the sample plate- and door trim materials are shown in Table 4.9 and 4.10, respectively. The density indicated in both tables was provided by Toyota during Schwenke's project [2].

Table 4.9: Calibrated parameters for sample plate material

E	ν	θ_{R1}	Q_{R1}	θ_{R2}	Q_{R2}	θ_{R3}	Q_{R3}
[MPa]	[-]	[MPa]	[MPa]	[MPa]	[MPa]	[MPa]	[MPa]
2696	0.267	254	2.74	25.3	-45.2	-62.4	-2.56
σ_T	α	β	$\dot{\epsilon}_0^p$	C	D_I	D_C	ρ
[MPa]	[-]	[-]	[1/s]	[-]	[-]	[-]	[t/mm ³]
26.8	1.22	1.88	6.25e-05	0.0546	0	0.529	9.05e-10

Table 4.10: Calibrated parameters for door trim material

E	ν	θ_{R1}	Q_{R1}	θ_{R2}	Q_{R2}	θ_{R3}	Q_{R3}
[MPa]	[-]	[MPa]	[MPa]	[MPa]	[MPa]	[MPa]	[MPa]
2696	0.267	254	2.74	25.3	-45.2	-62.4	-2.56
σ_T	α	β	$\dot{\epsilon}_0^p$	C	D_I	D_C	ρ
[MPa]	[-]	[-]	[1/s]	[-]	[-]	[-]	[t/mm ³]
26.8	1.22	1.88	6.25e-05	0.0546	0	0.469	9.05e-10

Verification of Material Model

Once the calibration was completed, verification of the SPM was important in order to ensure an accurate and realistic representation of the material in question. Therefore, numerical replicates of the material tests, performed through the experimental campaigns described in Chapter 3, were modelled and simulated in a suitable FEM software. This verification was essential since it allowed for the material characterisation to be extrapolated to other load cases. Hence, the validated material parameters, which in this case were calibrated from a uniaxial tensile test, could be used for numerical modelling of more intricate load conditions. This extrapolating method must, however, be used with great care. In this chapter, the validation procedure is presented.

5.1 Introduction

The procedure of verifying the material model and the calibrated parameters, which was found in Tables 4.9 and 4.10, was conducted through numerical representations of the uniaxial tensile tests at quasi-static and meso-dynamic strain rates. Several simulations were performed in order to compare the results obtained from the numerical model and the experimental test data. Furthermore, if the results from the simulation and the associated experiment are comparable, the material model is assumed to yield satisfactory performance when exposed to the relevant conditions. However, the uniaxial tensile tests are not necessarily representative of the biaxial stress state emerging in the impact testing, for which the model will be utilised. Additionally, potential shortcomings of the material model will be high-

lighted throughout the following sections.

5.2 Numerical model

The numerical model of the uniaxial tensile specimen was modelled in Abaqus/CAE. The geometry and nominal dimensions were defined according to Figure 3.2. For simplicity, the nominal dimensions were employed in the numerical model since only small variations in width and thickness were found. In order to compare the experimental and numerical results, the material parameters from Section 4.9 were included in the numerical model representing the sample plate- and door trim cutouts, respectively. The difference in nominal dimensions and fracture parameters between the two material sources, separate models were created.

Since the geometrical shape of the specimen allows for three planes of symmetry, simplification of the numerical representation was done by modelling only one eighth of the specimen. The plates of symmetry are displayed in red in Figure 5.1. Furthermore, since large portions of the specimens were utilised for clamping, they were excluded from the model. Hence, a considerable reduction in excessive computational time was attained. It should, however, be noted that exclusion of the clamping portion of the model implies that no slipping occurred in that region throughout the experiment. Nevertheless, the remaining portion, which was actually modelled, is highlighted in orange in figure. Additionally, the borders of the clamping regions are rendered as green planes.

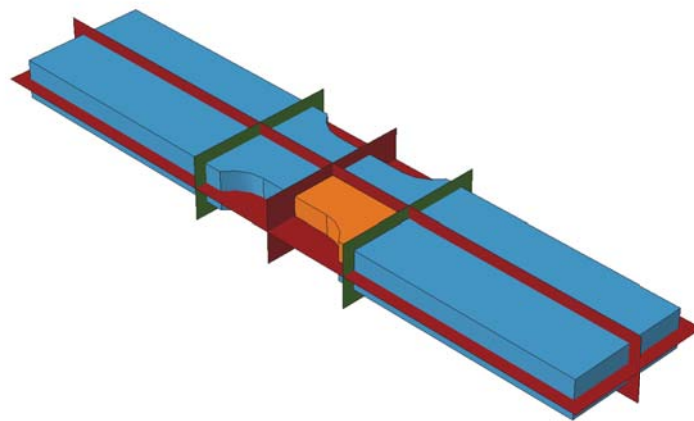


Figure 5.1: Simplification of the modelled tensile specimen

The meshed numerical model from the top and end views are shown in Figures 5.2a and 5.2b, respectively. To enable valid comparison between the numerical model

and the experimental data, an equivalent method of longitudinal strain extraction was essential. However, it turned out that this method does not require identical mesh sizes in the numerical model and in DIC. This facilitates the attainment of accurate results from the FEM software while at the same time allowing for utilisation of a suitable mesh size in eCorr. Implementation of an alternative procedure than the one presented in Section 2.2.2 was utilised here. The strain was extracted through a virtual extensometer, measuring the total displacement over its length. Furthermore, this displacement was converted into strains through Eq. (2.3) and (2.4), i.e. by measuring the relative change in distance between the two end points of the extensometer. In these figures, the red dot corresponds to one such end point. In Section 3.1 the strains were extracted from a column of elements over the zone prone to crack initiation and subsequent fracture. Here, however, the strains were calculated from the change in displacement between the two end points of the virtual extensometer. Hence, they were dispersed over a larger area.

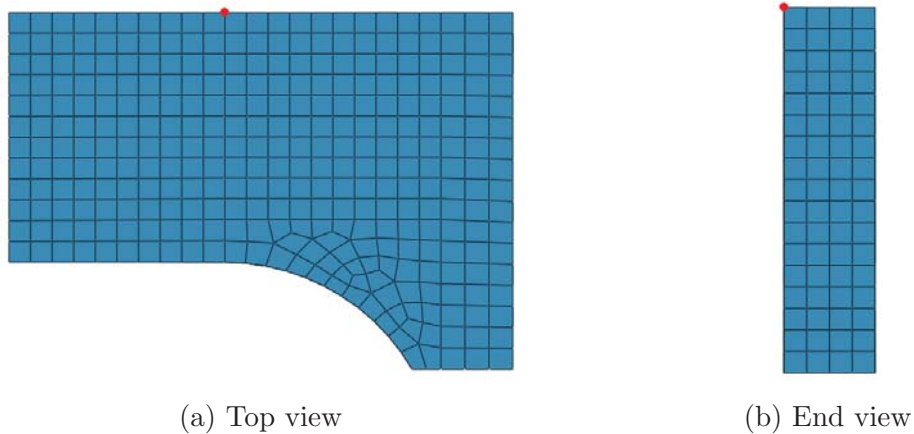


Figure 5.2: The numerical model of the tensile specimen, including the node of displacement extraction

A constant velocity, and thereby the relevant initial strain rate of each test shown in Table 3.2, were applied at the end face of the specimen shown in Figure 5.2b. Symmetric boundary conditions were utilised at the intersections of the symmetry planes rendered in Figure 5.1. Furthermore, both reaction forces and transverse strains were extracted at the symmetry plane along the longitudinal axis of the specimen. To check any influence of the symmetry, an identical simulation was run for a model of the whole specimen. No noteworthy differences were found in the results between the two models. Hence, the model representing one eighth of the specimen served as an obvious choice due to computational efficiency.

In this case, both implicit- and explicit solution methods were investigated. However, due to the dynamic nature of the impact testing in the drop tower and on the

component, including high levels of nonlinearity over a short period of time, an explicit method was chosen for these simulations. This enabled both accurate and more computationally efficient simulations, as discussed in Section 2.4.1. If, on the other hand, an implicit method was to be employed, accurate results would have been unattainable due to the larger time steps introduced by this solution method. Consequently, most emphasis was placed on the explicit solution method for the tensile specimen simulations as well.

The element formulation utilised for the numerical model of the uniaxial tensile specimen was a solid eight-node, full integration, general purpose, linear hexahedral, brick element. The method of full integration was employed in order to attain more accurate results, as described in Section 2.4.3. However, some issues of the brick element are related to volumetric- and shear locking which may arise if the material behaves isochoric or if bending is the dominating load condition [29, 46], respectively. However, since the material is compressible and the model only represents uniaxial tension, this is not a concern here.

5.3 Results

The SPM is unable to couple the calculated adiabatic heating back into the material parameters, as discussed in Chapter 4. Hence, the effect of the temperature rise was indirectly implemented in the material characterisation by utilising experimental data for which such effects were present. Therefore, the H strain rate was given the most emphasis throughout this section as well. All the tested strain rates were nonetheless examined to ensure validity of both the calibrated material model and the numerical representation of the problem. Once again, as seen throughout this thesis, the nominal stress was utilised for comparison between the numerical- and experimental results instead of the corresponding force.

5.3.1 Refinement of numerical model

A brief investigation regarding the mesh convergence was conducted in order to optimise the mesh size with respect to both accuracy and computational efficiency. This study was done by repeating similar simulations with several different mesh sizes for the numerical models representing the specimens extracted from both the material sample plates and the door trims. Figure 5.3 displays the peak nominal stress against the number of elements associated with the separate models in the convergence study. It is clear that convergence is reached when the number of

elements surpasses 1 000. Although a clear converging trend is evident from the figure, it should be noted that the maximum difference in peak nominal stress, found in the study, is less than 1.0 MPa. Hence, all models yielded decent results, despite the finer meshes proved better accuracy.

In Figure 5.4 the computational time versus the number of elements is plotted on a log-log scale. Here, it is obvious that the computational effort increases drastically with number of elements. Theoretically, when simulations are run on the same computing units this trend is found to be linear with respect to degrees of freedom in the system [47]. An interesting observation is the plateau seen in the curve between approximately 20 and 60 elements, and that the portion of the curve for less than 60 elements is not linear. These irregularities are believed to occur because the simulations were run through a computer cluster, where different computing units might have varying performance, ultimately providing distinctive computational times. Another potential explanation is that the discrepancies could be related to the fact that theory does not always comply with reality. However, the theoretical assumption seems to be appropriate for the approximate log-linear behaviour seen for the numerical models with more than 200 elements. The tendency of protracted computational times as a result of mesh refinement is nonetheless reported.

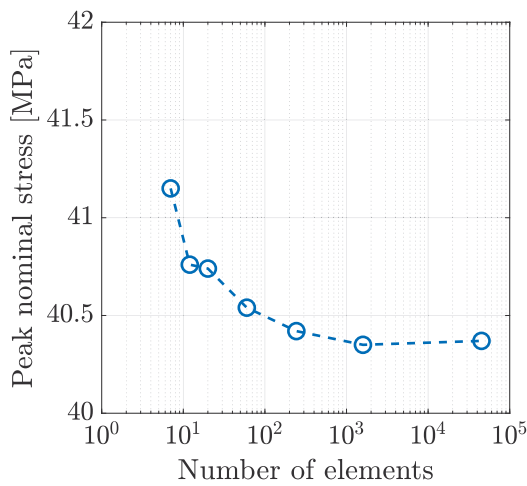


Figure 5.3: Peak nominal stress for different mesh sizes

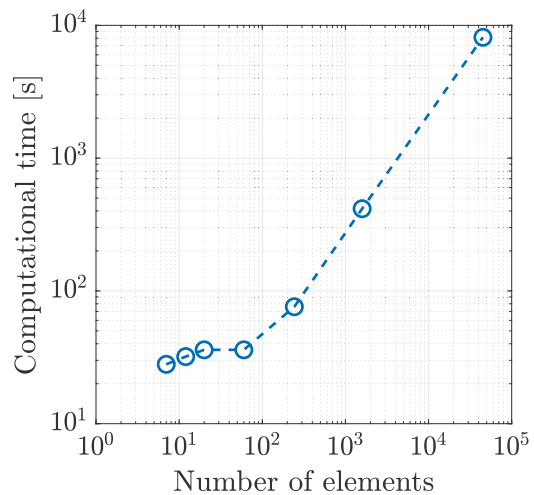


Figure 5.4: Computational time for different mesh sizes

The outcome of the mesh convergence investigation indicated that coarser meshes, with less than 200 elements, provide excellent computational efficiency, but less accurate results. Furthermore, the finer meshes, within the range of 200 to 2 000 elements, produces enhanced accuracy compared to the coarser meshes. Concurrently, they are relatively efficient with respect to computational time, thus providing high

performance. The finest mesh, however, with more than 45 000 elements, did not provide any significant increase in accuracy compared to the intermediate mesh refinements. Furthermore, it proved to be extremely inefficient with respect to computational time. All meshes including more than 200 elements provided satisfactory results with respect to the peak nominal stress, while the coarser meshes provided a slight overestimation. Additionally, the coarser meshes failed to accurately represent the strain at fracture when compared with the experiment, while the opposite was found for the finer meshes. To obtain a satisfactory balance between the accuracy and the computational cost, the model with approximately 1 500 elements was selected for further study.

Note also that to increase the computational efficiency of the numerical model, mass scaling was utilised. This effect could influence the curve relating mesh size and computational effort in Figure 5.4, and contribute to the unusual log-linear behaviour. As discussed in Section 2.4.2, this method must be used with great care due to possibly arising inertial effects. However, the resulting kinetic energy obtained in the simulations proved to be negligible compared to the internal energy of the specimen. Hence, accurate results and greater computational efficiency were achieved.

5.3.2 Verification

In Figure 5.5a, the experimental results from test specimen UT_S_00_H_-30_02 are compared to the numerical representation. Both explicit- and implicit solution methods were investigated, as stated earlier. By studying the curves from each integration scheme, it is evident that they are identical. The only difference between the explicit- and implicit results is that the former actually fractures, while the latter simulation data is plotted only until fracture occurs. This is due to the fact that element erosion can not be modelled using the implicit method. Since there is virtually no deviation with respect to the two numerical methods, the explicit model was selected as the basis model. In addition, mass scaling was enabled since inertial effects were assumed to be small. Thus, the computational cost was significantly reduced.

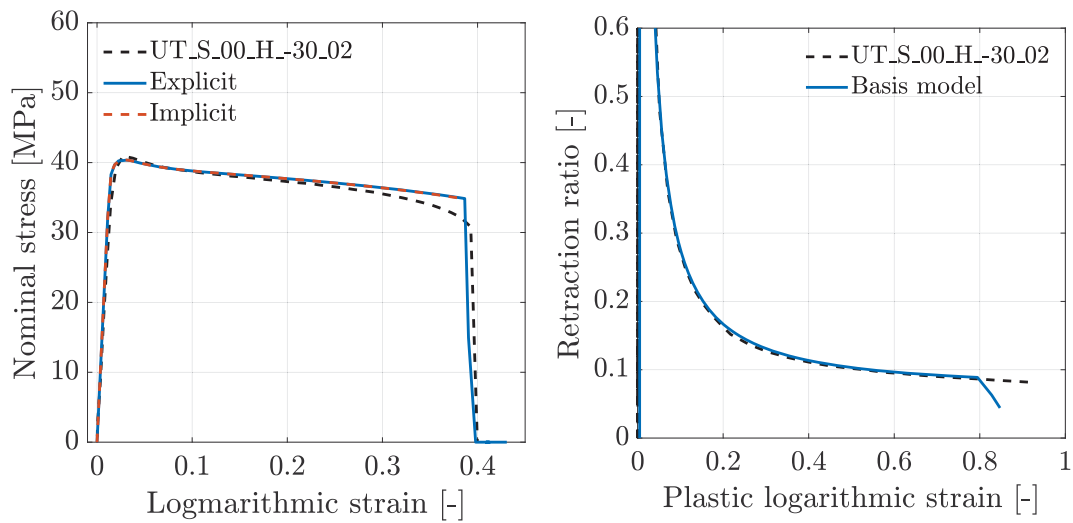
By comparing the numerical- and experimental results, it is obvious that numerical model is able to recreate the same behaviour as seen in the experiment. However, the peak nominal stress is slightly underestimated by the numerical representation. It is also apparent that the localisation effect in the numerical results tend to be somewhat less pronounced than what was seen in the experiment. The stress at

fracture is roughly 13 % higher in the numerical model, and the relative difference in strain at fracture is approximately 1.6 % compared to the experiment. These effects are correlated as higher stresses lead to smaller strains, and vice versa. Although the localisation effect is present in the numerical simulation, it is not as predominant as in the experiment. However, it should be emphasised that the localisation found in the experimental results is not believed to be as significant under other loading conditions imposing different stress triaxialities. Hence, the discrepancy found in stress and strain at fracture is believed to be less significant during impact loading.

The retraction ratios for the selected experiment and the numerical representation are plotted in Figure 5.5b. It is clear that the numerical model captures the behaviour in an accurate fashion. However, some deviation is evident after a plastic logarithmic strain of approximately 0.8. By comparing this result with what is seen in Figure 5.5a, it is evident that the different behaviour just before fracture may produce some disagreement with respect to the retraction ratio as well. It is believed that the response seen in Figure 5.5b is due to initiation of fracture in the numerical model, i.e. failure of some integration points within the column of elements for which the strains are extracted. Hence, this effect presumably causes the slightly premature drop in transverse strain, and thus retraction ratio. Note that the strains used in this figure were extracted through a column of elements in a similar procedure as the one utilised in Section 3.2.3.

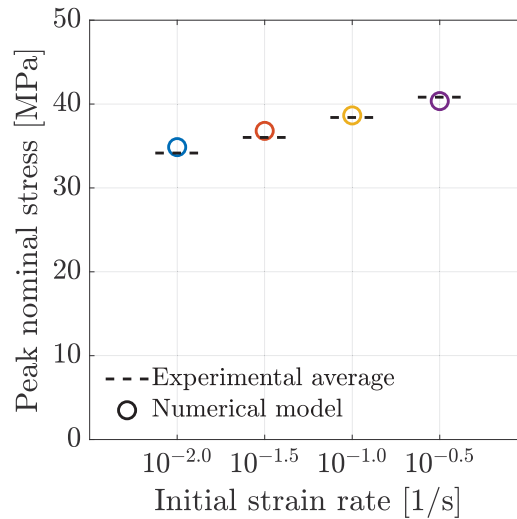
Figure 5.5c compares the peak nominal stress for both the experimental results and the numerical models. Here, only the numerical representation of the material sample plates are included as the strain rate parameters found in Chapter 4 are identical for both material sources. Hence, the equivalent simulations of the door trim cutouts yielded similar results. Due to the effective gauge area of the door trim cutout specimens, discussed in Section 3.1, the numerical results are not directly comparable to those found in Figure 3.24. By comparing the results found in Figure 5.5c to the curves displayed in Figure 4.6, it is clear that the two figures demonstrate the same trends. For VL and L strain rates, the peak nominal stress is overestimated, while a better representation was found for M and H strain rates.

It is evident that the numerical model is well capable of representing the experimental results, even for strain rates ranging over a span of one and a half decade. This means that the material model and the associated calibration proves to be accurate for the particular load condition reproduced numerically. Hence, the model can be extrapolated to more complex problems, including higher triaxialities. However, care must be taken when employing the model outside the domain for which it is based. Implementation of new loading regimes may introduce varying mate-



(a) Nominal stress-logarithmic strain

(b) Retraction ratio



(c) Peak nominal stress-strain rate

Figure 5.5: Comparing experimental results with numerical simulations

rial parameters or other emerging effects which are not present in the underlying experimental data. Therefore, the model could be incapable of accounting for such behaviour, and is perhaps vulnerable of producing inaccurate results for load cases outside its well-suited domain.

Drop Tower Impact Testing

In this project, two experimental campaigns were conducted in a drop tower in order to investigate the cold impact performance of PP under controlled conditions. This allowed for a load case that better resembles the component drop tests, with the possibility of acquiring recorded data of the material response, and thus enabling comparison with the numerical results. Although the material model was verified in uniaxial tension in Chapter 5, further validation was needed. In general, the SPM is capable of describing the material behaviour for different triaxialities. However, the material properties of polymers depend significantly on stress state and increased strain rate, both of which are present in impacts caused by dropped objects. Therefore, numerical simulations of the small-scale impact test were conducted in order to rule out possible discrepancies related to the material calibration. An extensive sensitivity study was also performed to reveal whether any parameters substantially affected the numerical results. The experimental programme and the numerical investigations will be discussed in the following.

6.1 Experiment

Two thorough experimental campaigns regarding drop tower testing of square PP plates, were used for determination of the cold impact resistance of the material. These experimental campaigns involved testing of the earlier mentioned material sample plates and door trim cutouts. By reconstructing the conditions found in the full-scale drop tests performed at Toyota Motor Europe (TME), representative results could be obtained. Such conditions include high strain rates, a biaxial

6.1. Experiment

stress state, adiabatic heating and low temperature. The conditions are believed to influence the material behaviour, -capacity and -characteristics. To further verify the material model, numerical representations were created in a FEM software and compared to the experimental tests.

Table 6.1 gives a brief description of the two experimental test campaigns that were conducted in the drop tower. As for the material testing, the two material sources are divided by a horizontal line in the table. The samples obtained from the actual door trims were mainly extracted from location C, illustrated in Figure 1.4. To avoid irregularities on the back of the door trim, care was taken when extracting the specimens. Two of the door trim cutout specimens were, however, extracted such that what appeared to be a weld line ran through the middle of the specimen. This weld was present at the same location on all door trims, and was believed to originate from the production process. The samples, denoted as CS, were therefore extracted in order to suggest whether this weld had any effect on the mechanical properties of the material. Table 6.1 also shows the number of successful replicates for each specific type of test. In the rightmost column, the ID is given for different test conditions. The structure of the ID is of the form: Type of test - Material source - Temperature - Replicate number.

Table 6.1: Drop tower test program

Material source	Temperature	Replicates	ID*
Sample plates	-30 °C	7	DT_S_-30_#
Door trim	-30 °C	5	DT_C-□_-30
Door trim	-30 °C	2	DT_CS-□_-30

*Material sample plates: # is a placeholder for the replicate number of each individual test

*Door trim cutouts: □ is a placeholder for the door trim number from which the specimen was extracted

6.1.1 Test specimens

The drop tower at SIMLab's facilities is instrumented in such a way that different types of test specimens can fit within the impact chamber. Additionally, different boundary conditions are possible, depending on the designated experimental requirements. The rig is suited for specimens of numerous thicknesses, widths and lengths. Furthermore, customisation of the rig is easily attained if needed. As stated above, the specimens that were tested during the two experimental campaigns originated

from two sources; the material sample plates and the door trims. Whereas the material sample plates required no modifications, the door trim cutouts were carefully sawn out of the door trims.

As the different plates originate from two separate sources, deviations between the specimen dimensions were evident. Figure 6.1 displays the general geometry of the drop tower test specimen. Here, w , h and t represents the width, height and thickness of the specimens, respectively. Some scatter with respect to the dimensional measurements were found between the distinct samples originating from the same source. However, the averaged dimensions listed in Table 6.2 act as fair representations for both material sources.

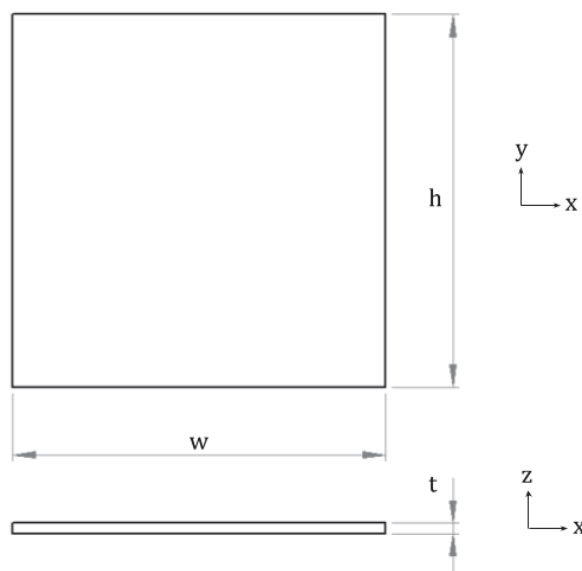


Figure 6.1: General geometry of the drop tower test specimen.

Table 6.2: Average test specimen dimensions

Dimensions	Material sample plates	Door trim cutouts
w	117.7 mm	104.2 mm
h	121.5 mm	104.4 mm
t	3.15 mm	2.45 mm

The location on the door trims, from which the test specimens were extracted, was primarily chosen based on the consistency of the results during Schwenke's work [2]. The choice was nonetheless dependent on the levelness for different regions of the door trim. Moreover, the location is in the vicinity of the position appointed for further investigation in the previous work. It should, however, be noted that the

6.1. Experiment

cutout specimens were chosen somewhat smaller than the material sample plates. This was done due to the complex geometry of the door trim.

6.1.2 Setup

All impact tests were performed in an *Instron CEAST 9350 Drop Tower Impact System* and at low temperature. Figure 6.2 shows an overview of the employed setup, where liquid nitrogen was used for cooling. Figure 6.3a depicts the corresponding drop tower test machine in an open configuration. Both figures include the mounted environmental chamber utilised in the cold impact tests. Furthermore, Figure 6.3b provides a principle overview of the impactor dimensions, and the support table mounted within the environmental chamber.

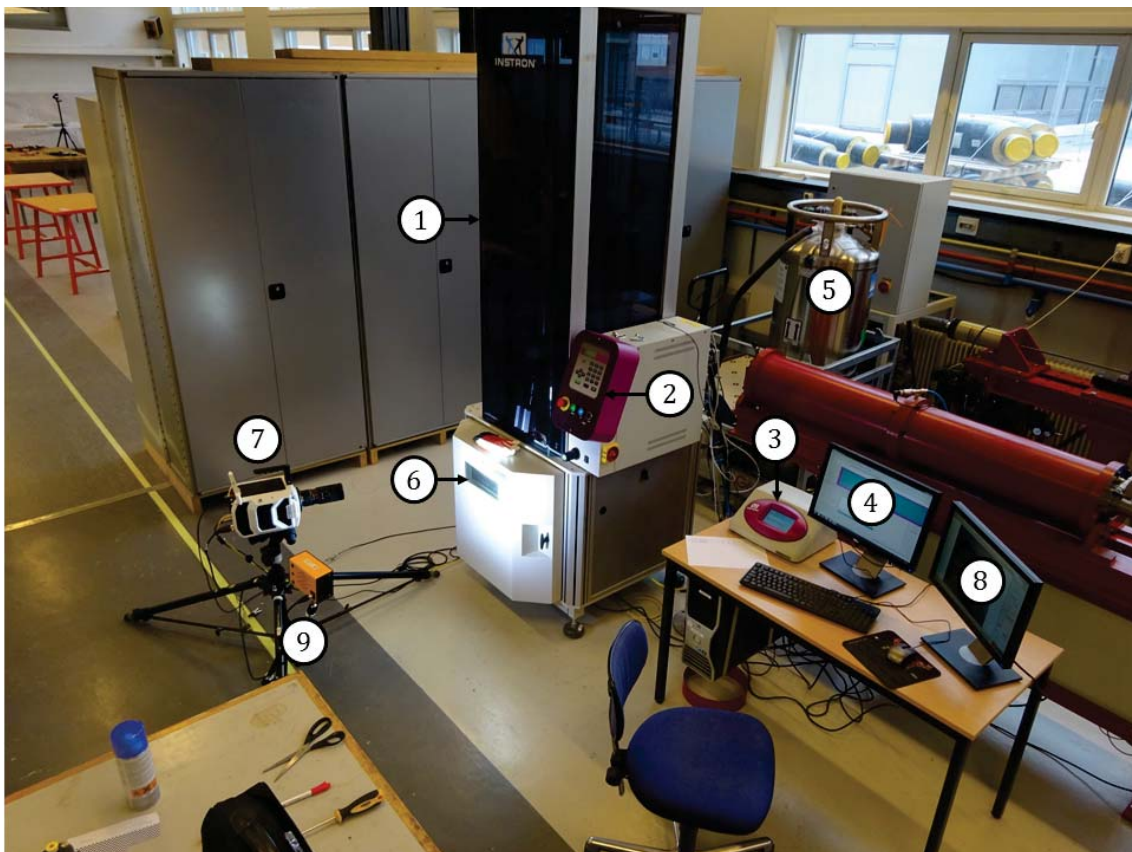
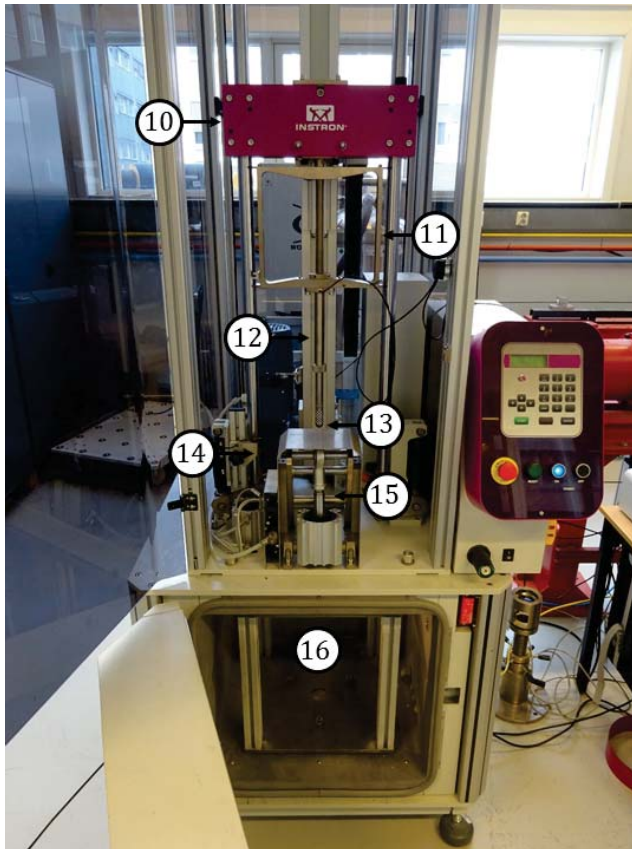


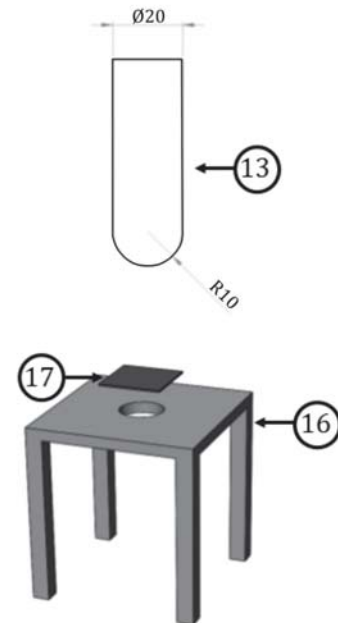
Figure 6.2: Small-scale impact test setup for low temperature testing

- ① Turret, ② Control box, ③ Data acquisition system, ④ VisualIMPACT software,
⑤ Liquid nitrogen container, ⑥ Environmental test chamber, ⑦ High speed camera,
⑧ High speed camera recording, ⑨ Additional light source

The drop tower has a maximal capacity of 1 800 J with respect to kinetic energy in the system [48], providing a wide range of possible load cases. As can be seen



(a) Principal overview of the drop tower turret in open configuration



(b) Principal overview of the impactor dimensions and stand

Figure 6.3: Detailed overview of different parts of the drop tower test setup

(7) High speed camera, (10) Striker lifter, (11) Striker-holder, (12) Instrumented striker, (13) Interchangeable nose insert, (14) Photocell, (15) Anti-rebound system, (16) Test sample stand, (17) Test sample

from Figure 6.3b, the test specimens were placed on top of a support table with a centred hole of 80 mm diameter. Hence, these experiments allowed for the use of a simply supported boundary, rather than clamping of the specimens. The reason for this choice was that such a boundary is well-defined. If the loading condition is well-defined, the numerical modelling is simplified. On the contrary, a clamped boundary is more complex. If the experimental tests are clamped, possible microscopic sliding or other types of small-scale movement may arise, meaning that fixation cannot be fully assured. This suggests that the experimental results obtained with the latter may deviate due to differences in boundary condition for every specimen.

Only one impactor shape was considered in this study; a hemispherical nosed impactor with a diameter of 20 mm, shown in Figure 6.3b. The standard instrumented

striker and striker-holder appurtenant to the machine were used in this experiment and can be seen in Figure 6.3a. In total, the hemispherical impactor, striker and striker-holder had a combined mass of 5.0445 kg. For such masses, the drop tower permits velocities up to 24 m/s, which also serves as the maximum recommended velocity [48]. The striker tip also included an option for interchangeable inserts, i.e. different nose shapes. In order to measure the force during the experiment, a calibrated load cell equipped with a strain-gauge was located approximately 150 mm above the tip of the striker. The force acting between the striker and the test specimen was measured from the strain-gauge at a resolution of 1 000 kHz, while a photoelectric cell measured the exact striking velocity just before impact.

To be able to test the impact resistance at $-30\text{ }^{\circ}\text{C}$, an environmental chamber was fitted within the lower part of the drop tower. Cooling of the interior of the chamber, i.e. the support table, test specimens and internal air, was possible by use of a high pressure container with liquid nitrogen, a suited hose and a thermocoupled sensor connected to a temperature regulator. Once again, the interior of the environmental chamber, and thus the lower part of the drop tower, was cooled for approximately one hour before mounting of the first test specimen. To ensure the correct temperature of the specimen, an additional 15 minutes of cooling was provided between mounting and testing of every specimen. Care was taken when mounting the door trim cutout specimens such that the textured surface was in compression, i.e. the surface first inflicted by impact. This was done in order to reconstruct the conditions of the full-scale component test. Additionally, it was found by Daiyan et al. [49] that any surface texture might cause brittle fracture when in tension beneath the striker.

Although the environmental chamber does not allow for free insight, the experiment can be monitored through a tiny window in the front door. The camera configuration illustrated in Figure 6.2 was employed during both experimental campaigns. This camera configuration incorporated a Phantom v2511 high-speed camera, taking pictures at a frame-rate of up to 1 000 kHz. Despite capturing most of the experimental events with the high-speed camera, the resulting camera angle and line-of-sight made DIC of the test specimens difficult. However, care was taken in order to confirm that the deviation between the results derived from the logged data, taken directly from the drop tower, and the corresponding DIC measurements were negligible. By attachment of a speckle patterned label to the impactor prior to testing, and monitoring of the impact test through the tiny window in the front door of the environmental chamber, this was enabled. As the difference proved to be insignificant, the acquisition of accurate data was permitted, even at the desired low temperature. The environmental chamber had no open slits providing a free line-of-sight. Thus, measurement of the potential temperature rise within the test

specimens was not possible.

6.1.3 Post processing

A MATLAB script supplied by the NTNU researcher Jens Kristian Holmen [50] was used for post processing of the experimental data from the drop tower. The script employs a numerical integration scheme to determine the velocity, v , and, in turn, the displacements, u , from the force measurements

$$\begin{aligned} v_{n+1} &= v_n - \left(\frac{F_{n+1} + F_n}{2m} - g_a \right) \Delta t, \\ u_{n+1} &= u_n - \left(\frac{v_{n+1} + v_n}{2} \right) \Delta t. \end{aligned} \quad (6.1)$$

Here, F is the force acting between the striker and the test specimen, m is the total impacting mass, $g_a = 9.81 \text{ m/s}^2$ is the gravitational acceleration and Δt is the sampling time of 0.001 ms. The subscript $n + 1$ denotes the current value of the variable, while n denotes its previous value.

Due to the placement of the load cell on the instrumented striker, some of the mass is located underneath the point of data extraction, affecting the force measurement. To determine the exact force acting between the impactor and the specimen, this must be accounted for. Using dynamic equilibrium, the corrected force can be expressed by

$$F = P \left(1 + \frac{m_1}{m_2} \right) \quad (6.2)$$

where F and P are the corrected- and measured forces, respectively. Here, m_1 corresponds to the mass below, while m_2 corresponds to the mass above the load cell. The derivation of the correction factor is provided in Appendix A. In this particular case, the masses were approximately 0.0665 and 4.978 kg below and above the load cell, respectively. Hence, the corrected force was found to be slightly higher than the measured force.

In addition to correcting the force, the MATLAB script cut the time and force recordings. Hence, all experimental data could be plotted from the instant the striker impacted the test sample, for which the velocity was recorded by the photoelectric cell. The velocity was also set to zero once full perforation of the test specimen had occurred, in order to highlight this point.

6.1.4 Results - Material sample plates

For the material sample plates, seven successful tests at three different impact velocities were obtained at low temperature. These are all listed in Table 6.3. Since the focus area of the thesis is related to the fracture drop height of the door trim, initial velocities in the drop tower were chosen accordingly. When fracture occurred for the two first replicates, the impact velocity was lowered such that fracture did not take place for the following specimens. An intermediate velocity was chosen for the final three replicates. More than one replicate was chosen for each velocity to get an impression of the variance of the results. In addition to the impact velocities, the table provides the corresponding residual velocities, measured after the impacts were completed. A negative residual velocity corresponds to rebound of the impactor and indicates that the sample was deformed, but that fracture did not take place. Positive residual velocities, however, mean that the impactor passed through the sample as a result of fracture. This process is called *perforation*. In penetration- and perforation mechanics, the *ballistic limit velocity* refers to the lowest velocity for which perforation of the plate occurs [51]. This term is similar to the fracture drop height for the full-scale drop tests, and will be used in the following discussion. The energy absorption was calculated based on conservation of energy and is given in the table below.

Table 6.3: Drop tower impact test results on material sample plates

ID	Impact velocity [m/s]	Residual velocity [m/s]	Energy absorption [J]
DT_S_-30_4	5.38	-2.06	62.3
DT_S_-30_5	5.37	-2.16	61.0
DT_S_-30_6	5.84	-1.60	79.6
DT_S_-30_7	5.84	2.78	66.5
DT_S_-30_8	5.85	1.90	77.2
DT_S_-30_1	6.31	1.97	90.6
DT_S_-30_3	6.31	1.38	95.6

For an impact velocity of approximately 5.84 m/s, rebound was found for the first replicate, while the second led to fracture. This can also be seen in Table 6.3, where the initial test at 5.84 m/s, i.e. DT_S_-30_6, resulted in a negative residual velocity, while the second replicate, i.e. DT_S_-30_7, perforated the sample. Hence, a third replicate was tested at this impact velocity, also leading to fracture. This result might indicate that the ballistic limit of the material sample plates is close to a velocity of 5.84 m/s.

Visual results

In all tests resulting in full perforation of the specimens, a plug was punched out of the sample plates with a size corresponding to the approximate diameter of the impactor. Such a failure mode is associated with high shear gradients on the periphery of the impactor [52, 53]. Due to the high strain rates that occur in an impact, adiabatic conditions are assumed. Hence, most of the work caused by plastic deformation is converted into heat, which cannot diffuse due to the high loading rates and low thermal conductivity of the polymer. The result is a significant reduction in the shear capacity of the material, since the work hardening is overcome by the thermal softening [51], as discussed in Section 2.1.4.

From the high-speed camera recordings of the impact at low temperature, softening of the specimen in the vicinity of the impactor was indicated. For the specimens tested at an impact velocity of approximately 5.38 m/s, a considerable amount of plastic deformation was seen before rebound. For the initial replicate tested at 5.84 m/s, clear indications of crazing was found. The two other specimens tested at this velocity, however, showed little sign of plastic deformation prior to fracture. Hence, a more brittle failure mode was observed for these samples. Interestingly, by increasing the impact velocity with an additional 0.5 m/s, the clear softening effect was again present in both replicates.

Figure 6.4 shows the difference between brittle- and ductile fracture observed at impact velocities of 5.84 m/s and 6.31 m/s, respectively. The figure shows a sequence of images obtained from the high-speed camera at intervals of approximately 0.15 ms for DT_S_-30_7 and DT_S_-30_1 in the left and right picture column. From the time of initial contact between the impactor and sample, indicated in each caption, it was found that fracture commenced later for the specimen tested at 6.31 m/s, compared to the test at 5.84 m/s. In addition to the visible differences in deformation, this illustrates that a larger amount of plastic deformation was found in the test with higher impact velocity. The difference in the visual nature of the plug resulting from the two impact velocities is also evident. Whereas the plug in DT_S_-30_7 has sharp edges and cracks, the edges of the plug in DT_S_-30_1 are more rounded. Also, a significant reduction in thickness was found at the higher impact velocity, due to large strains and stretching around the impactor. These are all signs of considerable amounts of plastic deformation.

The fact that the tests conducted at 5.84 m/s were less ductile, can also be seen in Table 6.3, where more energy is absorbed in the tests at higher impact velocity. This is due to the significant amount of plastic deformation and subsequent energy

absorption caused by ductile- compared to brittle fracture. For both impact velocities, however, the part of the plate that was not located directly under the impactor failed in a brittle fashion. Once the void coalescence occurred for the higher initial velocity tests, the crack propagated through the rest of the specimen, which remained cold. In turn, this caused the rest of the specimen to shatter in a highly brittle fashion. Hence, presence of adiabatic heating in the experimental drop tower impact test of the sample plates, was indeed indicated.

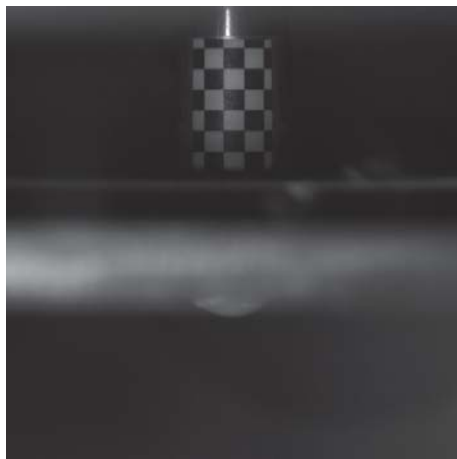
Measured results

Figure 6.5 shows the force obtained in six representative drop tower impact tests as a function of the displacement. In the following section, the replicates tested at the same impact velocity are given the same colour. Experimental data for each successful test can be found in Appendix C.

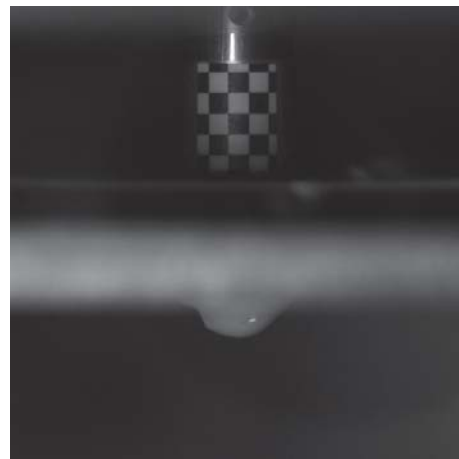
In all tests, an initial toe-region dominated by oscillations was followed by a linear region corresponding to elastic bending of the plate. As the slope of the curve declines, the material behaviour becomes predominately plastic before a peak force is reported, corresponding to a zero slope. Following this peak force, two different behaviours were found. One of which corresponded to a small region with negative slope, followed by a positive slope, i.e. elastic rebound. This behaviour was found for DT_S_-30_4, DT_S_-30_5 and DT_S_-30_6. For the second case, the curve contained a small amount of negative slope, followed by fracture, i.e. a vertical line in the force-displacement curve. This kind of behaviour was reported for DT_S_-30_7, DT_S_-30_1 and DT_S_-30_3.

A satisfactory repeatability was found in the experiments. The largest variations were related to the two replicates tested at an impact velocity of 5.84 m/s, for which both rebound and fracture occurred. Hence, both a region with positive slope and a vertical line can be seen in the force-displacement curves for the initial and second replicate, respectively. As discussed earlier, this discrepancy could be caused by the impact velocity being close to the ballistic limit of the material sample plates.

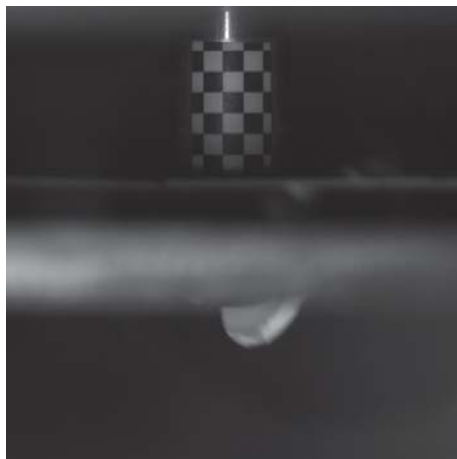
It should be noted that significant oscillations were observed in the beginning of the force-displacement curves, as seen in Figure 6.5. At some points, the measured forces even become negative, indicating that the instrumented striker is in tension. These oscillations are most likely a result of several elastic stress-waves propagating within the instrumented striker as contact is established with the sample plate. However, since fracture of the plates occurred at much larger deformations, the initial part of the curve is of little interest in this thesis. Therefore, further investigation of these



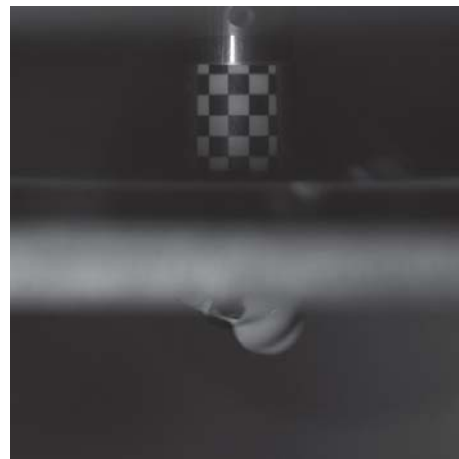
(a) DT.S.-30.7: $t = 3.76$ ms



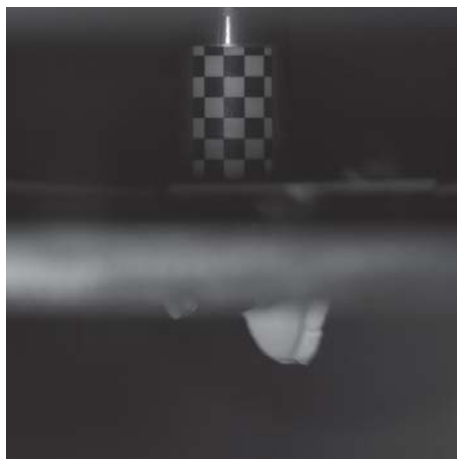
(b) DT.S.-30.1: $t = 5.00$ ms



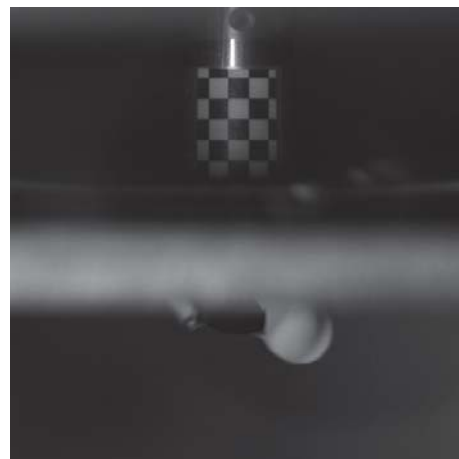
(c) DT.S.-30.7: $t = 3.91$ ms



(d) DT.S.-30.1: $t = 5.15$ ms



(e) DT.S.-30.7: $t = 4.06$ ms



(f) DT.S.-30.1: $t = 5.30$ ms

Figure 6.4: Difference between brittle- and ductile fracture in drop tower impact on material sample plates

effects was not conducted.

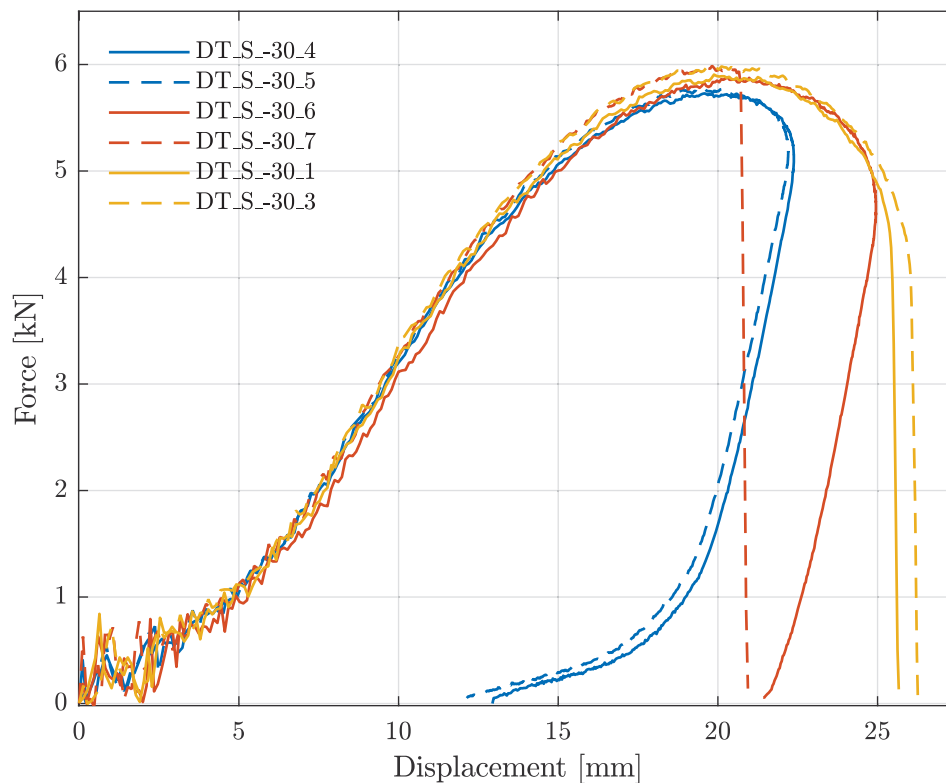


Figure 6.5: Drop tower impact results for material sample plate specimens

The velocity is plotted as a function of time for each test in Figure 6.6. The impact velocity is represented to the left in the curve, while the residual velocity is found to the right. The inflection point in each velocity-time curve, for which the second derivative is zero, corresponds to the peak force found in Figure 6.5. This is due to the acceleration being the derivative of the velocity. The acceleration is related to the measured force, through Newton's second law of motion. Hence, since the peak force corresponds to the first derivative of the force being zero, it coincides with the inflection point of the velocity-time curve. For the tests where the velocity becomes negative, rebound took place. The figure also shows large variations in residual velocity for impact velocities close to the ballistic limit, which emphasises the effect discussed earlier.

Figure 6.7 shows the peak forces reported for the different tests at their respective impact velocities. A slight positive correlation between peak force and impact velocity can be seen in the figure. The figure also confirms the consistency of the test results. Interestingly, the largest peak force was found for DT_S.-30.7, which resulted in brittle fracture. This result could possibly be explained by the increased

amount of thermal softening in the test with impact velocity of 6.31 m/s, causing a reduction in peak force.

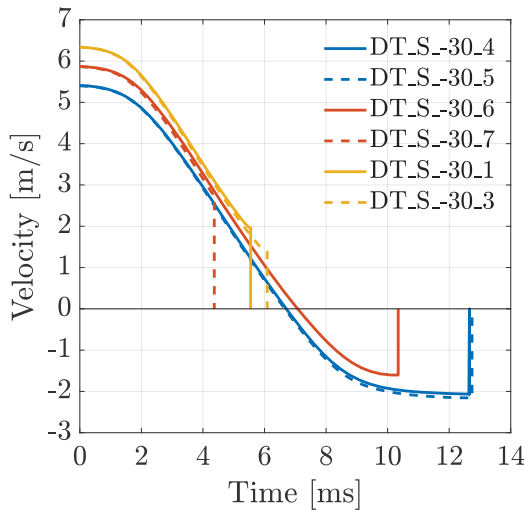


Figure 6.6: Velocity of impactor during experiment

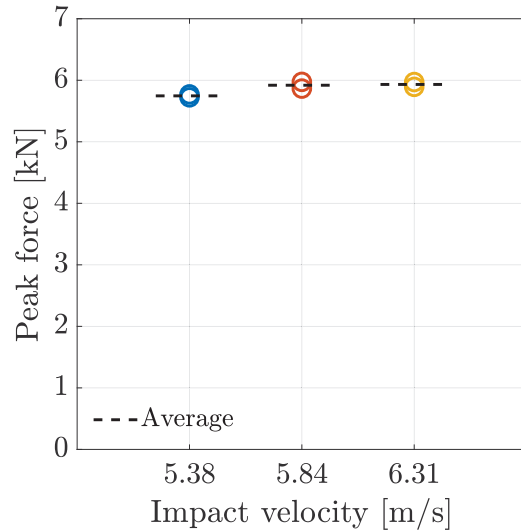


Figure 6.7: Peak force for different impact velocities

SEM results

In order to relate the visual results of the drop tower impact test to the microscopic behaviour, a brief SEM analysis was conducted for specimen DT.S-30.1. For this specimen, significant amounts of plastic deformation, possibly related to adiabatic heating, were found in the region directly under the impactor. The macroscopic fracture of the plate can be seen in Figure 6.4b, d and f. In order to compare the through-thickness fracture surfaces resulting from brittle and ductile fracture, a surface on the periphery of the specimen was compared to the surface of the plug, directly under the impactor.

The through-thickness fracture surface of the periphery can be seen in Figure 6.8, for two different magnifications. A large amount of cavities is indicated, from which brittle fracture occurred. These are believed to be caused by debonding of second phase particles, used to enhance the toughness of the material, as discussed in Section 2.1.3. Additionally, some spherical elastomeric particles of approximate size $0.5 \mu\text{m}$ are evident in Figure 6.8. Both the second phase particles and cavities are shown in white encircled areas in the figure. The morphology of the fracture surface on the periphery of the specimen shows sharp edges. A slight enlargement of the cavities was found, compared to the size of the rubber particles. This suggests that some amount of plastic deformation occurred here.

6.1. Experiment

For the through-thickness fracture surface directly under the impactor, however, the morphology is completely different. This is shown in Figure 6.9 for two different magnifications. Here, no cavities or elastomeric particles can be seen. Furthermore, the edges of the material are rounded, suggesting that adiabatic heating due to the high strain rates are indeed present under the impactor. The morphology resembles the fracture surface of the H strain rate test shown in Figure 3.15, although larger amounts of cavities were found there.

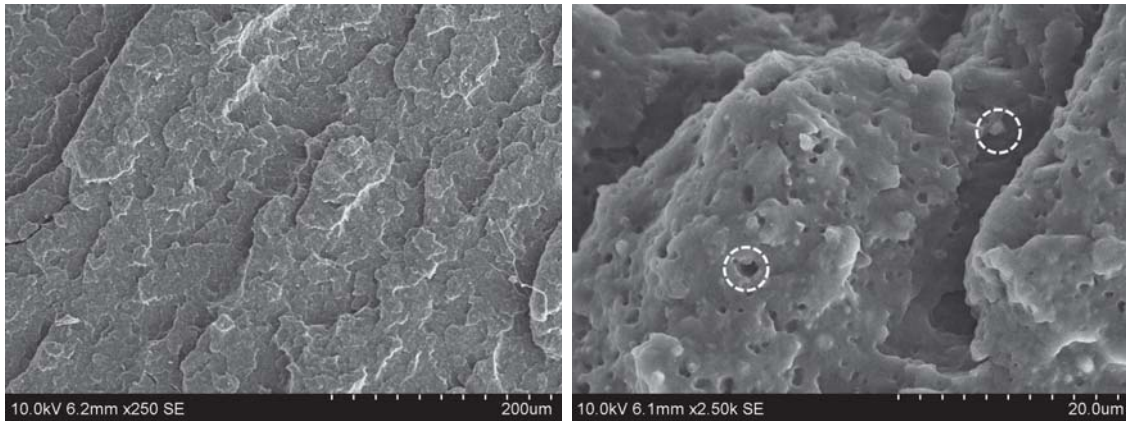


Figure 6.8: SEM micrographs of periphery of test specimen DT_S_-30_1

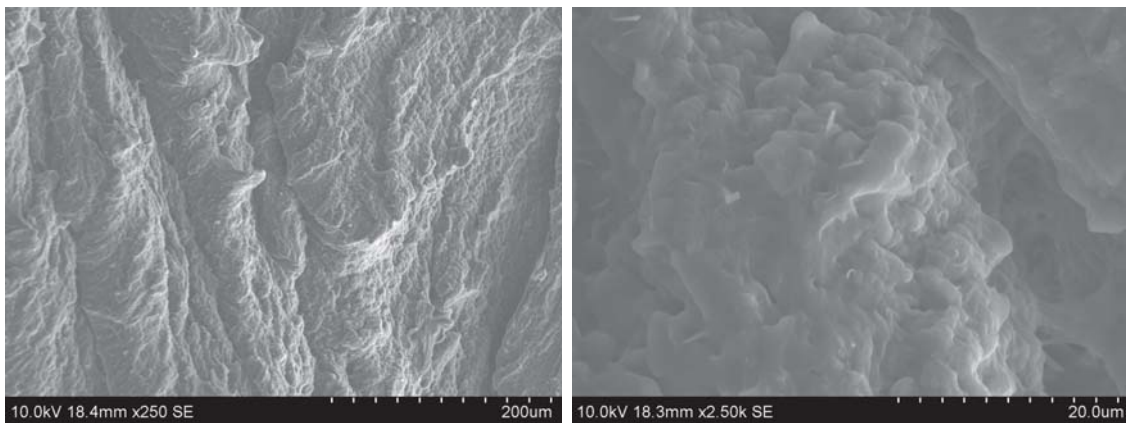


Figure 6.9: SEM micrographs of the plug of test specimen DT_S_-30_1

6.1.5 Results - Door trim cutouts

For the test specimens extracted from the actual door trim, seven successful tests at four different impact velocities were conducted and are shown in Table 6.4. The ballistic limit was of special interest also here. Hence, when the initial impact velocity of approximately 4.9 m/s led to fracture, the impact velocity was reduced to 3.5 m/s. Since fracture still occurred, a velocity of 3.0 m/s was tested for which the specimen remained intact. Thus, an intermediate value of 3.25 m/s was finally

tested. Since rebound resulted also at this velocity, it was clear that the ballistic limit velocity, v_{bl} , of the door trim cutouts is between 3.25 and 3.50 m/s. In addition to the impact velocities, Table 6.4 shows the residual velocities and the associated energy absorption corresponding to each test.

Table 6.4: Drop tower impact test results on door trim cutouts

ID	Impact velocity [m/s]	Residual velocity [m/s]	Energy absorption [J]
DT_C-8.-30	3.01	-1.72	15.4
DT_C-9.-30	3.25	-1.76	18.8
DT_CS-10.-30	3.25	-1.75	18.9
DT_C-7.-30	3.50	2.25	18.1
DT_CS-11.-30	3.50	0.784	29.3
DT_C-4.-30	4.94	4.30	14.9
DT_C-5.-30	4.96	4.41	13.0

Based on the square-cube law, the ballistic limit velocity of the thinner door trim cutout specimens can be estimated assuming their mechanical properties are similar. This is done by scaling of the lowest impact velocity leading to fracture of the material sample plates by the squared thicknesses. The respective thicknesses are given in Table 6.2. Hence, an estimate can be obtained by

$$v_{bl} = 5.84 \text{ m/s} \cdot \frac{(2.45 \text{ mm})^2}{(3.15 \text{ mm})^2} \approx 3.53 \text{ m/s}, \quad (6.3)$$

which is similar to the result that is shown in Table 6.4. Keeping in mind that the surface of the specimens from the two material sources are different, this is a good estimate, again suggesting that the mechanical properties are similar.

By comparing the results from the door trim specimens with the sample plates, a significant reduction in energy absorption was found. For the sample plates, energy absorptions of 66.5 and 77.2 J was obtained for the two replicates tested above the ballistic limit, respectively. For the door trim specimens, however, only 18.1 and 29.3 J were absorbed by the replicates tested at impact velocities higher than the ballistic limit, as seen in Table 6.4. Although the squared thickness scaling must be employed for comparison of the two sources in this case as well, it can not account for the entire difference in absorbed energy. Ultimately, this suggests that the door trim specimens are more brittle than the material sample plates.

Visual results

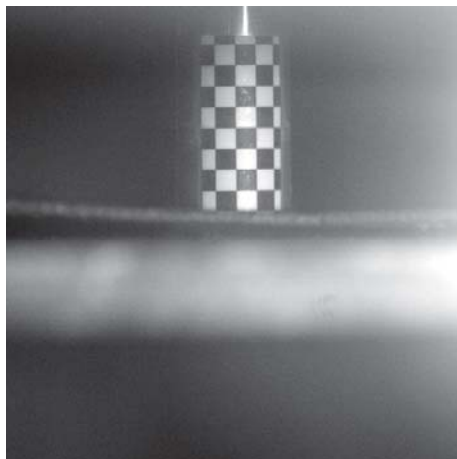
Similarly to what was found for the material sample plates, plugging was also observed as the perforation failure mode for the door trim cutouts. Fracture of the door trim samples were, however, always associated with brittle behaviour. No crazing was seen from the high-speed camera recordings. This could be due to the colour of the door trim specimens, making visual examinations harder because of the dark background of the environmental chamber. However, the results found during uniaxial tensile testing, presented in Chapter 3, also proposed that the door trim material is associated with smaller strains at fracture. This suggests that a similar effect can be seen in the drop tower test results as well.

One factor which could make the door trim cutouts more brittle, is the thickness of the plates. Any heat associated with plastic deformation can diffuse more easily in thinner plates compared to thicker plates, due to the relation between the surface area and the volume. Hence, the material sample plates could possibly experience more thermal softening than the door trim cutouts. Another factor that should be considered, is the process effects related to the door trim material, which could cause a reduction in strain at fracture. Also, the outer surface of the door trim samples were clearly rougher than that of the material sample plates. This might promote a more brittle failure mode.

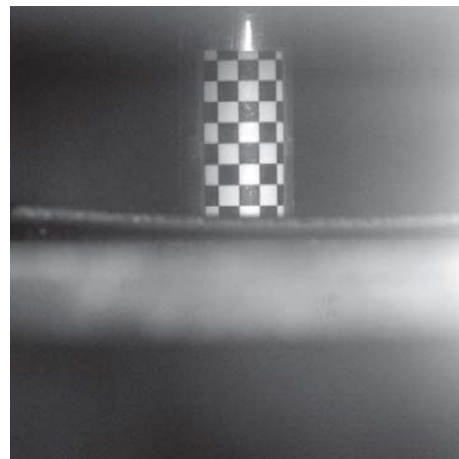
Figure 6.10 shows brittle fracture observed at initial velocities of 3.50 m/s. A sequence of images obtained from the high-speed camera with intervals of 0.30 ms, are shown in the left- and right column for tests DT_C-7_-30 and DT_CS-11_-30, respectively. The time, for which the impactor and test specimens establish contact, are noted in the captions of each image. A larger time period, and subsequently greater amounts of deformation, was observed before fracture in replicate DT_CS-11_-30. From visual inspections of the plugs after the test, sharp edges and cracks were found in both cases. This suggests that both specimens fractured in a brittle fashion.

Measured results

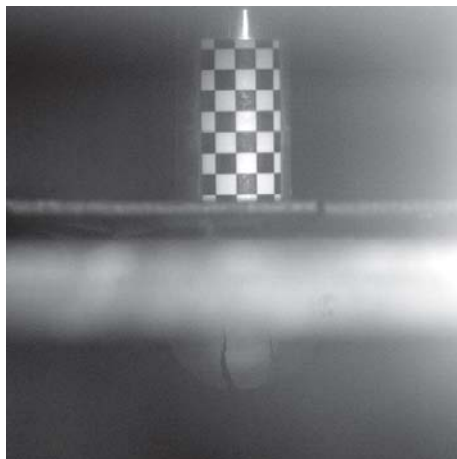
Figure 6.11 shows the force-displacement curves obtained from two replicates at each of the three different impact velocities, all of which were tested at -30 °C. The colours of the curves are chosen according to their tested impact velocity. As for the material sample plates, a more comprehensive summary of all experimental data is given in Appendix C.



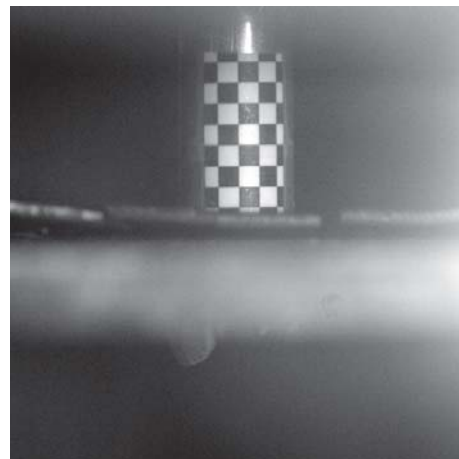
(a) DT_C-7_-30: $t = 4.24$ ms



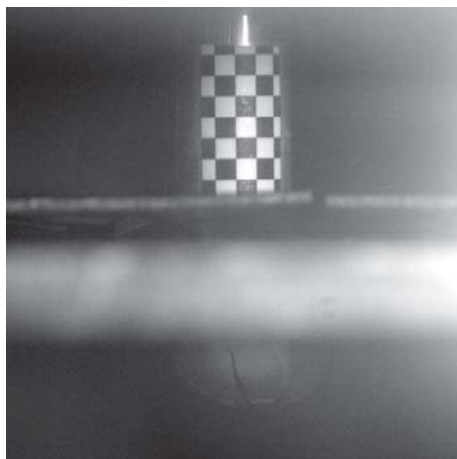
(b) DT_CS-11_-30: $t = 6.11$ ms



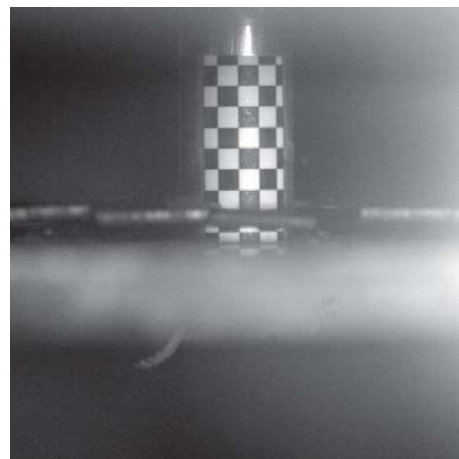
(c) DT_C-7_-30: $t = 4.54$ ms



(d) DT_CS-11_-30: $t = 6.40$ ms



(e) DT_C-7_-30: $t = 4.83$ ms



(f) DT_CS-11_-30: $t = 6.70$ ms

Figure 6.10: Fracture in drop tower impact on door trim cutout specimens

Similar characteristics of the force-displacement curves, as was reported for the material sample plates, were found in the results for the door trim cutouts as well.

6.1. Experiment

An initial toe-region, followed by a near linear region, is shown for all replicates in Figure 6.11. For the two specimens resulting in rebound, a small region of negative slope was present after the peak force. The elastic rebound is identified by a final positive slope for the door trim cutouts as well. For the replicates resulting in fracture, however, the behaviour differed from the material sample plates. Fracture was reported after the linear domain, for small amounts of plastic deformation, prior to the actual peak force. Hence, the peak force was associated with the deformation at fracture. No such effect was found for the material sample plates, where fracture always succeeded the peak force. This suggests that a more brittle failure mode occurred in the drop tower tests on the door trim cutouts.

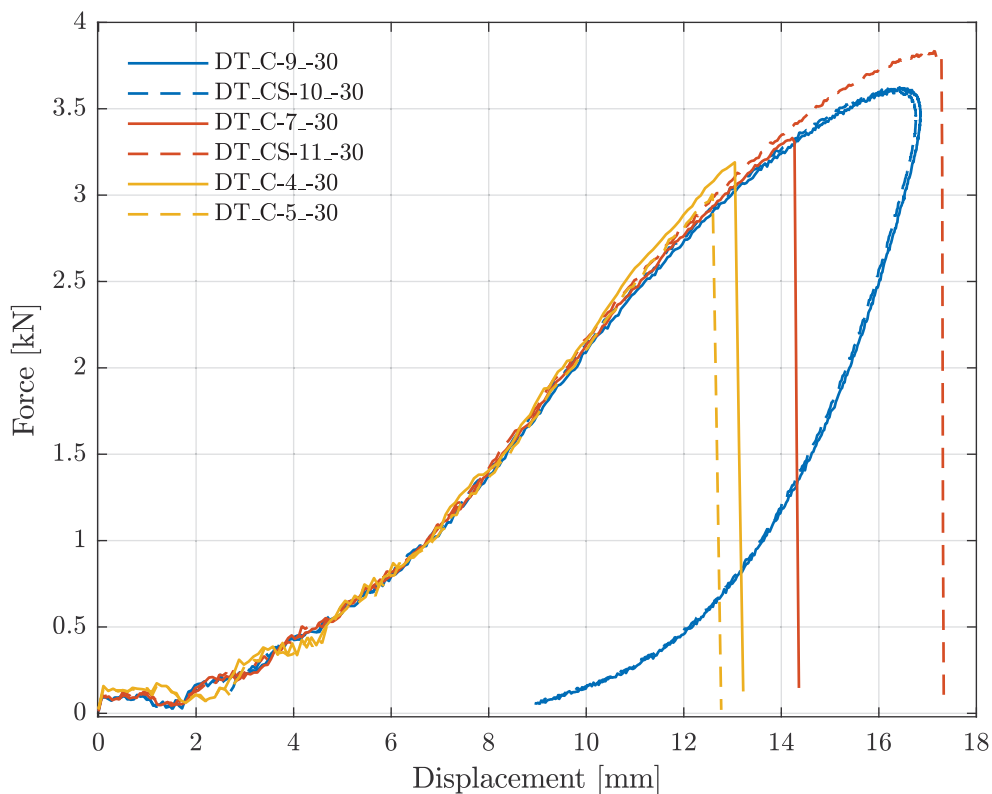


Figure 6.11: Drop tower impact results for door trim cutout specimens

The effect of the weld was also investigated in the drop tower, and two of the replicates shown in Figure 6.11 were extracted correspondingly. One of the specimens, i.e. DT_CS-10.-30, was tested at an impact velocity below the ballistic limit, and resulted in elastic rebound. From the figure, it is obvious that the result is consistent with the other replicate at this impact velocity. This suggests that the effect of the weld is negligible. However, test specimen DT_CS-11.-30 was tested above the ballistic limit, and therefore fractured. An interesting observation is that the

displacement at fracture is greater for the replicate containing the weld, than for the other replicate. This suggests that the ductility increases due to the weld. These results are, however, not sufficient to draw any conclusion with respect to the mechanical properties associated with the weld. An important factor, which could account for some of this discrepancy, is the fact these replicates were tested close to the ballistic limit. Additionally, by comparing the thickness of the two plates, it was found that DT_CS-10.-30 had an average thickness of 2.47 mm, while DT_C-7.-30 was slightly thinner, i.e. with an average thickness of 2.43 mm. Although this difference might seem insignificant, the capacity is related to the squared thickness. Thus, it might account for some of the inconsistency, in addition to the effect of the ballistic limit.

Large variations were found in residual velocity for the replicates tested close to the ballistic limit. The same effect was seen for the material sample plates. This is evident in Figure 6.12 for which the tests with an impact velocity of 5.0 m/s, fractured at approximately the same point in time. However, the large variation in residual velocity for the two replicates tested at 3.5 m/s, is also found in this figure. For the two replicates at 3.25 m/s, the elastic rebound is represented by a negative residual velocity here as well.

The peak forces for the six representative tests are shown in Figure 6.13. For the two replicates at an impact velocity of 3.25 m/s, the consistency of the test results is also recognised in this figure. The peak forces for the remaining replicates, however, does not correspond to the slope being zero, since fracture occurred prior this point. Therefore, no positive correlation can be seen between the impact velocity and peak force in Figure 6.13, in contrast to what was seen for the material sample plates.

It should be noted that dimensionless force-displacement curves were plotted for the door trim cutout specimens, due to the slight variations in thickness. The resulting curves are shown in Appendix C. Here, it is obvious that the measured difference in thickness can not account for the variations found for the specimens tested above the ballistic limit, although a reduction of approximately 1 % was found in the difference in displacement at fracture for the two specimens. This suggests that a large amount of the inconsistency is related to the effect of the ballistic limit.

SEM results

A SEM analysis, similar to the one conducted for the material sample plates, was also done for the door trim cutout specimen DT_C-7.-30. Hence, the through-thickness fracture surface on the periphery of the test specimen was compared to the fracture

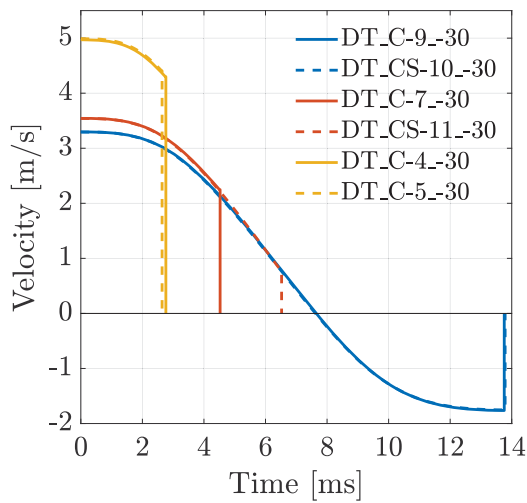


Figure 6.12: Velocity of impactor during experiment

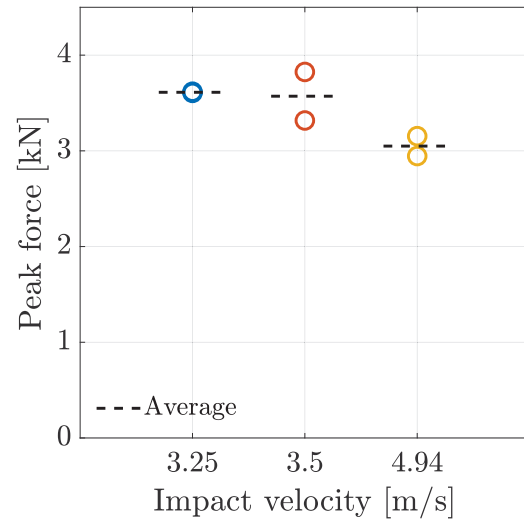


Figure 6.13: Peak force for different impact velocities

surface of the plug. The two respective fracture surfaces are shown in Figure 6.14 and 6.15 for increasing magnifications. The visual observations, suggesting that the entire door trim cutout specimen fractured in a brittle fashion, are confirmed by the micrographs. No clear difference can be seen in the morphology of the surface directly under the impactor and on the periphery of the specimen. Cavities and elastomeric particles of similar size and shape are evident in both cases, indicated by white encircled areas. Note that some sort of contamination can be seen in the fracture surface from the plug. A similar observation was found for the material sample plate in Figure 6.9.

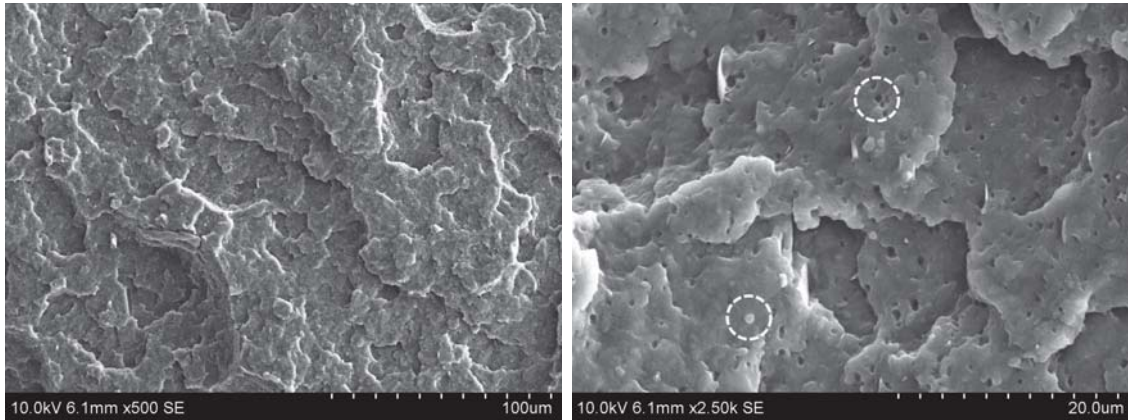


Figure 6.14: SEM micrographs of periphery of test specimen DT_C-7_-30

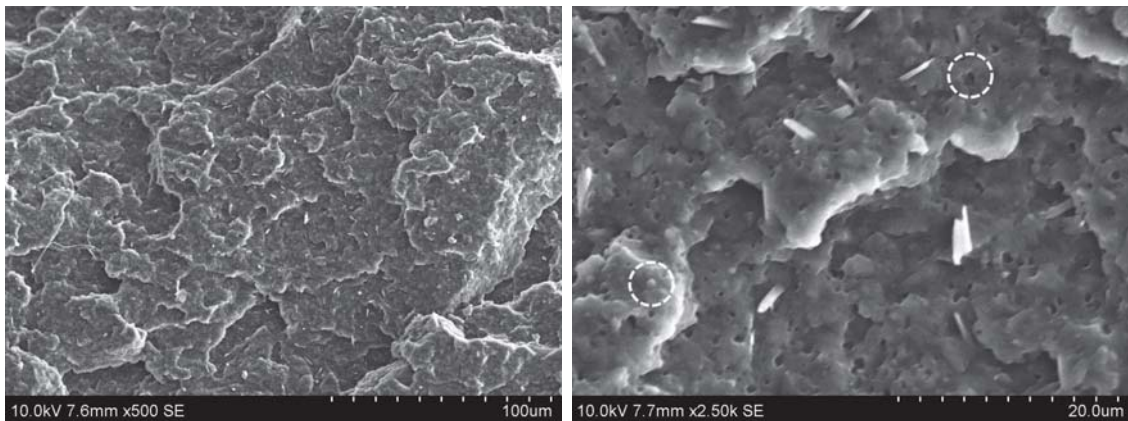


Figure 6.15: SEM micrographs of the plug of test specimen DT_C-7_-30

6.2 Numerical analysis

The drop tower test conditions were replicated in a numerical model. This was done in order to validate the material model in a small-scale impact test, where conditions such as strain rate and stress state better resemble that of the component drop test. A significant advantage associated with the drop tower, is that the force-displacement curves from the experimental test can be compared to the numerical results. This allows for easier assessment of the strengths and weaknesses of the calibrated material model. Another advantage of the drop tower impact test is the well-defined boundary. As opposed to the clamped alternative, this boundary condition can be accurately replicated in the numerical model. Additionally, since the conditions are similar to the component drop test, inverse modelling of fracture parameters might produce satisfactory results in the full-scale component simulation.

6.2.1 Numerical model

The numerical model was simulated in Abaqus/Explicit due to the transient dynamic nature of the drop tower impact test. Shell elements were chosen to model the test specimen, since the thickness is small compared to its overall dimensions [29]. Additionally, the full-scale door trim test was modelled using such elements. Employing shell elements therefore enabled more accurate comparison between the two models. The impactor and support were modelled as analytical rigids, since these parts are much stiffer than the impacted specimen. Hence, their deformation was considered negligible in comparison to the test specimen. Analytical rigid representations are also less computationally expensive than the discrete rigid alternative [35]. Only the small sections of the impactor and support table in contact with the specimen were modelled, such that the computational cost of the simulations could be reduced even further. The entire drop tower model assembly is shown in Figure 6.16.

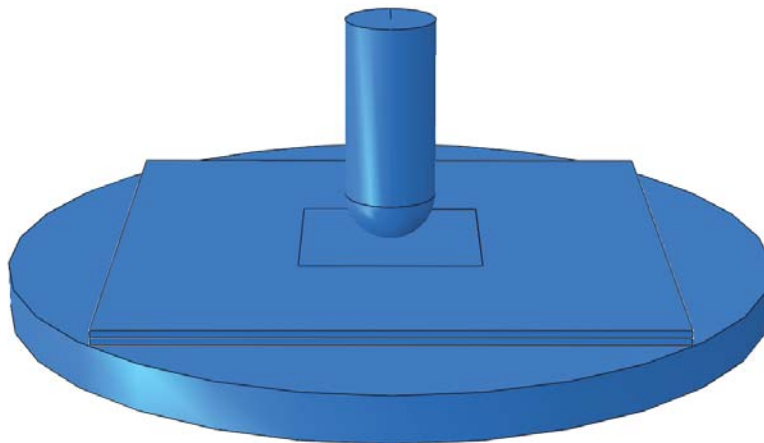


Figure 6.16: 3D shell element model assembly

One model was created for the two respective material sources due to the difference in sample thickness, given in Table 6.2, and in critical damage. However, a reduced integration shell element formulation, i.e. S4R, was employed for both models. These elements are associated with low computational cost, and also prevent shear and membrane locking [35]. A discussion regarding the different element integration methods and possible spurious modes, which might be related to these, is given in Sections 2.4.3 and 2.4.4. In order to accurately reproduce the behaviour of the plate in bending, five integration points were chosen over the shell thickness. The plate itself was partitioned such that different mesh densities could be assigned for the

parts in contact with the impactor and support table. A higher density mesh was chosen for the impact area, due to the large amounts of deformation that occurred here. For the material sample plate model, an approximate mesh size of 3.0 mm was utilised in the impact area, as opposed to 2.0 mm for the door trim cutout model. The latter corresponds to the mesh size of the numerical door trim model, facilitating more accurate comparison between the two.

A general contact formulation was specified, due to the simplicity of the numerical model. Hence, the contact pairs are automatically established by the software. A penalty reinforcement of the contact constraint was utilised such that a friction coefficient of 0.3 could be assigned between all surfaces. This coefficient of friction was determined through a simple experiment, described in Appendix G. It should be noted that only the static coefficient of friction was established here, and will merely serve as a starting point for further investigation in the sensitivity study. Both the impactor and support table sections were given reference points. These were used to apply boundary conditions to both parts and to specify the mass of the impactor. The impactor was constrained in all degrees of freedom, except for the translational direction related to its velocity, while the support table was fully fixed. In order to account for the inertia of the impactor, the mass of 5.0445 kg used in the experimental setup was also assigned in the numerical model.

6.2.2 Results - Material sample plates

Figure 6.17 shows the force-displacement curve obtained from the numerical basis model, compared to the experimental test DT_S_-30_7. The impact velocity of the numerical model was set to 6.0 m/s, corresponding to the lowest velocity leading to fracture in the experiment. Since impact on material sample plates was modelled, the material parameters used in the numerical simulation were chosen accordingly. The associated calibrated parameters can be found in Table 4.9.

Comparing the experimental- and numerical force-displacement curves, good correlation is observed between the two results. The general shape of the curve is well-captured by the numerical model, although some inconsistencies are present. The toe-region of the curve, corresponding to the initial contact between the impactor and test specimen, is also present in the numerical results. The oscillations observed in the experimental test are, however, not as evident in the simulation. One explanation could be the fact that the force in the experimental test is measured a larger distance from the impactor. This allows for elastic stress waves to propagate back and forth in the instrumented striker. In order to replicate this behaviour

in the numerical model, the impactor must be modelled using solid elements and a metal material model, as opposed to an analytical rigid representation. The force must also be extracted at a distance from the impactor nose, corresponding to what is done in the drop tower. Since fracture is the topic of interest in this thesis, no such investigation was conducted here.

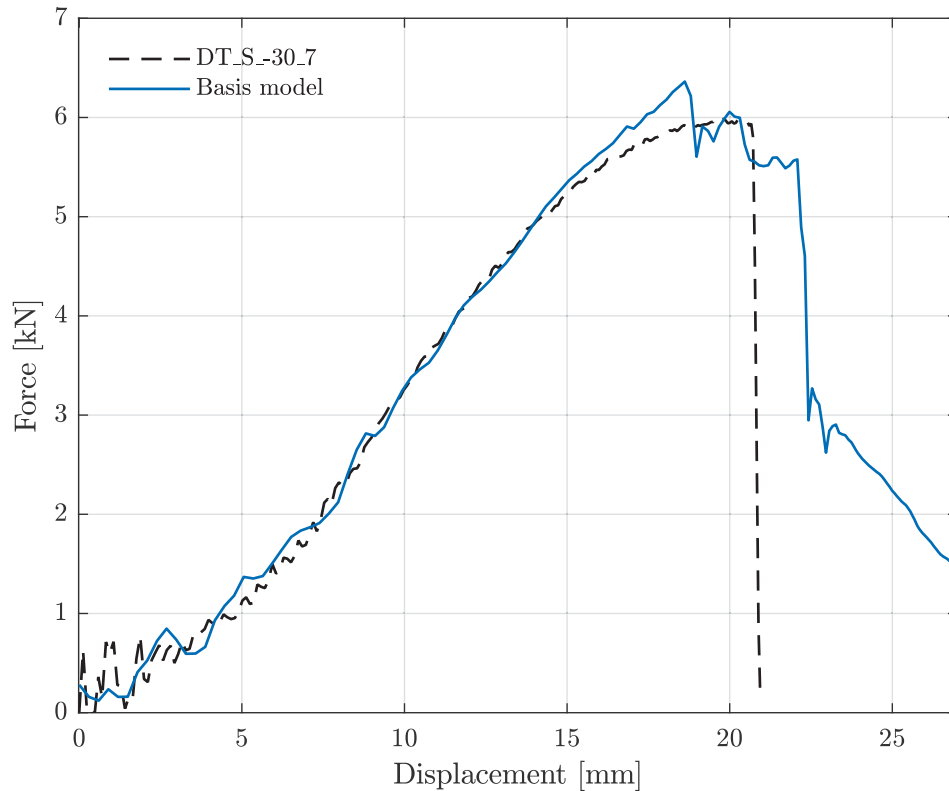


Figure 6.17: Numerical basis model for the material sample plates

The region of the curve corresponding to predominant elastic bending of the plate is also reproduced in an accurate fashion by the numerical model. However, as the slope starts to decline in the experimental results, the discrepancy between the two curves increases. Hence, the peak force is somewhat overestimated in the simulation. This could suggest that the hardening parameters of the material model should be calibrated from a tensile test with a larger amount of softening, than what was already employed here. The strain rate occurring in the drop tower impact test, can be estimated by the numerical model. An estimated strain rate in the range of $10^2 - 10^3 \text{ s}^{-1}$ confirms that calibration from a tensile test at initial strain rate of $10^{-0.5} \text{ s}^{-1}$ might not be satisfactory. By increasing the strain rate, a larger amount of adiabatic heating is likely to occur in the specimen, resulting in more thermal softening.

The initial drop in the numerical force-displacement curve, succeeding the peak force, does not correspond to elements being eroded. Critical damage is reached in one of the integration points in tension for the shell elements directly under the impactor. Hence, the load carrying capacity of these integration points are set to zero, resulting in a drop in the force-displacement curve. The corresponding deformation of the model is shown in Figure 6.19a. The elements are, however, not eroded before critical damage is reached in all five integration points over the thickness of the element. This is a default setting in Abaqus, which can not be altered by the user. In Figure 6.17, the first elements are eroded at a displacement of approximately 22.1 mm. This point corresponds to the deformation shown in Figure 6.19b, where several elements are clearly eroded.

The velocity-time curve obtained for the numerical basis model is compared to the experimental data in Figure 6.18. The impact velocity is indicated to the left in the figure, for which the time is zero, while the residual velocity is indicated by a horizontal line. This was done in order to enable easier comparison with the numerical results, with respect to element erosion. Since the velocity corresponds to the integral of the acceleration, which is scaled by the mass to obtain the force, it results in a smoothing of any discrepancies present in the force-displacement curve. An interesting observation here, is the shattering effect observed in the experimental test, which results in an abrupt change for both the force-displacement and velocity-time curves. Once fracture occurred, no resistance to further deformation was retained in the specimen. For the numerical model, however, a ductile material behaviour was assigned for the entire plate. Hence, following element erosion, the modelled specimen still resists the motion of the impactor. Element erosion is indicated in the velocity-time curve by the unusual change in slope, at time $t = 4.85$ ms. The behaviour of the numerical model after element erosion will, however, not be considered in this thesis.

Since fracture of the plate in the numerical model is defined by the point of initial element erosion, the velocity-time curve in Figure 6.18 shows that the residual velocity is underestimated numerically. Whereas the residual velocity resulting from the experiment corresponded to 2.78 m/s, the first element was found to erode at a velocity of 2.22 m/s in the simulation. Hence, a larger ductility was predicted by the numerical model, corresponding to a larger amount of absorbed energy prior to fracture. This result is also indicated in the force-displacement curve, where fracture is observed at a larger displacement in the numerical result.

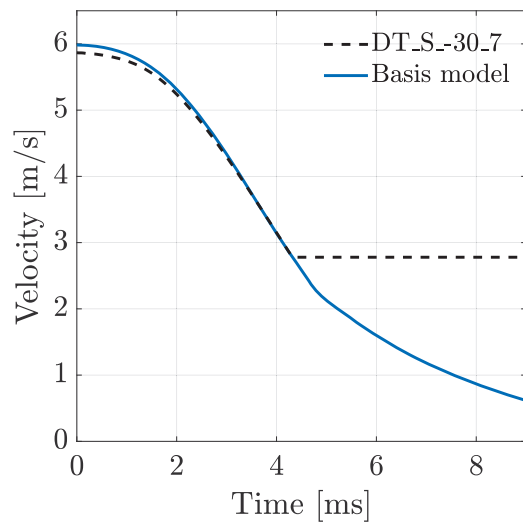


Figure 6.18: Velocity-time curve for the basis numerical model

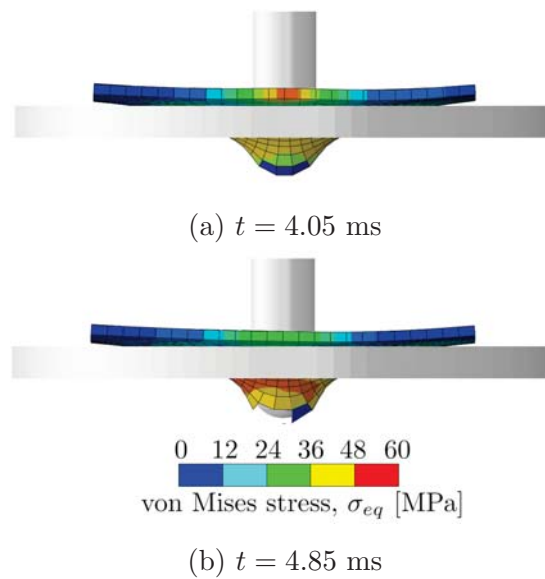


Figure 6.19: Deformation of the numerical model

6.2.3 Results - Door trim cutouts

In order to validate that the material characterisation for the door trim still applied in conditions similar to the full-scale component test, the drop tower impact test was also simulated for door trim cutout specimens. The resulting force-displacement curve from the initial numerical model is compared to experimental test DT_C-7_-30 in Figure 6.20.

While brittle behaviour was found for the door trim cutout specimens in the experiment, a highly ductile behaviour was predicted by the numerical model. This can be observed in Figure 6.20, where DT_C-7_-30 fails following the predominantly linear domain, while elastic rebound resulted from the numerical simulation. This can also be observed in the velocity-time curve in Figure 6.21. Although the absolute value of the velocity is reduced by approximately 60 %, the negative velocity suggests that no fracture occurred.

Whereas the material characterisation leads to accurate modelling of the impact on the material sample plates, the capacity of the door trim is highly overestimated. The experimental results suggested that a much more brittle failure mode occurred for the door trim, compared to the sample plates. Since calibration of the material model was based on tensile testing at strain rates where exclusively ductile deformation was found, the brittle fracture of the door trim samples could not be modelled

accurately. A similar result was found by Schwenke during the previous work [2]. At that time, inverse modelling of the fracture parameters was attempted in order to model the brittle behaviour observed at dynamic strain rates. However, a different approach will be employed in this project, involving tensile testing at strain rates closer to those estimated in the impact test. The test procedure and recalibration is described in the following chapter.

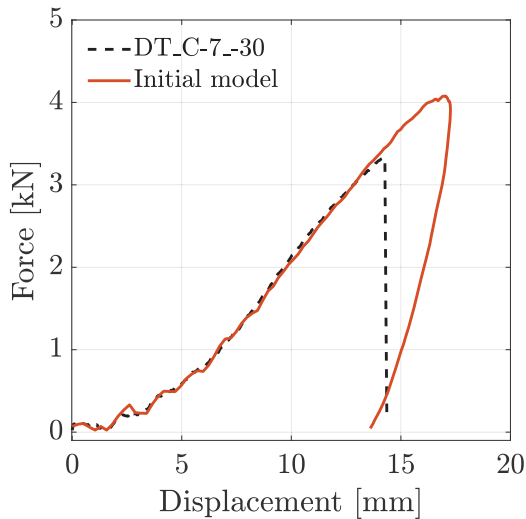


Figure 6.20: Initial numerical model of drop tower test on door trim samples

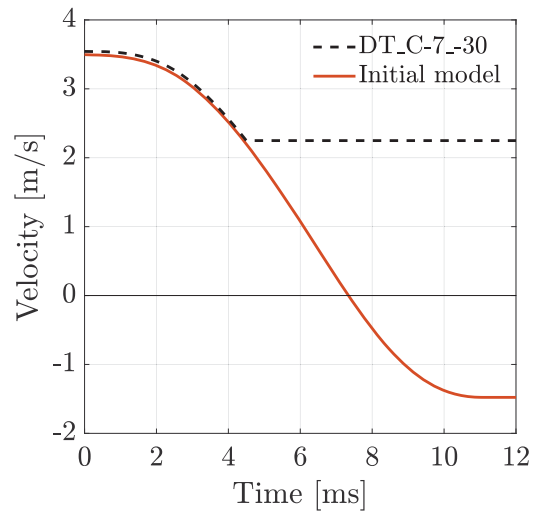


Figure 6.21: Velocity-time curve for the initial model

6.3 Sensitivity study

A sensitivity study was conducted for the numerical basis model of the drop tower impact test on the material sample plates. This was done in order to investigate the validity of the parameters that were chosen in the model by studying their influence on the results. The sensitivity study involved making changes in one of the defined parameters of the model, while keeping the remaining parameters constant. This allowed for determination of the most critical parameters with respect to the results obtained in the drop tower simulations. The effect of a selection of material parameters, specimen thickness, mesh size, element formulation and friction coefficient was investigated here. Although the numerical models for the material sample plates and door trim cutouts were slightly different with respect to thickness and material characteristics, it was believed that the results obtained in this sensitivity study were applicable for both models. Note that in the following subsections, the numerical basis model will always be represented by the blue curve,

while the experimental data corresponds to the dashed black curve, equivalently to what is seen in Figures 6.17 and 6.18.

6.3.1 Material parameters

A large variance was found for some mechanical properties during characterisation of the material. Hence, this was the main focus of this sensitivity study. Table 6.5 shows the approximate difference in the Young's modulus, plastic dilatation parameter and critical damage for the tested specimens in Chapter 3. These three parameters were chosen for different reasons. Since the material is believed to be viscoelastic, while no such relation was included in the material model, the effect of Young's modulus was investigated. The two other parameters, the plastic dilatation and critical damage, are related to damage evolution and fracture in the model. From the numerical results on the door trim material, it was obvious that large uncertainties were related to these parameters. Hence, their effect was studied in this section. In order to investigate the influence of these parameters on the numerical results of the drop tower test, different values in the intervals displayed in the table were used in the simulations.

Table 6.5: The variance in calibrated material parameters

	Young's modulus, E [MPa]	Plastic dilatation, β [-]	Critical damage, D_C [-]
Min.	1600	1.730	0.4540
Max.	3100	1.955	0.5670

Since several different strain rates were tested in this project, and no viscoelastic constitutive relation was employed, its effect on the numerical results was investigated. Numerical models using four different Young's moduli were simulated. The results showed that the general shape of the force-displacement and corresponding velocity-time curve was practically unaffected by the elastic modulus. The velocity associated with failure in one integration point over the thickness of the element, is shown in Figure 6.22 for different Young's moduli. The residual velocity obtained from the experiment is also plotted in the figure. Here, it is obvious that possible viscoelastic effects have only a small influence on the numerical results, possibly because the deformation is predominantly plastic. Thus, no viscoelastic constitutive relation is needed in the numerical representation.

The plastic dilatation parameter implemented in the SPM was based on the assumption of a constant retraction ratio. This assumption was not fulfilled for small

strains, resulting in some variations in the calibrated β parameter. Since the plastic dilatation parameter governs the development of volumetric strain and consequently damage in the model, it should be further studied. Similarly to the Young's modulus, the velocity corresponding to the first through-thickness integration point reaching failure, is plotted for different dilatation parameters in Figure 6.23. Since the lowest β resulted in rebound, and thus no element erosion, such a property was compared here. From the figure, it is clear that the velocity associated with initial failure of an integration point is affected by the plastic dilatation parameter. This agrees with how the material model is established, since a larger β results in a larger amount of damage being accumulated, which in turn leads to an earlier fracture. An interesting observation here, is the plateau in the positive correlation between the velocity at failure of an integration point and the dilatation parameter. A further investigation of this tendency will, however, not be conducted.

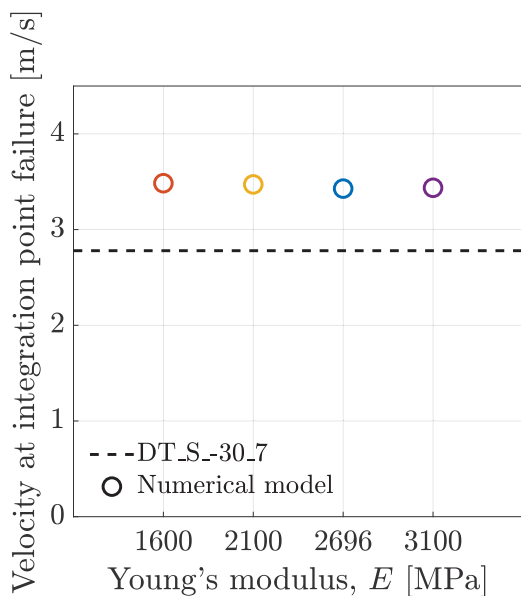


Figure 6.22: Velocity at failure of integration point for different Young's moduli

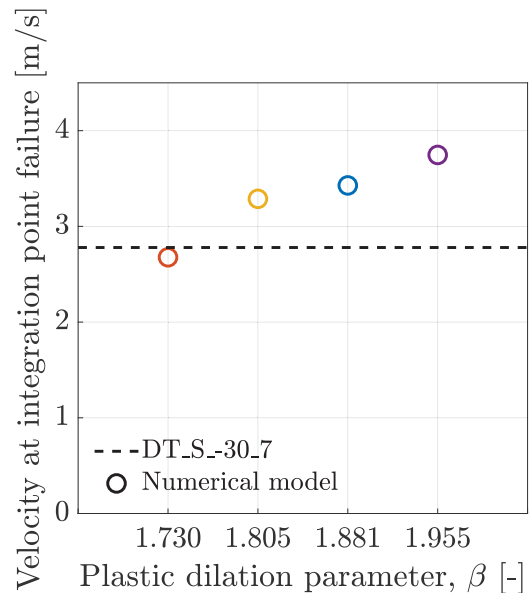


Figure 6.23: Velocity at failure of integration point for different plastic dilatation parameters

Large variations were found in the volumetric plastic strain at fracture, especially for the door trim material. Since this property is directly related to the critical damage parameter, causing fracture in the numerical model, it was of great interest in this sensitivity study. The force-displacement and velocity-time curves for different critical damage parameters are plotted in Figure 6.24a and 6.24b, respectively. It is obvious that only the final displacements, and the forces prior to failure of the model, increase with the critical damage parameter. At a critical damage of 0.4920, the velocity corresponding to the first element erosion is seen to correspond to the

residual velocity in the experiments. For the largest D_C , however, elastic rebound occurred in the numerical model. The fact that critical damage is reached in at least one integration point, can be seen by the drop in the force-displacement curve at approximately 20.5 mm. This point corresponds to the displacement at fracture for the experimental data. However, since no elements were eroded, a negative velocity and subsequently no fracture was found at the largest critical damage.

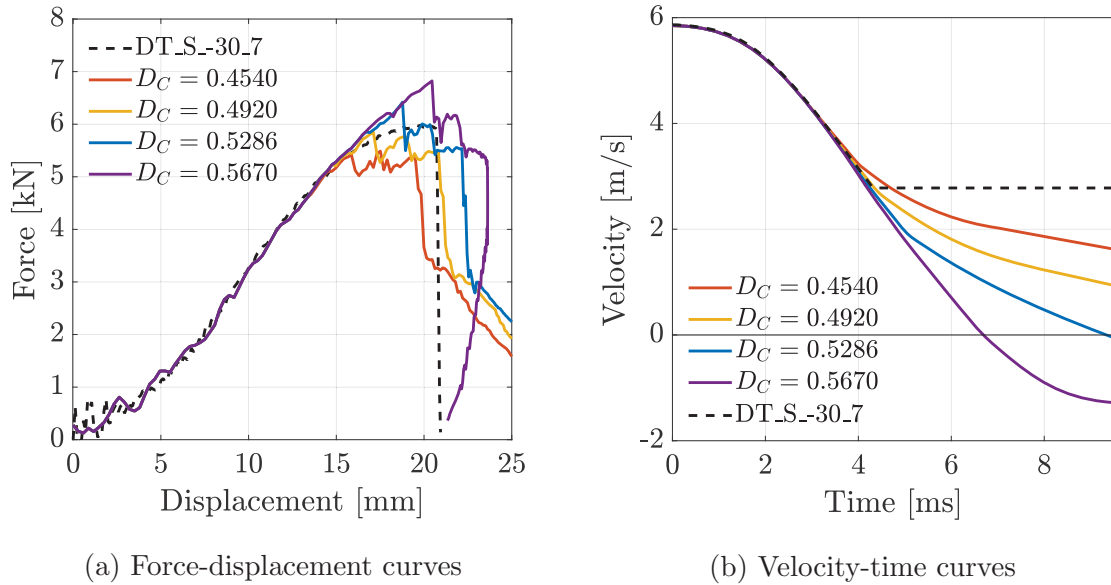


Figure 6.24: Sensitivity study of the critical damage parameter

6.3.2 Plate thickness

Even though the deviations found in the thickness of the material sample plates were insignificant, this was not the case for the door trim cutouts. When extracting test specimens from the door trim at location C, the thickness was found to vary between 2.42 and 2.60 mm. Since the thickness of the plate is closely related to its capacity, a sensitivity study was performed to investigate the effect on the numerical results. Hence, thicknesses of 2.65, 2.90 and 3.40 mm were defined in the numerical model, in addition to the basis model, and simulations were conducted.

Figure 6.25a and 6.25b show the force-displacement and velocity-time curves resulting from the different plate thicknesses, respectively. The slope, peak force and displacement at fracture of the force-displacement curves were found to increase with plate thickness. Since the work is related to the area underneath the force-displacement curve, this suggests that the energy absorption is positively correlated with the plate thickness.

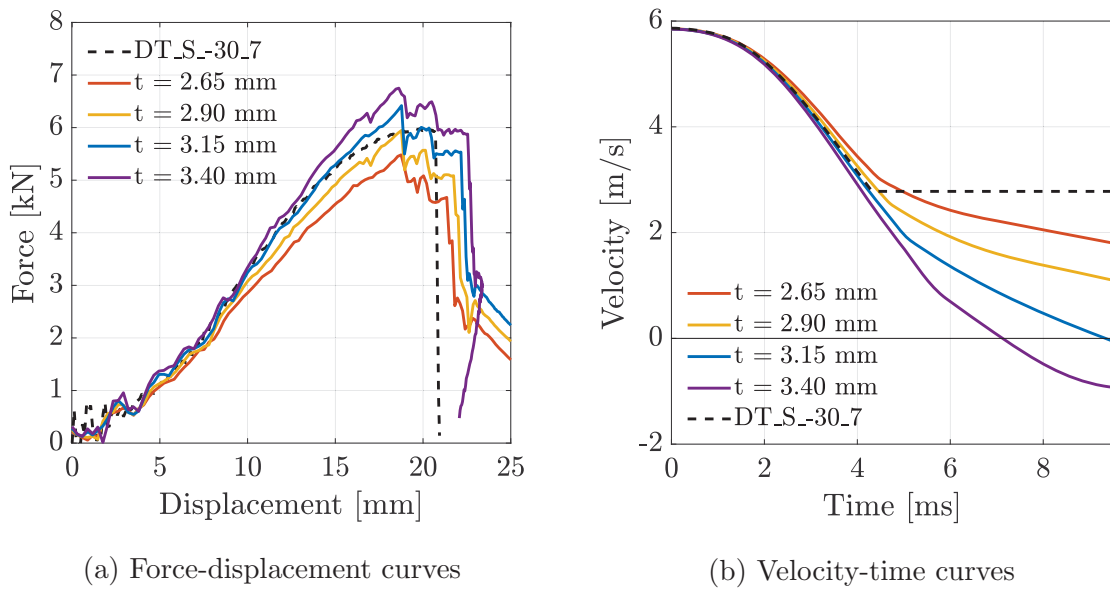


Figure 6.25: Sensitivity study of the plate thickness

6.3.3 Mesh size

A sufficiently small mesh size is necessary in order to obtain accurate results in FEA [29]. Thus, the effect of mesh size was studied here. Shell elements with sizes of 0.5, 1.0, 3.0 and 5.0 mm were therefore applied to the impact area of the numerical model. It should be noted that for shells, the aspect ratio, i.e. the characteristic element size relative to the corresponding thickness, could be associated with inaccuracies for cases where the size is smaller than three times the thickness. Thus, care should be taken when interpreting these results, since refinement of shell elements might not produce accurate numerical results.

The resulting force-displacement and velocity-time curves from the mesh size investigation are shown in Figure 6.26a and 6.26b, respectively. In these figures, it is obvious that mesh refinement significantly affects the fracture in the numerical representations. When critical damage is reached in one of the integration points for the two coarser meshes, indicated by small drops in force-displacement curve, entire elements are eroded for the more refined alternatives. This is believed to be caused by fracture being a highly localised phenomenon, which is smoothed over a larger area for the two coarser mesh alternatives. The force-displacement curves in Figure 6.26a also show that the small drops corresponding to failure of the through-thickness integration points for a mesh with element size of 3.0 mm, vanish with mesh refinement. Consequently, the large drop in the experimental force is captured in a much more accurate fashion for element sizes of 0.5 and 1.0 mm. However, this

result also suggests that the displacement at fracture is somewhat underestimated by the numerical model, meaning that a larger critical damage should be chosen to replicate the test data more accurately. This effect is recognised in the velocity-time curve as well, where fracture occurs at a overly high velocity for the numerical models with the most refined meshes.

Note that if the element surface length become smaller than the shell thickness, the contact thickness is reduced automatically in Abaqus/CAE [35]. This consequently lead to delayed contact initiation, which may lead to inaccurate results. In Figure 6.26a, the force-displacement curves for the finer meshes are slightly translated horizontally. This suggest that contact is somewhat delayed in these simulations. However, this effect is barely noticeable and are believed to have little influence on the results.

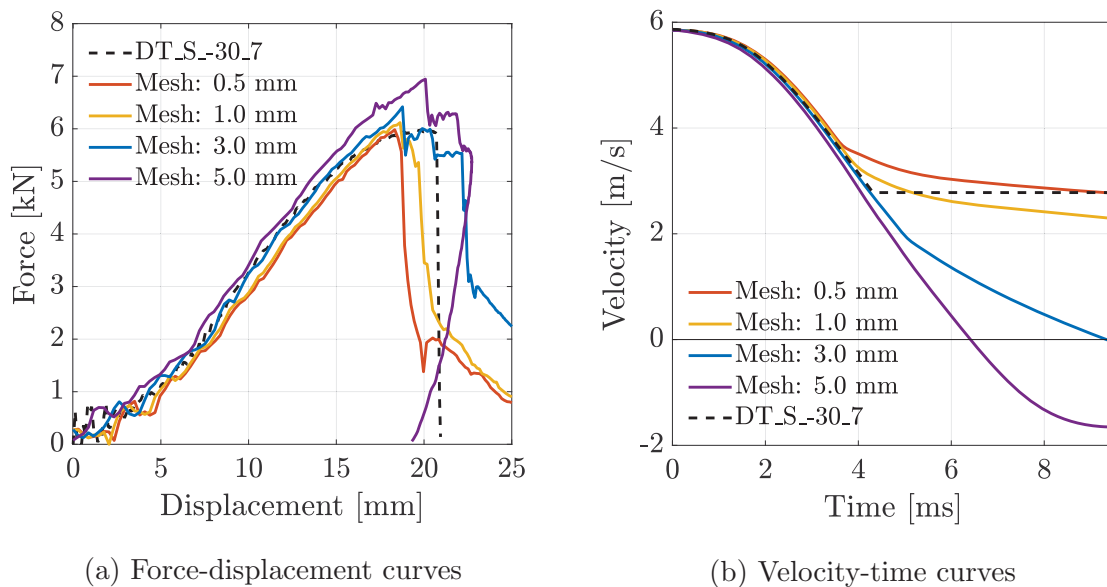


Figure 6.26: Sensitivity study of the mesh size

Although the experimental behaviour seems to be more accurately represented in the numerical models with refined mesh, it comes at a price. The computational cost was found to increase by a factor of 55 for an element size of 0.5 mm, in comparison with the basis model. For the 1.0 mm alternative, the computational time was reduced by more than a half, for a similar result with respect to initial element erosion. Hence, the overall deduction of the mesh sensitivity investigation, is that a relatively fine mesh is required in order to replicate the localised fracture in the numerical model. A mesh size study should, however, always be conducted, in order to find the desired balance between accuracy and computational time.

6.3.4 Element formulation

Although shell elements are ideal for representing the behaviour of thin-walled structures, the accuracy of solid elements are generally better. In cases where two dimensions are much greater than the third, at least three solid elements are needed over the thickness to accurately model bending of the member. This results in a high computational cost, even for simple models such as the one presented here. For the drop tower impact test, however, use of 2D axisymmetry circumvents this problem. Hence, for comparison, the drop tower impact test was modelled using axisymmetric solid elements, CAX4R, with reduced integration. The model assembly with associated impactor and support table can be seen in Figure 6.27. Axisymmetry allowed for the plate to be modelled with 40 elements over the thickness, at a relatively low computational cost. The contact and boundary conditions were defined in a similar fashion as for the shell model, while an additional axisymmetric condition was applied, indicated by the symmetry line in the figure.

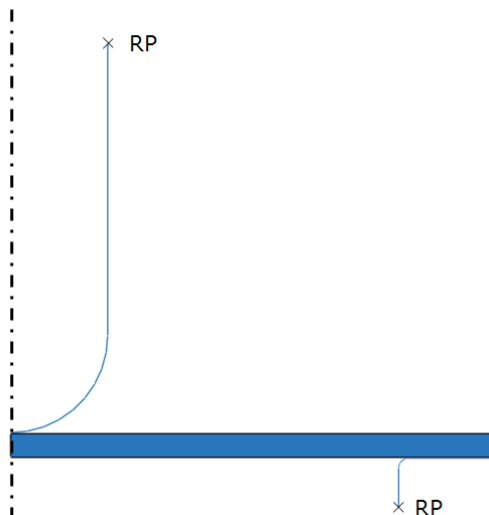


Figure 6.27: 2D axisymmetric element model assembly

In Figure 6.28, the axisymmetric solid element model is compared to a full integration four-node shell element, in addition to the reduced formulation used in the basis model. From the force-displacement curves in Figure 6.28a, it is clear that the results from the three different element formulations coincide initially. Approaching the point where one through-thickness integration point of the shell models fails, some oscillations were found for the axisymmetric model. This is likely caused by a small number of elements being eroded prior to plugging of the plate, indicated by the largest drop in its force-displacement curve. The oscillations following plugging, are caused by the friction between the test specimen and impactor, in addition to

further element erosion. An interesting observation is that the drop in the force-displacement curve is equally, if not better, represented in the refined shell model shown in Figure 6.26a. This suggests that a refined shell element formulation is desirable for accurate modelling of the drop tower and component impact test. The damage accumulation and failure modes resulting for the two models are compared in Figure 6.29 for different points in time during the impact.

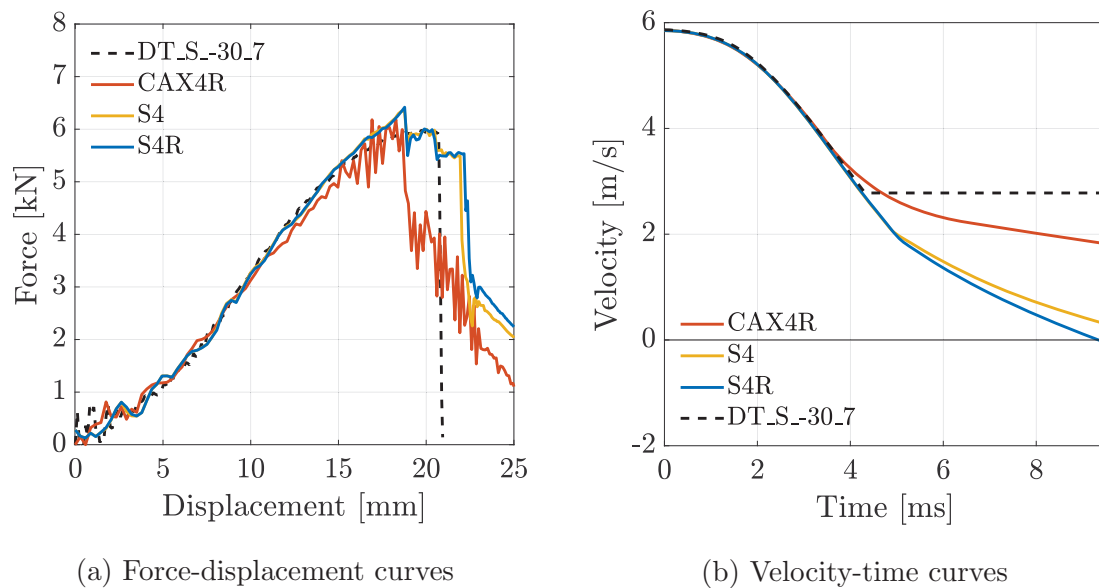


Figure 6.28: Sensitivity study on the element formulation

Due to the four integration points in the element plane, for the full integration S4 element, an accurate representation of the bending behaviour of the element is obtained. Since, the S4R element only has one integration point over the area, it requires hourglass control when bending is modelled, as discussed in Sections 2.4.3 and 2.4.4. However, it is not prone to either shear- or membrane locking [35], and is computationally less expensive than fully integrated elements. From Figure 6.28, the difference between the full- and reduced integration alternatives are negligible until the first elements are eroded. At this point, however, a somewhat stiffer response can be observed for the S4 elements. Since only the part of the curves until element erosion is of any interest, the reduced integration element is satisfactory here.

6.3.5 Coefficient of friction

Even though the static coefficient of friction was determined experimentally, as described in Appendix G, it is related to some uncertainties. First of all, the classical Coulomb friction model was assumed, where the kinetic friction is independent of

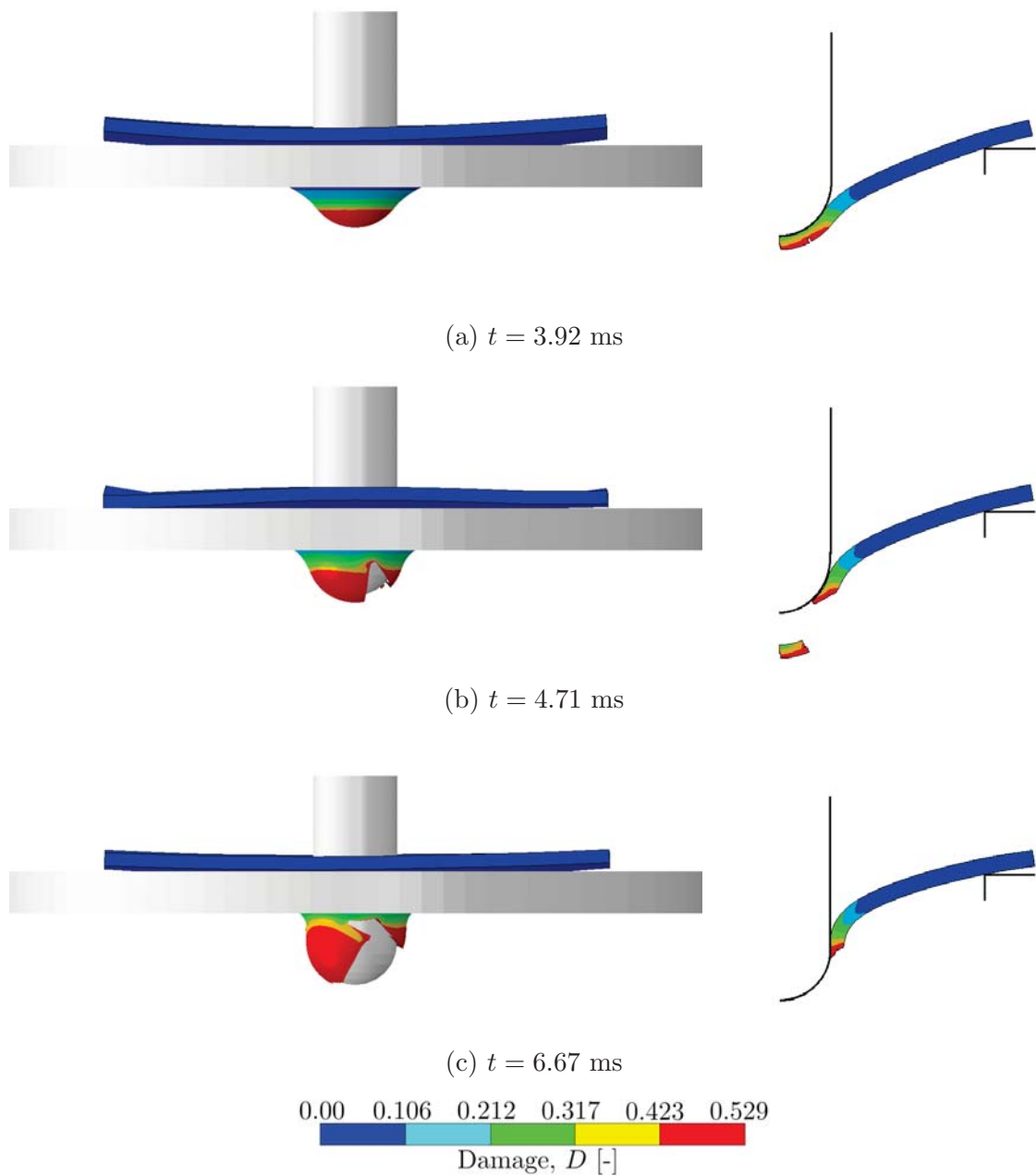


Figure 6.29: Comparison between refined shell- and axisymmetric element model

the sliding velocity. It must be emphasised that the coefficient of friction is an empirical quantity. Finding a representative value for impact applications is therefore a concerning problem. Secondly, the dynamic nature of the drop tower impact test implies that the kinetic coefficient of friction will likely act between the surfaces, rather than its static counterpart. Since the kinetic coefficient of friction is generally lower, this might result in overestimated forces arising in the simulation. Finally, the simplicity of the experimental setup for friction testing, might result in some inaccuracies as well. Hence, the influence of the coefficient of friction was

investigated in this sensitivity study.

As discussed in Section 6.2.2, an overestimated peak force could be caused by a large amount of softening, which occurs in the experiment. From Figure 6.30, however, it is clear that other factors could contribute to overestimated forces as well. One of which is the coefficient of friction. From the force-displacement curves in Figure 6.30a, a clear positive correlation is seen between the peak force and the coefficient of friction. Increasing μ is believed to increase the resistance of the movement with respect to impactor, giving rise to larger forces and therefore overestimating the peak force. Additionally, a larger amount of the energy is dissipated due to friction, as opposed to deformation of the plate. Hence, reducing the coefficient of friction not only results in a more realistic peak force, it also produces a more accurate element erosion according to the experimental test, as suggested by the velocity-time curve in Figure 6.30b.

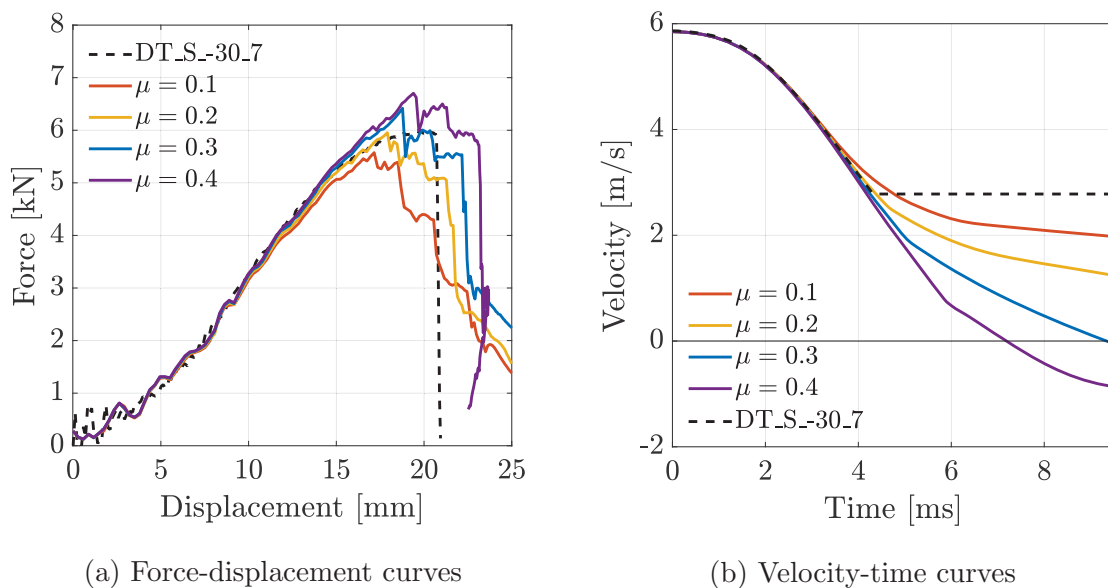


Figure 6.30: Sensitivity study on the coefficient of friction

6.4 Discussion

Different failure modes were found for the sample plate- and door trim materials in the drop tower. A similar tendency was suggested from the visual-, measured- and SEM results. Visually, large amounts of plastic deformation and respective crazing was observed for the material sample plates, as opposed to sharp-edged plugs resulting from the door trim cutout specimens. The force-displacement curves showed fracture prior to reaching the peak force for the door trim cutouts, whereas

fracture generally followed the zero derivative for the material sample plates. A through-thickness SEM analyses conducted on the plug and periphery of two specimens from each respective material source indicated different microscopic failure mechanisms. One suggestion is that the PP matrix governs the failure mode of the material sample plates, while fracture is controlled by rupturing of the elastomeric second phase particles in the door trim material.

The fact that the door trim material generally seemed more brittle than the sample plate material, could be explained by their difference in thickness. Conducting low-velocity impact testing on injection moulded, mineral- and elastomer modified PP, Daiyan et al. [54] found that a reduction of the plate thickness had the same effect as reducing the temperature or increasing the velocity. It was suggested that plates with thickness below a critical value resulted in brittle fracture. Furthermore, a borderline case was found for a thickness of 2.4 mm at an impact velocity of 4.4 m/s at -30 °C. Although the impact velocity was somewhat lower in this project, a different PP grade was also used. Hence, the fact that the door trim cutouts are thinner than the material sample plates, might provoke further material embrittlement.

The SPM is developed for ductile thermoplastics, which suggests that it is established on the assumption of large plastic strains. The material characterisation based on a meso-dynamic strain rate of $10^{-0.5} \text{ s}^{-1}$, provides an accurate estimate of the deformation in the sample plate specimen since ductile behaviour was found for both cases. However, the model failed once the behaviour became predominantly brittle, since it can not describe the ductile-brittle transition. Hence, the brittle behaviour observed for the door trim cutout specimens could not be replicated in the numerical model, suggesting that it should be calibrated in a correspondingly brittle state.

The most important result, obtained from the sensitivity study of the numerical model representing the drop tower impact test, was that element erosion was facilitated by mesh refinement. Since fracture is a highly localised phenomena, a sufficiently small mesh size must be chosen in the impact area to capture such effects. In Abaqus, element erosion is associated with all through-thickness integration points reaching a critical damage. Thus, if an overly coarse element size is chosen, the locally high strains will be averaged over a larger area, consequently overestimating the ductility in the numerical model. Since fracture in the numerical representations is defined by element erosion, which is the main concern for the component drop test, an adequate element size must be defined in the impact area. Additionally, the effect of Young's modulus was found to be minimal, suggesting that no viscoelastic effects are required for accurate modelling. Finally, a reduction in the coefficient

6.4. Discussion

of friction was observed to be appropriate in the drop tower simulation, since the static alternative was too high.

Dynamic Material Testing

Through the experimental campaign conducted in the drop tower, it became evident that both increased strain rates and stress triaxialities caused embrittlement of the door trim material. Since exclusively ductile behaviour was found from the quasi-static and meso-dynamic material testing, extrapolation of the corresponding characteristics into the dynamic domain produced artificially ductile numerical results for the door trim cutouts. Thus, a better representation of the dynamic behaviour was attempted through further material characterisation at higher strain rates. This chapter provides a potential solution that accounts for transition from ductile to brittle material behaviour.

7.1 Introduction

In order to investigate the mechanical properties of the material at higher strain rates than the quasi-static and meso-dynamic regimes presented in Chapter 3, further characterisation in the dynamic regime was conducted. The three different regimes that were investigated in this thesis are shown in Figure 7.1. In addition, the respective test devices used in each of them are indicated. The SHTB was utilised for material testing in the dynamic regime. Unlike the lower strain rates, internal equilibrium of the material can no longer be assumed here. Additionally, the inertia effects that were neglected for the quasi-static and meso-dynamic regimes, become increasingly important. Further generation of heat due to plastic straining is also associated with the dynamic regime, although significant amounts of adiabatic heating were also found for meso-dynamic strain rates. That is, if the amounts of

7.2. Split-Hopkinson tension bar testing

plastic strains prior til fracture are sufficiently large. It should be noted that these regimes are developed for metals, which are less strain rate sensitive than polymers.

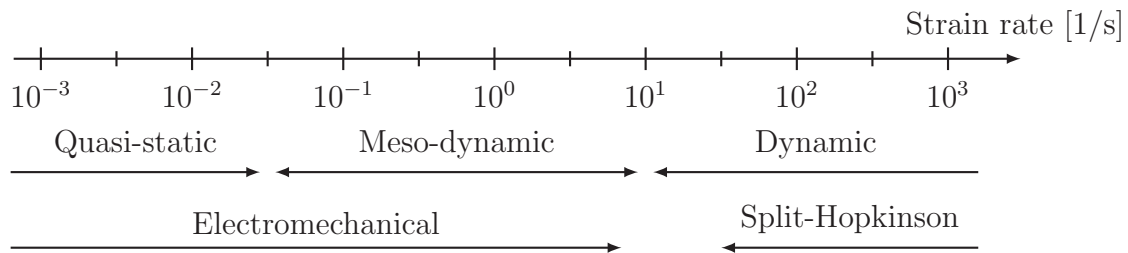


Figure 7.1: Schematic drawing of different strain rate regimes and the associated test devises

To account for any different mechanical behaviour observed at dynamic strain rates, a recalibration of the material model was attempted. It was believed that a characterisation of the material in a brittle state was necessary in order to model such a behaviour. This allowed for the dynamic nature of the impact tests to be replicated in the numerical simulations. However, utilisation of the material model in a simulation of a load case associated with lower rates and subsequently larger deformations would yield artificially brittle behaviour. This is due to the SPM not being able to represent the brittle-ductile transition. Hence, to accommodate such an issue, an alternative model was introduced and calibrated in addition to the SPM.

The two models were further verified through a series of numerical simulations using a similar approach as the one described in Chapter 5. The focus was, however, placed on reproducing the dynamic behaviour of the material. Hence, the SHTB test was modelled using the recalibrated material parameters, and compared to the experimental data. This allowed for investigation of possible weaknesses of the model. Special emphasis was placed on the fracture parameters of the two material models, since the strain measurements associated with the SHTB test were likely to produce inaccurate results. Hence, an inverse modelling procedure was attempted such that the model, in turn, could be used to reproduce the impact behaviour of the full-scale component.

7.2 Split-Hopkinson tension bar testing

As of today, the Split-Hopkinson Bar is probably the most important experimental device for testing at higher strain rates [55]. These types of dynamic tests can be performed at strain rates between approximately 100 and 1500 s^{-1} . Tensile tests at

this regime provide useful information with respect to the dynamic behaviour of the material at elevated strain rates.

7.2.1 Test specimens

The SHTB at SIMLab's facilities is instrumented in such a way that both axis-symmetric and dog-bone shaped specimens can be tested, i.e. cylindrical and flat. As discussed in Section 3.2.1, planar specimens were the most appropriate choice in this thesis. However, the dog-bone specimens employed in the SHTB testing differed slightly from those used in the EM test machine. Figure 7.2 displays the SHTB test specimen geometry.

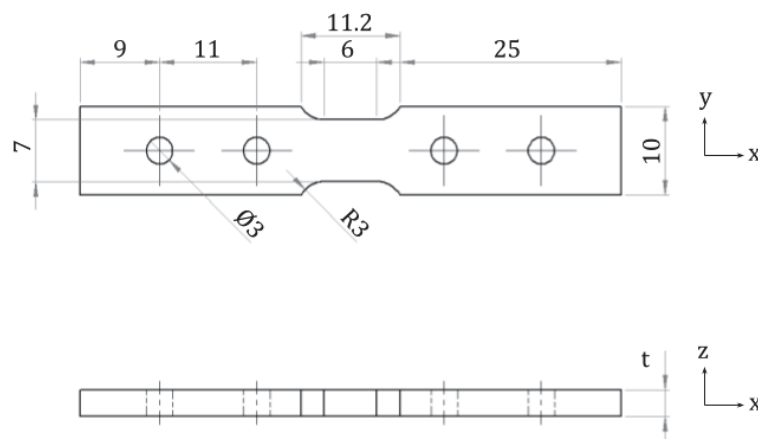


Figure 7.2: Tensile specimen geometry for the SHTB tests [mm]

Due to a different mounting for the SHTB, compared to the one used in the EM machine, more material and longer specimens are required. However, the gauge area of two different test specimens was identical. Furthermore, only specimens extracted from the door trim were tested in the SHTB rig, as most concern was related to the actual door trim material behaviour. The averaged thickness, t , was found to be approximately 2.40 mm for SHTB. It should be noted that the specimen cutouts were extracted in the 0° -orientation from location B, only. Neither the specimen orientation nor the cutout location was investigated in the SHTB since such effects were studied at quasi-static and meso-dynamic strain rates.

7.2.2 Setup

A principal overview of the SHTB test rig is shown in Figure 7.3 below. It consists of two bars of lengths 8 140 and 7 100 mm, with diameter of 10 mm. Both the incident bar ABC and the transmission bar DE are made from Tibnor 52SiCrNi5 steel with a Young's modulus of 210 GPa and yield strength of 900 MPa at room temperature [56]. Such steel grades are used to ensure solely elastic behaviour of the incident bar [57]. For testing of polymers, however, this is not considered a problem. The specimens were mounted between points C and D, and care was taken to ensure that the frictional forces between the samples and mounting brackets were sufficiently high.

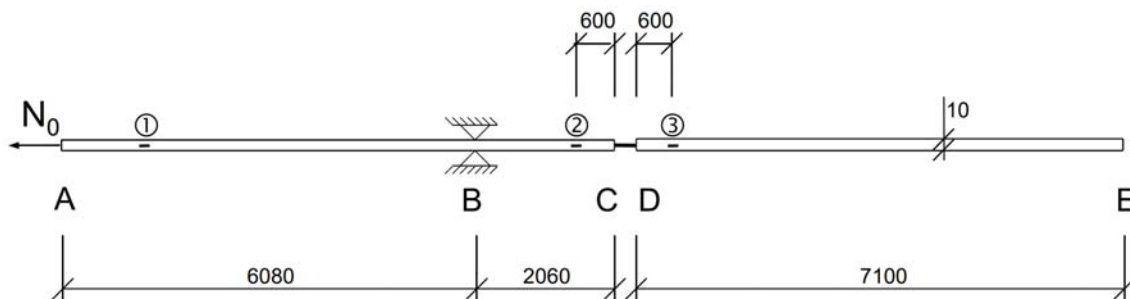


Figure 7.3: Principal overview of the SHTB rig at SIMLab [55] [mm]

Subsequent to the mounting of the test specimen, the incident bar was clamped by a friction based locking mechanism at point B, preventing movement in portion BC. A detailed view of this mechanism is rendered in Figure 7.4. Clamping is achieved by applying pressure, by means of a hydraulic jack, at the lower part of the mechanism. The pressure ensures frictional fixation of point B in the longitudinal direction of the bar. The essential component of the friction lock is a high-strength bolt with threaded diameter of 12 mm, containing a central notch with diameter 6 mm. The bolt is made of cold worked tool steel and hardened to amplify the brittleness [57]. Thus, an abrupt fracture of the bolt is caused by a certain amount of applied pressure.

The pressure applied to the locking mechanism is dependent on the desired pre-tension force, N_0 , inflicted at point A. This pre-stretching was achieved by utilisation of a hydraulic jack, similarly to the clamping mechanism. Hence, the tensile stress in portion AB of the incident bar was increased until the desired amount of straining was measured by strain gauge 1. Furthermore, the clamping pressure at point B was increased until sudden breakage of the notched bolt. Consequently, causing a tensile strain wave to propagate through portion BC of the incident bar,

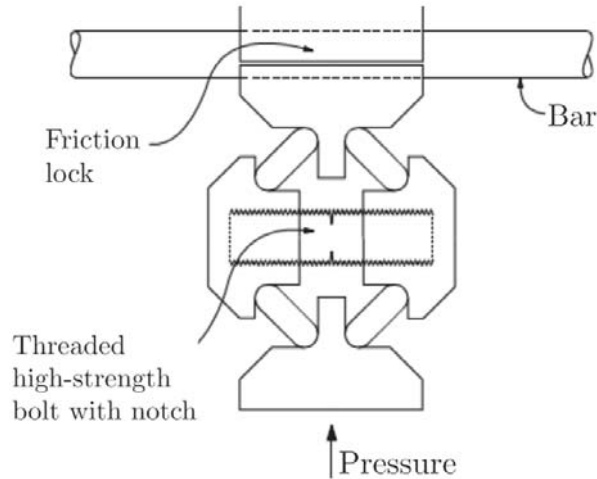


Figure 7.4: Detailed view of the clamping at point B [55]

before being transmitted into the test specimen causing it to fracture. A more comprehensive description of the strain- and stress waves occurring in the SHTB is given in Appendix D.

The three strain gauges shown in Figure 7.3 are used to measure the respective strains at each location in the two bars. While strain gauge 1 is positioned on portion AB of bar ABC, strain gauges 2 and 3 are located 600 mm from point C and D, respectively. Each strain gauge provides the following information during testing:

- ① Pre-tension force, N_0 .
- ② Incident- and reflected strain waves, $\varepsilon_I(t)$ and $\varepsilon_R(t)$.
- ③ Transmitted strain wave, $\varepsilon_T(t)$.

Since this project concerns cold impact performance, all tests were performed at a temperature of $-30\text{ }^\circ\text{C}$. Cooling of the SHTB tests was conducted in a similar fashion as for the quasi-static and meso-dynamic tensile tests. Hence, a PC environmental chamber, a high pressure container of liquid nitrogen and a thermocouple temperature sensor, equivalent to those described in Section 3.2.2, were utilised. The sensor was connected to a temperature regulator letting bursts of nitrogen gas cool the interior of the PC chamber.

The interior of the environmental chamber and all test specimens were initially cooled for approximately one hour before mounting of the first test specimen. To ensure the correct specimen temperature, an additional 15 minutes of cooling was provided between mounting and testing of every specimen. The desired temperature of the most critical portion of the specimen was obtained by placing the sensor as close to

the gauge section as practically possible.

The employed SHTB test setup is shown in Figure 7.5. Similarly to the quasi-static and meso-dynamic testing, cooling of the interior of the PC chamber was, also here, attained through a suited hose leading the liquid nitrogen into the chamber. Again, this led to a substantial temperature difference between the inside and outside of the environmental chamber. Since the volume of the chamber employed in the SHTB testing was only one third of the size of the chamber utilised in the quasi-static and meso-dynamic testing, a larger amount of condensation and consecutive icing occurred. However, a fan providing continuous airflow onto the exterior walls of the chamber inhibited such effects. Additionally, the smaller volume of the environmental chamber introduced larger temperature fluctuations. By taking temperature readings just before and immediately after the release of the liquid nitrogen, the variations were found to fluctuate within the range of -26 to -36 °C.

Since the strain rates in the SHTB are very high, monitoring of the experimental event and extraction of the associated data is relatively complex. Once again, DIC measurements were employed. Two Phantom v2511 high-speed cameras were monitoring the tested specimens at a frame-rate of 1 000 kHz. The high-speed cameras were triggered by strain gauge 2, such that premature or delayed recordings could be avoided. Furthermore, to obtain suitable conditions for the DIC measurements, additional lighting was used. Due to the low temperature, the conventional method of spraying aerosol paint to create the speckle pattern fails. To enable the DIC measurements, a method using a speckle patterned sticker was availed. This resembles the traditional method, as opposed to the grease used at lower strain rates. These stickers are developed for cold climate testing of polymers, where low strains are expected prior to fracture.

For monitoring of any possible adiabatic heating, the FLIR SC7000 thermal camera utilised for quasi-static and meso-dynamic tensile testing was also used here. This was accomplished by placing the thermal camera behind the PC chamber such that its monitoring sector operated within a rectangular slit in the back wall, as shown in Figure 7.5.

7.2.3 Post processing

Similarly to the tensile data from the EM test machine, DIC was an important tool used to extract the strains occurring in the SHTB tests. However, unlike the quasi-static and meso-dynamic tests, where the forces and subsequent stresses could be extracted directly from the test machine, the procedure was slightly more com-

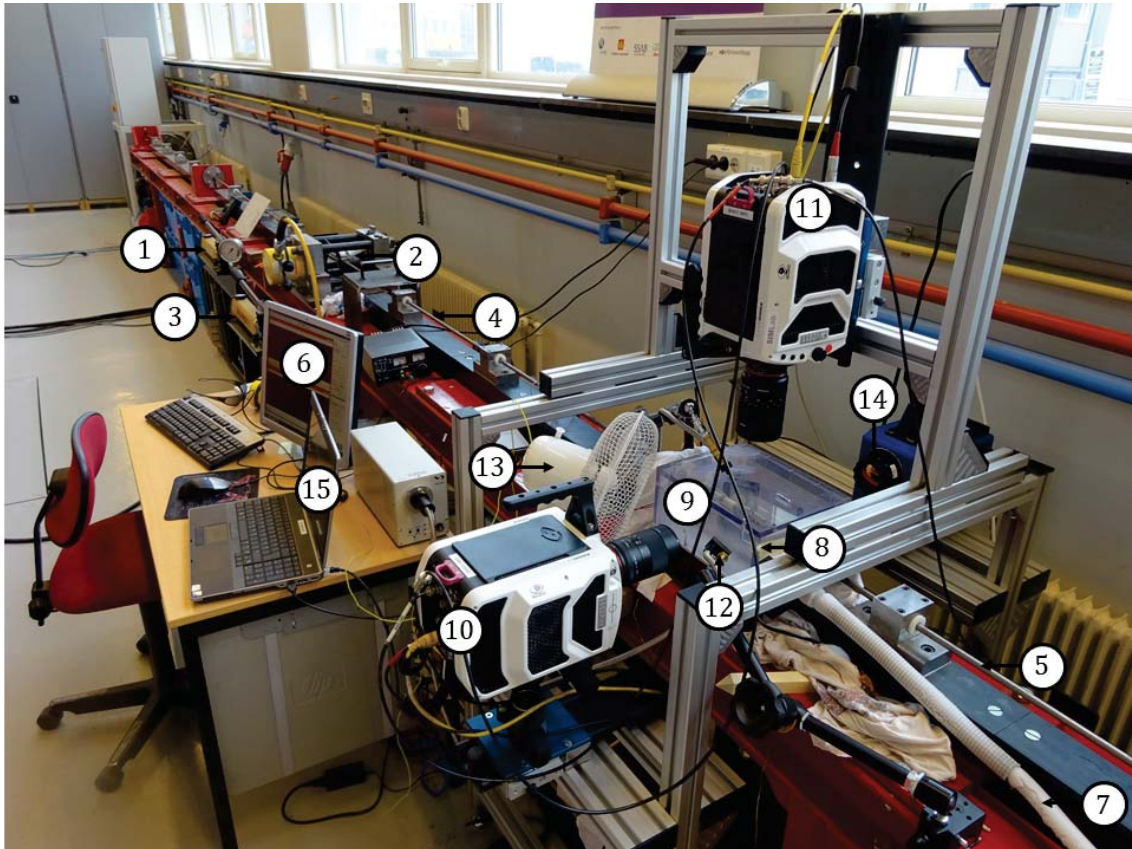


Figure 7.5: SHTB test setup at low temperature

① Hydraulic jack for pre-tensioning of incident bar, ② Friction lock, ③ Hydraulic jack for application of pressure onto the friction lock, ④ Incident bar, ⑤ Transmission bar, ⑥ Logging program and DIC data recording, ⑦ Nitrogen supply hose, ⑧ Polycarbonate chamber, ⑨ Mounted test specimen, ⑩ DIC camera 1, ⑪ DIC camera 2, ⑫ Additional lighting, ⑬ Fan, ⑭ IR camera, ⑮ IR camera recording

plicated in this case. The stress, strain and strain rates, were derived based on one-dimensional stress wave theory and the use of the two strain gauges on either side of the specimen [55], as shown in Figure 7.3. A MATLAB script supplied by Schwenke was therefore employed for post processing of all experimental data from the SHTB.

Strain measurements

The process in which the strain fields were extracted for the EM test machine, was replicated for the SHTB. However, since high-speed cameras were required in order to capture the deformation, the recordings initially had to be separated into a sequence of images. A reference image of the undeformed specimen was further

utilised for choosing and positioning of the mesh. Quadrilateral, structured elements of size 30×30 pixels were used in order to represent the strain fields accurately. Although a smaller amount of pixels were employed per element in this case, the mesh density was lower than for the quasi-static and meso-dynamic tests. This may seem counterintuitive, but was due to the low resolution of the high-speed camera recordings.

The DIC analyses were conducted in eCorr, which allowed for the surface displacements and subsequent strains to be determined. In some cases, the mesh had to be repositioned or adjusted such that frozen condensation drops on the specimen surface could be avoided. Due to the brittle nature of the fracture found in the SHTB testing, no high local strains were used as reference for extracting logarithmic strains. Hence, an arbitrary column of elements was chosen. The process was repeated for both sides of the specimen, such that logarithmic strains in all spatial directions could be obtained.

Stress measurements

Once the DIC analyses were completed, the MATLAB script was used for further post processing. Several operations were conducted by the script, starting with processing of the strain signals from all three strain gauges. This allowed the signals to be separated into the incident-, reflected- and transmitted strain waves. Additionally, the correct pre-tension of the incident bar could be calculated. Furthermore, the small portion of the signal corresponding to the actual test was established, such that the nominal stress and strain could be computed here. Finally, the DIC results were synchronised with the strain gauge data, and interpolated to obtain an identical amount of vector entry. As a result, the true stress could be calculated, as discussed in Section 2.2.1.

7.2.4 Results

Five successful tests were conducted in the SHTB at $-30\text{ }^{\circ}\text{C}$, and are given in Table 7.1. The specimens were extracted from location B, at an orientation of 0° , such that any location- and orientation-dependent mechanical properties could be neglected. Since the objective of the SHTB test campaign was to study the material properties of the door trim in the dynamic strain rate regime, three separate pre-tension forces and subsequent average strain rates were tested. Different decades of strain rates are usually employed when characterising the viscoplastic properties of a material, which

are generally log-linear. Hence, two additional half decades could be investigated in the SHTB, at approximately $10^{1.5}$ and $10^{2.0} \text{ s}^{-1}$.

Table 7.1: Split-Hopkinson tension bar test results of door trim cutouts

ID	Temperature [°C]	Pre-tension [kN]	Average analytic strain rate [1/s]
SH_B-3_02	-30	5.96	36.9
SH_B-10_02	-30	5.50	34.3
SH_B-5_01	-30	12.9	101
SH_B-4_01	-30	21.5	157
SH_B-4_02	-30	21.7	152

Visual results

A brittle failure mode was observed for all tests conducted in the SHTB. Although the material was still ductile at a strain rate of $10^{-0.5} \text{ s}^{-1}$, an increase in strain rate with two additional decades resulted in a completely different behaviour. The high-speed camera recordings from test SH_B-10_02 can be seen in Figures 7.6a-c. Here, the initial frame corresponds to the deformation just before fracture occurs in the specimen. The three images in the sequence are extracted with intervals of 29 μs . From these images, only small deformations can be observed prior to fracture, indicating highly brittle behaviour.

The fracture observed in test SH_B-4_02, can be seen in Figures 7.6d-f. This test was conducted at a strain rate that was approximately half a decade higher than that of SH_B-10_02. Comparing the frames just before fracture for the two specimens, even less deformation can be seen in the latter. Immediately after fracture, the two remaining parts contracted, suggesting that predominantly elastic strains arose within the specimen.

Measured results

The true stress-logarithmic strain curves for the five successful tests conducted in the SHTB are shown in Figure 7.7. Due to the amount of noise present in both the strain gauge- and DIC readings, a moving average filter was employed for both. The raw, unfiltered data from each test in SHTB can be found in Appendix D.

Figure 7.7 shows that only small strains developed in the specimens before fracture occurred at these elevated strain rates. For specimen SH_B-5_01, SH_B-4_01 and

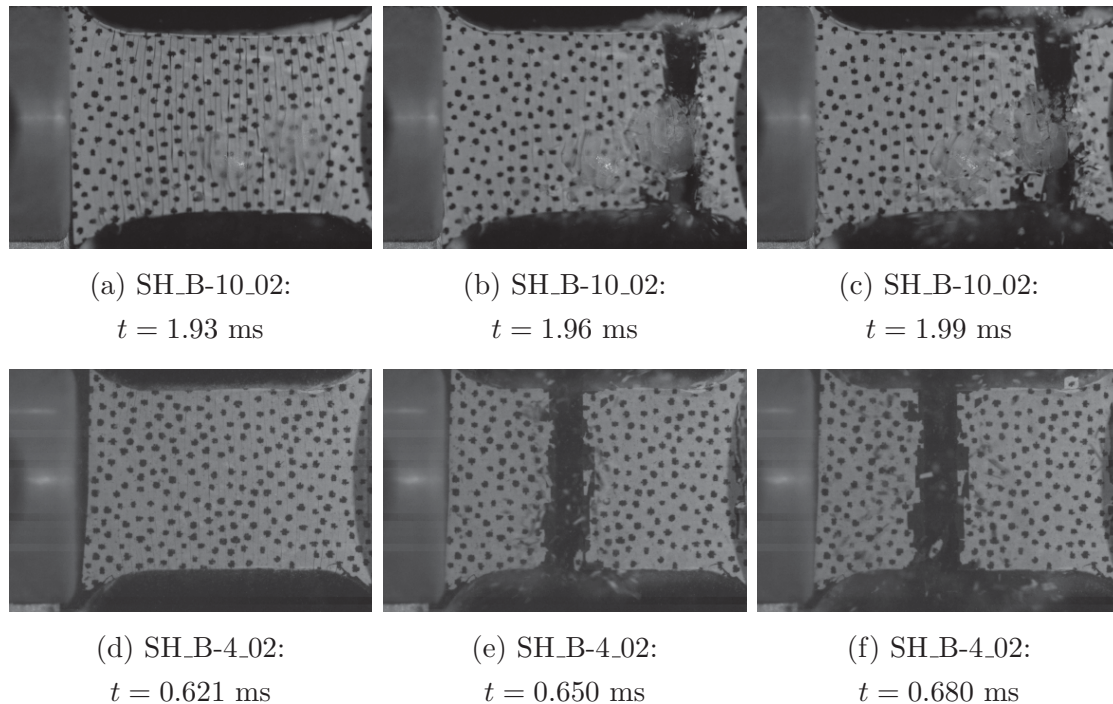


Figure 7.6: Brittle fracture in the SHTB tests for two different strain rates

SH_B-4.02, tested at strain rates of approximately $10^{2.0} \text{ s}^{-1}$, fracture transpired already in the linear elastic domain. No clear signs of yielding are indicated in the curves. For the two replicates tested at strain rates of $10^{1.5} \text{ s}^{-1}$, however, a plateau in the true stress-logarithmic strain curves can be observed in the figure, which is associated with yielding of the material. This suggests that, at least, some plastic deformation developed in the material, prior to fracture.

A disadvantage of the moving average filter, is the fact that the peak stresses in Figure 7.7 seem to be larger for the two replicates tested at strain rates of $10^{1.5} \text{ s}^{-1}$. By inspecting the raw data, however, the peak stresses were found to be higher for the replicates at $10^{2.0} \text{ s}^{-1}$, suggesting that the visoplastic material characteristic is still present in the dynamic regime. In Figure 3.24, a 5.6 MPa increase in peak nominal stress occurred when increasing the strain rate from $10^{-2.0}$ to $10^{-1.0} \text{ s}^{-1}$. By extrapolating the log-linear relation to a strain rate of $10^{2.0} \text{ s}^{-1}$, a peak stress of approximately 58 MPa was found. Compared to the test results obtained here, the peak stress is clearly underestimated by this relationship. This effect of increased strain rate sensitivity at higher strain rates has been widely observed for several polymers [10], suggesting that such strain rates should be taken into account during calibration.

The logarithmic strain components and volumetric strain are plotted as functions of time for SH_B-10_02 and SH_B-4_02 in Figure 7.8a and 7.8b, respectively. Since

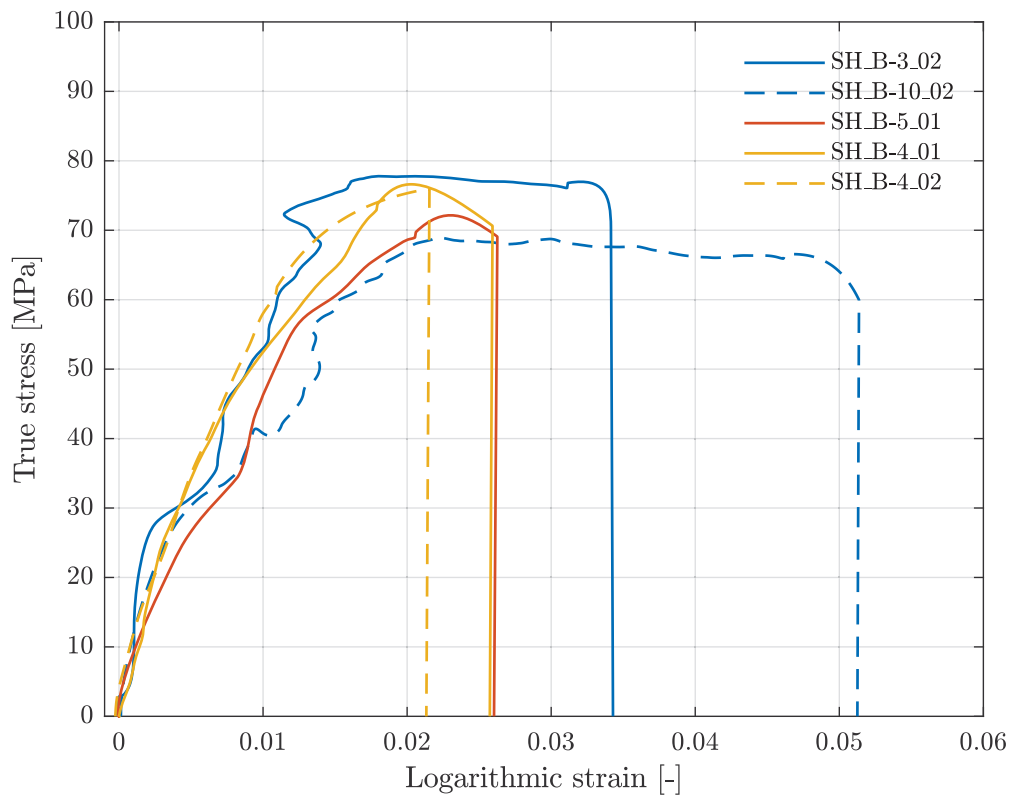


Figure 7.7: Split-Hopkinson test results for door trim cutouts

all recordings were triggered by the stress wave reaching strain gauge 2, the two respective specimens were loaded approximately 0.5 and 0.4 ms, after triggering took place. The two transverse strain components, ε_{yy} and ε_{zz} , were also here found to be comparable in size. As opposed to the quasi-static and meso-dynamic test results, however, their size is similar to the longitudinal strain, ε_{xx} . Hence, the development of volumetric strains is small. This difference can be explained by the strains being predominantly elastic at dynamic strain rates. Large volumetric strains only develop once large plastic deformations occur in the material.

In order for the measurements obtained in the SHTB to be accurate, equilibrium of the test specimen must be fulfilled, implying that the force applied to either side must be equal. If not, inertia forces or transient effects might yield inaccurate test results [55]. The equilibrium can be evaluated by the following between the strain data from strain gauge 2 and 3, ε_2 and ε_3

$$\begin{aligned}\varepsilon_2 &= \varepsilon_3 \\ \varepsilon_I + \varepsilon_R &= \varepsilon_T,\end{aligned}\tag{7.1}$$

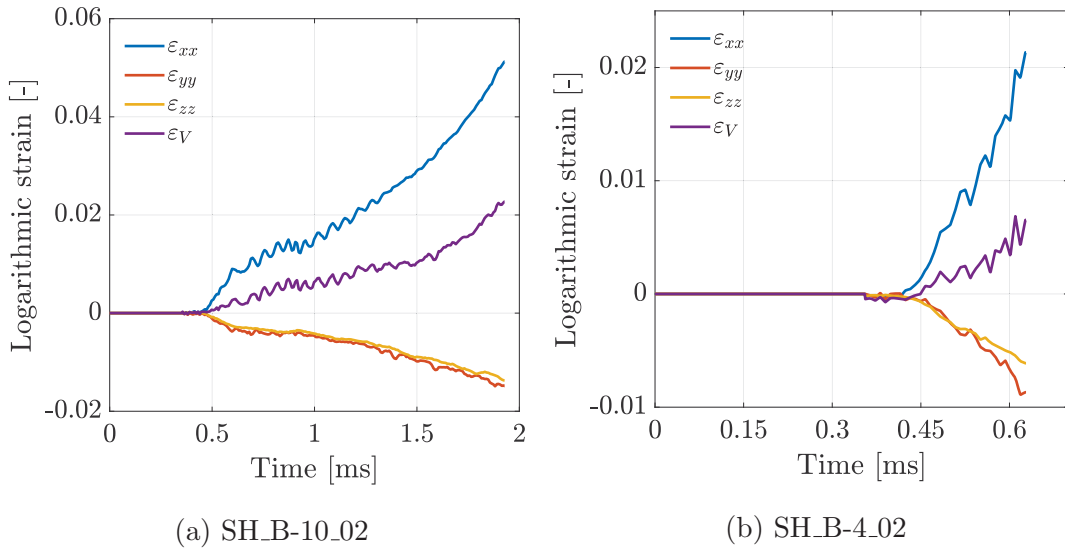


Figure 7.8: Logarithmic strain components and volumetric strain for door trim cutout specimens at different strain rates

where ε_I , ε_R and ε_T corresponds to the incident-, reflected- and transmitted strains, respectively. In Figure 7.9, the signal from strain gauge 2 and transmitted strain is plotted in addition to the signal boundaries, indicating the test durations. Strain gauge 2 in the figures, corresponds to the left hand side of Eq. (7.1). For test SH_B-10_02 in Figure 7.9a, the equilibrium criterion is fulfilled, although some oscillations were present in the signal from strain gauge 2. For test SH_B-4_02, the strains are shown in Figure 7.9b. In this case, equilibrium is not satisfied initially. Hence, the accuracy of the test results obtained at small strains could be questioned.

Although the strain rate obtained in the SHTB can be estimated using analytical expressions, these are often associated with some inaccuracy. Therefore, the actual strain rates were computed and can be seen for SH_B-10_02 and SH_B-4_02 in Figures 7.10a and 7.10b, respectively. Since the strain rate is obtained through differentiation of the strain recordings, enhancing any noise which is already present, a moving average filter was utilised also here. This enabled some of the high-frequency fluctuations in the signal to be smoothed. The nominal strain rate of the specimen, $\dot{\varepsilon}_s$, can be obtained using the following analytical relation

$$\dot{\varepsilon}_s = -2 \frac{c_0}{L} \varepsilon_R, \quad (7.2)$$

where c_0 is the wave propagation velocity of the tested material and L is the gauge length of the specimen. The averaged value of the analytical strain rate is also shown in the figures. For test SH_B-10_02, the strain rate seems to be accurately predicted

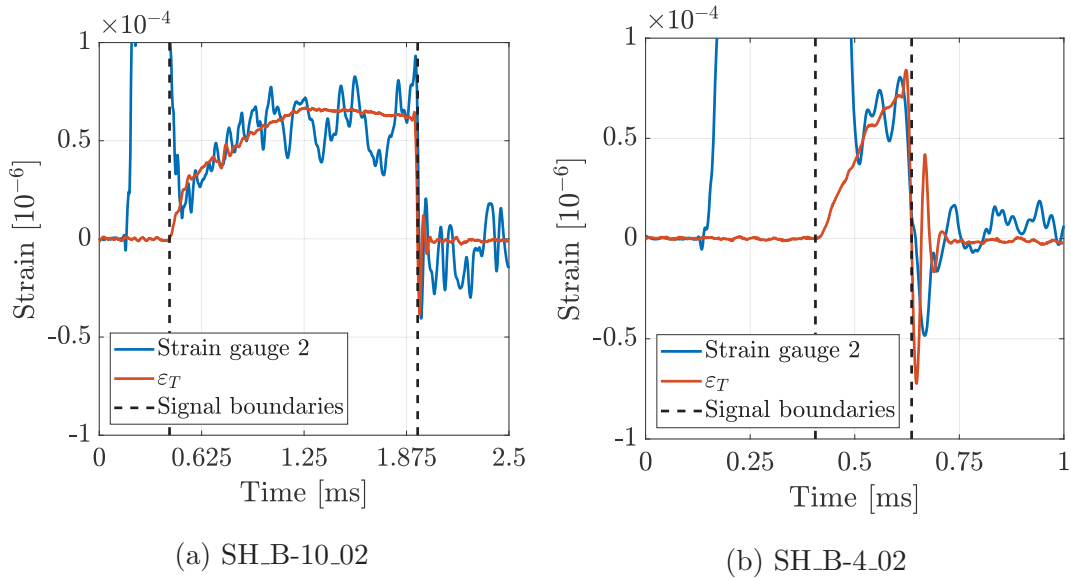


Figure 7.9: Comparison of different strain data obtained from the SHTB

by the analytical expression. The actual strain rate goes from being lower, to higher than the estimated value. For test SH_B-4_02, the actual strain rate is observed to be increasing. By comparison to the analytical average, it seems to be somewhat overestimated.

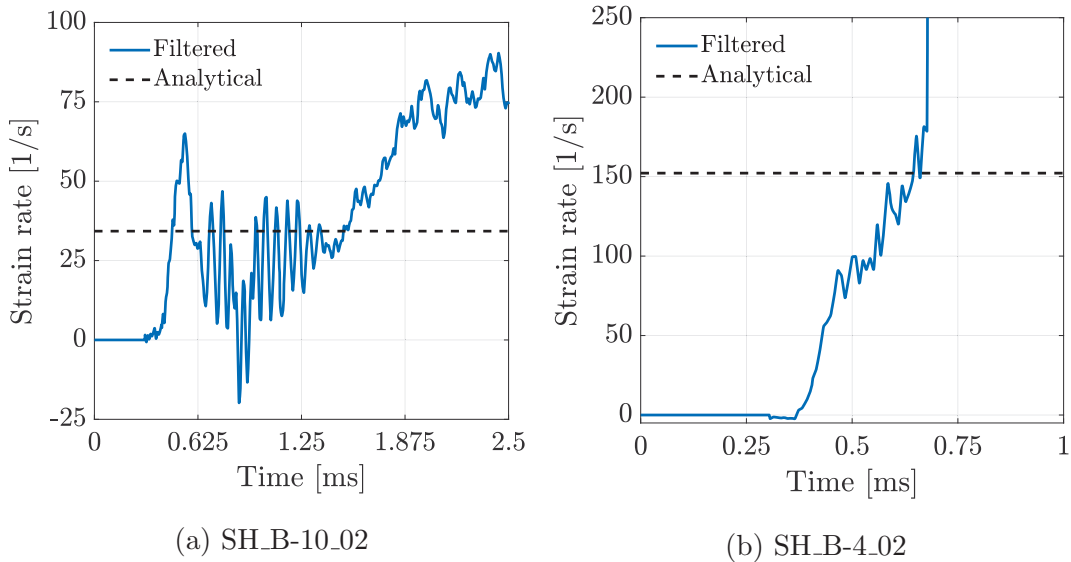


Figure 7.10: Comparison between filtered strain rate and analytical expression

When processing the recordings from the thermal camera, obtained in the SHTB tests, no temperature increases over the threshold of $-20\text{ }^{\circ}\text{C}$ were found. This result is likely explained by the brittle material behaviour, which was observed in the dynamic regime. Due to the deformations being predominantly elastic, no heat

generation arose due to the lack of plastic work.

Figure 7.11 shows the log-bilinear relation between peak nominal stress and strain rate, discussed earlier. Here, the peak nominal stress corresponds to the local maximum of the nominal stress-strain curve. As opposed to Figure 3.13, the strain rates for the quasi-static and meso-dynamic strain rates are computed as the average of the entire test duration, in a similar fashion as for the SHTB test result. This was done in order to allow for more accurate comparison between the two. A moving average filter was also here applied to the dynamic nominal stress-strain curves, although smoothing of the peak nominal stresses was avoided. The effect shown in the figure was first observed for PP by Chou et al. [58] and was recently also evidenced in a more comprehensive study spanning eight decades, conducted by Okereke et al. [59] for three different grades of PP. However, this study was based on uniaxial compression tests.

Two facts should be noted when interpreting the results displayed in Figure 7.11. Firstly, the increased strain rate sensitivity occurs for rates where inertia might have an effect on the strength of the polymer. Secondly, the transition corresponds to the intermediate regime, where the strain rate is too high for the ordinary EM test setup and too low for the SHTB. Hence, it could simply be related to the difference in test devices.

SEM results

A SEM analysis was conducted for a representative specimen from the SHTB test campaign. Although both the visual- and measured results suggested that brittle fracture occurred in the dynamic regime, inspection of the fracture surface was believed to confirm this suspicion. Additionally, comparison with the SEM results found from the specimens tested in the drop tower was of special interest. This would allow for brittle fracture to be confirmed, also here.

The results from the SEM analysis conducted on the fracture surface of specimen SH.B-4.02 are shown in Figure 7.12. Here, the elastomeric particles, with approximate size of $0.5 \mu\text{m}$, are evident in the PP matrix from the micrograph with the highest magnification. These rubber particles are similar to the ones found in the fracture surface of the H strain rate test for the material sample plates. In addition, cavities resulting from debonding of the second phase particle can be seen in the figure. The shape and size of these cavities are similar to that of the particles, which could be explained by the dynamic loading conditions. Due to the high strain rate in the SHTB test, the cavities have no time to grow prior to fracture, which occurs

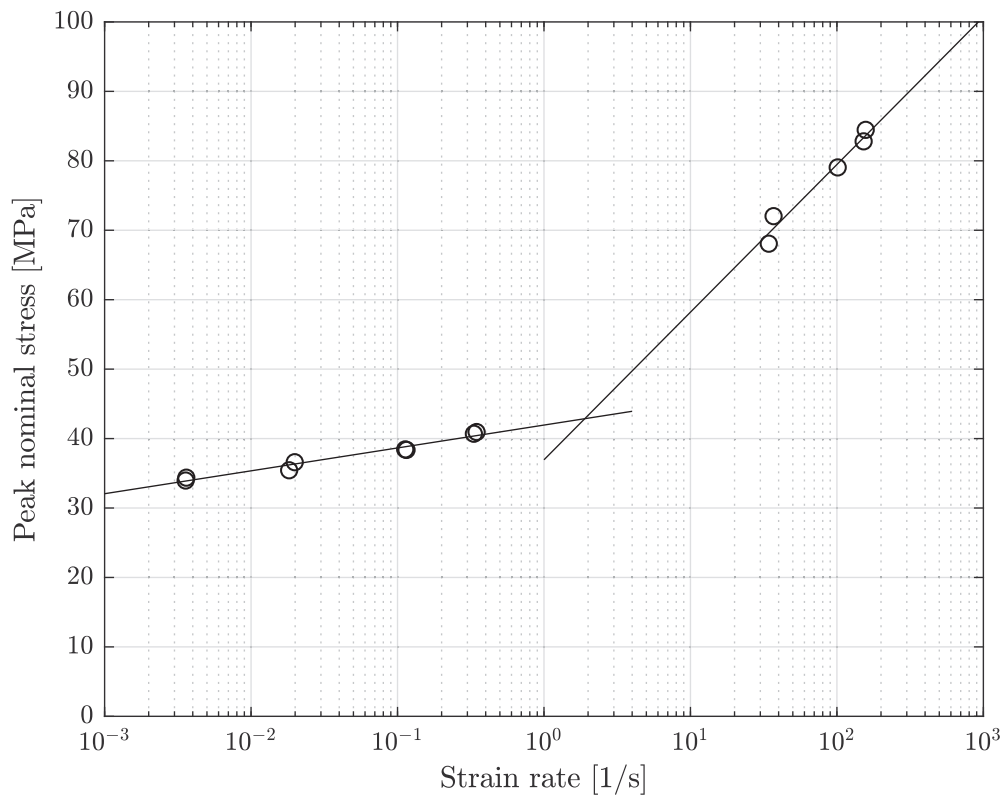


Figure 7.11: Strain rate dependent response in the different regimes

due to rupture of the particles. A larger number of cavities was, however, found in the SHTB test specimen, compared to the H strain rate in Figure 3.15. Both particles and associated cavities are encircled in the figure below.

The morphology of the material surrounding the particles also differs from the meso-dynamic case. Here, the presence of sharp edges is much more pronounced compared to Figure 3.15. One explanation is the lack of plastic deformation and subsequent adiabatic heating in the SHTB tests, resulting in such sharp edges. A similar morphology was found on the periphery of the material sample plates, tested in the drop tower. For the door trim cutout specimens, a similar through-thickness fracture surface was found both under the impactor and on the periphery. This suggests that brittle fracture occurred, also here. Note that, some contamination is evident at the highest magnification.

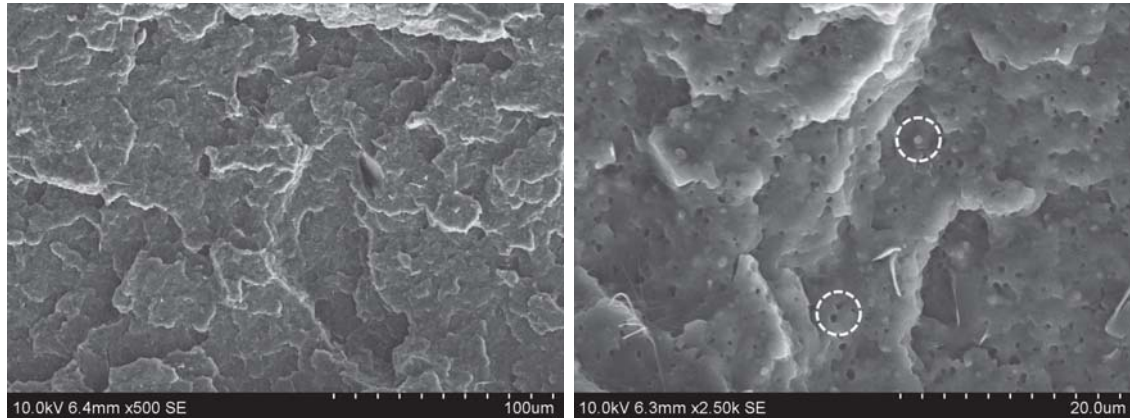


Figure 7.12: SEM micrographs of test specimen SH.B-4.02

7.3 Recalibration of material model

In order to account for the brittle behaviour observed in the drop tower- and SHTB testing of the door trim cutouts, a recalibration of the material model was attempted. Since the model was initially calibrated from tensile tests with exclusively ductile behaviour, a possible solution to the overestimated ductility could be to include the brittle behaviour observed in the SHTB tests. Although the SPM can not predict the brittle-ductile transition itself, a calibration from tests where such behaviour is found might replicate the embrittlement in a more accurate fashion. Additionally, since the SPM is developed for ductile polymers exhibiting large plastic strains, calibration of an alternative material model was attempted.

7.3.1 Alternative material model

The alternative material model was based on a linear elastic-perfectly plastic behaviour. This model was chosen due to its simplicity, and since similar material characteristics were observed in the SHTB tests. The von Mises yield surface was employed, for which yielding is independent of the stress state. This yield criterion is suitable for metallic materials, while the PP material used in this thesis experiences pressure-dependent yielding, as discussed in Section 2.3.3. Since the impact properties of the material are believed to be governed by the behaviour in tension, this effect will be neglected in this simplified model. Due to the predominantly elastic behaviour observed in the SHTB tests, perfect plasticity was adopted. Isotropic hardening was also employed, although no change in the yield surface related to plastic straining occurs for perfect plasticity. Unlike the SPM, an associated flow rule was utilised for the simplified model. Even though a such relation generally

overestimates the plastic strains of polymers, all strain components were in the same order of magnitude in the SHTB tests. This suggests that such a relation is acceptable for predominantly elastic strains.

In order to replicate the log-bilinear relation between yield stress and strain rate observed for the material, the Cowper-Symonds viscoplastic relation [60] was adopted. This relation offers a non-linear description of the viscous stress as a function of the strain rate. Thus, it is often employed in dynamic load cases where such behaviour is found. The constitutive relation for the equivalent plastic strain rate, $\dot{\varepsilon}^p$, is given below

$$\dot{\varepsilon}^p = \begin{cases} 0 & \text{if } f \leq 0 \\ D_v \left[\left(\frac{\sigma_{eq}}{\sigma_T} \right) - 1 \right]^q & \text{if } f > 0, \end{cases} \quad (7.3)$$

where D_v and q are constants in the Cowper-Symonds relation, while σ_T is the yield stress in uniaxial tension. Solving the expression with respect to equivalent stress, σ_{eq} , the constitutive relation can be expressed by

$$\sigma_{eq} = \sigma_T \left[1 + \left(\frac{\dot{\varepsilon}^p}{D_v} \right)^{1/q} \right] \quad \text{if } f > 0. \quad (7.4)$$

A simple equivalent plastic strain-based fracture criterion was chosen in order to model fracture in the material. The model is based on the equivalent plastic strain, ε^p , that occurs in an integration point [35]. Fracture is assumed once the damage parameter ω exceeds 1, determined by the following expression

$$\omega = \frac{\sum \Delta \varepsilon^p}{\varepsilon_f^p}, \quad (7.5)$$

where ε_f^p is the equivalent plastic strain at fracture and $\Delta \varepsilon^p$ is the increment of equivalent plastic strain, given by the integral

$$\varepsilon^p = \int_0^t \sqrt{\frac{2}{3} \dot{\varepsilon}^p : \dot{\varepsilon}^p} dt. \quad (7.6)$$

Here, $\dot{\varepsilon}^p$ is the equivalent plastic strain rate tensor. This fracture model is suitable for modelling of dynamic situations [35], and allows for limitation of the load carrying capacity of an element through element erosion. Element removal occurs once the criterion in Eq. (7.5) is reached in all through-thickness integration points for a shell element in Abaqus/Explicit. This is similar to what was used for the SPM earlier.

An important feature of the simplified material model is that it allows for the fracture parameter to be modelled as a function of the plastic strain rate, stress triaxiality and temperature. Since the strain rate was found to provoke embrittlement of the material in this project, the equivalent plastic strain at fracture was modelled accordingly. This was done simply by defining representative strains at fracture and their associated strain rates using tabular data.

7.3.2 Calibration procedure

Elasticity

Due to the somewhat viscoelastic material behaviour observed for polymers, some increase in Young's modulus is likely to be found for dynamic strain rates compared to the quasi-static and meso-dynamic regimes. An accurate calibration of the elastic behaviour of the material requires a large amount of sample points as well as a more accurate strain measurement technique than what was used here. This was not satisfied by the SHTB results. Additionally, equilibrium of the test specimen in the SHTB was first found after some amount of straining. Hence, since the effect of Young's modulus was found to have a minimal influence in the sensitivity study presented in Section 6.3.1, no recalibration was conducted here.

Strain rate dependence

In an attempt to model the log-bilinear viscoplasticity of the material, the SHTB test results were included in the calibration process here. Due to the lack of plastic straining in the SHTB tests, the yield stress and associated strain rate was used for calibration of the parameters governing the strain rate dependence in the two models. This process was conducted manually, without the use of MatPrePost. The lowest quasi-static yield stress was chosen for the parameter, σ_T , and the remaining parameters were fitted to the experimental data, as shown in Figure 7.13.

Figure 7.13 shows the calibrated Cowper-Symonds viscoplastic relation used in the alternative model, in addition to the recalibrated SPM. The associated calibrated parameters are listed in Tables 7.2 and 7.3, respectively. From the figure, the relation between stress and strain rate is well captured by both viscoplastic relations. However, the Cowper-Symonds relation somewhat overestimates the stress both at quasi-static and dynamic strain rates. The log-bilinear shape is, however, replicated in an accurate way by the recalibrated SPM. Although practically neglecting the strain rate dependence at lower rates, it accurately mimics the behaviour in the

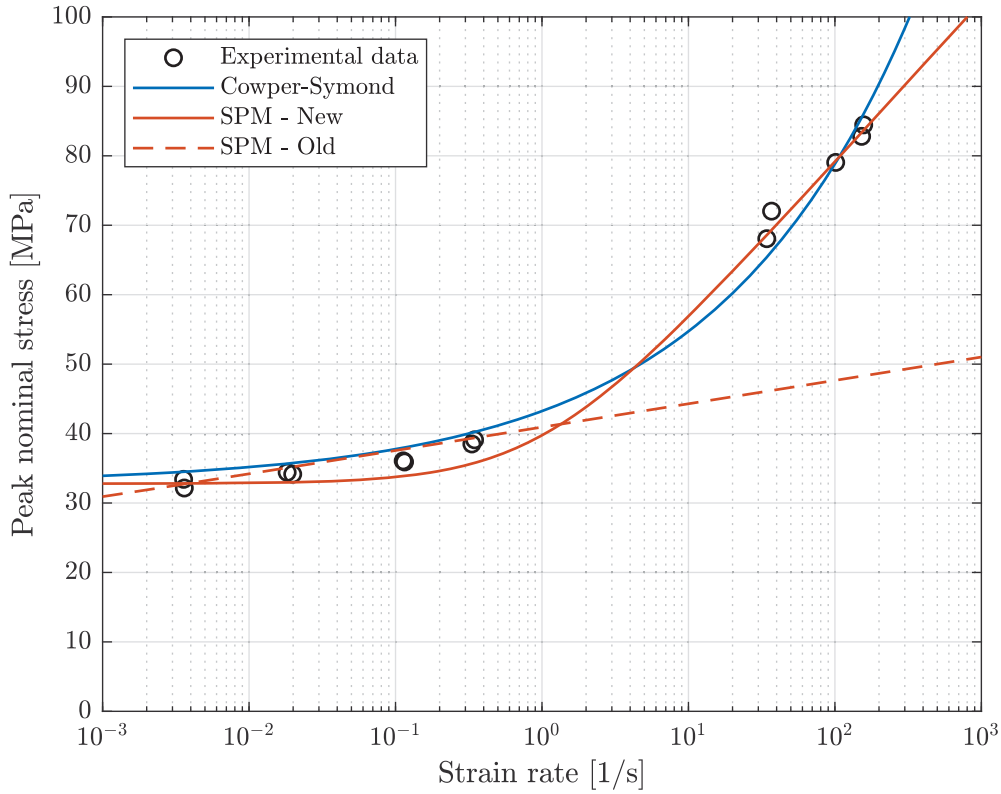


Figure 7.13: Calibration of log-bilinear viscoplastic relation

dynamic regime. Since the rates were estimated to the range of $10^2 - 10^3 \text{ s}^{-1}$ in the numerical simulations of the drop tower test, an accurate viscoplastic characterisation might not be crucial for the lower strain rates. The old log-linear viscoplastic characterisation of the SPM is also plotted in this figure. It should be noted that this calibration significantly underestimates the stress at dynamic strain rates.

Table 7.2: Alternative model parameters

Parameter	Value	Unit
σ_T	32.8	MPa
q	3.11	-
D_v	34.8	1/s

Table 7.3: New SIMLab polymer model parameters

Parameter	Value	Unit
σ_T	32.8	MPa
C	0.307	-
$\dot{\epsilon}_0^p$	1.00	1/s

Fracture

Calibration of the damage parameters using the SHTB test results is associated with a large amount of inaccuracy. First of all, determination of the yield point

is complicated due to the slight non-linearity associated with the elastic domain of the polymer. Secondly, for the replicates at the highest strain rates, fracture seemed to occur already in the elastic domain, suggesting that no plastic straining was associated with fracture. Setting the critical damage parameters to zero is, however, not a solution in the numerical model, since element erosion could arise from elastic stress waves, resulting in an artificially brittle behaviour. Finally, since equilibrium of the test specimens was found after some time in the SHTB tests, the initial strains in the elastic domain might be affected by inertia effects. Thus, an inverse modelling approach was conducted, using the velocity-time curve obtained in the drop tower impact test.

7.4 Verification of material models

In Chapter 5, it was shown that the SPM was able to reproduce the ductile behaviour of the PP material accurately. However, to verify whether the new calibration allows for an accurate prediction of the brittle failure mode, numerical simulations replicating the test conditions of the SHTB and the drop tower were conducted. Both numerical models employed here were introduced in Sections 5.2 and 6.2.1, respectively.

7.4.1 Split-Hopkinson tension bar test

In order to verify that the calibrated models could replicate the strain rate sensitivity of the material, each strain rate tested in the quasi-static, meso-dynamic and dynamic regimes were simulated. Since large inaccuracies were related to the strains obtained in the SHTB, these were not of any particular interest. Whether the peak nominal stress of the models resembled those found experimentally was, however, essential.

Results

The peak nominal stresses resulting from simulations using the three different models are shown in Figure 7.14, in addition to the experimental log-bilinear relation. It should be noted that the estimated initial strain rates are used here, rather than the averaged strain rates for the entire test durations. However, it is clear that the general trends found in the calibration procedure, shown in Figure 7.13, are present here as well. The peak nominal stresses, resulting from the alternative model is

slightly lower than those obtained with the old SPM characterisation at the low strain rate. This is inconsistent with the calibration, where the two were found to be practically equal. The fact that the alternative model was based on perfect plasticity, as opposed to the initial peak being included in the hardening calibration of the SPM, might account for some of this discrepancy. This can also be seen at the two dynamic strain rates, where the recalibrated SPM results in somewhat higher peak nominal stresses than the alternative model. The figure also highlights the significant underestimation of stresses at such rates for the old SPM. Hence, the old calibration of the SPM is expected to produce large errors in the drop tower simulation results, where dynamic strain rates are likely to occur.

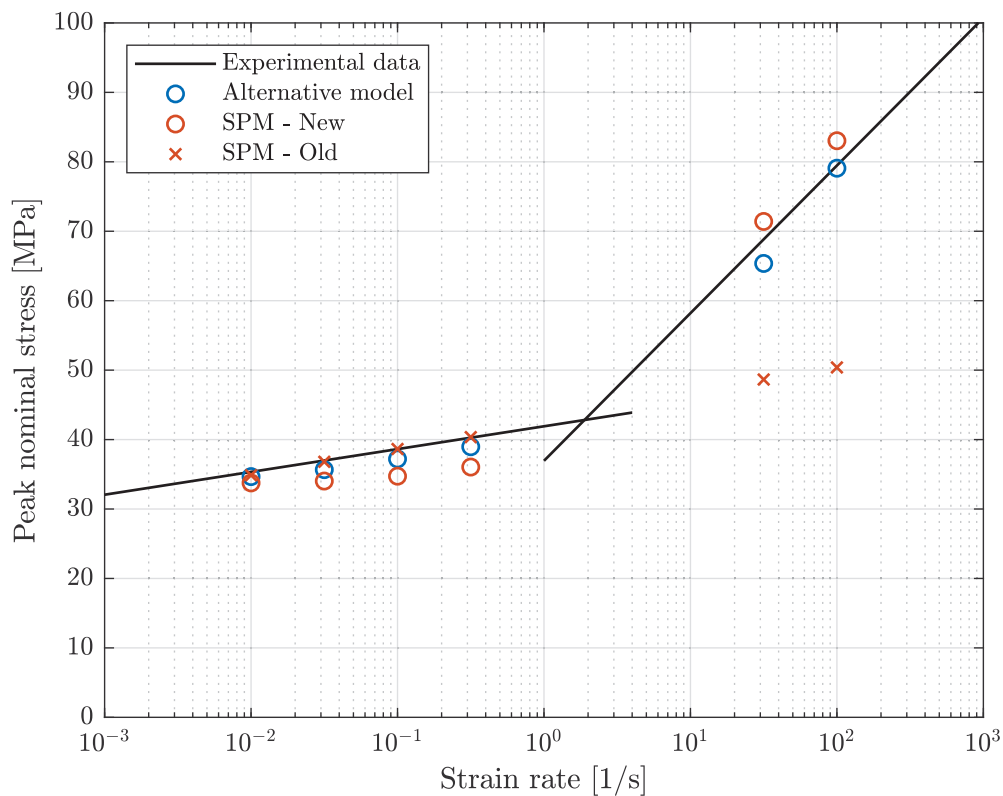


Figure 7.14: Numerical peak nominal stress for all three models

7.4.2 Drop tower impact test

Once it was verified that the calibrated material models could replicate the strain rate sensitivity of the material, the drop tower impact tests were simulated. Hence, the numerical model for the drop tower impact test of the door trim cutouts, introduced in Section 6.2.1, could be simulated using the newly acquired parameters.

Here, the ultimate goal was to inverse model the fracture parameters according to the experimental results obtained in the drop tower. Since similar strain rates, and the same biaxial stress state were expected in the full-scale component drop test, inverse modelled parameters could then be utilised in order to reproduce the drop height a fracture. The coefficient of friction was set to 0.1 due to the results obtained in the sensitivity study in Section 6.3.5.

Inverse modelling

The inverse modelling procedure involved manual adjustment of the fracture parameters such that the behaviour found in the experiment, was replicated by the numerical model. Since fracture was defined by the point of initial element erosion, the target for the numerical model was to erode an element at approximately 2.25 m/s, corresponding to the residual velocity subsequent to fracture found in the experiment. Figures 7.15a and 7.15b, describe the process of determining the correct fracture parameters for the alternative model, as well as the new- and old SPM characterisation, respectively.

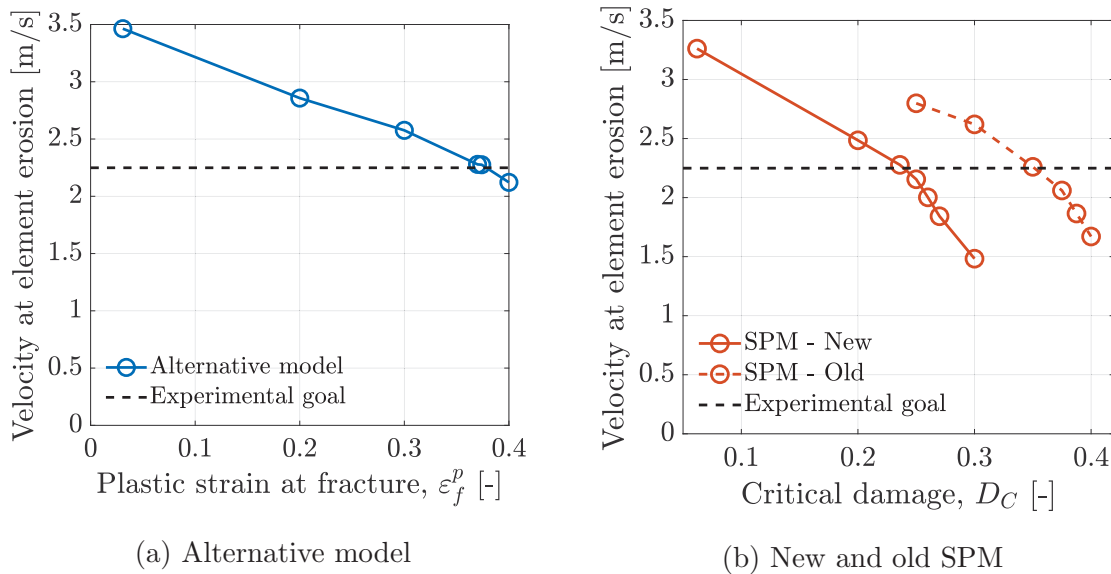


Figure 7.15: Inverse modelling of fracture parameters from drop tower simulations

The fracture parameters resulting from the inverse modelling procedure are given in Tables 7.4, 7.5 and 7.6 for the alternative model, recalibrated SPM and old SPM, respectively. All parameters were found to replicate the residual velocity of the experiment, simply because they were designed to do so. These values are all assumed to represent the brittle failure mechanism observed in the drop tower impact test on the door trim cutout specimens, rather than the ductile nature of

the uniaxial tensile tests at quasi-static and meso-dynamic strain rates. It should, however, be noted that the parameters found here suggest that a substantial amount of plastic deformation is indeed present in the numerical models prior to fracture.

Table 7.4: Alternative model parameters

Parameter	Value
ε_f^p	0.379

Table 7.5: New SPM parameters

Parameter	Value
D_C	0.234

Table 7.6: Old SPM parameters

Parameter	Value
D_C	0.357

Results

Figure 7.16 shows the force-displacement curves obtained from numerical simulations of the drop tower impact test on the door trim cutout specimens, for the three material calibration introduced above. The experimental data from test replicate DT_C-7.-30, represented by the black dashed line, is plotted as well, since its residual velocity was used during inverse modelling of the fracture parameters.

From the figure, it is evident that the alternative model and the recalibrated SPM generally have a stiffer behaviour in the linear region of the force-displacement curve, compared to the old SPM calibration. Although all models recreate the toe-region of the curve accurately, the peak force is somewhat overestimated by the two former models. The fact that the highest force was found for the alternative model, can be explained by the Cowper-Symonds viscoplasticity, being overly strain rate sensitive at dynamic rates. Element erosion occurs for an approximate displacement of 14 mm for all models, replicating the experimental result.

The peak force is somewhat underestimated by the old SPM with inverse modelled fracture parameters, while its accuracy in the remaining sections of the curve is far better than the two other models. The linear region of the experimental curve is well-represented by the model as well as the displacement at element erosion. Since the material was found to be more strain rate sensitive at rates associated with the drop tower impact test, this suggests that the incorrect viscoplasticity of the old SPM calibration might be disguised in some way. In the sensitivity study conducted in Section 6.3, the only parameter found to considerably affect the slope of the linear region in the force-displacement curve, was the plate thickness. However, substantial changes were required for the parameter to yield any significant effect. Thus, the small deviations found when measuring the door trim cutout specimens, could not account for the entire discrepancy.

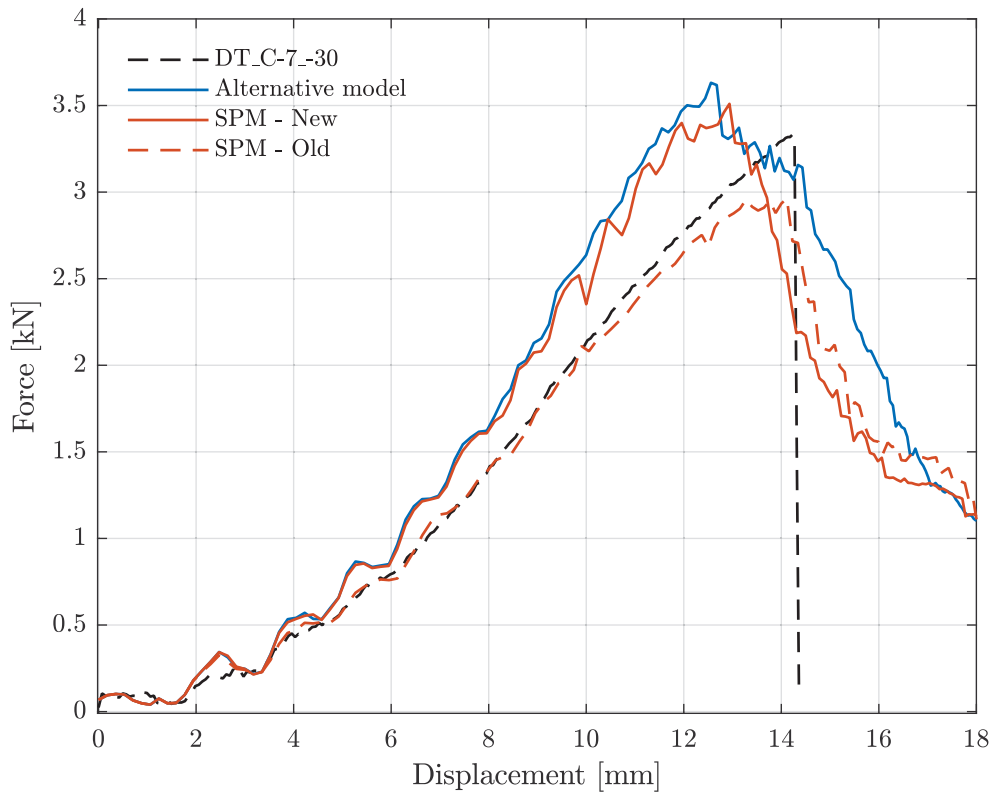


Figure 7.16: Comparison of the three inverse modelled material calibrations

It is worth noting that the alternative material model provides a similar result as that of the recalibrated SPM, while being significantly simpler. The linear elastic-perfectly plastic model only requires calibration of six parameters, as opposed to the fifteen parameters that the SPM utilises. This suggests that for a brittle failure mode, the complexity of the material model can be greatly reduced. To enable modelling of the ductile nature of the polymer, however, a larger amount of constitutive relations and associated parameters are needed. As discussed earlier, the alternative model also allowed for strain rate dependent fracture parameters. This could be useful when accurate representation of the behaviour on both sides of the brittle-ductile transition is needed. The strain rate dependence of the plastic strain at fracture is plotted in Figure 7.17, resulting from the tabulated data shown in Table 7.7.

7.4.3 Calibrated material parameters

The calibrated material parameters for the three models discussed in this chapter are given in this section. For the alternative model, the calibrated parameters are

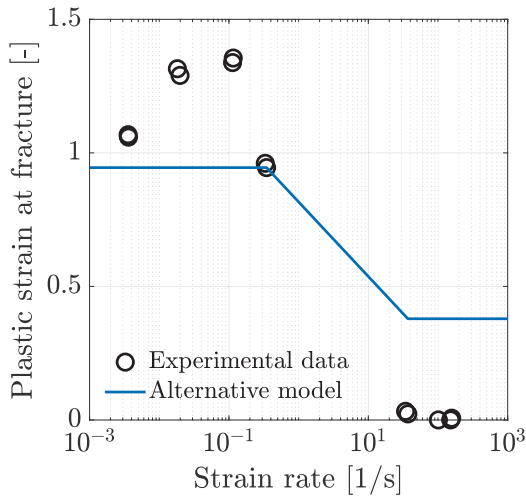


Table 7.7: Tabulated fracture data for alternative model

Strain rate [s ⁻¹]	Plastic fracture strain [-]
0.0	0.945
10 ^{-0.5}	0.945
10 ^{1.5}	0.379
10 ^{3.0}	0.379

Figure 7.17: Strain rate dependent fracture parameters

presented in Table 7.8. The tabulated data relating plastic fracture strain to strain rate, shown in Table 7.7, was also added. Table 7.9 and 7.10 show the parameters used in the recalibrated and old SPM calibrations, respectively.

Table 7.8: Calibrated parameters for alternative model

E	ν	σ_T	q	D_v	ε_f^p	ρ
[MPa]	[-]	[MPa]	[1/s]	[-]	[-]	[t/mm ³]
2696	0.267	32.8	3.11	34.8	0.379	9.05e-10

Table 7.9: Recalibrated parameters for SPM

E	ν	θ_{R1}	Q_{R1}	θ_{R2}	Q_{R2}	θ_{R3}	Q_{R3}
[MPa]	[-]	[MPa]	[MPa]	[MPa]	[MPa]	[MPa]	[MPa]
2696	0.267	254	2.74	25.3	-45.2	-62.4	-2.56
σ_T	α	β	ε_0^p	C	D_I	D_C	ρ
[MPa]	[-]	[-]	[1/s]	[-]	[-]	[-]	[t/mm ³]
32.8	1.22	1.88	1.0	0.3066	0	0.234	9.05e-10

Table 7.10: Calibrated parameters for old SPM

E	ν	θ_{R1}	Q_{R1}	θ_{R2}	Q_{R2}	θ_{R3}	Q_{R3}
[MPa]	[-]	[MPa]	[MPa]	[MPa]	[MPa]	[MPa]	[MPa]
2696	0.267	254	2.74	25.3	-45.2	-62.4	-2.56
σ_T	α	β	$\dot{\epsilon}_0^p$	C	D_I	D_C	ρ
[MPa]	[-]	[-]	[1/s]	[-]	[-]	[-]	[t/mm ³]
26.8	1.22	1.88	6.25e-05	0.0546	0	0.357	9.05e-10

7.5 Discussion

There are several conditions that could provoke brittle fracture of polymers in addition to decreasing the temperature. The results obtained from the SHTB testing suggest that the material fractures in a brittle manner for dynamic strain rates, i.e. $10^{1.5}$ and $10^{2.0} \text{ s}^{-1}$ at $-30 \text{ }^\circ\text{C}$. The fact that the material was found to be ductile for quasi-static and meso-dynamic strain rates, at the same low temperature, indicates that its brittle-ductile transition is associated with some intermediate strain rate. Hence, the time-temperature superposition effect, discussed in Section 2.1.4, is clearly observed in the material. Furthermore, since strain rates in the dynamic regime are assumed to arise in the component drop test, brittle material behaviour is also expected here. Additionally, the biaxial stress state of the drop tower test is likely to cause further embrittlement of the material. Hence, care should be taken when extrapolating the ductile behaviour observed at the lower strain rates to a more dynamic load case, such as the SHTB tests.

The fact that a clear difference was found in the microstructure of the fracture surfaces resulting from the separate strain rate regimes, suggests that a ductile-brittle transition is indeed present in the material. Although this was observed visually and indicated in the measured data, it was confirmed from the SEM analyses. In the ductile domain, the polymer matrix seems to govern the mechanical properties of the material. In the brittle domain, however, clear signs of second phase particles were found. Thus, suggesting that rupture of the elastomeric particles control the fracture of the polymer here.

Although the experimental results from the drop tower test, used for inverse modelling suggested a brittle failure mode, the resulting fracture parameters were still high. The parameters for both the alternative model and the recalibrated SPM indicated that large amounts of plastic deformation occurred prior to fracture. The results obtained in the SHTB, however, suggested something completely different.

Here, the largest volumetric strain at fracture was found to be approximately 0.024, corresponding to a longitudinal strain of 0.050. Nevertheless, a clear reduction was seen in the critical damage parameters, by comparing the recalibrated- and old SPM. Although the resulting force-displacement curves were less accurate, the alternative material model and the recalibrated SPM corresponded to a more brittle behaviour than the latter.

One reason for the seemingly ductile critical damage parameters for the two SPM calibrations, could be the plastic dilatation parameter. The SHTB results showed that the size of the transverse strain components were similar to the longitudinal. For the quasi-static and meso-dynamic test results, however, they were found to be much smaller than that of the longitudinal. This suggests that the plastic dilatation parameter should have been recalibrated as well. A decreased β would result in smaller amounts of plastic volumetric strains, less development of damage and ultimately a reduction in the inverse modelled critical damage parameters. However, due to the inaccuracies associated with strain measurements from the SHTB results, this was not attempted here.

Another effect that might account for some of the differences in the fracture parameters suggested from the SHTB tests, and the inverse modelled parameters from the drop tower results, is the stress triaxiality. As discussed in Section 2.1.4, increased triaxiality promotes more brittle behaviour in polymers. However, a biaxial stress state is assumed for the drop tower test, which is associated with a higher triaxiality than the uniaxial tension found in the SHTB tests. Hence, a more brittle behaviour should be expected for the inverse modelled parameters. One explanation could be the large shear gradients resulting from plugging. For a pure shear state, the triaxiality is even lower than for uniaxial tension. Hence, this could potentially cause a more ductile failure mode in the drop tower impact tests.

Component Impact Testing

The main task of this project was to reproduce the behaviour observed in cold impact testing of PP door trims using numerical simulations. Hence, an experimental campaign involving drop tests on the component was conducted. More specifically, a 1.0 kg ball was dropped onto different locations of the door trim at $-30\text{ }^{\circ}\text{C}$. The goal was to determine the largest height from which the ball could be dropped without the occurrence of fracture. The experimental test conditions were further reproduced using the explicit FEM software, LS-DYNA, in addition to the calibrated material models. Although these material models had been validated for the results obtained in the drop tower, as discussed in Chapter 7, it was still not certain whether the behaviour associated with the full-scale drop test could be replicated accurately. A thorough numerical refinement study was therefore conducted in order to discover for which parameters the model was the most sensitive. In the following sections, the experimental campaign and the numerical analyses are presented.

8.1 Experiment

To enable full-scale cold impact testing of the door trims, a relatively large environmental chamber was necessary. In the laboratories at the R&D centre of the TME headquarters in Zaventem, Belgium, one such chamber is utilised for this type of testing. In order to investigate the variance of test results, a total of 21 door trims were tested. All tests were based on the conditions and regulations specified in the TS.

8.1.1 Test components

A representative door trim is shown in Figure 8.1. Here, all impact locations investigated during the experimental campaign at the TME headquarters are marked with a white circle and a distinct letter, respectively.

The door trims are composed of several parts and modules, including the main board, the speaker grill- and pocket module, and the arm rest module. These are partly or entirely made from injection moulded PP. However, some modules contain parts or areas including other materials, such as metal or fabric. Additionally, a styrofoam block and two pieces of felt were attached to the back of the door trim, for isolation and noise cancelling purposes. Since these parts were not included in the numerical model, and possibly contributed to additional stiffness, they were removed from all door trims prior to testing.



Figure 8.1: Impact locations investigated during the experimental campaign

The choice of impact test location is usually based on previous experience regarding what sections of the door trims that are most susceptible to fracture. Often, these regions include sudden geometrical transitions or close vicinity to boundaries or fixations, and are thus among the stiffest areas of the tested component. In this thesis, however, fairly plane regions were initially chosen to facilitate extraction of test specimens for both the uniaxial tensile- and the drop tower testing discussed in Chapters 3, 6 and 7. Additionally, these positions were believed to contribute to an accurate numerical response, as no influential irregularities were evident here. The determination of locations H and J were, however, chosen during the experimental campaign since fracture was unattainable at locations A and C from Figure 1.4. Locations H and J were based on the proximity to boundaries and abrupt geometrical

transitions, and being within the weakest region of the door trim. Location C was made substantially more flexible due to the removal of the styrofoam block, while location A was found to be less prone to fracture than locations B, H and J. Therefore, due to the limited time of the experimental campaign at the TME, emphasis was placed on locations B, H and J. Even though location J is of great interest for Toyota, being considered the weakest region of the door trim, it is also the most complex section, which significantly complicates the numerical modelling. Hence, these locations will not be given any particular emphasis during the numerical investigation.

8.1.2 Setup

In order to replicate realistic test conditions of cold impact loading on the door trim, it was mounted onto a Toyota Yaris metal door frame prior to testing. Subsequent to mounting, the assembly consisting of both the door frame and the door trim was placed on the floor, inside the cooling chamber. To ensure sufficient support for the rig, such that it could not tilt, rotate or in any other way move considerably during testing, a steel block and two foldable support pads were placed under three of the corners of the door frame. Thus, the test rig was stabilised in an approximately horizontal configuration. Figure 8.2 shows the test rig and the associated supports. It should be noted that some tests were performed on locations that are not representative for the majority of the tested door trims. This is indicated by the white circle drawn at location A on the door trim in the figure. The experimental setup is nonetheless illustrated here.

The actual testing involved dropping a steel ball at the selected locations visualised in Figure 8.1. In the TS, two different ball sizes are specified for testing of different parts and locations. These balls have approximate masses of 0.5 and 1.0 kg, respectively. Since Schwenke's work [2] showed no breakage of the door trims using the smaller ball, only the larger ball was employed throughout the recent experimental campaign. During the previous work, the ball was dropped from increasing heights until fracture was obtained, starting at a height of 100 mm. This was done based on earlier experience from Toyota, where it was assumed that repeatedly dropping of the ball on the same location of the door trim had no effect on the local material properties. Furthermore, if fracture did not occur using the smallest ball, the larger ball was utilised. However, the assumption of no accumulation of damage, possibly influencing the local mechanical behaviour of the door trims, was not investigated in the recent experimental campaign. To avoid potential accumulation, the door trims were tested only once at each location.

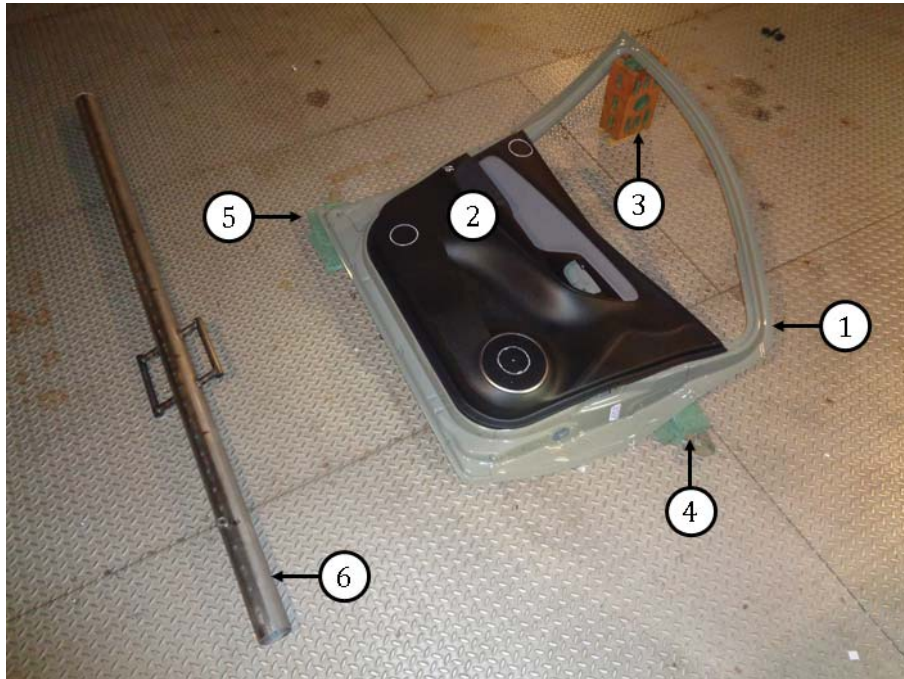


Figure 8.2: Setup of full-scale testing at TME headquarters

- ① Metal door frame, ② Door trim, ③ Steel block, ④ Foldable support pad 1, ⑤ Foldable support pad 2, ⑥ Test jig

In order to ensure accurate drop heights and locations, a test jig was provided by Toyota. The jig is shown in Figure 8.3 and consists of three main parts; a guiding tube including holes with a spacing of 50 mm allowing for different drop heights, fitted handles for easy manoeuvring, and a retaining pin which was used to hold the steel ball in place within the guiding tube at the predetermined drop height.

To further ensure good repeatability, white circular markings were drawn onto the door trims at every relevant impact location to be investigated. These markings enabled easy and precise positioning of the guiding tube before release of the steel ball. Hence, a consistent impact location was obtained for every test. The test jig allowed for drop heights of the steel ball within the range of 50 to 1 900 mm. Three people were needed in order to operate the test jig: One person ensuring that the guiding tube was correctly aligned with the marking on the door trim. One person holding the guiding tube at a small distance from the door trim, such that it was not resting against the panel. One person releasing the ball by pulling the retaining pin, allowing the ball to drop from the predetermined height.

Since the main purpose of the experimental campaign was to determine the cold impact performance of the door trims, cooling was necessary. To ensure adequate cooling, all 21 door trims and the accompanying test equipment utilised for the ex-

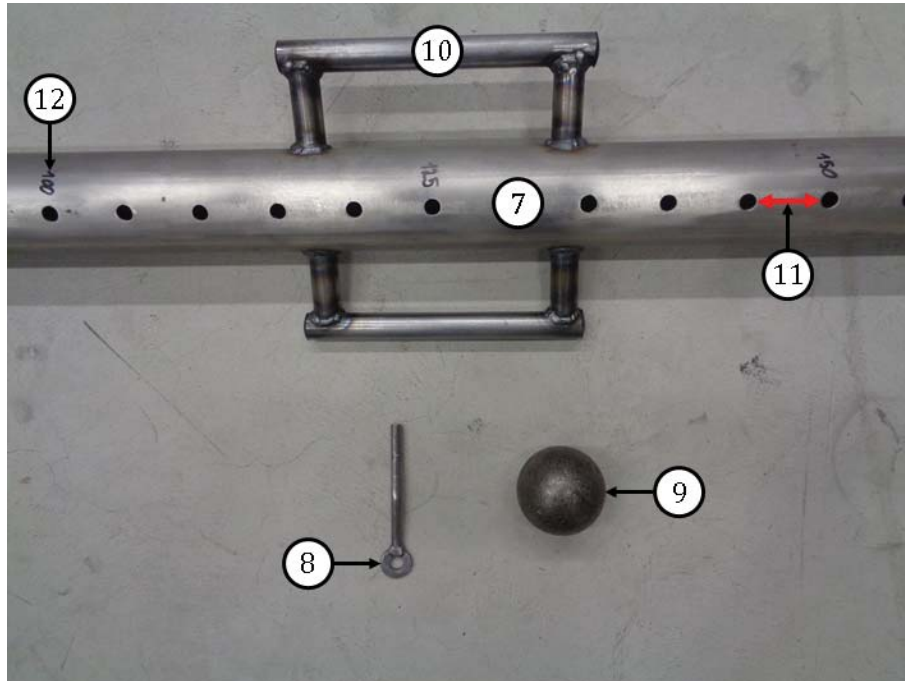


Figure 8.3: Detailed view of the test jig employed in the full-scale testing

- ⑦ Guiding tube, ⑧ Retaining pin, ⑨ Steel ball, ⑩ Handles, ⑪ Holes with 50 mm spacing, ⑫ Height measures

perimental campaign were soaked for three hours. Hence, all employed instruments and tested components were sufficiently cooled before testing. Since the associated air circulation system, providing $-30\text{ }^{\circ}\text{C}$, caused relatively windy conditions, heavy winter clothing was utilised to ensure the safety of the personnel executing the experiment. For the same reason, the time spent inside the chamber was strictly limited, and a break was taken between testing of every door trim.

8.1.3 Results

Visual results

A total of 39 representative drop tests were conducted on 14 representative door trims. An initial drop height of 1 900 mm was employed for all three relevant test locations to ensure that fracture could be obtained. In a similar way as for the drop tower tests, an iterative procedure was utilised such that the lowest drop height causing fracture could be determined. Once the drop tests were conducted, the results were noted before the next door trim was tested. The experimental data for all door trims can be found in Appendix E.

8.1. Experiment

Different failure modes were observed for each of the three test locations. For location B, fracture was exclusively found in the clip connecting the door trim to the frame. Although some stress-whitening were observed upon inspection, no signs of fracture or cracking were indicated in the panel itself. For location H, however, cracking was found in every test where fracture occurred. At a drop height of 1 900 mm, relatively large sections of the door trim were torn loose during fracture. A similar failure mode was found for the speaker grill at location J. Here, the initial drop height resulted in catastrophic fracture. Closer to the lowest fracture drop height, however, small cracks were found in the honeycomb structure on the back of the speaker grill. Little or no plastic deformation could be observed at any of the test locations, suggesting that a brittle failure mode was present in all tests.

A summary of the test results is shown in Figure 8.4 for the three test locations. Highly consistent results were obtained using the test jig. The repeatability of the experiment was facilitated by three persons performing individual tasks. Average fracture drop heights and variances found for location B, H and J are indicated in Table 8.1. The largest deviation was related to location B and corresponded to 150 mm. It must, however, be emphasised that all results displayed in Figure 8.4 are heights leading to fracture after a single drop. Hence, there is no guarantee that a lower drop height than the one related to the largest deviation would not result in fracture.

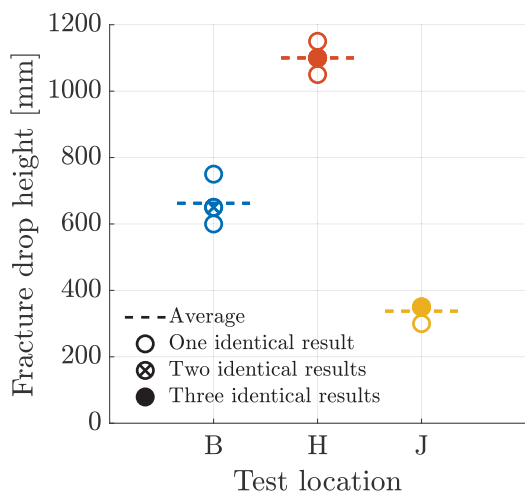


Table 8.1: Full-scale test results

	Test location		
	B	H	J
Mean [mm]	662.5	1100	337.5
Variance [mm ²]	3958	1250	625.0

Figure 8.4: Experimental results from full-scale component drop test

Compared to Schwenke’s results [2], a significant improvement was found with respect to the consistency. This could be explained by three factors. Firstly, the test jig utilised during the experimental campaign was custom made for this project,

and therefore not available during the previous work. Hence, both the impact location and drop height could be reproduced in a highly accurate fashion for each individual drop test. Secondly, only a single test was conducted for each location during this project. Even if fracture occurred or not, a new door trim was used for the next drop test. Such an approach was taken in order to prevent any damage accumulation effects, which could not be accounted for in the numerical simulations. During the previous project, however, it was believed that the material properties were unaffected by repeated dropping of the ball on the same area until fracture. Finally, the styrofoam block and the two felt cushions were removed from the back of the door trim prior to testing. Since these parts are not included in the numerical model, their influence on the experimental results was ruled out.

The production dates of the door trims were noted in order to investigate whether they had any effect on the test results. All successful drop tests are plotted in Figure 8.5. Here, the door trims are arranged according to their production dates, and the drop heights used for each respective door trim and location are indicated. The colour scheme used in Figure 8.4, is utilised here as well. It was found that the production dates ranged from approximately 2.5 years to 2 months prior to testing, while the same mould was used for all door trims. Since factors like moulding parameters could be altered over such a long period of time, it was believed that this might affect the mechanical properties of the door trims. From Figure 8.5, an initial positive correlation can be seen between the production date and fracture drop height for test location B. No similar correlation was found for the two other test locations. It should, however, be noted that fracture occurred for door trim 11, 12, and 17 at locations H and J. This suggests that these door trims might have less structural integrity than the others.

SEM results

Although the component drop test resulted in cracking for all ball drops that caused fracture at location H, some pieces of the door trim broke off during the initial ball drop. Hence, to enable comparison of the microscopic failure mechanisms for all tests conducted in this thesis, a brief SEM analysis was performed on two such pieces associated with location H on door trim 6. Similarly to the drop tower specimens, two fracture surfaces were studied in order to distinguish between possible brittle and ductile behaviour. Thus, one fracture surface on the periphery of the impact area and one fracture surface directly underneath the ball was studied.

The through-thickness fracture surface for the periphery of the impact area is shown for different magnifications in Figure 8.6. At the highest magnification, a large

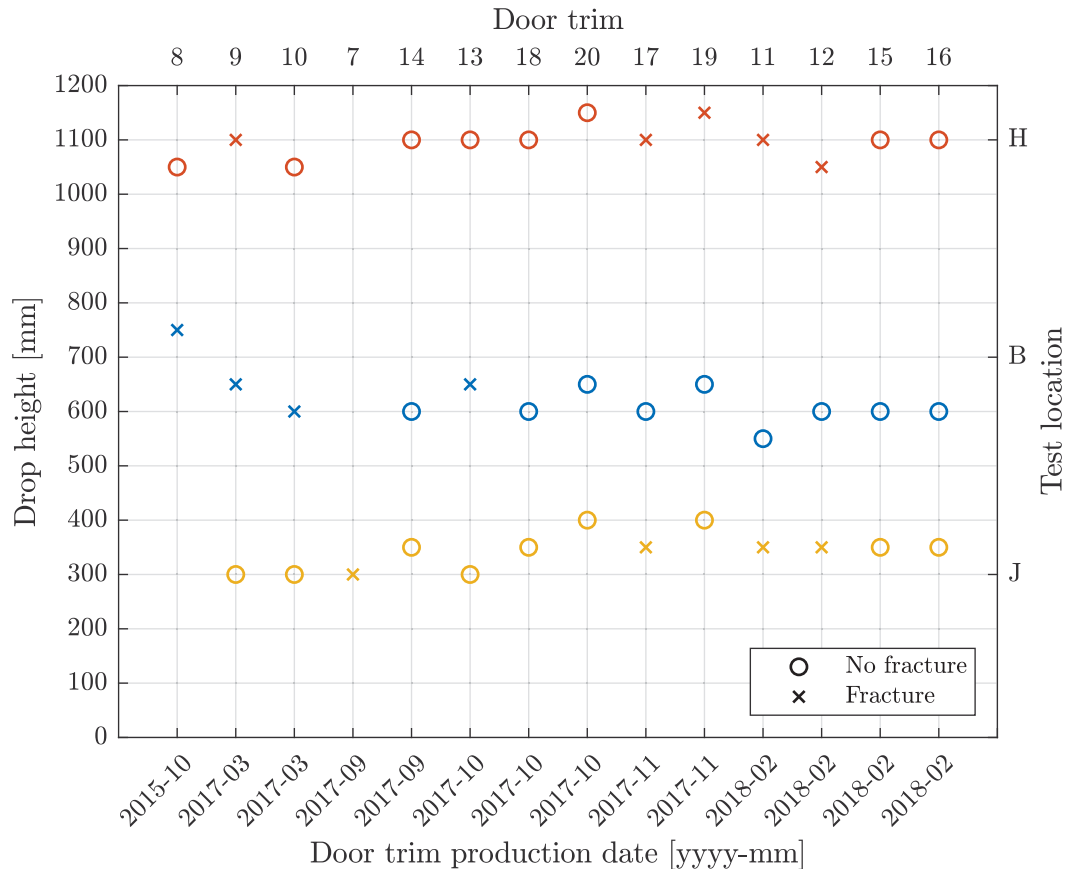


Figure 8.5: Summary of experimental data for the successful door trim drop tests

amount of cavities and some elastomeric particles can be observed and are indicated by white encircled areas. The regular shape of the cavities suggests that little deformation occurred prior to fracture. The same characteristics can be seen for the fracture surface directly underneath the ball, shown in Figure 8.7. By comparing the PP material surrounding these cavities, however, some differences were found in their morphology. The edges of the surface on the periphery of the impact area seem less sharp than those directly under the ball. This could indicate that small amounts of adiabatic heating are indeed arising due to the high strain rates resulting from the ball drop.

It should be noted that whether the crack initiates directly under the ball, or on the periphery of the impact area can not be determined with the simple experimental setup described earlier. Additionally, the two points studied here were not located a large distance apart. Hence, differences as those illustrated for the material sample plates in the drop tower, could not be detected if they were present.

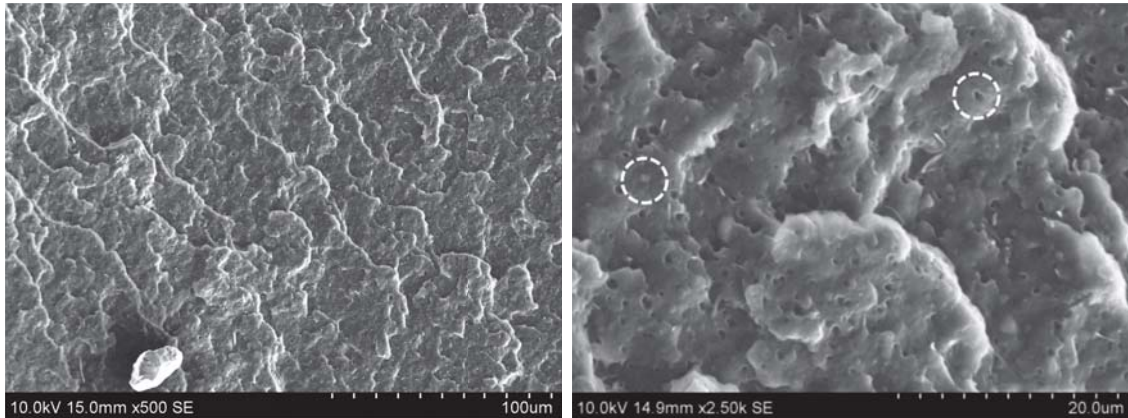


Figure 8.6: SEM micrographs of peripheral section directly under impact

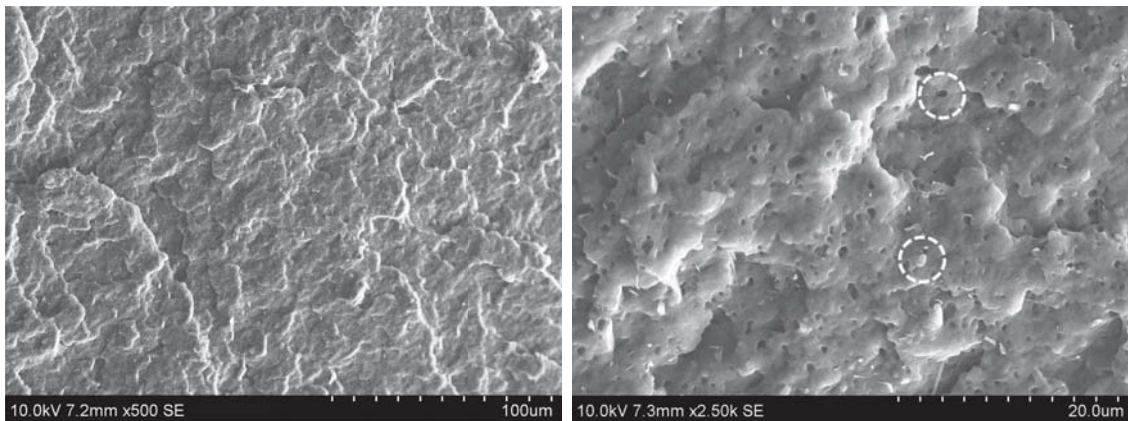


Figure 8.7: SEM micrographs of central section directly under impact

8.2 Numerical analysis

In the numerical investigation of the cold impact performance of the door trim, the explicit solver in the FEM software LS-DYNA was employed. There were mainly two reasons for this. Firstly, the convenience of adapting the same software as utilised by Toyota restricts the possibility of communicative misunderstandings. Secondly, the software and solver is suitable for modelling of this specific problem as it is developed for highly nonlinear transient dynamic FEA using explicit time integration. Furthermore, to facilitate an accurate representation the physical response of the door trim due to the inflicted impact, correct geometrical representation, suitable element- and contact formulations, and realistic boundary conditions were carefully modelled and investigated through a sequence of numerical analyses. The modelling procedure and numerical results are described in the following sections.

8.2.1 Numerical model

To enable accurate modelling, it is important to understand the physical interpretation of the designated problem, and the assumptions that are made when creating a FE model. The choice of element formulation is one important factor. If the ratio $L/t > 10$, where L is a characteristic length- and t is the thickness of the door trim, transverse shear strains become small and may be neglected [29]. In such cases, the structure is regarded as thin-walled, and shell elements may be applied with good accuracy. The Belytschko-Lin-Tsay shell element formulation is the default shell formulation in LS-DYNA. They are general-purpose quadrilateral elements that combine both membrane- and bending stiffness, and allow for transverse shear deformation. However, they should not be included in models comprising coarse meshes, as the formulation treat warped configurations in a poor manner.

The Belytschko-Lin-Tsay formulation utilises a one-point quadrature rule, i.e. a reduced integration scheme, which greatly diminish the computational cost compared to other quadrature rules [61]. As discussed in Section 2.4.3, this quadrature rule is primarily intended to increase computational efficiency. Nevertheless, the reduced shell elements are outperformed by the corresponding full integration element in cases where warping occurs due to e.g. in-plane bending, and in cases of severe hourglassing [33].

Geometry and mesh

To be able to simulate the full-scale impact of the door trim, Toyota provided a mesh file consisting of 184 404 shell elements with variable thickness including geometry data for utilisation in LS-DYNA. The door trim assembly contains three separate parts, namely the main board, the speaker grill- and pocket module and the speaker grill ring. Although these parts were modelled as PP, the speaker grill ring is in reality made of metal. Its effect was, however, assumed to be negligible because the impact load was believed to affect the local behaviour only. Figure 8.8 depicts an overview of the numerical model, including both the PP door trim and the impacting steel ball.

It should be noted that a circular local mesh refinement of size corresponding to the approximate diameter of the impacting ball was applied to the main board in the numerical basis model. This refinement is illustrated in Figure 8.9. The mesh was refined in order to better capture potential crack initiation and -propagation due to the brittle behaviour observed in the experiments. In general, more accurate results

were believed to be obtained with this refinement, as opposed to the original mesh rendered in Figure 8.8.

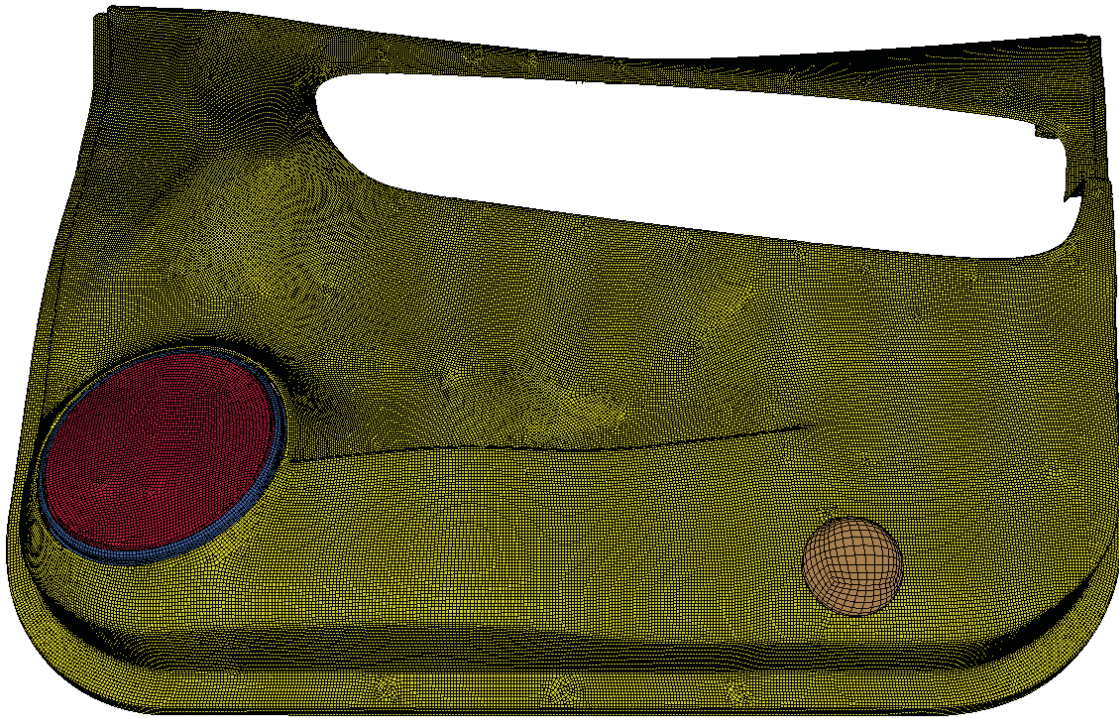


Figure 8.8: Overview of the numerical model

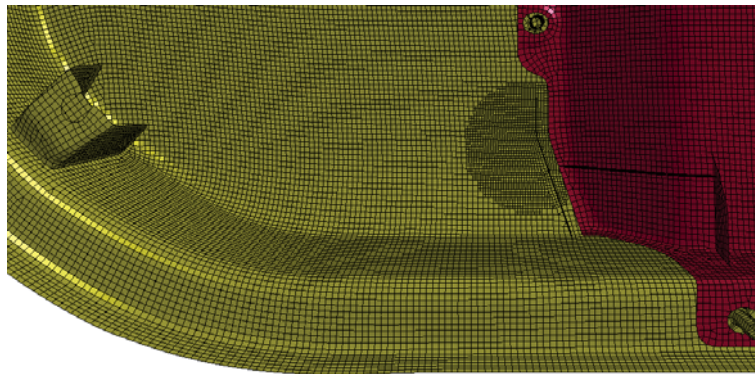


Figure 8.9: Refinement of basis model

The front and back of the actual door trim are rendered in Figures 8.10a and 8.10b, respectively. Furthermore, the numerical representations are displayed in Figures 8.10c and 8.10d. Here, it is evident that the numerical model corresponds to the passenger side of the vehicle, while the experimental campaign was performed on door trims from the driver side. However, since these door trims are identical, with the exception of having mirrored geometry, this was considered unimportant. Additionally, it is obvious that the armrest module is missing in the numerical

representation. Since only local effects of the impact load were presumed, this part was excluded and the computational cost was reduced. Due to the geometrical complexity of the speaker grill it was represented by an even plate in the numerical model. Note also that the two felt cushions and the styrofoam block were removed from the physical component prior to testing, as discussed earlier.

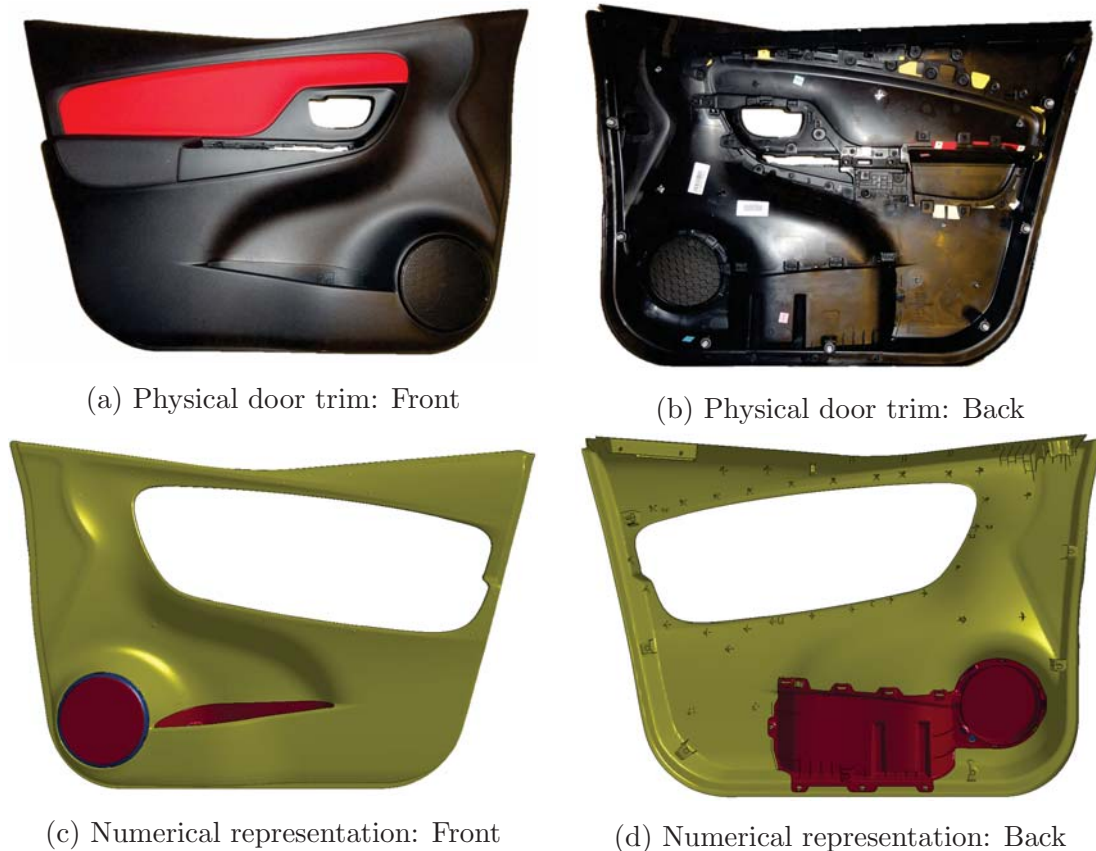


Figure 8.10: Physical door trim and corresponding numerical representation

As for the impacting ball, the numerical representation is shown in Figure 8.8. This ball was modelled with a nominal diameter of 60 mm. Hence, to obtain a total impacting mass of 1.0 kg, the density of the material was calculated to $8.842 \cdot 10^{-9}$ tonne/mm³. The massive steel ball was assumed to be rigid as its stiffness is much larger than the PP door trim. Hence, the ball was modelled using 7 000 rigid solid elements. The impact velocity, v_i , was calculated by employing conservation of energy and by neglecting drag due to air resistance and the friction during interaction with the guiding tube. The simple calculations were performed by

$$v_i = \sqrt{2g_a h}, \quad (8.1)$$

where g_a is the gravitational constant, and h is the drop height.

Boundary conditions

Definition of boundary conditions is usually one of the major uncertainties when creating a numerical model of a real life load case. When the complexity of the model increases, the boundary conditions are no longer well-defined, making it difficult to attain a realistic numerical representation. In this particular case, it was assumed that the component response is mainly local. Nevertheless, to ensure that this assumption is reliable, a study exploring both stiffer- and softer boundary conditions than those believed to occur in the experiment, was performed.

All boundary conditions and constraints that were imposed in the numerical basis model of the door trim are illustrated in Figure 8.11. Furthermore, a detailed view of the local conditions in the area of interest are shown in Figure 8.12. In these figures, the regions of the door trim that are in contact with the test rig, as well as internal connecting areas between every module of the assembly, are marked with respective colours and enclosed by the dotted outlines. The clips connecting the door trim to the frame are indicated by blue circles and *Primary clips* in the figure. Due to the geometry of these clips, only the edge of the mounting bracket on the door trim, highlighted within the blue circle in Figure 8.12, is assumed to be fixed in all translational directions. This is because some clearance and accompanying play are permitted, in reality.

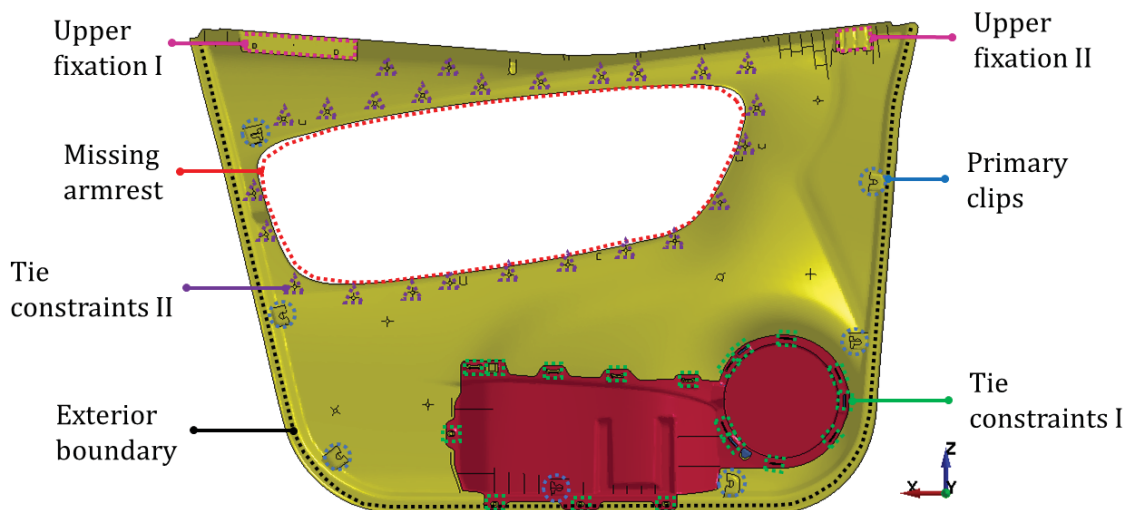


Figure 8.11: Boundary conditions imposed in the numerical model

In Figure 8.11, clips that connect the main board and speaker grill- and pocket module are marked with green rectangles and *Tie constraints I*. This is another type of clip that is coalesced through a welding process involving heat compression, which essentially means that it is melted and compressed in order to join the two modules.

It is, however, obvious that these clips are not welded in the numerical model. In an attempt to model this connection, every clip and respective counterpart were modelled using a tie constraint. This meant that all nodes in a region surrounding each clip, i.e. from both the main board and speaker grill- and pocket module, were confined to maintain their relative distance to each other.

The two regions marked with pink rectangles and *Upper fixation I* and *Upper fixation II* in Figure 8.11 were modelled as fixed in the vertical and one transverse translational direction, i.e. the y- and z-directions. This was done because the top portion of the armrest module, in reality, is fitted under the metal door frame at several locations along the top of the frame. However, the simply supported boundary conditions were applied as a best estimate. In addition, these regions were assumed to be sufficiently far away from the impact zone to affect the simulation results.

When mounting the door trims onto the frame, it was evident that its exterior edges were only in slight contact with the frame, suggesting that some leeway was allowed. Also, since there is a small flange on the outmost edge along most of the door trim boarder, the vertical- and both transverse displacements eventually experienced some resistance. However, this occurs only if the door trim moves relative to the frame. In spite of the latter possibly obstructing boundary, only the vertical translational direction was fixed in the numerical representation. Thus, the vertical displacement of all elements along the dotted black line, marked by *Exterior Boundary* in Figure 8.11, were fixed. Although the displacement was fixed in the vertical direction in the numerical model, the possibility of moving transversely along- and vertically away from the frame was nonetheless present in reality.

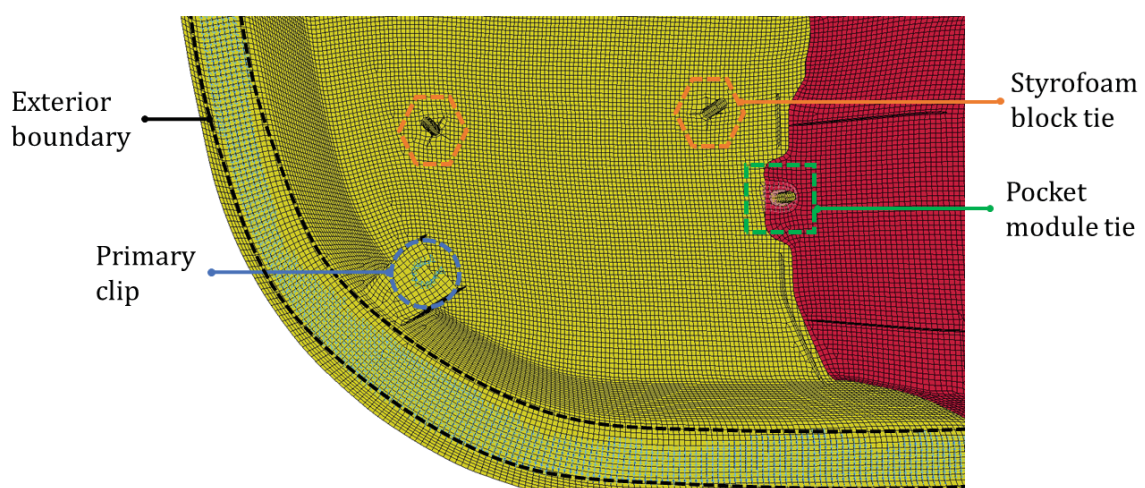


Figure 8.12: Detailed view of the boundary conditions in the area of interest

To account for the missing armrest module of the numerical model, similar tie con-

straints as those defined for the connection of the main board and the speaker grill- and pocket module were applied to the cylindrical pins marked with purple triangles and *Tie constraints II* in Figure 8.11. For the physical door trim, these pins join the two modules, through the same welding process as described above. Thus, to represent this, and the armrest module itself, tie constraints were applied. Once again, the relative displacement of a selection of nodes associated with the pins were confined. Hence, by constraining the corresponding nodes for every pin, the missing armrest module was recreated in the simulation by means of a close to rigid module transmitting loads over the area marked in red and by *Missing armrest* in Figure 8.11.

Several redundant cylindrical pins, like those marked by orange hexagons in Figure 8.12, are present in the numerical model. They are not subjected to any constraints and are assumed to be insignificant for the simulation results besides contributing with some minor local stiffness effects.

Contact formulation

The automatic, general purpose, surface-to-surface contact algorithm incorporated in LS-DYNA was employed in the numerical simulations. This contact formulation is simple yet robust and generally recommended for most explicit crash- and impact simulations [36]. Because the average element size was larger for the impacting ball compared to the door trim, it was selected as master surface while the door trim was chosen as the slave surface. This was done in order to avoid problems where nodes penetrate surfaces during contact [29]. Since the numerical representation of the door trim contains three parts, the same contact formulation was employed for self-contact within the assembly as well.

When the contact formulation was properly defined, friction was the next important entity for a realistic representation of the assigned problem. All surfaces were given the same static- and kinetic coefficient of friction, i.e. $\mu = 0.1$. This included the contact surfaces between the steel ball and the PP main board, as well as between all parts of the door trim assembly. This value of the coefficient of friction was employed based on the results from the sensitivity study of the drop tower tests, discussed in Section 6.3.5.

Strategy and means of comparison

Validation of the numerical model of the door trim is related to large uncertainties. Two of the main reasons for this is the limited experimental data attained through the full-scale testing, and modelling of an intricate loading situation of a complex part like the door trim. Hence, the results obtained in the numerical simulations are questionable as it is not known whether the model manages to properly represent the physical experiment.

In order to establish a structured means of comparison, a basis model was created based on the assumptions and restrictions described in the preceding sections. As observed from the experimental results, the material behaviour was found to be highly brittle. Hence, the material recalibration and the inverse modelled fracture criterion from Chapter 7 was utilised.

The only data acquired from the experimental campaign was the largest average drop height causing fracture in the door trims. Hence, a simple yet appropriate measure is the residual velocity, v_r , just before initiation of fracture, i.e. at the instant for which the first element is eroded from the numerical model. Whenever the door trim did not break, however, this method failed to produce comparable results. Thus, it was only applicable for simulations where fracture of the door trim occurred. A requirement for the method to provide reasonable results is that the elements erode during loading. On the contrary, if elements erode during unloading, i.e. during rebound of the ball, it is presumed that fracture did not occur. This choice is related to the complexity of representing unloading in a numerical simulation. Because the results obtained during rebound are inaccurate and unreliable, and since the criteria given in the TS only consider whether the part breaks or not, unloading effects are justifiably omitted as a basis of comparison.

8.2.2 Results

Despite all efforts exploring different aspects of the numerical representation, reproduction of the experimental behaviour, and thus a valid numerical model, could not be obtained. No signs of fracture were found when the experimental drop heights were used, suggesting an overestimated flexible- and ductile response of the numerical representation. The opposite was found during Schwenke's work [2], where the inverse modelled damage parameter resulted in a behaviour that was overly brittle. Since the recent numerical results did not comply with the experiments, no sensitivity study was conducted. Instead, a different approach was taken in order

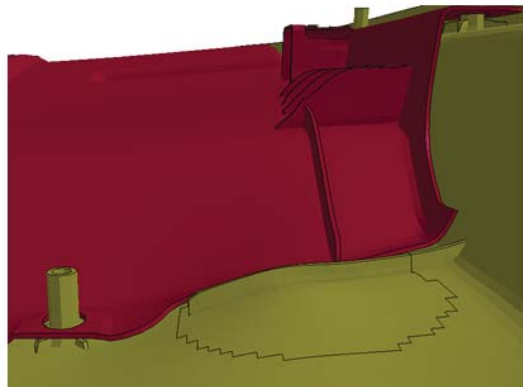
to investigate the possible reasons for this discrepancy. The ultimate goal of the comprehensive numerical study, discussed in the following section, was not to accurately predict the experimental drop height at fracture, but rather to establish the influence of different parameters. It was believed that any trends, with respect to these effects and the assumptions that were utilised, could be valuable for more accurate modelling of the full-scale component drop test.

Refinement of contact

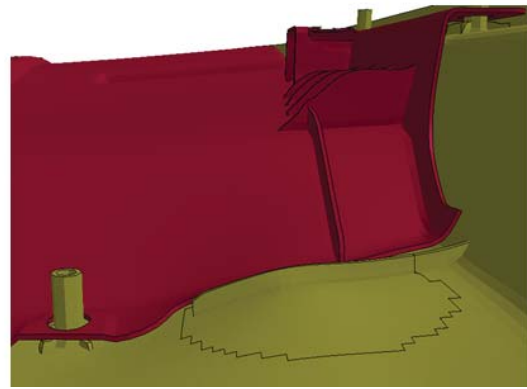
Initially, the failure mode observed in the simulations did not resemble that of the experimental tests. In the numerical representation, fracture was found in a stiffening structure underneath the impact zone on the back of the main board, and not in the panel itself. It was believed that this mechanism was caused by sliding of the pocket module along the surface on the back of the main board during impact. Due to this, the pocket module imposed a transverse load onto the stiffener, resulting in element erosion. This phenomenon is highlighted by white circles to the left in Figures 8.13a, c and e. The black line surrounding the stiffening structure in the figure marks the boarder of the local mesh refinement. Erosion of elements occurred exclusively in the stiffener, even for elevated drop heights. Although the wrong failure mode was triggered, no fracture was found for drop heights below 3 000 mm. This suggested that the numerical model was unable to produce comparable results to that of the experiments, since both drop height and failure mode are completely different for the two cases.

In order to obtain more reasonable numerical results, one attempt was to remove the stiffener from the contact between the main board and the pocket module. There were mainly two intentions for this effort. Firstly, because the basis of comparison was defined at first element erosion in the numerical model, and since this occurred in the stiffener, it should be avoided. Secondly, the fracture that occurred in the stiffener was believed to possibly affect the behaviour of the main board panel itself, subsequently causing inaccurate results. This method is obviously not correct, and incorporates a nonphysical phenomenon where the pocket module penetrates the stiffener. It was nonetheless attempted in order to obtain the correct failure mode of the door trim in the simulation. The resulting penetration is rendered to the right in Figures 8.13b, d and f, and indicated by white circles.

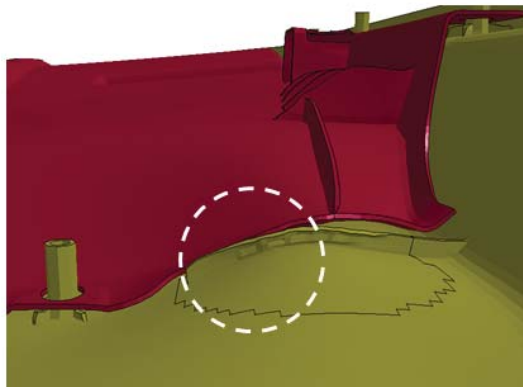
When the stiffener was excluded from the contact, new simulations showed a substantial reduction in stress levels. In spite of the new contact definition, fracture did not occur for heights below 6 750 mm, where one single element was found to erode during loading of the door trim. Thus, the capacity was overestimated by a



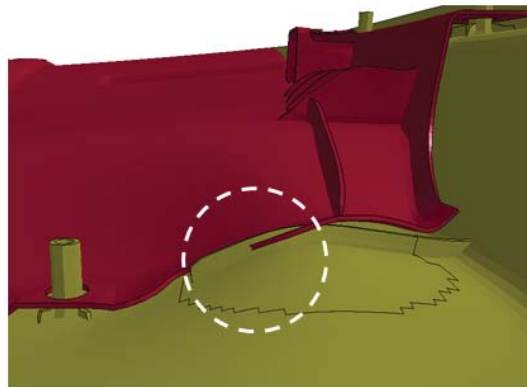
(a) Transverse loading, $t = 1.0$ ms



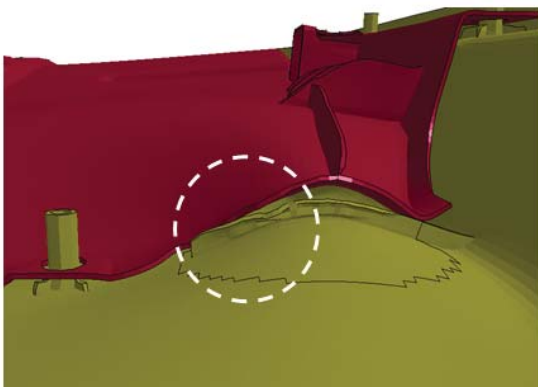
(b) Penetration, $t = 1.0$ ms



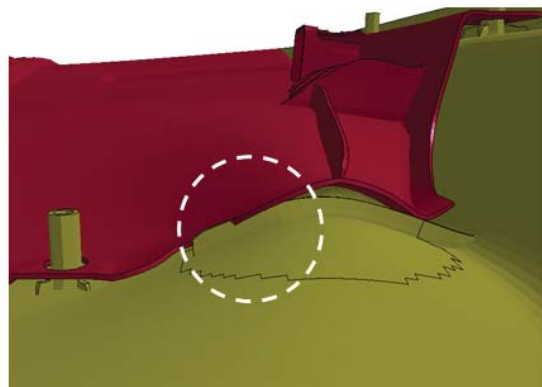
(c) Transverse loading, $t = 2.0$ ms



(d) Penetration, $t = 2.0$ ms



(e) Transverse loading, $t = 3.0$ ms



(f) Penetration, $t = 3.0$ ms

Figure 8.13: Comparison of the two contact definitions

factor of six. However, the fracture occurred in the pocket module, meaning that the incorrect failure mode still emerged. Note that only the recalibrated version of the SPM was simulated at this point. Nevertheless, this contact definition was

employed throughout the rest of the numerical analyses in this section in order to avoid fracture in the stiffening structure.

Material model

In order to investigate whether the SPM was capable of describing the behaviour of the component test, two sets of different material calibrations were studied. Furthermore, the material's sensitivity to changes in the viscoplastic parameters and their influence on the behaviour of the numerical model was also explored. The three material calibrations, i.e. both versions of the SPM and the alternative model, were introduced in Chapters 2 and 7, respectively. The ultimate goal of the brief investigation was to check whether alteration of the material model influenced the door trim simulation. Another interesting consideration was whether the numerical model of the door trim produced consistent results compared to those obtained in the simulations of the uniaxial tensile- and drop tower tests.

Three identical numerical models, each assigned with different material representations, were simulated. The velocity-time curves of the ball are plotted for each material calibration in Figure 8.14. It is evident that the only simulation exhibiting fracture, marked by a cross in the figure, was the recalibration of the SPM. By studying the slope of the velocity-time curves, an interesting observation is that the ball appears to exhibit a slightly softer response, i.e. more gradual slope, for the old calibration of the SPM than for the two other calibrations. Furthermore, the lower residual velocity subsequent to rebound of the ball indicates that more energy is dissipated during the impact. Hence, the old calibration of the SPM absorbs more energy than the two other material representations. A similar trend is also seen for the new calibration of the SPM compared to the alternative model. These results could be explained by Figure 7.16, where the same tendencies are found.

The stress levels obtained in the simulations corresponded to the tendencies found in Chapter 7. the old calibration of the SPM produced significantly lower stresses than both the recalibrated version of the SPM and the alternative model. For the latter calibration, the maximum equivalent stress was found to be just over 174 MPa. In contrast, the corresponding measure obtained for both new- and old calibration of the SPM reached just over 120 and 68.4 MPa, respectively.

None of the three models exhibited fracture at any of the drop heights tested in the experiments. In fact, no fracture was found for drop heights below 6 750 mm in these simulations either. However, erosion of elements during loading only occurred for the new SPM calibration. For the same drop height, the numerical models employing

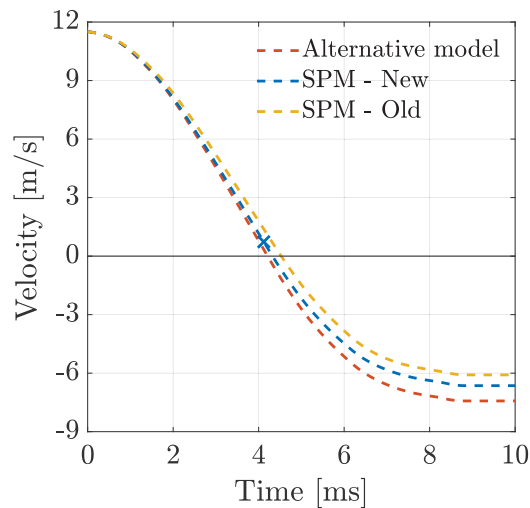


Figure 8.14: Comparison of different material models

the old calibration of the SPM and the alternative material model both fractured during unloading. Nevertheless, based on what was stated earlier, this ultimately meant that no fracture was assumed to occur for the two latter simulations.

The fact that the alternative model does not result in fracture during loading could be explained by the Cowper-Symonds viscoplastic relation. Since the velocity and subsequent strain rates found in the component simulation were higher than those obtained in the simulation of the drop tower test, overestimated yield stresses could transpire into underestimated plastic strains. Consequently, an overestimated ductile response might lead to large elastic deformations and no consecutive fracture. This result also explains the notably lower energy absorption of the alternative model relative to the other material calibrations. The opposite, however, is seen for the old calibration of the SPM, where underestimated yield stresses allow for more plastic straining. Since the critical damage parameter is larger than for the new calibration of the SPM, the door trim is permitted to undergo more plastic deformation and absorb more energy before fracture.

Neither the old calibration of SPM nor the alternative model were investigated further in the following numerical analyses. They were excluded because these representations showed the least promising results with respect to onset of element erosion. Furthermore, based on the observations in Chapter 7, it was believed that they under- and overestimates the stress levels that were expected in the experimental tests.

Impact locations

By use of the test jig described earlier, accurate impact locations and subsequently consistent results were obtained in the experimental campaign. However, in an attempt to achieve a more realistic failure mode, different impact locations were investigated. Figure 8.15 displays the different positions, marked with white circles. The initial representation of the impact location, i.e. location I, was assumed to correspond to position H illustrated in Figure 8.1. However, to investigate whether small variations in impact location could produce more realistic results, three additional positions were suggested. With reference to the coordinate system given in the figure, Table 8.2 lists the translations relative to location I. It should be noted that this method is not representative for the experiments, but serves as an attempt to model more realistic fracture. The impact locations and increased drop heights simulated in this section deviate considerably from what was employed in the experimental campaign.

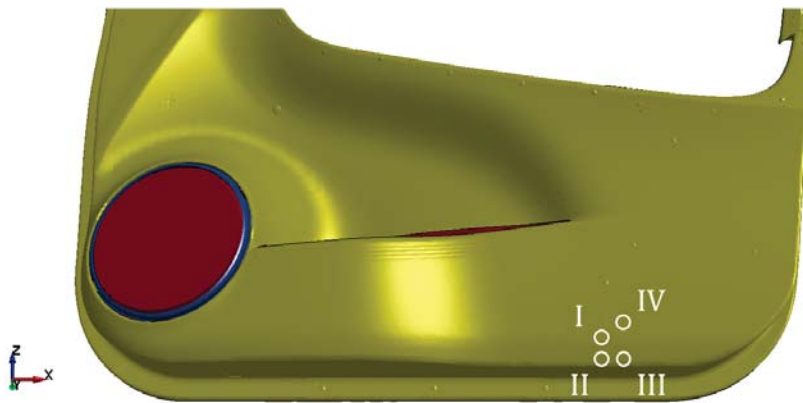


Figure 8.15: Variation in impact location

Table 8.2: Different impact locations relative to position H

Impact location	Translation in	
	x-direction [mm]	z-direction [mm]
I	0	0
II	0	-20
III	20	-20
IV	20	20

The results obtained at location IV did not resemble the experimental results due to extensive flexing of the door trim. Locations II and III, however, showed more promising results with respect to the failure mode. In these simulations, somewhat

higher stress levels in the stiffer region of the panel enabled cracks to develop and propagate along the edge of the door trim. This resembled the failure mode that was found in the experiments. Figure 8.16 shows a sequence of pictures displaying the crack propagation that occurred at location III with a drop height of 6 750 mm during impact. Note that the ball is concealed in the figures such that the crack can be better visualised.

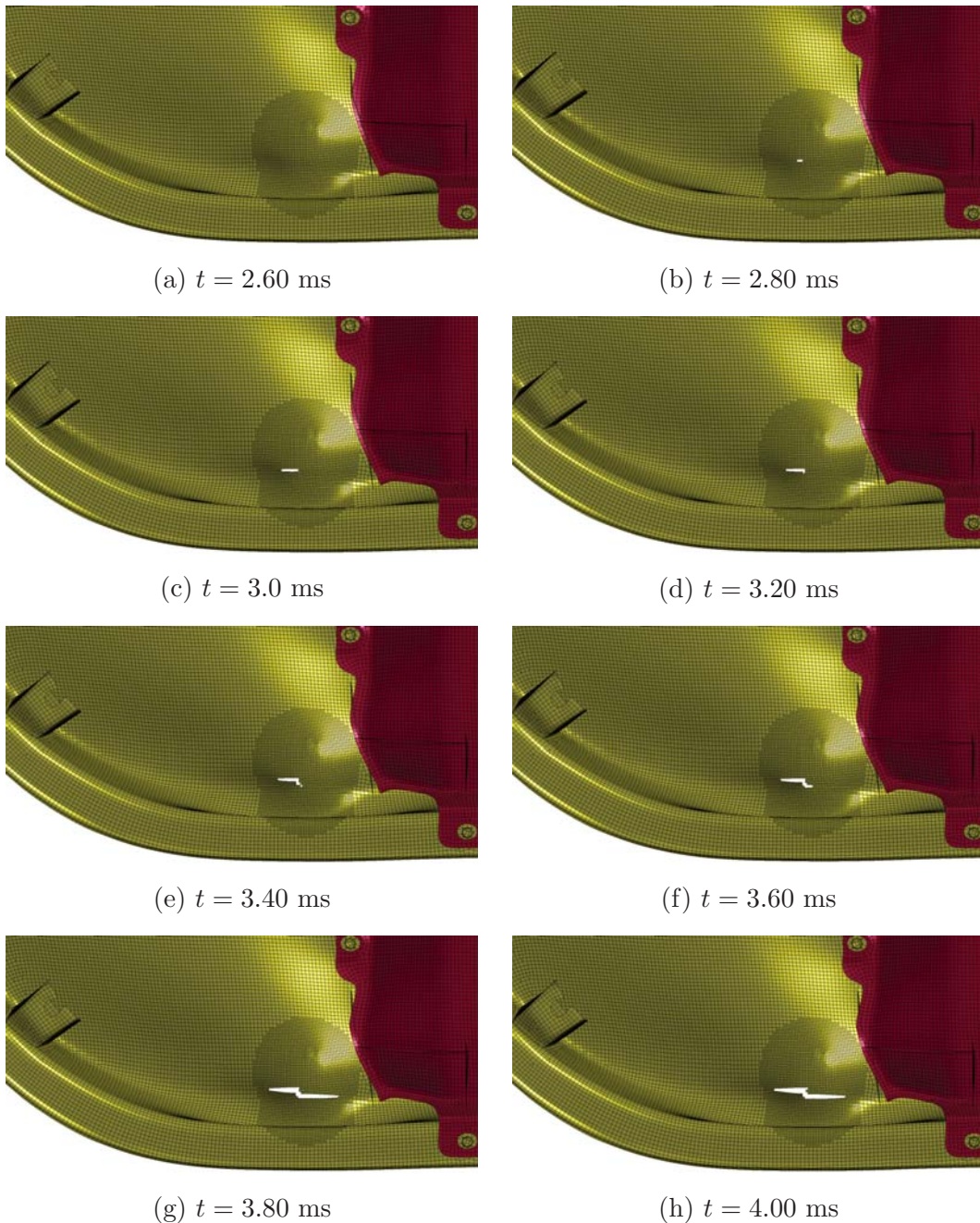


Figure 8.16: Crack propagation at location III

Since location II was affected by the pocket module, only location III was utilised

in the further investigation as this showed the most promising results. Numerical simulations of different heights were conducted in order to determine the ballistic limit of the model. The procedure is shown in Figure 8.17. Here, the ballistic limit curve is rendered with respect to different drop heights and associated velocities extracted at the onset of element erosion in the numerical model. Note that all simulations that did not result in fracture are set to zero velocity. No fracture was found for drop heights below 6 500 mm. However, since no drop heights between 6 250 and 6 500 mm were simulated, and because the response attained at the latter drop height only resulted in erosion of eight elements, the ballistic limit of the door trim was expected to be somewhere in between the two.

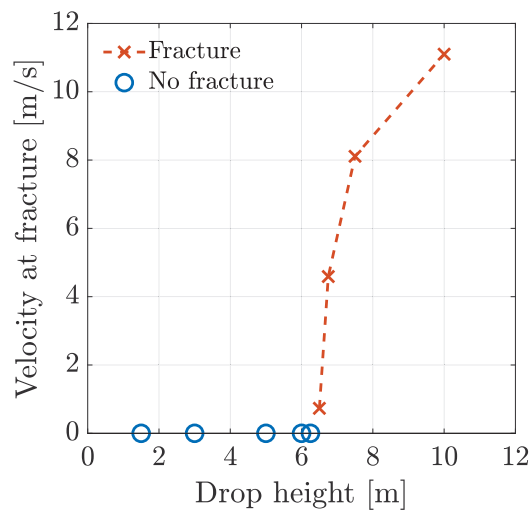


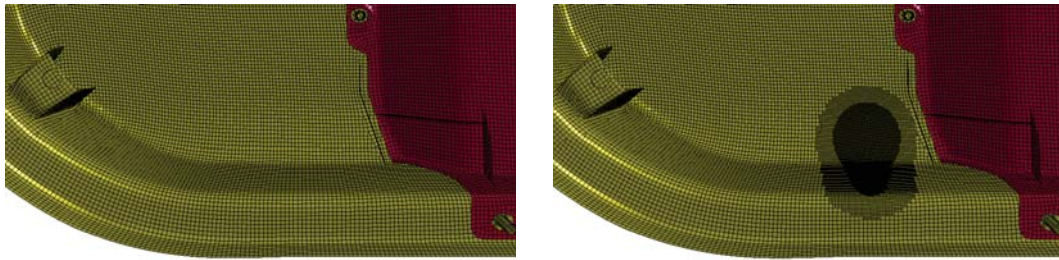
Figure 8.17: Ballistic limit curve for numerical model at location III

Even though the drop height and impact location did not mirror those found in the experiments, a resembling failure mode was nonetheless obtained in the numerical results. This suggests that the model is capable of representing the failure mode indicated by the experiments.

Local mesh size and element formulation

In general, a finer mesh provides more accurate results in numerical simulations. Therefore, different levels of mesh refinements were studied in order to evaluate the effect of initiation and propagation of cracks. This refinement was, however, only performed locally, such that the computational time of the simulation was kept adequately low. Three different mesh sizes were investigated, corresponding to average element lengths of approximately 2.00, 0.500 and 0.125 mm. Note that the average element length of 0.500 mm is equivalent to the mesh size that was used in

the basis model, illustrated in Figure 8.9. Furthermore, the coarse mesh, with an average element length of 2.00 mm, corresponds to the original model provided by Toyota. In the finest mesh, another local refinement was performed, such that the average element length became 0.125 mm. The two latter meshes are rendered in Figures 8.18a and 8.18b, respectively. Additionally, since the model is too complex for simulation with solid elements, only full- and reduced integration shell element formulations were compared.



(a) Mesh size: 2.00 mm

(b) Mesh size: 0.125 mm

Figure 8.18: Different local mesh sizes in the impact area

Figure 8.19 shows the velocity-time curves of the ball associated with the results obtained with each mesh size. For the coarser mesh, no fracture occurred, suggesting that the strains were sufficiently smoothed over the element planes in the impact area such that no erosion occurred. Fracture was, however, found for the two finer meshes, marked with crosses in the figure. The time before erosion of the first element was 2.04 ms for the finest mesh compared to 2.68 ms for the mesh size of 0.500 mm. Furthermore, the velocity of the ball at onset of fracture was found to be 7.10 m/s for the former, while the same measure was 4.59 m/s for the latter. Additionally, by studying the slope of the curves, a slightly steeper velocity-time curve is observed for the coarse mesh, suggesting that a somewhat stiffer response is caused since no element is eroded. As expected, a better representation of the crack propagation was found by refining the mesh size in the numerical model. The stress concentrations seemed more accurately described for the finer meshes, compared to that of the coarse alternative. This is because the values of the strains and stresses emerging within every element is being interpolated between each nodal value. Hence, in the finer meshes, the localised nature of fracture is better represented than for a coarser mesh.

By simulating the same numerical model as the one used for the mesh size of 0.500 mm, but employing full- rather than reduced integration shell elements, it was clear that crack initiation and -propagation were better captured. Notable differences were found in time before first element erosion and corresponding velocity. Figure

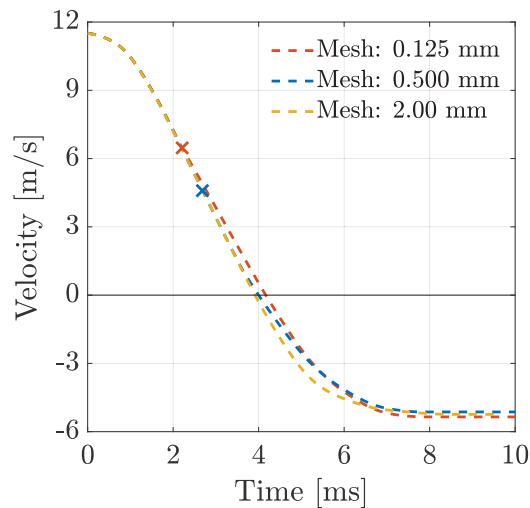


Figure 8.19: Comparison of different mesh sizes

8.20 shows the difference between the simulation results where full- and reduced integration were employed. Their respective points of fracture are marked as crosses in figure also here. The time before element erosion for the full integration element formulation was found to be approximately 2.08 ms. This is more than 22 % lower than for the reduced alternative. Furthermore, the corresponding velocity of the ball at fracture was 6.91 m/s, which implies an increase of more than 50 % compared to the reduced integration element. An interesting observation is that almost identical results were obtained from the model employing full integration and the model with the mesh size of 0.125 mm. Only negligible differences were found in velocity just before fracture, corresponding time and even residual velocity of the ball subsequent to rebound for the two simulations. The stress levels, however, were found to be somewhat lower for the model employing full integration elements, compared to the one with the finest mesh. Nevertheless, they were higher than what was found for the identical model employing reduced integration. The similar results obtained for the model employing full integration and the model with the finest mesh employing reduced integration was not unexpected. As the difference in mesh size is a factor of approximately four, and since the same factor is found in number of integration points between the full- and reduced integration elements, it is obvious that roughly the same number of integration points are present in the area of interest.

By means of comparing the performance of the separate numerical models, their respective computational times were evaluated. Regarding the computational times for the three different mesh sizes and the different integration schemes, it is obvious that the finest mesh and the full integration elements are the most expensive. The coarse mesh was clearly the least demanding alternative. The model using a mesh

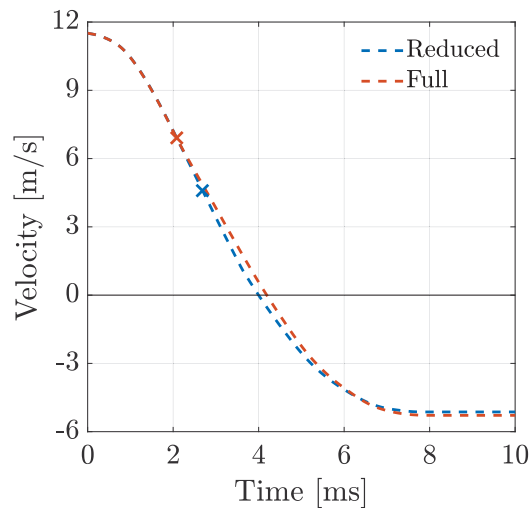


Figure 8.20: Comparison of full- and reduced integration

size of 0.500 mm mesh, on the other hand, showed an increase in computational time of just 9 % compared to the unrefined model, while still being able to represent the crack development and propagation more accurately. The model with the finest mesh, yielded a computational time that was more than 52 % higher than that of the coarse mesh. This increase is quite significant as only localised refinements were conducted. However, the finest mesh captured the crack initiation and -propagation even better.

Although the results obtained from the model using the finest mesh and reduced integration, and the intermediately refined model employing full integration elements were virtually identical, their respective computational times were not. The computational cost of the model employing full integration was almost 250 % higher than that of the model with the finest mesh. Hence, with respect to the performance of the numerical model, local mesh refinement is the preferred choice in this particular case.

Other considerations

In addition to the parameters described in the preceding sections, several other measures may influence both the reliability and accuracy of the simulation results. Such considerations could highlight possible sources of error related the numerical representation. These were investigated briefly, and are discussed here:

- **Boundary conditions:** In order to rule out any significant effects of the boundary conditions, both stiffer and softer representations than what was

described for the basis model were investigated. The most interesting result was that the stiffest configuration provoked fracture somewhat earlier in time than what was seen for the soft- and intermediate configurations. Additionally, it became evident that the velocity of the ball at first element erosion, the associated residual velocity subsequent to rebound and the stress levels within the component increased with stiffness of the boundary conditions. These results are believed to be related to the softer configuration being prone to substantial elastic flexing, while slightly more restricted deformation was seen for the stiffest configuration. This suggests that the intermediate configuration, employed in the basis model, was somewhere between the two. However, only small differences were found between the three configurations, which is analogous to the results obtained by Schwenke during the previous work [2]. Hence, the large deviation in experimental- and numerical results could not be explained by the definition of boundary conditions.

- **Friction:** In general, little influence was found by altering the coefficient of friction, even when it was entirely excluded. Nevertheless, by increasing the friction between the ball and the main board, somewhat lower stress levels and velocities of the ball at fracture were obtained. However, for the highest value of the coefficient of friction investigated, i.e. $\mu = 0.5$, the velocity at fracture and the residual velocity subsequent to rebound increased slightly compared to that of that of the intermediate value. Thus, an almost opposite behaviour compared to what was seen in the sensitivity study in Section 6.3.5 was found for the component simulations. The ball and main board are in contact over a larger area during impact, suggesting that the effects of friction could be more pronounced in this particular case. However, since the results obtained from the simulation of the component drop test are questionable, no deduction can be drawn by these tendencies. Note that by altering the coefficient of friction with respect to the self-contact, only negligible differences were found.

Inverse modelling

In order to reproduce more realistic results, the critical damage parameters, i.e. D_c , of the new calibration of the SPM was altered. However, it should be noted that the failure mode resulting from this approach was not comparable to the one seen in the experiments. Moreover, if the impact location is changed, the result may transpire into premature fracture of the numerical model, and possibly cause fracture in the simulations although no such observation was found in the experiments.

Since the ballistic limit of the door trims corresponded to a drop height of approx-

imately 1 100 mm in the experiments, this drop height was also utilised during the inverse modelling investigation. For the recalibrated SPM, the most promising results were obtained with $D_C = 0.143$. Here, two elements were eroded during loading of the door trim, whereas one additional element eroded during unloading. All of which were found in the main board, directly underneath the ball. Fracture occurred at the instant the ball was decelerated to zero velocity, i.e. after 4.44 ms. Hence, the simulation provided a result that was exactly on the ballistic limit.

In order to verify that this value of D_C really yields a ballistic limit drop height of 1 100 mm for the numerical model, a drop height of 1 050 mm was simulated as well. The results showed no fracture during loading. However, a total of two elements eroded from the main board during unloading. The first element eroded only 0.150 ms subsequent to onset of rebound, when the velocity of the ball was -0.213 m/s. This suggests that the numerical model almost fractured during loading.

By aiming for the predetermined experimental result, possible misrepresentations of the numerical model might be concealed by the inverse modelled damage parameter. Thus, care must be taken when employing the result found in this section.

8.3 Discussion

Material models and calibration

By use of the newly acquired test jig, and since only one drop test was conducted at each location of the door trim, the consistency of the results was significantly improved in comparison to Schwenke's work [2]. The results obtained in the experimental campaign on the component, indicated a brittle failure mode. This brittle material behaviour was confirmed in a SEM analysis, where a clear resemblance was found with the fracture surfaces observed for the SHTB test specimens.

Two different material models were investigated in the numerical analyses of the full-scale component drop test, i.e. the SPM and the alternative model. Even though the SPM was able to accurately describe the behaviour of the door trim material at lower strain rates, one limitation of the model is that it is developed for ductile polymers. The ductile behaviour, which is present in the quasi-static and meso-dynamic strain rate regimes, was well-captured by the material model. However, its suitability for modelling of brittle behaviour is questionable. The strain rates that occurred in the door trim were estimated to be dynamic. Therefore, based on the findings in the numerical analyses, the material model appears to be

inadequate in this particular case. Also, a deficiency of the SPM is that the damage parameter is not dependent on strain rate. Hence, the brittle-ductile transition that was discovered in the different experimental test campaigns conducted throughout this project, could not be described by the material model. Despite the fact that the alternative model could represent the strain rate dependency of the strain at fracture, overestimated stresses and subsequently underestimated plasticity meant that this model was unable to realistically represent the experimental findings.

The fracture parameters used in the full-scale component simulation were based on an inverse modelling approach from a drop tower impact test. This approach was attempted, since conditions such as strain rate and stress state were believed to be similar for the two experiments. Additionally, the uncertainties associated with the strains obtained in the SHTB tests were likely to produce incorrect numerical results. However, the validity of this procedure relies on the test conditions being similar. Even though the drop tower testing resembles the full-scale component testing to some extent, clear differences were evident with respect to specimen- and component response. It could also be argued that the imposed load conditions in the two cases are different. Whereas the boundary conditions were well-defined in the drop tower, they were far more complex for the component test. Furthermore, the span for which the specimen was allowed to deform in the drop tower tests was only 80 mm at maximum. The corresponding span for the door trim, between two or more nearby fixations, is much larger, allowing for substantial elastic bending and flexing of the door trim. Although this behaviour was indicated in the numerical model, a stiffer and more brittle behaviour was suggested from the experiment.

Instrumentation

It could be argued that the lack of instrumentation associated with the component drop test, translates into large uncertainties with respect to the failure mode. Where and when the crack initiated in the experiments was unclear, making the attempt of replicating the failure mode in the numerical model questionable. Additionally, the amount of plastic deformation occurring in the component drop test was challenging to determine, with no recordings available. The fracture parameters employed in the simulations assume a substantial amount of plastic deformation prior to fracture. However, the visual inspection of the door trims, subsequent to the experimental tests, signified that no such plasticity was present in reality. This was also suggested by the SEM analyses performed on the debris material taken from the door trims during the experimental campaign at TME, since a fracture surface similar to that of the SHTB test specimens was found here.

Mesh size, element formulation and software

When creating an FE model, the element formulation and mesh size are important parameters. However, it is important to decide whether accuracy, computational efficiency or a combination of the two, results in the desired performance of the model. Furthermore, the different element formulations might introduce distinctive and unrealistic behaviour due to e.g. locking effects or undesirable deformation modes, as discussed in Sections 2.4.3 and 2.4.4.

In general, the aspect ratio of a shell element should be defined such that the characteristic element length is more than three times its respective thickness in order to ensure accurate results. In this case, however, accurate results become unattainable if the mesh was too coarse. The average element size in the original mesh file was just below 80% of the averaged shell thickness. This violates the recommended aspect ratio. Hence, it might be argued that the predominant bending in the numerical representation could give rise to inaccurate results if the aspect ratio is below the limit for which the element formulation is based. However, whether the results are reliable when employing smaller element sizes greatly depends on the load conditions. Care should nonetheless be taken when significant refinement of shell elements is conducted. In order to reduce the smoothing of strains within the elements, and thereby better capture the crack initiation, only finer meshes were investigated in this thesis. Also, since warping may be an issue for the Belytschko-Lin-Tsay reduced integration shell element formulation [33], adequately small elements are necessary in order to obtain accurate results.

A drawback using shell elements is possible contact problems occurring as the element size becomes small. Since the contact thickness is unable to exceed the surface edge length, it is automatically reduced in Abaqus/CAE when the element size becomes small [35]. A direct consequence is that contact is delayed, which may lead to corrupted results. In Figure 6.26a, a slight horizontal shift of the curves are indicated for finer meshes. Hence, this suggests that delayed contact may occur in the simulations of the drop tower tests. In LS-DYNA, however, such automatic scaling is not done in the two-way surface-to-surface contact algorithm employed for this particular case [36]. Thus, the contact thickness is set to the defined shell thickness, and accurate results are still obtained. Even though the two softwares differ at this point, the effect on the results obtained in the sensitivity study of the drop tower tests are believed to be negligible compared to the otherwise large discrepancy between the numerical- and experimental results.

Although reduced integration shell elements were employed for the numerical mod-

els in both FEM softwares utilised in this project, their formulations are slightly different. The S4R and the Belytschko-Lin-Tsay shell elements are general purpose, quadrilateral elements employing reduced integration. Thus, both formulations have four nodes, each with six global degrees of freedom, and one integration point over the element plane. Furthermore, to obtain accurate results in bending, five integration points were utilised over the shell thickness in both softwares. However, the default number of integration points that must fail in order for the element to be eroded is different in Abaqus/Explicit and LS-DYNA. Whereas all through-thickness integration points must fail before onset of element erosion in the former, a more brittle failure mode should be obtained in the latter, where elements are eroded as soon as one integration point has failed. However, through the numerical study of the component test, it became clear that the opposite occurred. This could be explained by a larger amount of flexibility and subsequently more elastic deformations in the component test. In this thesis, fracture was defined as the instant for which the first element erodes in the simulation. Hence, since this number could not be altered in Abaqus/Explicit, the occurrence of failure in the first integration point was highlighted in the simulations of the drop tower tests.

The main disadvantage by utilisation of hourglass control is that the algorithm imposes artificial energy to the numerical results. To completely eliminate hourglassing, and to obtain more accurate results, fully integrated elements could be employed in the model, but at the cost of higher computational times. In the case of reduced integration, it turned out that the artificial hourglass energy in the system was much smaller than the internal energy. According to the Abaqus/CAE documentation [35], artificial strain energy should be negligible compared to the internal energy of the system. No exact value has been found for this requirement, but it is believed that the obtained ratio of 0.1 % should be well within the recommended limit. Hence, sensible results were ensured.

As discussed in Section 2.4.4, there are two common hourglass control algorithms, one viscosity- and one stiffness based. Since the former is the default type in LS-DYNA despite the latter is more efficient in restricting the arising spurious modes, the result from both algorithms were compared. Figure 8.21 displays the difference in introduced artificial hourglass energy between the two control algorithms for a drop height of 6 750 mm. An abrupt change of slope in the hourglass energy imposed by the viscosity based algorithm is seen just after the onset of fracture, i.e. at approximately 2.7 ms. This sudden rise in hourglass energy is imposed at crack initiation. During the subsequent propagation, where the elements undergo substantial deformation and distortion before they erode, this algorithm impose even more artificial energy. After approximately 4.3 ms, the ball was decelerated to zero

velocity and rebound commenced. However, since only loading is considered here, the succeeding data is not emphasised in particular. The curves are nonetheless plotted for the whole time duration of the simulation in order to better demonstrate the differences.

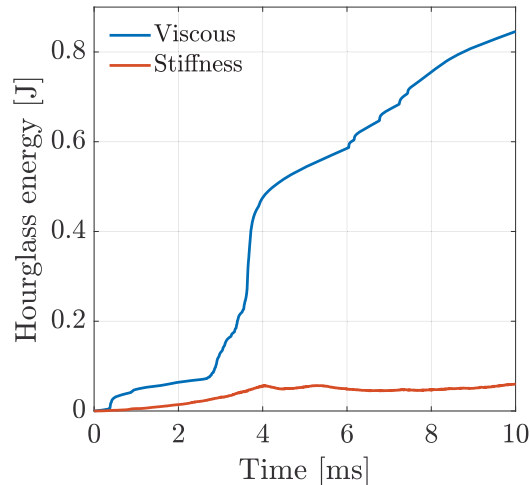


Figure 8.21: Comparison of the two hourglass control algorithms

Although the failure modes were similar for the two simulations, utilisation of the stiffness based algorithm resulted in a significantly stiffer response of the door trim, causing fracture at an earlier point in time. Furthermore, the viscosity based algorithm imposed a substantially larger amount of artificial energy to the model, compared to that of the stiffness based type. Hence, these findings suggest that a stiffness based algorithm could be the most appropriate choice in this particular case.

Numerical representation of door trim

During the uniaxial tensile testing conducted on the door trim cutouts, the specimens extracted from locations A, B and C were measured to allow for accurate stress calculations. These measurements also served as a way of verifying the numerical representation of the door trim with respect to shell thickness. The internal thickness variation was represented by the meshed geometry in the sense that each node in the model had its individual thickness. During simulation, the software interpolates the element thickness between the nodes to obtain an approximate value over the element plane. Hence, by comparing the measured thicknesses to those found in the numerical model, one fundamental assumption could be confirmed or disproved. Probed element values, rendered in Figures 8.22 and 8.23, were compared to the measured thicknesses from the same respective locations.

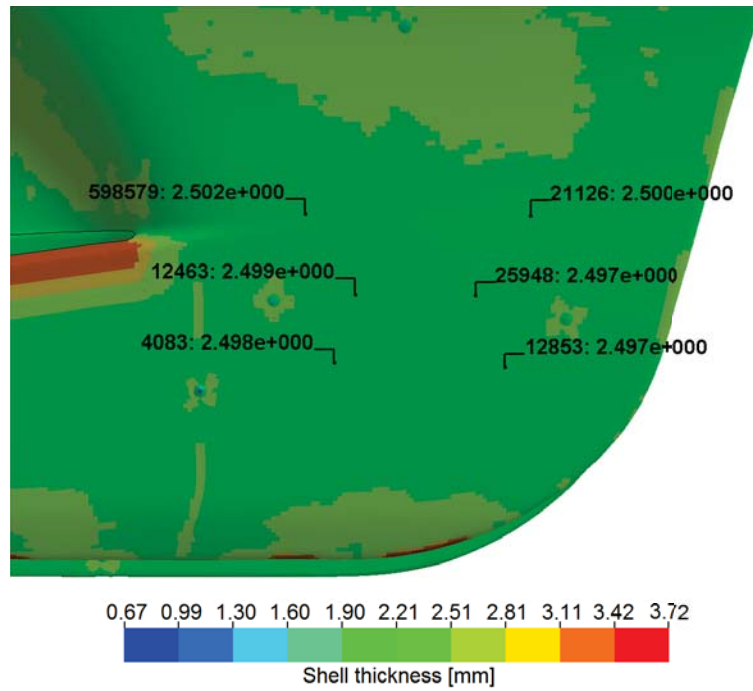


Figure 8.22: Numerical representation of the door trim thickness at locations CL and CR

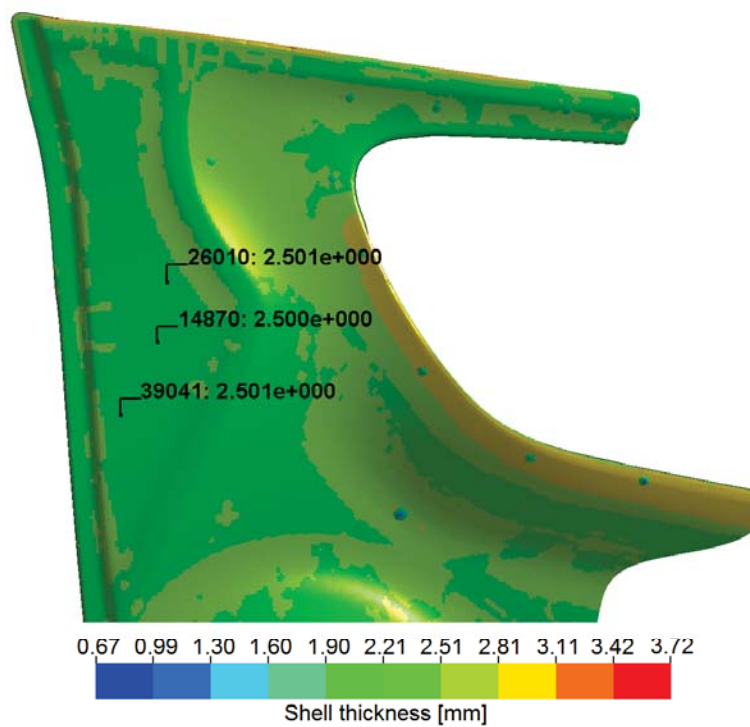


Figure 8.23: Numerical representation of the door trim thickness at location B

The averaged thicknesses and corresponding discrepancies for locations B and C are listed in Table 8.3. Location A was not checked because impact testing was not

conducted at this point. One explanation for these discrepancies could be thermal shrinkage, that occur in the physical door trim subsequent to injection moulding. Even though the numerical model is believed to account for this effect to some extent, it might be notably thicker than the physical part. Furthermore, since the capacity of the structure is closely related to its thickness, this might lead to an overestimated fracture drop height in the numerical model. However, it is clear that the discrepancy at location B is approximately 8 % of the measured value, while the same measure reads less than 2 % for location C. Hence, it is presumed that the discrepancies are small enough to be insignificant with respect to the substantial difference that was found between the numerical- and experimental results.

Table 8.3: Measured thickness and resulting discrepancy

Location	Averaged thickness [mm]		
	Measured	Probed	Discrepancy
B	2.320	2.501	0.1810
C	2.456	2.499	0.04300

Boundary conditions and friction

The steel ball employed in the full-scale testing was considerably larger than the impactor utilised in the small-scale impact tests, i.e. a diameter of 63 and 20 mm, respectively. The small diameter of the impactor and short span of the plate in the drop tower, might translate into a different failure mode than what transpired in the full-scale test. The plug resulting from perforation of the plate in the drop tower is associated with large shear gradients over a section along the periphery of the impactor. For the component drop test, however, the flexible boundary conditions and larger span might result in more membrane stresses due to elastic bending. Furthermore, frictional effects may have played a greater role in the full-scale- as opposed to the small-scale testing, as higher forces and larger sliding surfaces are evident there. Consequently, this suggests that the behaviour observed in the small-scale impact tests correspond to different load conditions than what are assumed to arise in the component drop test.

Conclusion

In this thesis, the cold impact performance of the PP material used in Toyota Yaris door trims was investigated. The ultimate goal was to reproduce the behaviour of the door trim in a drop test at $-30\text{ }^{\circ}\text{C}$ accurately, using numerical simulations. Since the mechanical properties of polymers are highly sensitive to strain rate and temperature, the comprehensive SPM, developed for ductile thermoplastics, was utilised to achieve an accurate material representation.

Initially, a uniaxial tensile test programme at quasi-static and meso-dynamic strain rates was conducted to characterise the behaviour of the PP material. The assumptions related to the material model were also of interest. Material sample plates and door trim cutouts were investigated in order to discover whether the process effects associated with the door trim influenced the mechanical properties. Both material sources were found to be ductile, strain rate dependent, dilatating, isotropic and uniform at $-30\text{ }^{\circ}\text{C}$. The only difference between the two material sources was the strain at fracture, which was observed to vary within the door trim as well. Substantial adiabatic heating effects were measured in the meso-dynamic regime, violating the assumption of isothermal conditions. This was indirectly accounted for through the hardening parameters of the material model, which were calibrated from a test where thermal softening occurred.

Both material sources were further tested in a drop tower equipped with an environmental chamber, providing a small-scale cold impact test under controlled conditions. Whereas clear signs of ductile deformation were found for the material sample plates, brittle fracture resulted from the door trim cutout specimens. Hence, the calibrated material model reproduced the behaviour of the former accurately, while

it significantly overestimated the ductility of the door trim cutouts. An extensive sensitivity study was conducted for the validated numerical model of the material sample plates, where the critical damage parameter was found to be crucial for accurate modelling. Due to the highly localised behaviour of brittle cracking, mesh refinement also produced a more realistic numerical representation.

In order to describe the observed brittle behaviour, further characterisation of the door trim material was conducted in the dynamic strain rate regime. By use of the SHTB, exclusively brittle material response was found at strain rates of order 10^2 s^{-1} . Furthermore, a brief SEM analysis confirmed a brittle-ductile transition when comparing the fracture surfaces from all strain rate regimes. This embrittlement violated the assumptions of small elastic and finite plastic strains, since predominately elastic deformations were found. However, isothermal conditions were again present when the response turned brittle. Additionally, a log-bilinear strain rate dependence was observed in all tensile test results. Attempting to account for these new findings, three different approaches were taken in the numerical simulations: Introduction of an alternative material model, recalibration of the SPM, and modification of the fracture parameter of the old calibration. The fracture parameters for all calibrations were inverse modelled from the results obtained in the drop tower, due to uncertainties related to the strain measures associated with the SHTB.

The full-scale experimental campaign, involving drop tests on the component at $-30 \text{ }^\circ\text{C}$, resulted in brittle fracture. Despite all attempts to accommodate the brittle behaviour in the material representation, the ductility of the numerical model was still significantly overestimated compared to the experimental results. The recalibration of the SPM was observed to better reproduce the behaviour. A comprehensive refinement study, related to the many parameters of the model, was conducted. It was discovered that the numerical model was highly sensitive to impact location with respect to replicating the experimental failure mode. Additionally, crack initiation and -propagation were improved by mesh refinement and the use of a full integration shell element formulation.

Suggestions for Further Work

Brittle-ductile transition

The door trim material was found to be ductile at the quasi-static and meso-dynamic strain rates tested in this project, while a brittle failure mode was observed in material tests at dynamic strain rates. Hence, it was proposed that the brittle-ductile transition is associated with some intermediate strain rate. Further investigation of the strain rates related to this transition would be of great interest. This could be conducted by use of the EM test machine and a high-speed camera configuration. Hence, an additional decade can be investigated in the meso-dynamic regime, possibly provoking embrittlement of the material. It could also permit more accurate strain extractions, which in turn could be used for calibration of a critical damage parameter based on brittle behaviour. Another related issue is whether the material sample plates experience a brittle-ductile transition under the same test conditions.

Dynamic strain rate testing

A log-bilinear strain rate dependence was found for the PP material investigated in this project. Although five successful SHTB tests at two strain rates resulted from the campaign, a more comprehensive programme would be beneficial. Emphasis should be placed on obtaining results from a larger amount of replicates for each rate, as well as testing at even higher strain rates. This would allow for the projection of the log-bilinear relation, to be verified or disproved.

Some differences were found in the plastic strain at fracture during tensile testing

of the material sample plates and door trim cutouts. The two material sources were also found to behave quite differently in the drop tower. Although some of the latter discrepancy could be related to the variation in thickness, a trend was nonetheless indicated by these results. For further comparison of the two material sources, a SHTB test campaign based on the material sample plates, could provide knowledge of whether the properties deviate in the dynamic regime.

Validation of shell element representation of the door trim

The process of material calibration produced highly accurate results for the drop tower impact simulation. Although some inconsistencies were related to the fracture parameters, the general behaviour was well-captured by the numerical model. When the same material calibration was utilised in the component drop test simulation, a highly overestimated ductility was found. This suggests that a broader perspective should be taken, to validate some of the fundamental assumptions of this project. One proposal is to check whether the stiffness representation of the door trim shell model is correct. This could be done through a quasi-static bending test, allowing for instrumented comparisons of the forces and displacements.

Instrumentation of component drop test

The complexity of this project is, to a large extent, related to the lack of instrumentation during the actual component drop test. Although the full-scale test does not allow for instrumentation, an approach where larger specimens are tested in the drop tower could be beneficial. This would allow for comparison with the numerical results to check whether the same amounts of forces arise in the physical part. An impactor with larger diameter could be machined, resembling the ball used at TME. This configuration would also permit high-speed camera recordings of the impact test.

Alternative material model

Although the SPM was able to produce highly accurate numerical results for the ductile behaviour of the PP material, it is not developed for brittle materials that fail before experiencing significant plastic deformations. Further investigation of an alternative material model could therefore be interesting. A more sophisticated prediction of the brittle behaviour found in the material is believed to translate into

accurate results. Additionally, an alternative model accommodating the brittle-ductile transition of the material would, in turn, allow for load conditions on both sides of this transition to be modelled.

Further experimental component testing

During the experimental campaign at TME, location H was chosen due to the brittle failure mode observed here, in addition to geometrical considerations. However, this could cause increased complexity with respect to accurate numerical modelling. This is due to the interaction between the main board and pocket module, located on the back of the door trim, which might be complicated to reproduce numerically. During experimental testing on the component, the test location should be chosen further away from any separate parts in the door trim assembly. Hence, facilitating simpler and possibly more accurate modelling of the component drop tests.

Bibliography

- [1] Carnow. https://carnow.com/cars/6138/mdp_photo_thumbnails. Accessed: 2018-06-08.
- [2] Schwenke E. Cold impact performance of polypropylene (PP). Master thesis, Norwegian University of Science and Technology (NTNU), 2017.
- [3] Brinson H. F. Brinson L. C. *Polymer Engineering Science and Viscoelasticity, An Introduction*. Springer, Second edition, 2015.
- [4] Callister W. D. Rethwisch D. G. *Material Science and Engineering*. John Wiley & Sons, Ninth edition, 2015.
- [5] Kinloch A. J. Young R. J. *Fracture Behaviour of Polymers*. Springer, First edition, 1995.
- [6] Anderson T. L. *Fracture Mechanics: Fundamentals and Applications*. Taylor & Francis Group, Third edition, 2005.
- [7] Sun Z. Yu F. Sem study on fracture behavior of ethylene/propylene block copolymers and their blends. *Makromolekulare Chemie*, Vol. 192(6):1439–1445, 1990.
- [8] Sun Z. Yu F. Qi Y. Characterization, morphology and thermal properties of ethylene-propylene block copolymers. *Polymer*, Vol. 32(6):1059–1064, 1991.
- [9] Gómez del Río T. Rodríguez J. Compression yielding of polypropylenes above glass transition temperature. *European Polymer Journal*, Vol. 46:1244–1250, 2010.
- [10] Siviour C. R. Jordan J. L. High strain rate mechanics of polymers: A review. *Journal of Dynamic Behavior of Materials*, Vol. 2:15–32, 2016.
- [11] Orowan E. Fracture and strength of solids. *Reports on Progress in Physics*, Vol. 12(185), 1949.

- [12] Ward I. M. Sweeney J. *An Introduction to the Mechanical Properties of Solid Polymers*. John Wiley & Sons, 2004.
- [13] Kendal M. J. Siviour C. R. Experimentally simulating adiabatic conditions approximating high rate polymer behavior using low rate experiments with temperature profiles. *Polymer*, Vol. 54(18):5058–5063, 2013.
- [14] Vincent P. I. The tough-brittle transition in thermoplastics. *Polymer*, Vol. 1:425–444, 1960.
- [15] Harlin G. Willis J. R. The influence of crack size on the ductile-brittle transition. *Mathematical and Physical Sciences*, Vol. 415(1848):197–226, 1988.
- [16] Christensen R. M. A comprehensive theory of yielding and failure for isotropic materials. *Journal of Engineering Materials and Technology*, Vol. 129(2):173–181, 2007.
- [17] Groover M. P. *Principles of Modern Manufacturing*. John Wiley & Sons, Fifth edition, 2013.
- [18] Kantz M. R. Newman Jr. H. D. Stigale F. H. The skin-core morphology and structure–property relationships in injection-molded polypropylene. *Journal of Applied Polymer Science*, Vol. 16:1249–1260, 1972.
- [19] Kim S. G. Suh N. P. Performance prediction of weldline structure in amorphous polymers. *Polymer engineering and science*, Vol. 26:1200–1207, 1986.
- [20] Zhu Y.-K. Tian G.-Y. Lu R.-S. Zhang H. A review of optical NDT technologies. *Sensors*, 11(8):7773–7798, 2011.
- [21] Polanco-Loria M. Clausen A. H. Berstad T. Hopperstad O. S. Constitutive model for thermoplastics with structural applications. *International Journal of Impact Engineering*, Vol. 37(12):1207–1219, 2010.
- [22] Sælen K. Validation of material model for polypropylene (PP). Master thesis, Norwegian University of Science and Technology (NTNU), 2012.
- [23] Vange K. Validation of material model for polypropylene (PP). Master thesis, Norwegian University of Science and Technology (NTNU), 2012.
- [24] Røstum H. H. Behavior and modeling of injection molded PP. Master thesis, Norwegian University of Science and Technology (NTNU), 2014.
- [25] SIMLab. *SIMLab Polymer Model - Theory, user's and example manual*, 2015.

-
- [26] Hopperstad O. S. Børvik T. Materials mechanics - Part 2. Structural Impact Laboratory (SIMLab), Norwegian University of Science and Technology (NTNU), 2017.
- [27] Raghava R. Caddell R. Yeh G. The macroscopic yield behaviour of polymers. *Journal of Materials Science*, Vol. 8(2):225–232, 1973.
- [28] Hopperstad O. S. Børvik T. Materials mechanics - Part 1. Structural Impact Laboratory (SIMLab), Norwegian University of Science and Technology (NTNU), 2017.
- [29] Cook R. D. Malkus D. S. Plesha M. E. Witt R. J. *Concepts and Applications of Finite Element Analysis*. John Wiley & Sons, Fourth edition, 2002.
- [30] Bathe K. J. Guillermin O. Walczak J. Chen H. Y. Advances in nonlinear finite element analysis of automobiles. *Computers & Structures*, Vol. 64(5/6):881–891, 1997.
- [31] Hopperstad O.S. Børvik T. Lecture notes impact mechanics - Part 1: Modelling of plasticity and failure with explicit finite element methods, August 2017.
- [32] Langseth M. Hopperstad O. S. Berstad T. Crashworthiness of aluminium extrusions: validation of numerical simulation, effect of mass ratio and impact velocity. *International Journal of Impact Engineering*, Vol. 22(9/10):829–854, 1999.
- [33] Haufe A. Schweizerhof K. DuBois P. Properties & limits: Review of shell element formulations, September 2013.
- [34] Bell K. *An engineering approach to finite element analysis of linear structural mechanics problems*. Fagbokforlaget, First edition, 2013.
- [35] Dassault Systèmes Simulia Corp., Providence, Rhode Island, USA. *Abaqus Analysis User's Manual*, 6.9 edition, 2009.
- [36] Livermore Software Technology Corporation, Livermore, California, USA. *LS-DYNA Keyword User's Manual Volume I*, R10.0 edition, 2017.
- [37] Muralisrinivasan N. S. *Polymer testing: New instrumental methods*. Momentum Press, New York, N.Y., First edition, 2012.
- [38] Ross R. J. *Scanning Electron Microscopy*. ASM International, Sixth edition, 2011.
- [39] Pettersen J. E. Experimental tests of injection moulded PE/PP plates, June 2017.

- [40] Johnsen J. Grytten F. Hopperstad O. S. Clausen A. H. Experimental set-up for determination of the large-strain tensile behaviour of polymers at low temperatures. *In: Polymer Testing*, Vol. 53, 2016.
- [41] Fagerholt E. *Field measurements in mechanical testing using close-range photogrammetry and digital image analysis*. PhD thesis, Norwegian University of Science and Technology (NTNU), N-7491 Trondheim, Norway, 2012.
- [42] Fagerholt E. Lecture notes - Digital image correlation, September 2017.
- [43] Peterlin A. Plastic deformation of polymers with fibrous structure. *Colloid and Polymer Science*, Vol. 253:809–823, 1974.
- [44] Galeski A. Strength and toughness of crystalline polymer systems. *Progress in Polymer Science*, Vol. 28:1643–1699, 2003.
- [45] Donato G. H. B. Bianchi M. Pressure dependent yield criteria applied for improving design practices and integrity assessments against yielding of engineering polymers. *Material research and technology*, Vol. 1(1):2–7, 2012.
- [46] Dhondt G. *The Finite Element Method for Three-Dimensional Thermomechanical Applications*. John Wiley & Sons, First edition, 2004.
- [47] Mathisen K. M. Lecture notes - TKT4197 Nonlinear Finite Element Analysis: Solution of the dynamic equilibrium equations by explicit direct integration, September 2017.
- [48] Ceast 9350 drop tower impact system. <http://www.instron.se/sv-se/products/testing-systems/impact-systems/drop-weight-testers/9350-drop-tower>. Accessed: 2018-04-13.
- [49] Daiyan H. Andreassen E. Grytten F. Lyngstad O. V. Luksepp T. Osnes H. Low-velocity impact response of injection-moulded polypropylene plates – Part 2: Effects of moulding conditions, striker geometry, clamping, surface texture, weld line and paint. *Polymer Testing*, Vol. 29:894–901, 2010.
- [50] Holmen J. K. Olovsson L. Børvik T. Discrete modelling of low-velocity penetration in sand. *Computers and Geotechnics*, Vol. 86:21–32, 2017.
- [51] Børvik T. Hopperstad O. S. Langseth M. Lecture notes in TKT4128 Impact Mechanics: An introduction to penetration and perforation mechanics, September 2017.
- [52] Børvik T. Langseth M. Hopperstad O. S. Malo K. A. Perforation of 12 mm thick steel plates by 20 mm diameter projectiles with flat, hemispherical and

-
- conical noses: Part I: Experimental study. *International Journal of Impact Engineering*, Vol. 27(1):19–35, 2002.
- [53] Børvik T. Langseth M. Hopperstad O. S. Malo K. A. Ballistic penetration of steel plates. *International Journal of Impact Engineering*, Vol. 22(9/10):855–886, 1999.
- [54] Daiyan H. Andreassen E. Grytten F. Lyngstad O. V. Luksepp T. Osnes H. Low-velocity impact response of injection-moulded polypropylene plates – Part 1: Effects of plate thickness, impact velocity and temperature. *Polymer Testing*, Vol. 29:648–657, 2010.
- [55] Clausen A. H. *The Kolsky-Hopkinson Bar Machine, Chapter 2*. Springer International Publishing AG, 2018.
- [56] Vilemosa V. Clausen A. H. Fagerholt E. Hopperstad O. S. Børvik T. Local measurement of stress-strain behaviour of ductile materials at elevated temperatures in a split-hopkinson tension bar system. *International Journal of Impact Engineering*, Vol. 38(10):824–836, 2011.
- [57] Clausen A. H. Auestad T. Split-hopkinson tension bar. Experimental set-up and theoretical considerations. Draft. Technical report, Department of Structural Engineering (DSE), Norwegian University of Science and Technology (NTNU), October 2002.
- [58] Chou S. C. Robertson K. D. Rainey J. H. The effect of strain rate and heat developed during deformation on the stress-strain curve of plastics. *Experimental Mechanics*, Vol. 13(10):422–432, 1973.
- [59] Okereke M. I. Buckley C. P. Siviour C. R. Compression of polypropylene across a wide range of strain rates. *Mechanics of Time-Dependent Materials*, Vol. 16(4):361–379, 2012.
- [60] Cowper G. Symonds P. Strain hardening and strain-rate effects in the impact loading of cantilever beams. Technical report, Brown University Division of Applied Mathematics, 1957.
- [61] Livermore Software Technology Corporation, Livermore, California, USA. *LS-DYNA Theory Manual*, 2018.
- [62] Langseth M. Clausen A. H. Børvik T. Lecture notes in TKT4128 impact mechanics: Impact and energy absorption, August 2017.

Mathematical Derivation

A.1 Plastic dilatation parameter

The relation between the plastic dilatation parameter, β , and the retraction ratio, R_r , given in Eq. (4.1), is derived here. The development of volumetric plastic strains is controlled by the flow potential, $g = g(\hat{\boldsymbol{\sigma}})$, given in Eq. (2.21), in the material model. The flow potential can be expressed in terms of the stress invariants, I_1 and J_2 , by

$$g(I_1, J_2) = \frac{(\beta - 1)I_1 + \sqrt{(\beta - 1)^2 I_1^2 + 12\beta J_2}}{2\beta}. \quad (\text{A.1})$$

By performing a partial differentiation of the flow potential with respect to the corotational stress tensor, one obtain

$$\frac{\partial g}{\partial \hat{\sigma}_{ij}}(I_1, J_2) = \frac{\partial g}{\partial I_1} \frac{\partial I_1}{\partial \hat{\sigma}_{ij}} + \frac{\partial g}{\partial J_2} \frac{\partial J_2}{\partial \hat{\sigma}_{ij}}. \quad (\text{A.2})$$

For an arbitrary stress state, the four different partial derivatives are given by

$$\frac{\partial g}{\partial I_1} = \frac{1}{2\beta} \left[(\beta - 1) + \frac{(\beta - 1)^2 I_1}{\sqrt{(\beta - 1)^2 I_1^2 + 12\beta J_2}} \right], \quad (\text{A.3})$$

$$\frac{\partial g}{\partial J_2} = \frac{3}{\sqrt{(\beta - 1)^2 I_1^2 + 12\beta J_2}}, \quad (\text{A.4})$$

$$\frac{\partial I_1}{\partial \hat{\sigma}_{ij}} = \begin{bmatrix} 1 & 0 & 0 \\ 0 & 1 & 0 \\ 0 & 0 & 1 \end{bmatrix}, \quad (\text{A.5})$$

$$\frac{\partial J_2}{\partial \hat{\sigma}_{ij}} = \begin{bmatrix} \frac{2}{3}\sigma_{11} - \frac{1}{3}\sigma_{22} - \frac{1}{3}\sigma_{33} & 2\sigma_{12} & 2\sigma_{13} \\ 2\sigma_{21} & -\frac{1}{3}\sigma_{11} + \frac{2}{3}\sigma_{22} - \frac{1}{3}\sigma_{33} & 2\sigma_{23} \\ 2\sigma_{31} & 2\sigma_{32} & -\frac{1}{3}\sigma_{11} - \frac{1}{3}\sigma_{22} + \frac{2}{3}\sigma_{33} \end{bmatrix}. \quad (\text{A.6})$$

For the uniaxial stress state, which is of interest in this case, the following stress components and invariants are given

$$\sigma_{11} = \sigma, \quad \sigma_{ij \neq 11} = 0, \quad (\text{A.7})$$

$$I_1 = \sigma, \quad J_2 = \frac{1}{3}\sigma^2. \quad (\text{A.8})$$

Thus, substituting these conditions into the partial derivatives, the two products in Eq. (A.2), can be determined

$$\frac{\partial g}{\partial I_1} \frac{\partial I_1}{\partial \hat{\sigma}_{ij}} = \frac{1}{2\beta} \left[(\beta - 1) + \frac{(\beta - 1)^2 \sigma}{\sqrt{(\beta - 1)^2 \sigma^2 + 4\beta \sigma^2}} \right] \begin{bmatrix} 1 & 0 & 0 \\ 0 & 1 & 0 \\ 0 & 0 & 1 \end{bmatrix} \quad (\text{A.9})$$

$$= \frac{\beta - 1}{\beta + 1} \begin{bmatrix} 1 & 0 & 0 \\ 0 & 1 & 0 \\ 0 & 0 & 1 \end{bmatrix}, \quad (\text{A.10})$$

$$\frac{\partial g}{\partial J_2} \frac{\partial J_2}{\partial \hat{\sigma}_{ij}} = \frac{\sigma}{\sqrt{(\beta - 1)^2 \sigma^2 + 4\beta \sigma^2}} \begin{bmatrix} 2 & 0 & 0 \\ 0 & -1 & 0 \\ 0 & 0 & -1 \end{bmatrix} \quad (\text{A.11})$$

$$= \frac{1}{\beta + 1} \begin{bmatrix} 2 & 0 & 0 \\ 0 & -1 & 0 \\ 0 & 0 & -1 \end{bmatrix}. \quad (\text{A.12})$$

In order to related the plastic dilatation parameter to the retraction ratio, the plastic rate-of-deformation tensor given in Eq. (2.20), must be introduced. Here, the plastic

parameter, $\dot{\lambda}$, corresponds to the plastic strain rate, $\dot{\varepsilon}^p$, for the uniaxial case. If it is further assumed that the relation between the longitudinal- and transverse strain components is constant, the plastic flow can be expressed by

$$\hat{D}_{ij}^p = \begin{bmatrix} \dot{\varepsilon}_1^p & 0 & 0 \\ 0 & \dot{\varepsilon}_2^p & 0 \\ 0 & 0 & \dot{\varepsilon}_3^p \end{bmatrix} = \dot{\varepsilon}_1^p \begin{bmatrix} 1 & 0 & 0 \\ 0 & -R_r & 0 \\ 0 & 0 & -R_r \end{bmatrix}. \quad (\text{A.13})$$

By using the relation between the plastic flow and flow potential, given by Eq. (2.20), and substituting Eq. (A.9) and (A.11) into the expression for the partial derivatives of the flow potential, one obtain

$$\hat{D}_{ij}^p = \dot{\lambda} \frac{\partial g}{\partial \hat{\sigma}_{ij}} \quad (\text{A.14})$$

$$\dot{\varepsilon}_1^p \begin{bmatrix} 1 & 0 & 0 \\ 0 & -R_r & 0 \\ 0 & 0 & -R_r \end{bmatrix} = \dot{\varepsilon}_1^p \left(\frac{\beta - 1}{\beta + 1} \begin{bmatrix} 1 & 0 & 0 \\ 0 & 1 & 0 \\ 0 & 0 & 1 \end{bmatrix} + \frac{1}{\beta + 1} \begin{bmatrix} 2 & 0 & 0 \\ 0 & -1 & 0 \\ 0 & 0 & -1 \end{bmatrix} \right). \quad (\text{A.15})$$

Finally, by solving the Eq. (A.15), the relation between the plastic parameter, β , and the retraction ratio R_r can be expressed by

$$\beta = \frac{2 - R_r}{R_r + 1}. \quad (\text{A.16})$$

A.2 Force correction factor

In order to account for the mass located both above and below the strain gauge in the instrumented striker, the measured force must be corrected. A relation between the actual force, acting between the striker and impacted specimen, and the measured force must therefore be derived. The main components of the striker are shown in Figure A.2.1, below.

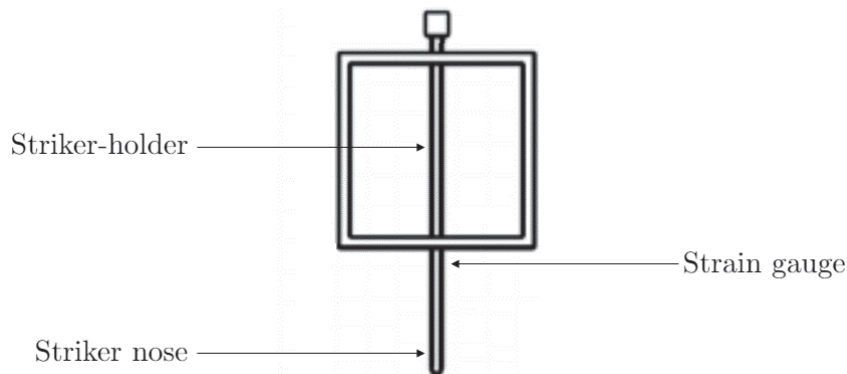


Figure A.2.1: Main components of the impacting striker

The derivation is based on a section made at the point where the measured force is extracted from the striker, i.e. the strain gauge location indicated in the figure above. The forces and accelerations acting on the two sections, below and above the strain gauge, are shown in Figure A.2.2a and A.2.2b, respectively. Note that only a small section of the striker above the strain gauge is drawn here.



(a) Section 1: Below strain gauge

(b) Section 2: Above strain gauge

Figure A.2.2: Free-body-diagram for the two sections

The following assumptions were made for this derivation:

1. The mass of the strain gauge is negligible.
2. The entire impacting striker acts as one rigid body.

Dynamic equilibrium is used in order to relate the measured force, P , to the actual force, F . Applying Newton's second law of motion to Section 1, one obtain

$$\Sigma F_y = ma_y : \quad -P + F = m_1 a_1, \quad (\text{A.17})$$

where a_1 corresponds to the acceleration of mass m_1 . A similar equilibrium can be expressed for Section 2,

$$\Sigma F_y = ma_y : \quad P = m_2 a_2, \quad (\text{A.18})$$

where a_2 corresponds to the acceleration of the mass above the strain gauge, m_2 . Due to assumption 2, the acceleration must be equal for both masses, $a_1 = a_2 = a$. Thus, Eq. (A.18) can be substituted into Eq. (A.17), and an expression for the actual force as a function of the measured force is obtained

$$-P + F = \frac{m_1}{m_2} P \quad (\text{A.19})$$

$$\Rightarrow F = P \left(1 + \frac{m_1}{m_2} \right). \quad (\text{A.20})$$

Material Tests

In this appendix, all successful tests conducted in the EM test machine are archived. For each test specimen, the test specifics, dimensions and a picture of the deformed geometry is provided. In addition, three different graphs are plotted displaying the force, two stress measures and the strain components. All recorded data is cut at fracture.

The following abbreviations are used in this appendix:

\angle	Test specimen orientation
$\dot{\epsilon}_0$	Initial strain rate
T	Temperature
t_0	Initial gauge area thickness
w_0	Initial gauge are width
t_d	Test duration
ϵ_f	Logarithmic fracture strain

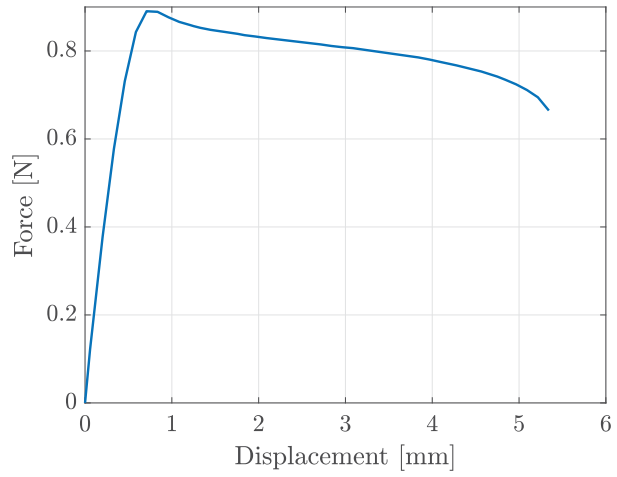
B.1 Material sample plates

B.1.1 UT_S_00_H_-30_01

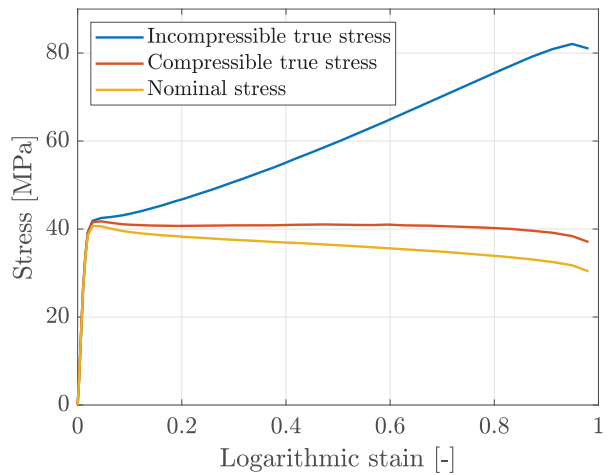
Material	S
\angle	0°
$\dot{\epsilon}_0$	$10^{-0.5} \text{ s}^{-1}$
T	$-30 \text{ }^\circ\text{C}$
Replicate	1
t_0	3.13 mm
w_0	6.99 mm
t_d	3 s
ϵ_f	0.98



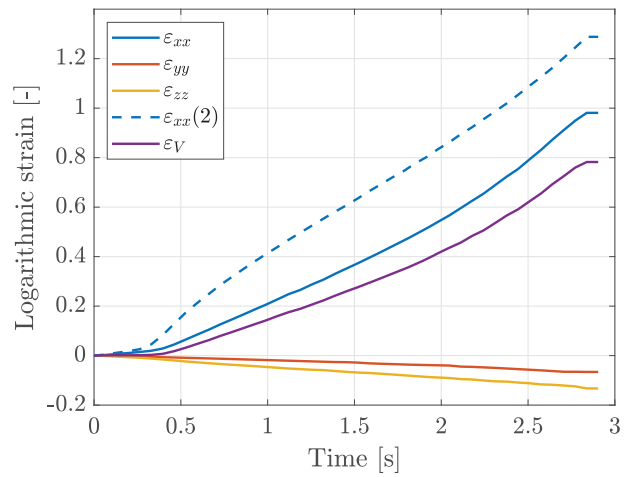
(a) Specimen



(b) Force - displacement



(c) Stress - logarithmic strain



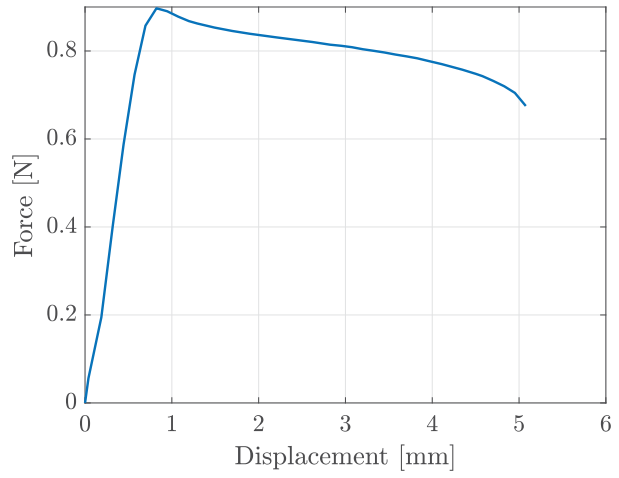
(d) Strain components - time

B.1.2 UT_S_00_H_-30_02

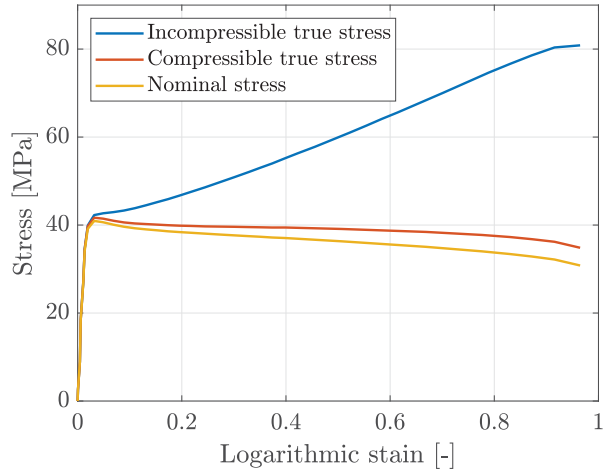
Material	S
\angle	0°
$\dot{\epsilon}_0$	$10^{-0.5} \text{ s}^{-1}$
T	$-30 \text{ }^\circ\text{C}$
Replicate	2
t_0	3.13 mm
w_0	7 mm
t_d	3 s
ϵ_f	0.96



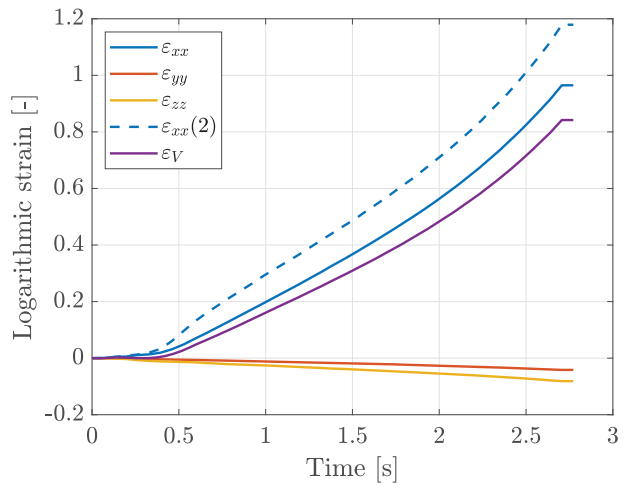
(a) Specimen



(b) Force - displacement



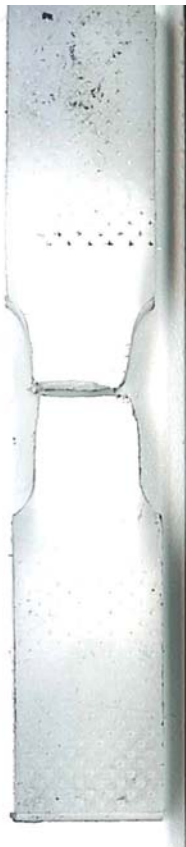
(c) Stress - logarithmic strain



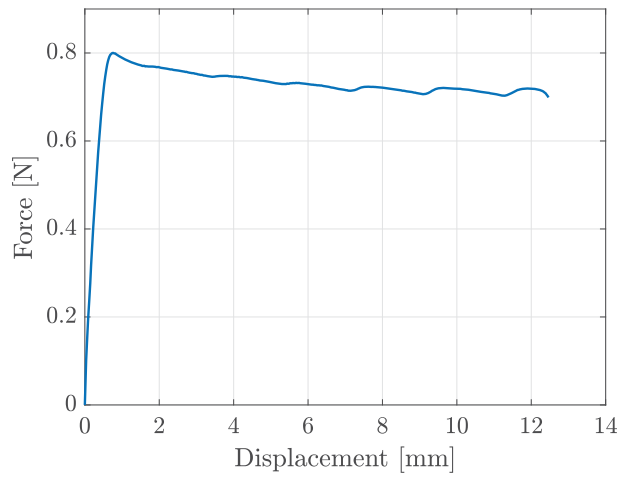
(d) Strain components - time

B.1.3 UT_S_00_L_-30_02

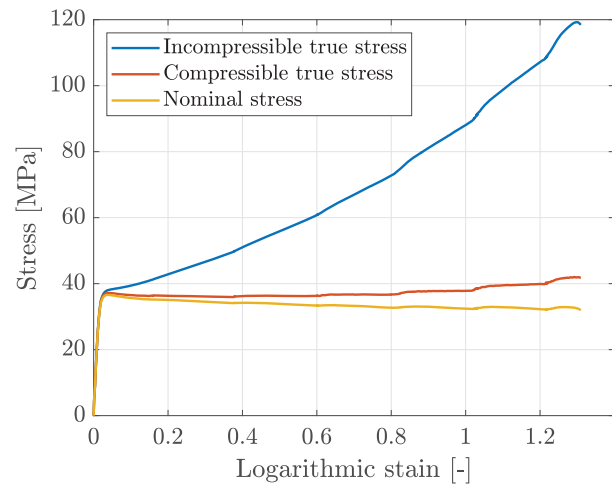
Material	S
\angle	0°
$\dot{\epsilon}_0$	$10^{-1.5} \text{ s}^{-1}$
T	$-30 \text{ }^\circ\text{C}$
Replicate	2
t_0	3.12 mm
w_0	7 mm
t_d	66 s
ϵ_f	1.31



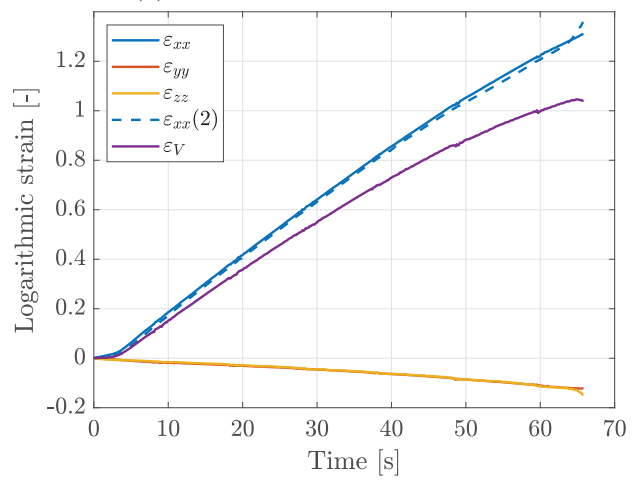
(a) Specimen



(b) Force - displacement



(c) Stress - logarithmic strain



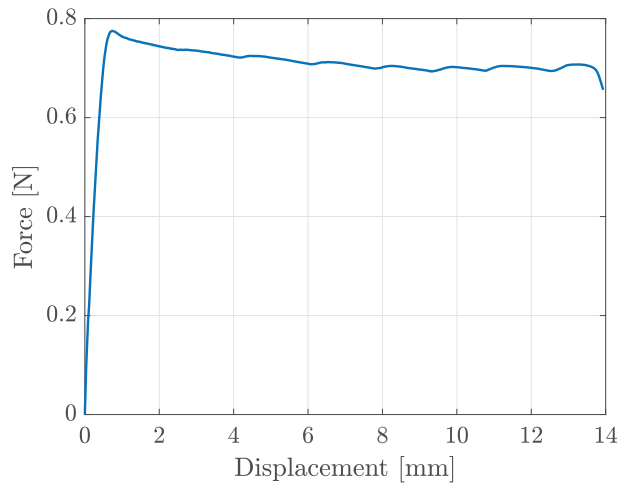
(d) Strain components - time

B.1.4 UT_S_00_L_-30_03

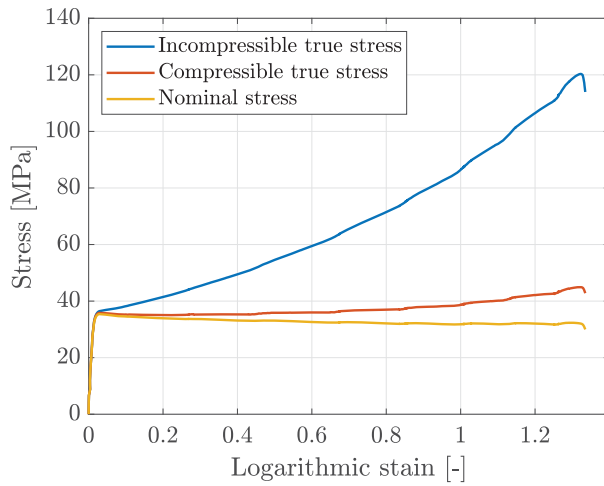
Material	S
\angle	0°
$\dot{\epsilon}_0$	$10^{-1.5} \text{ s}^{-1}$
T	-30 °C
Replicate	3
t_0	3.13 mm
w_0	6.99 mm
t_d	74 s
ϵ_f	1.33



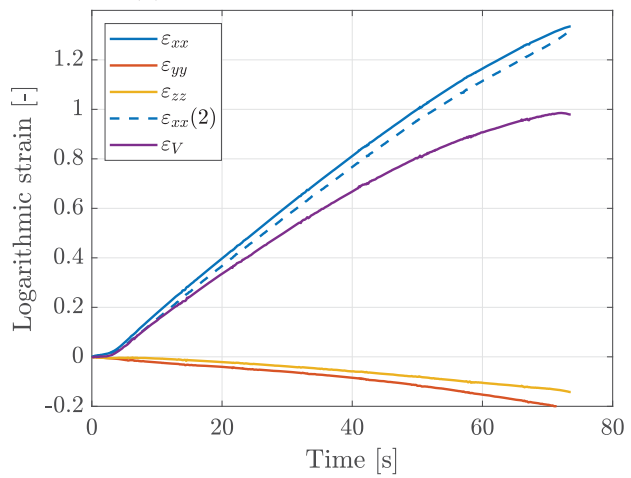
(a) Specimen



(b) Force - displacement



(c) Stress - logarithmic strain



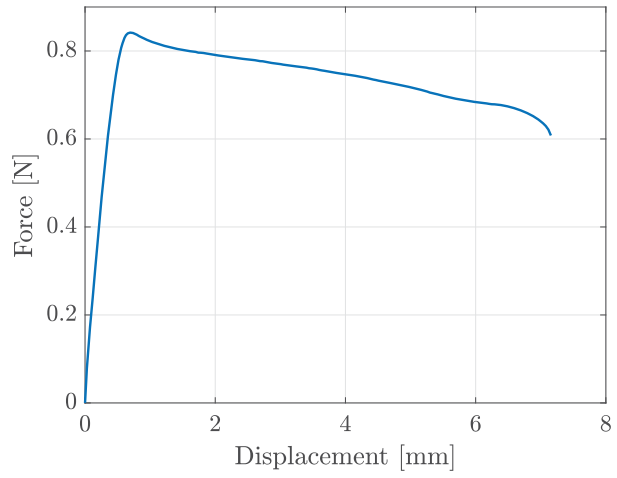
(d) Strain components - time

B.1.5 UT_S_00_M_-30_01

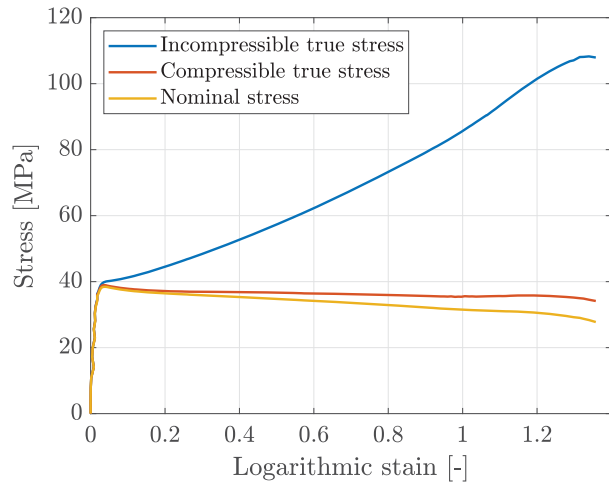
Material	S
\angle	0°
$\dot{\epsilon}_0$	$10^{-1.0} \text{ s}^{-1}$
T	$-30 \text{ }^\circ\text{C}$
Replicate	1
t_0	3.13 mm
w_0	6.99 mm
t_d	12 s
ϵ_f	1.36



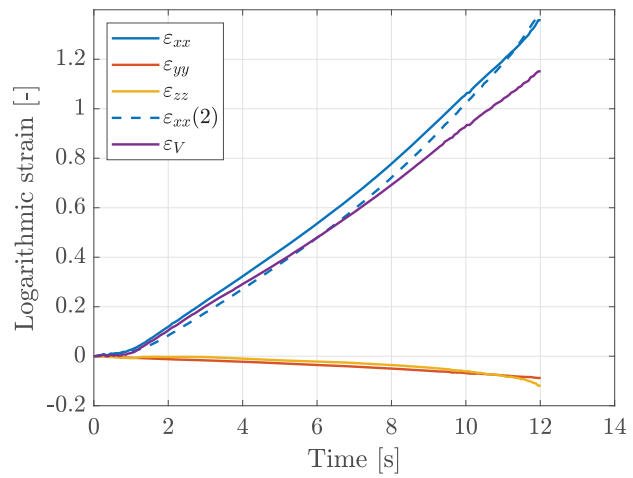
(a) Specimen



(b) Force - displacement



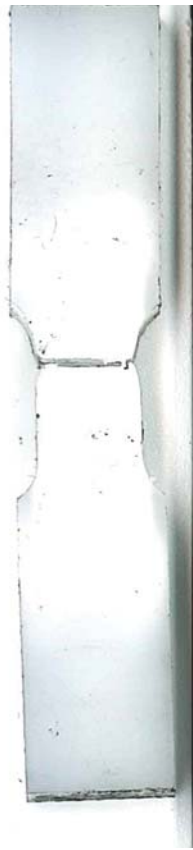
(c) Stress - logarithmic strain



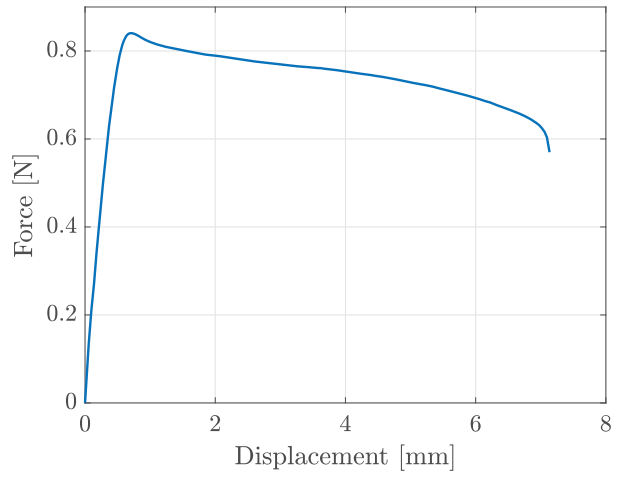
(d) Strain components - time

B.1.6 UT_S_00_M_-30_02

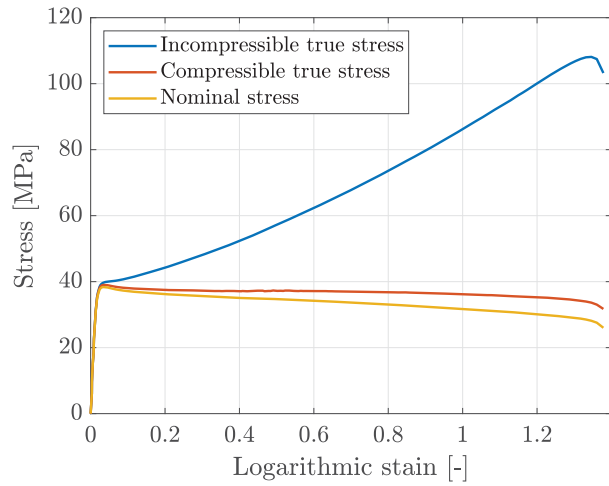
Material	S
\angle	0°
$\dot{\epsilon}_0$	$10^{-1.0} \text{ s}^{-1}$
T	-30 °C
Replicate	2
t_0	3.13 mm
w_0	7 mm
t_d	12 s
ϵ_f	1.38



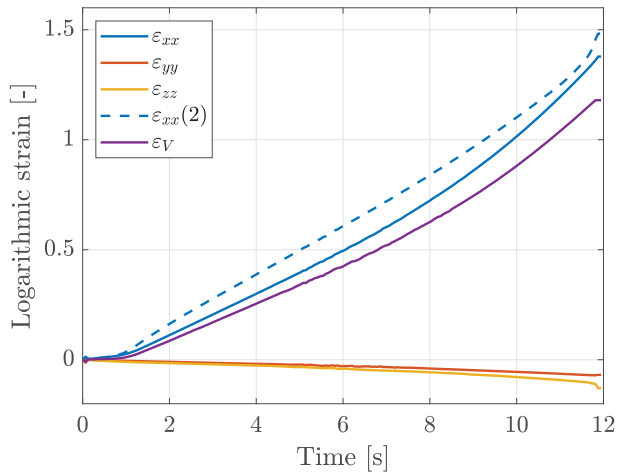
(a) Specimen



(b) Force - displacement



(c) Stress - logarithmic strain



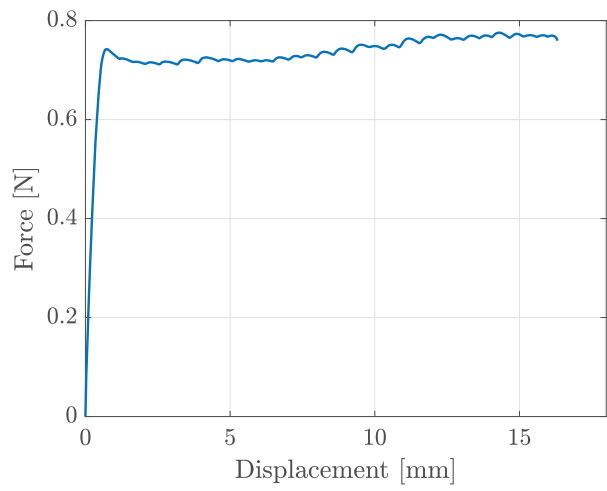
(d) Strain components - time

B.1.7 UT_S_00_VL_-30_02

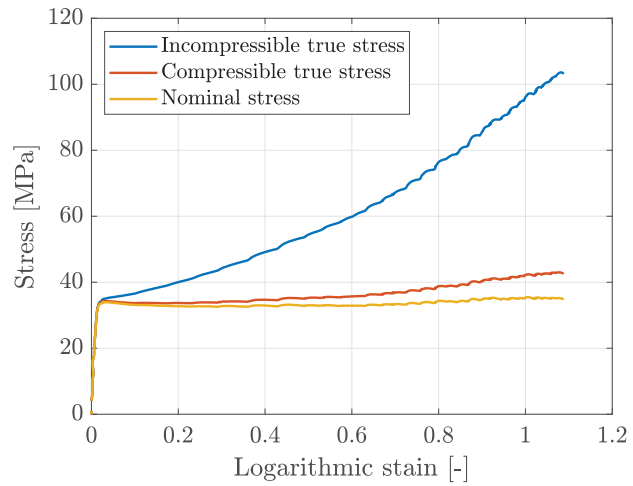
Material	S
\angle	0°
$\dot{\epsilon}_0$	$10^{-2.0} \text{ s}^{-1}$
T	$-30 \text{ }^\circ\text{C}$
Replicate	2
t_0	3.13 mm
w_0	6.99 mm
t_d	307 s
ϵ_f	1.09



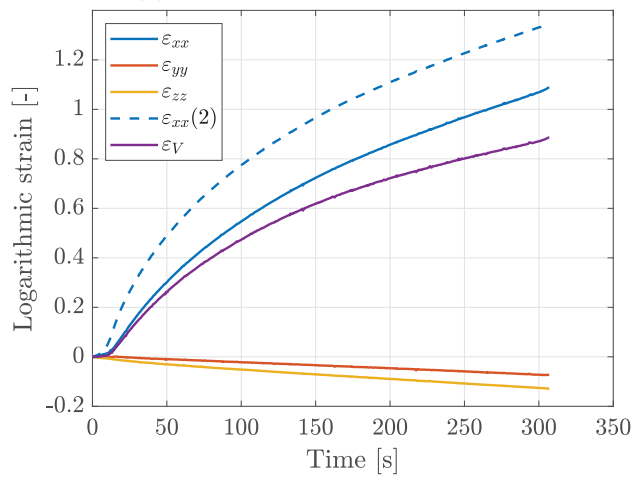
(a) Specimen



(b) Force - displacement



(c) Stress - logarithmic strain



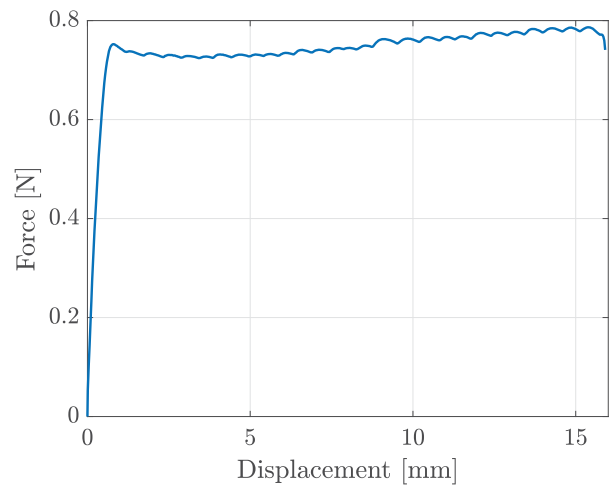
(d) Strain components - time

B.1.8 UT_S_00_VL_-30_03

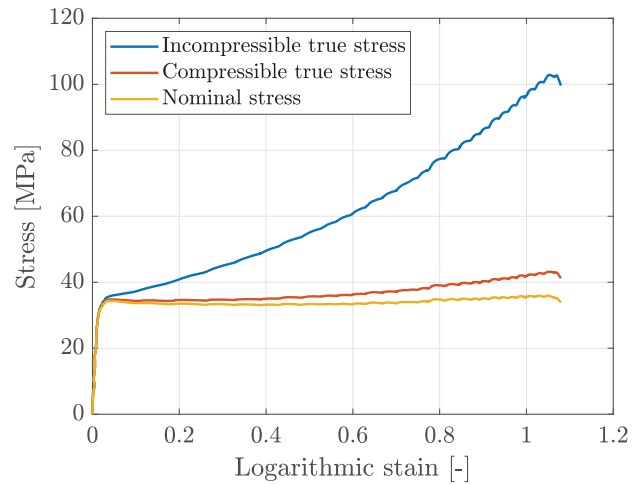
Material	S
\angle	0°
$\dot{\epsilon}_0$	$10^{-2.0} \text{ s}^{-1}$
T	$-30 \text{ }^\circ\text{C}$
Replicate	3
t_0	3.13 mm
w_0	7 mm
t_d	300 s
ϵ_f	1.08



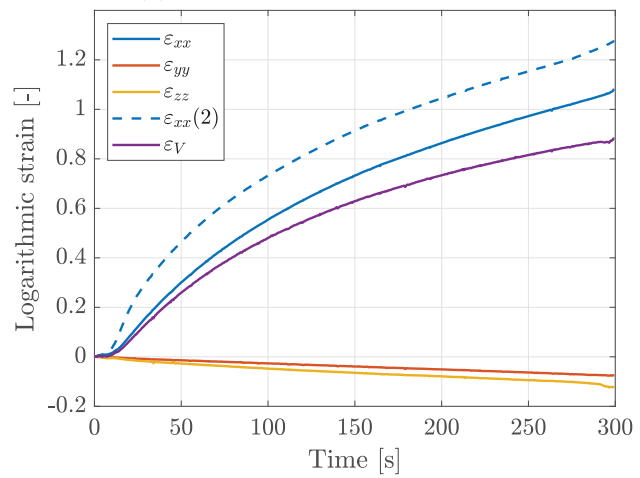
(a) Specimen



(b) Force - displacement



(c) Stress - logarithmic strain



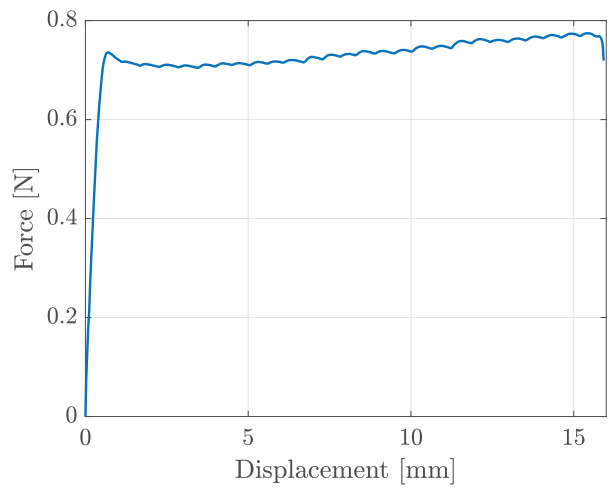
(d) Strain components - time

B.1.9 UT_S_00_VL_-30_01

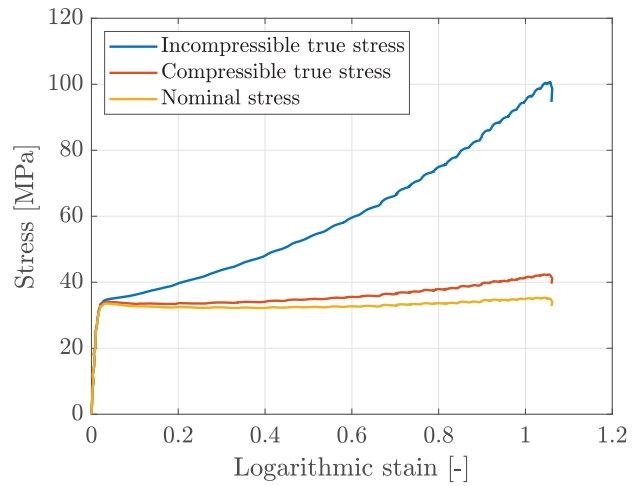
Material	S
\angle	0°
$\dot{\epsilon}_0$	$10^{-2.0} \text{ s}^{-1}$
T	$-30 \text{ }^\circ\text{C}$
Replicate	1
t_0	3.13 mm
w_0	7 mm
t_d	267 s
ϵ_f	1.06



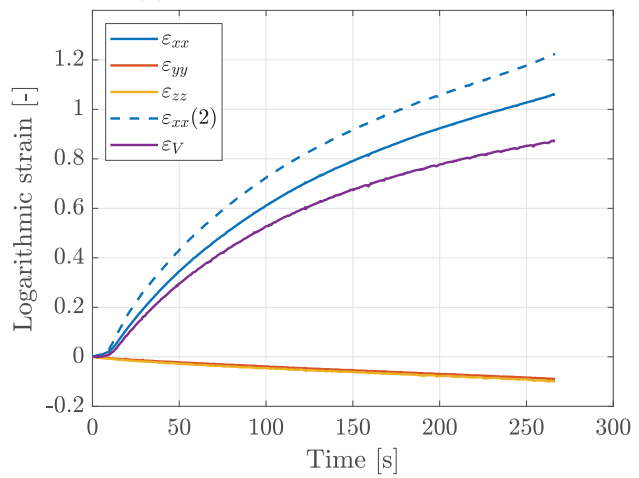
(a) Specimen



(b) Force - displacement



(c) Stress - logarithmic strain



(d) Strain components - time

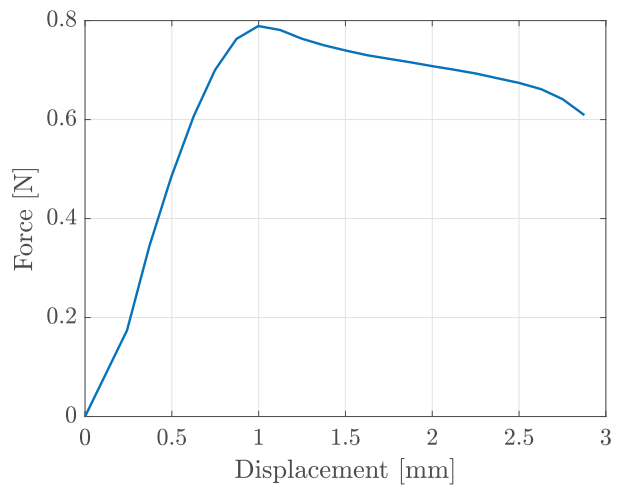
B.2 Door trim cutouts

B.2.1 UT_A-10_00_H_-30

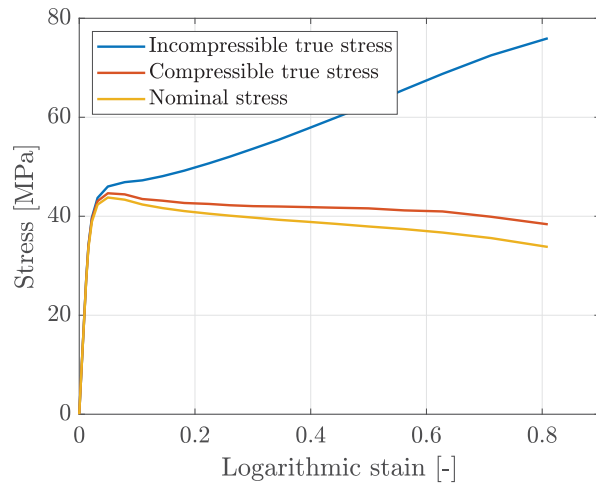
Location	A
\angle	0°
$\dot{\epsilon}_0$	$10^{-0.5} \text{ s}^{-1}$
T	-30 °C
Door trim no.	10
t_0	2.56 mm
w_0	7.03 mm
t_d	2 s
ϵ_f	0.81



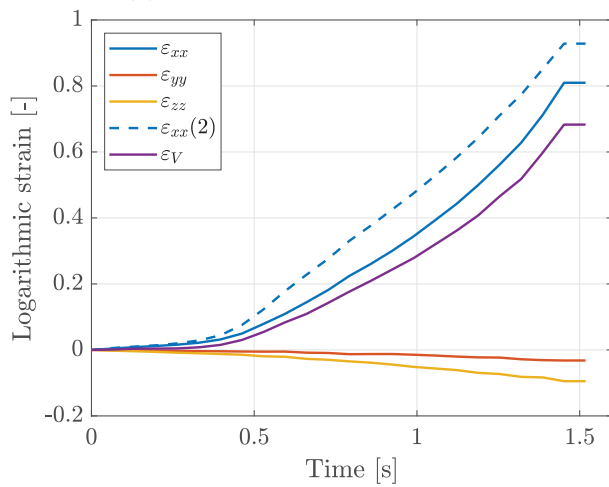
(a) Specimen



(b) Force - displacement



(c) Stress - logarithmic strain



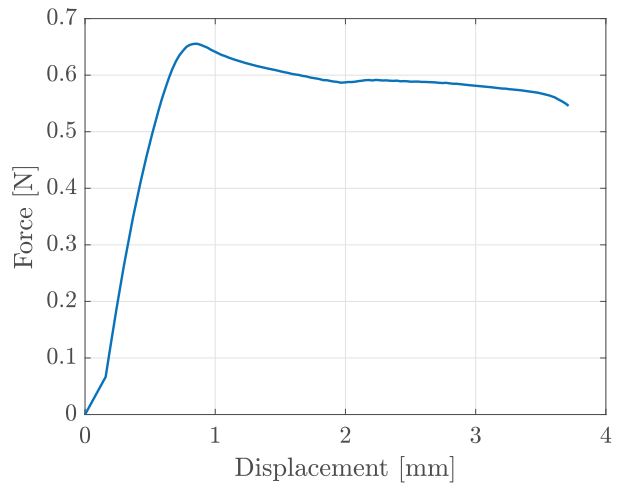
(d) Strain components - time

B.2.2 UT_A-10_00_L-30

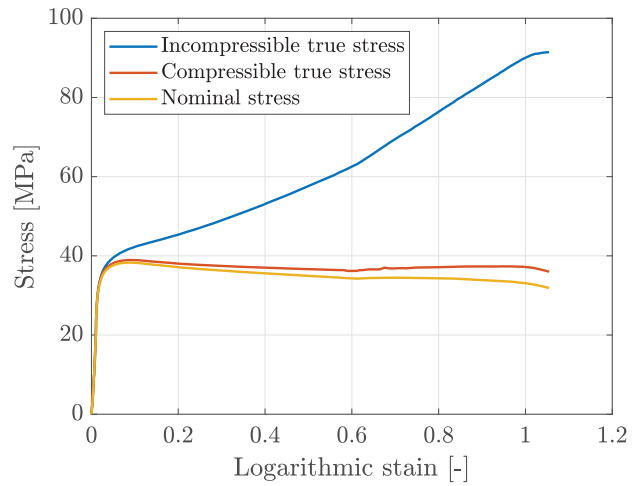
Location	A
\angle	0°
$\dot{\epsilon}_0$	$10^{-1.5} \text{ s}^{-1}$
T	-30 °C
Door trim no.	10
t_0	2.43 mm
w_0	7.05 mm
t_d	19 s
ϵ_f	1.05



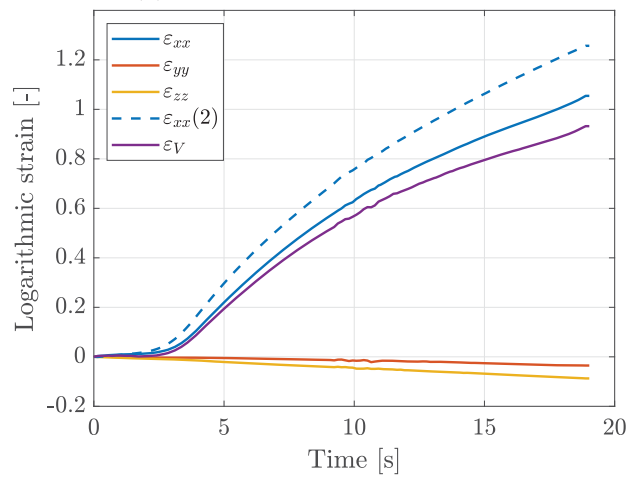
(a) Specimen



(b) Force - displacement



(c) Stress - logarithmic strain



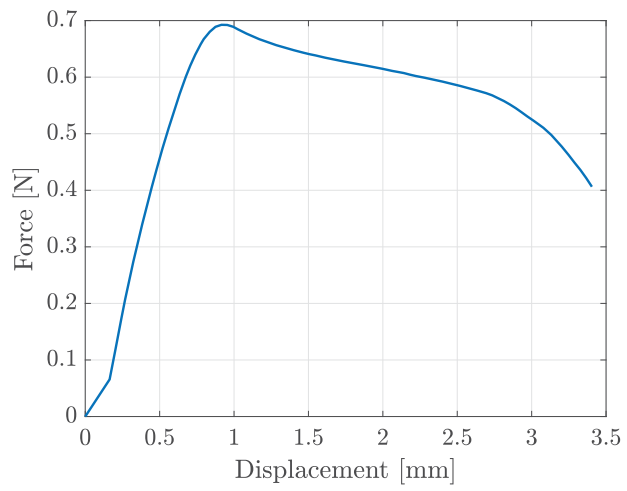
(d) Strain components - time

B.2.3 UT_A-10_00_M_-30

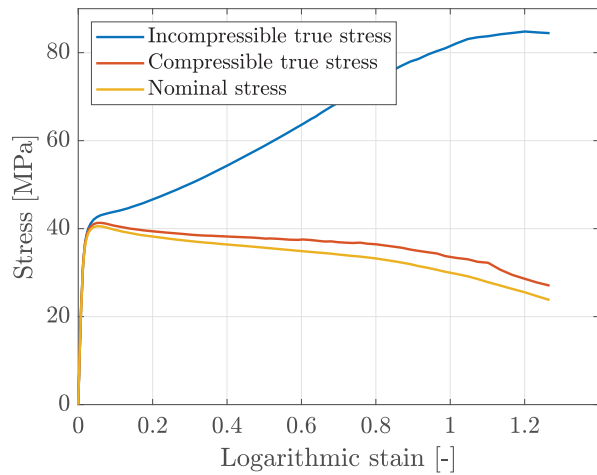
Location	A
\angle	0°
$\dot{\epsilon}_0$	$10^{-1.0} \text{ s}^{-1}$
T	$-30 \text{ }^\circ\text{C}$
Door trim no.	10
t_0	2.43 mm
w_0	7.03 mm
t_d	6 s
ϵ_f	1.27



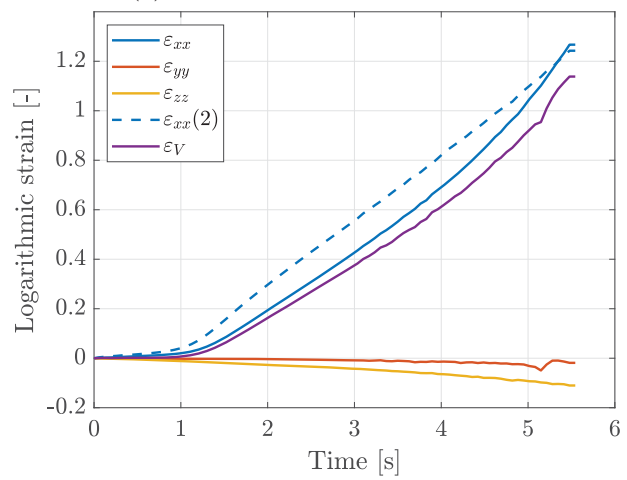
(a) Specimen



(b) Force - displacement



(c) Stress - logarithmic strain



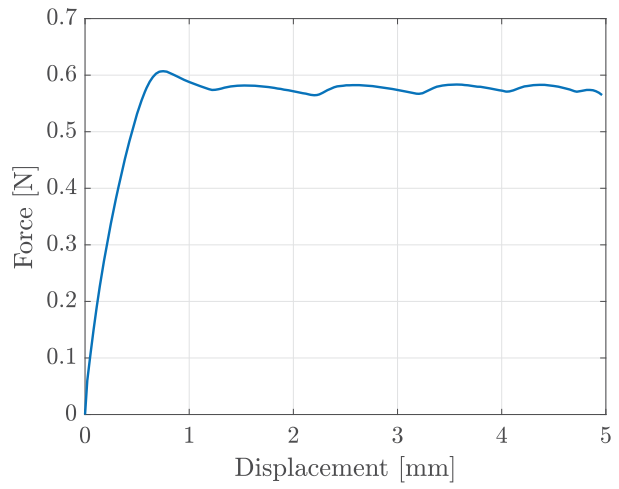
(d) Strain components - time

B.2.4 UT_A-1_00_VL_-30

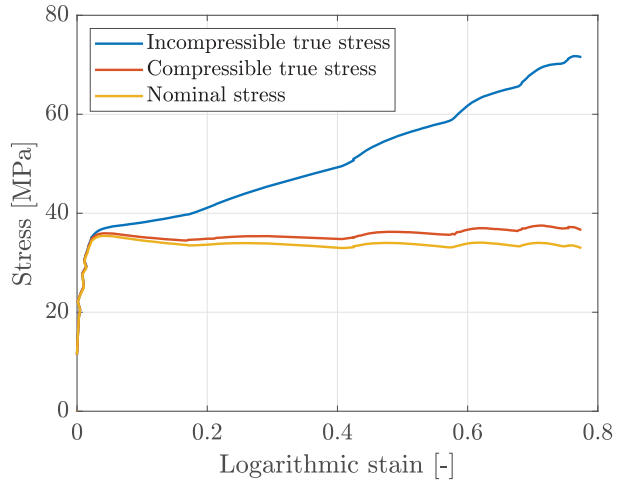
Location	A
\angle	0°
$\dot{\epsilon}_0$	$10^{-2.0} \text{ s}^{-1}$
T	-30 °C
Door trim no.	1
t_0	2.43 mm
w_0	7.04 mm
t_d	83 s
ϵ_f	0.77



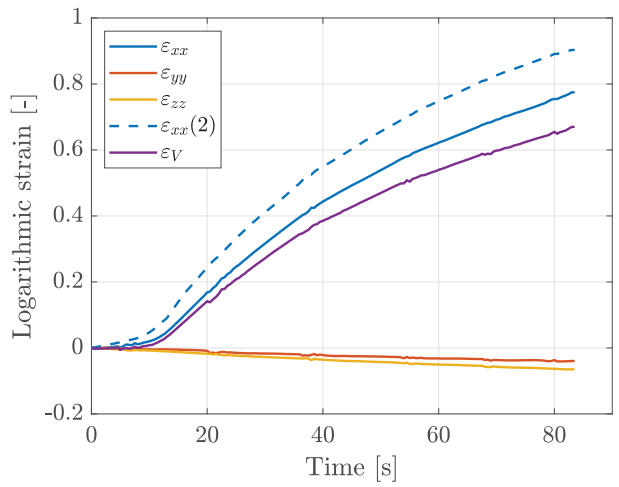
(a) Specimen



(b) Force - displacement



(c) Stress - logarithmic strain



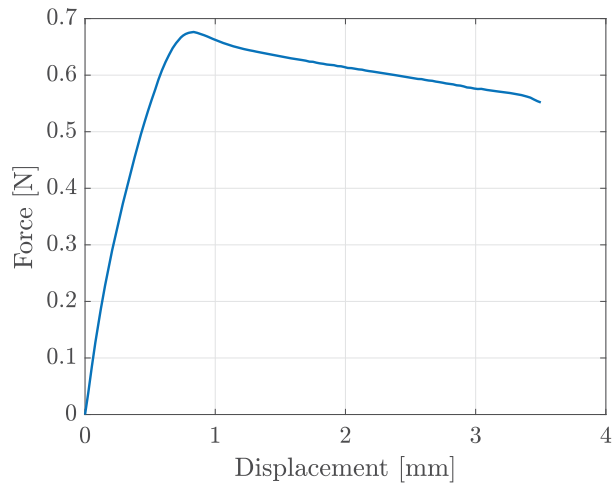
(d) Strain components - time

B.2.5 UT_A-2_00_L_-30

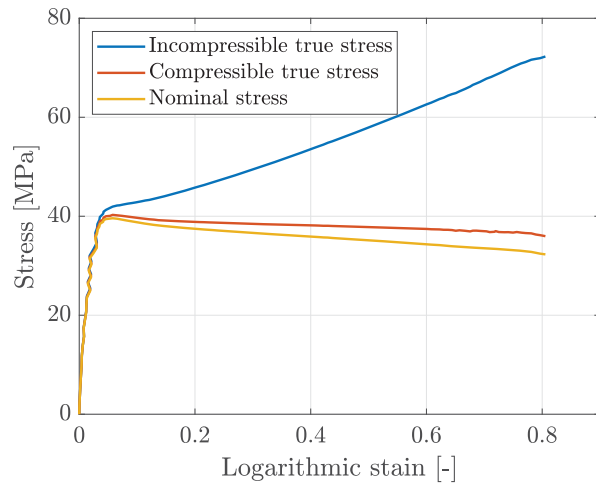
Location	A
\angle	0°
$\dot{\epsilon}_0$	$10^{-1.5} \text{ s}^{-1}$
T	-30 °C
Door trim no.	2
t_0	2.42 mm
w_0	7.05 mm
t_d	19 s
ϵ_f	0.81



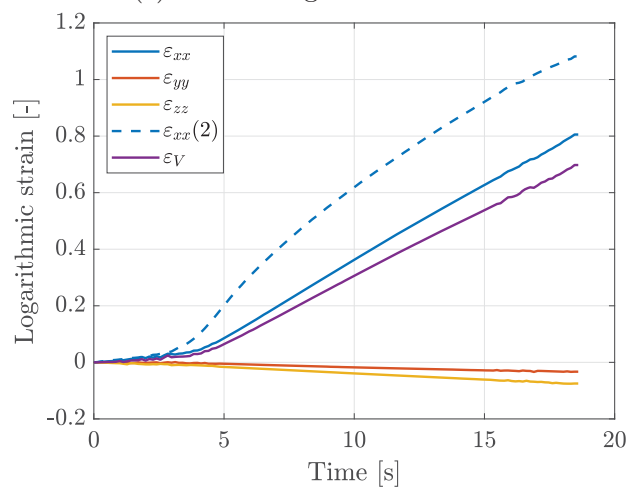
(a) Specimen



(b) Force - displacement



(c) Stress - logarithmic strain



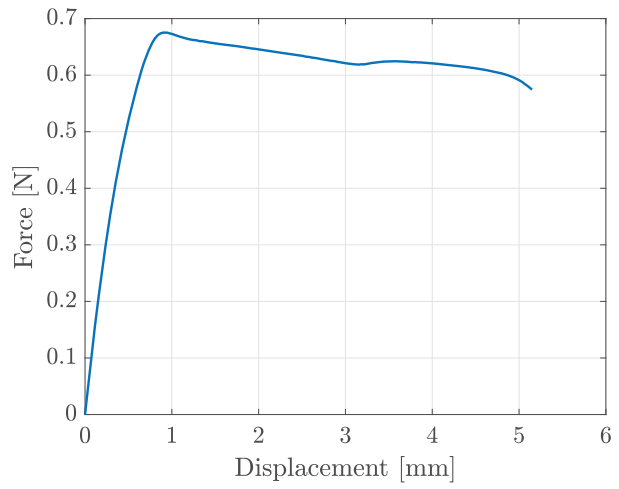
(d) Strain components - time

B.2.6 UT_A-2_45_L_-30

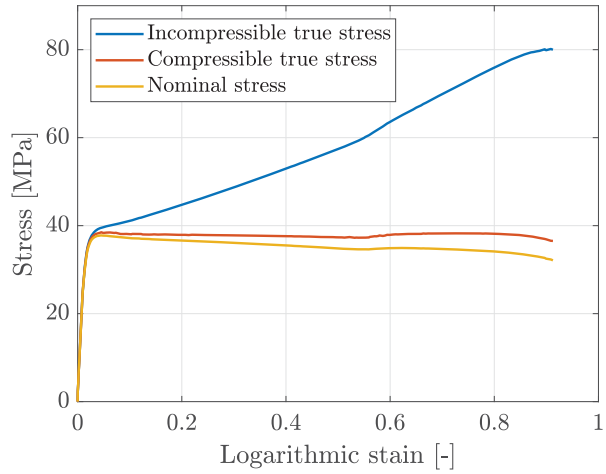
Location	A
\angle	45°
$\dot{\epsilon}_0$	$10^{-1.5} \text{ s}^{-1}$
T	-30 °C
Door trim no.	2
t_0	2.54 mm
w_0	7.05 mm
t_d	27 s
ϵ_f	0.91



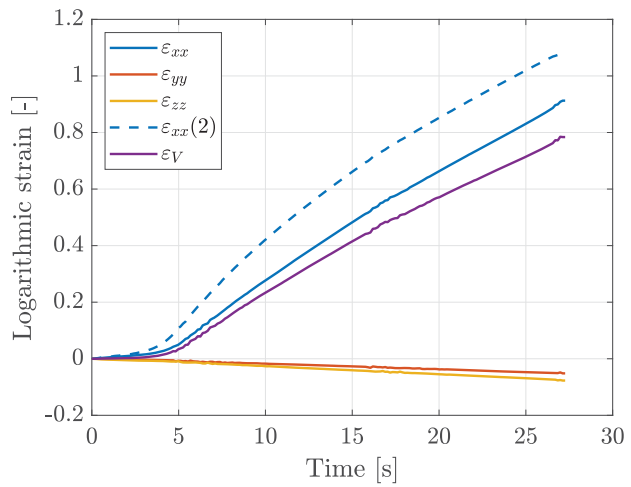
(a) Specimen



(b) Force - displacement



(c) Stress - logarithmic strain



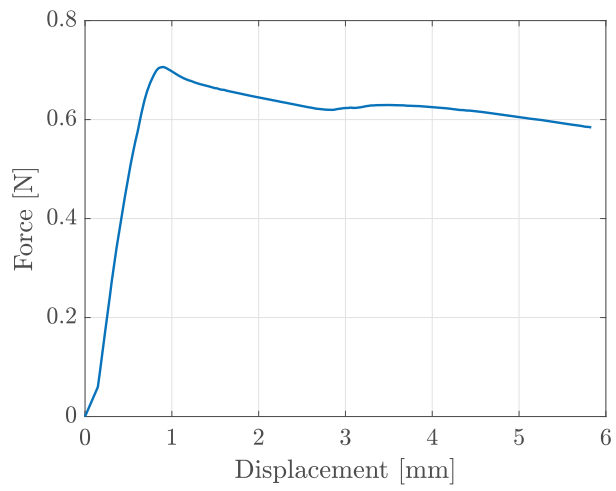
(d) Strain components - time

B.2.7 UT_A-2_90_L_-30

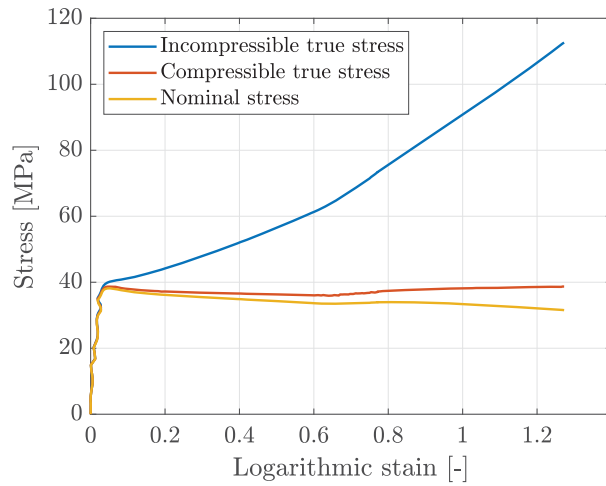
Location	A
\angle	90°
$\dot{\epsilon}_0$	$10^{-1.5} \text{ s}^{-1}$
T	-30 °C
Door trim no.	2
t_0	2.62 mm
w_0	7.06 mm
t_d	30 s
ϵ_f	1.27



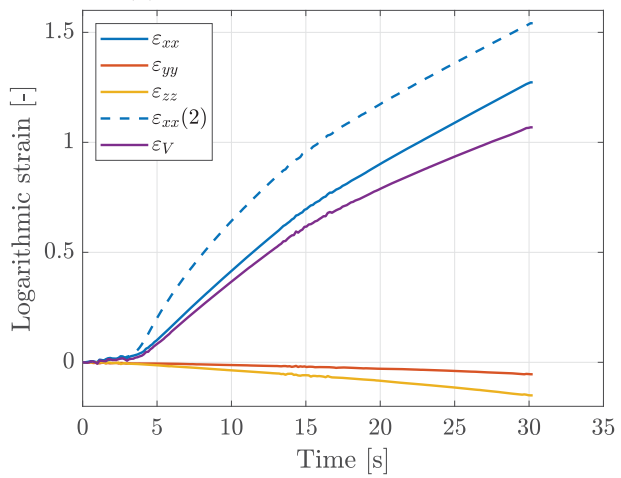
(a) Specimen



(b) Force - displacement



(c) Stress - logarithmic strain



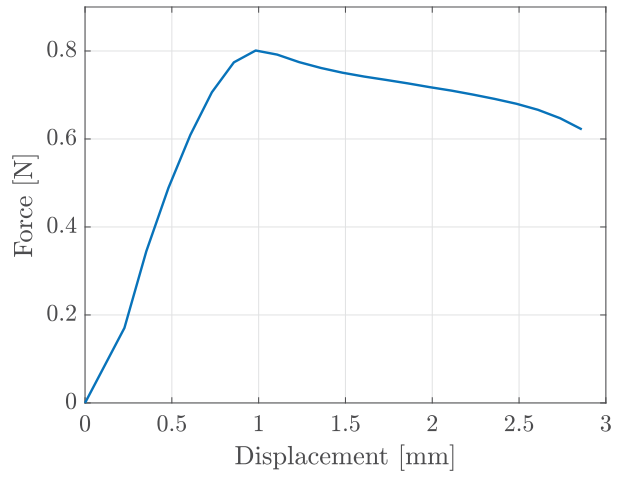
(d) Strain components - time

B.2.8 UT_A-3_00_H_-30

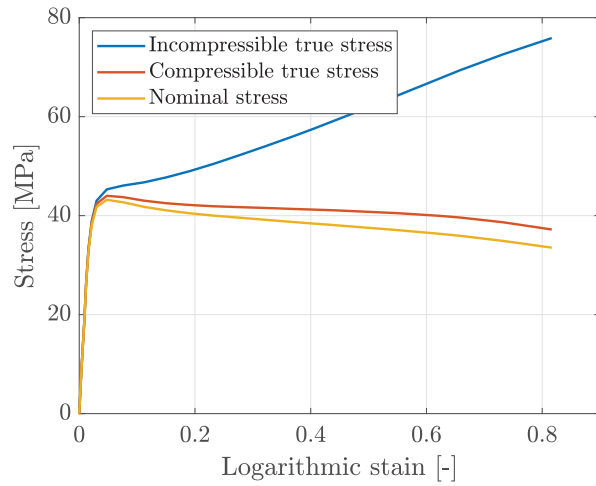
Location	A
\angle	0°
$\dot{\epsilon}_0$	$10^{-0.5} \text{ s}^{-1}$
T	-30 °C
Door trim no.	3
t_0	2.63 mm
w_0	7.05 mm
t_d	2 s
ϵ_f	0.82



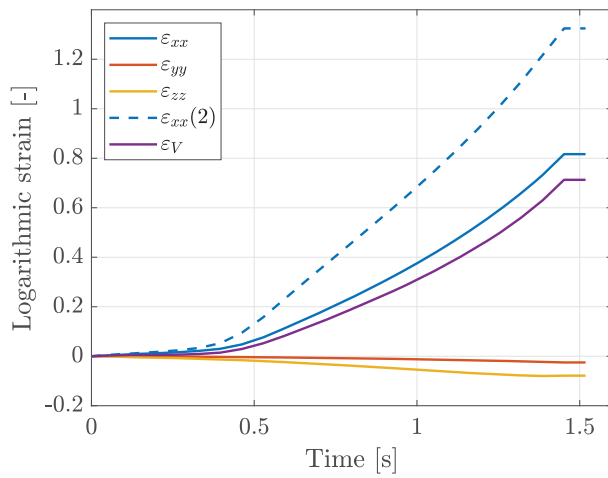
(a) Specimen



(b) Force - displacement



(c) Stress - logarithmic strain



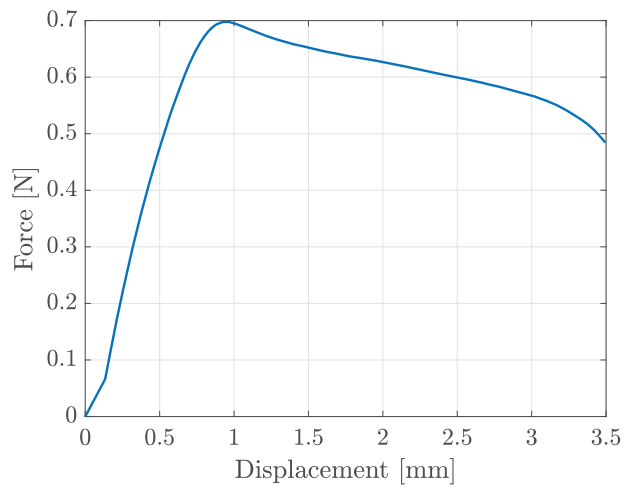
(d) Strain components - time

B.2.9 UT_A-3_00_M_-30

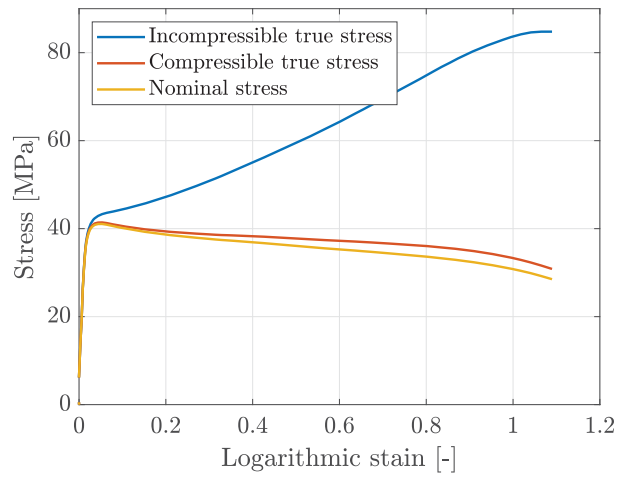
Location	A
\angle	0°
$\dot{\epsilon}_0$	10 ^{-1.0} s ⁻¹
T	-30 °C
Door trim no.	3
t_0	2.41 mm
w_0	7.05 mm
t_d	6 s
ϵ_f	1.09



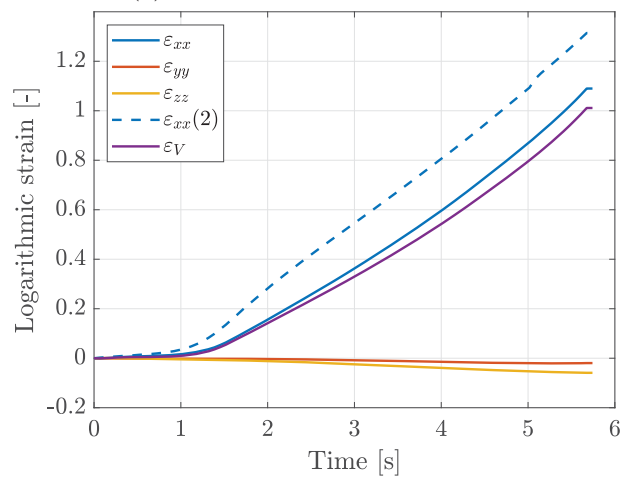
(a) Specimen



(b) Force - displacement



(c) Stress - logarithmic strain



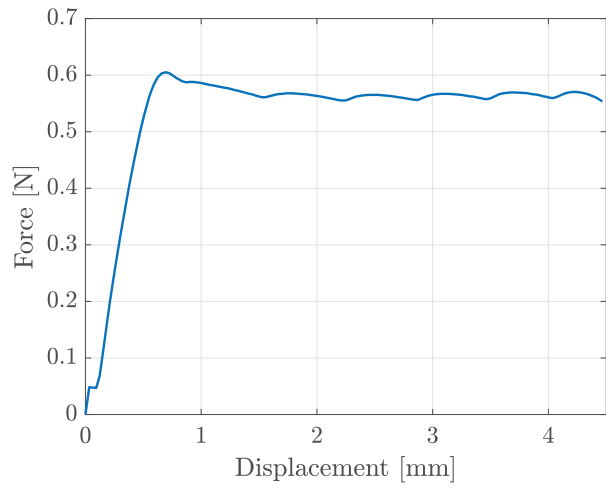
(d) Strain components - time

B.2.10 UT_A-3_00_VL_-30

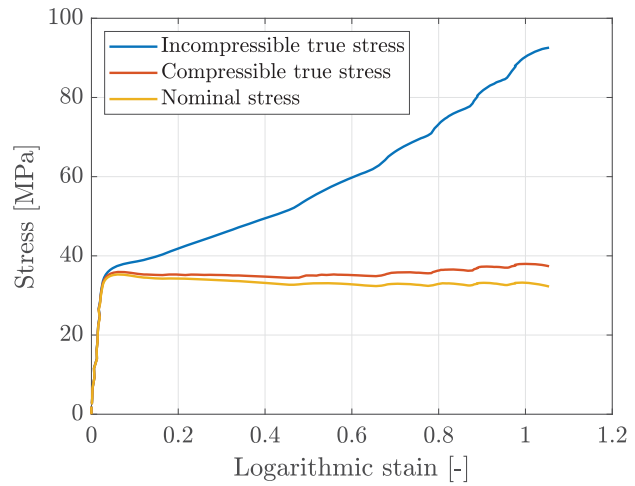
Location	A
\angle	0°
$\dot{\epsilon}_0$	$10^{-2.0} \text{ s}^{-1}$
T	-30 °C
Door trim no.	3
t_0	2.44 mm
w_0	7.04 mm
t_d	75 s
ϵ_f	1.05



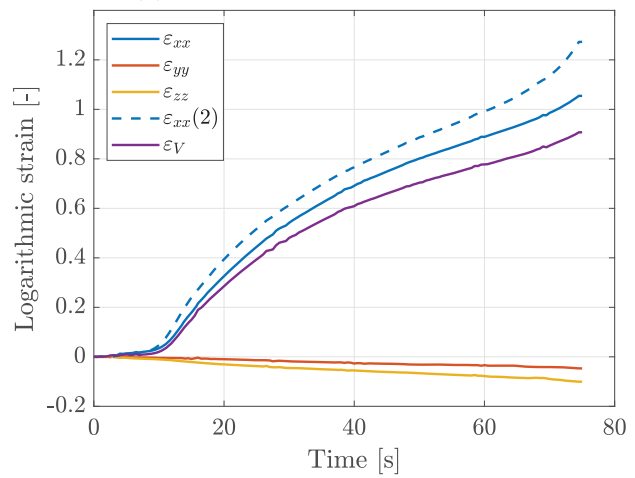
(a) Specimen



(b) Force - displacement



(c) Stress - logarithmic strain



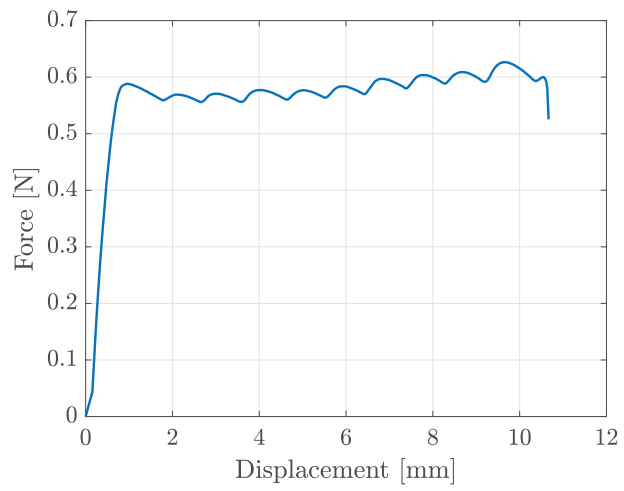
(d) Strain components - time

B.2.11 UT_B-10_00_VL_-30

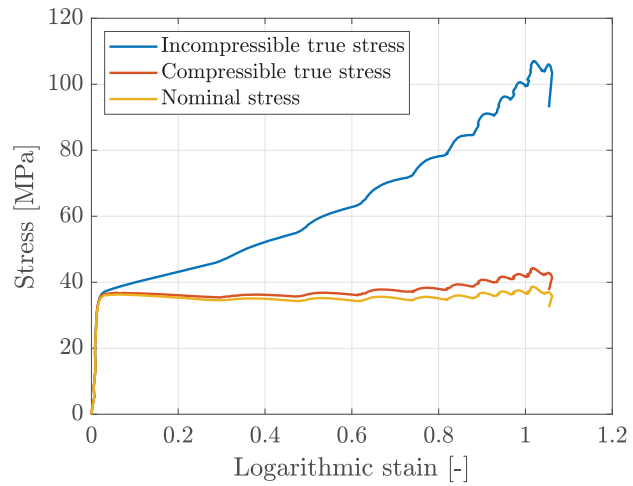
Location	B
\angle	0°
$\dot{\epsilon}_0$	$10^{-2.0} \text{ s}^{-1}$
T	-30 °C
Door trim no.	10
t_0	2.3 mm
w_0	7.04 mm
t_d	177 s
ϵ_f	1.05



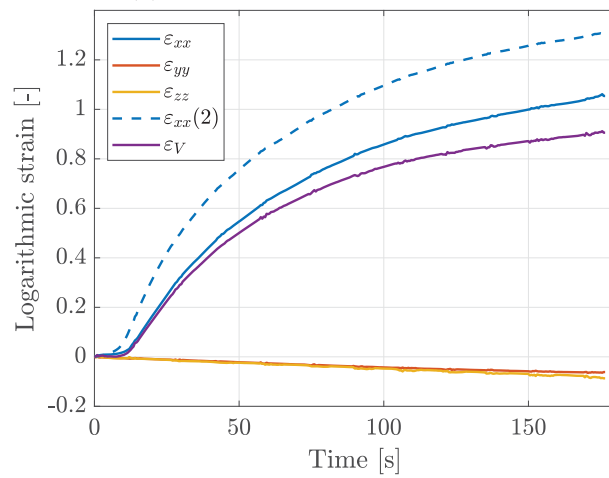
(a) Specimen



(b) Force - displacement



(c) Stress - logarithmic strain



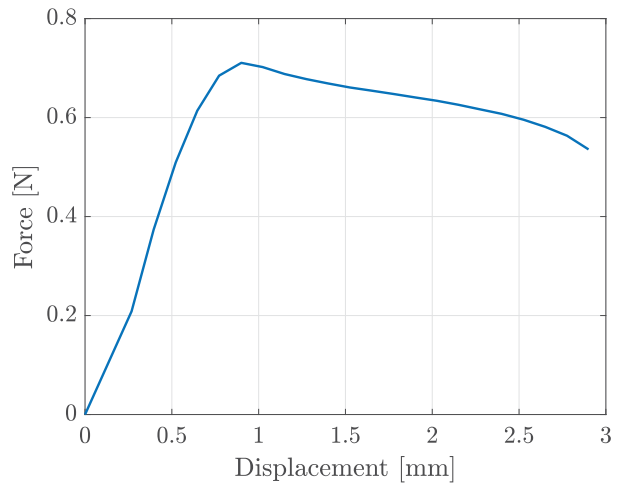
(d) Strain components - time

B.2.12 UT_B-11_00_H_-30

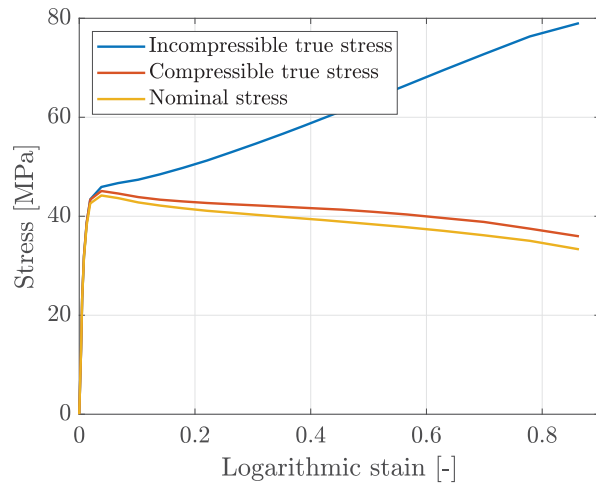
Location	B
\angle	0°
$\dot{\epsilon}_0$	$10^{-0.5} \text{ s}^{-1}$
T	-30 °C
Door trim no.	11
t_0	2.29 mm
w_0	7.03 mm
t_d	2 s
ϵ_f	0.86



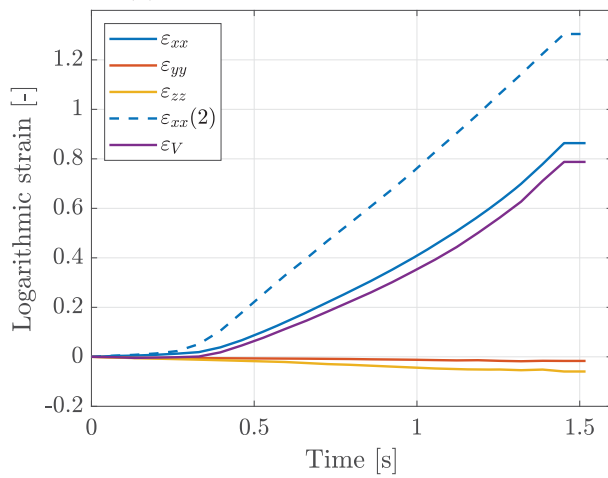
(a) Specimen



(b) Force - displacement



(c) Stress - logarithmic strain



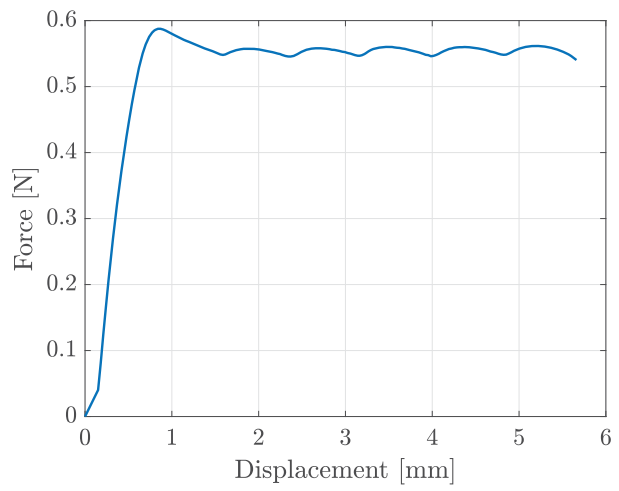
(d) Strain components - time

B.2.13 UT_B-11_00_VL_-30

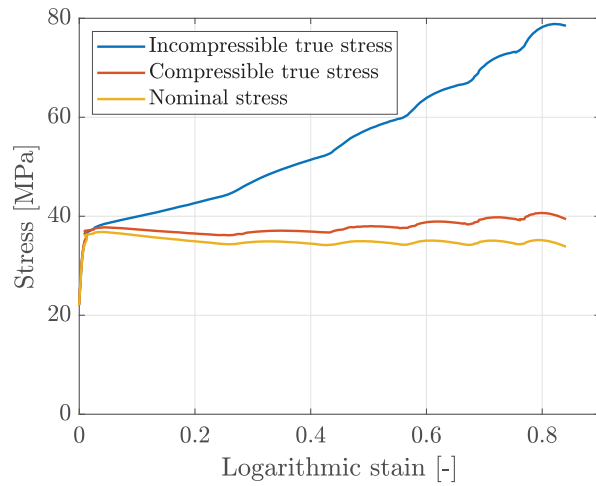
Location	B
\angle	0°
$\dot{\epsilon}_0$	$10^{-2.0} \text{ s}^{-1}$
T	-30 °C
Door trim no.	11
t_0	2.27 mm
w_0	7.04 mm
t_d	93 s
ϵ_f	0.84



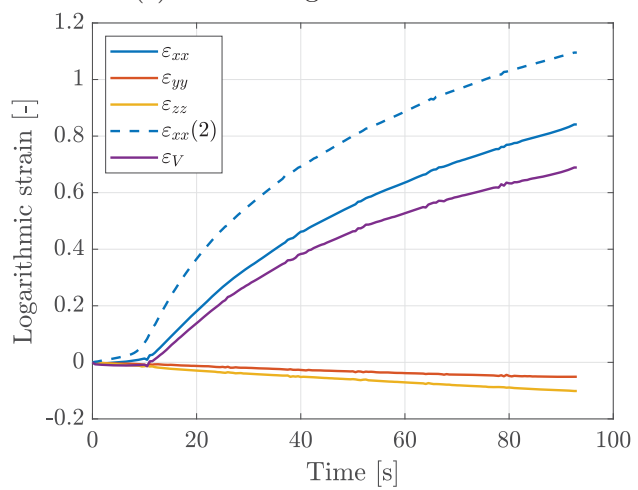
(a) Specimen



(b) Force - displacement



(c) Stress - logarithmic strain



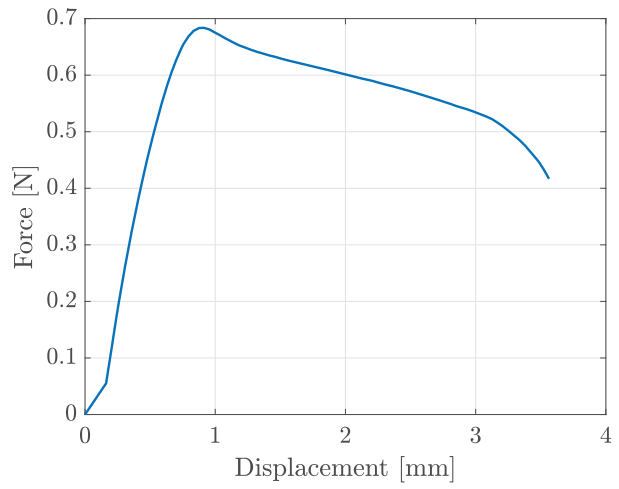
(d) Strain components - time

B.2.14 UT_B-11_00_M_-30

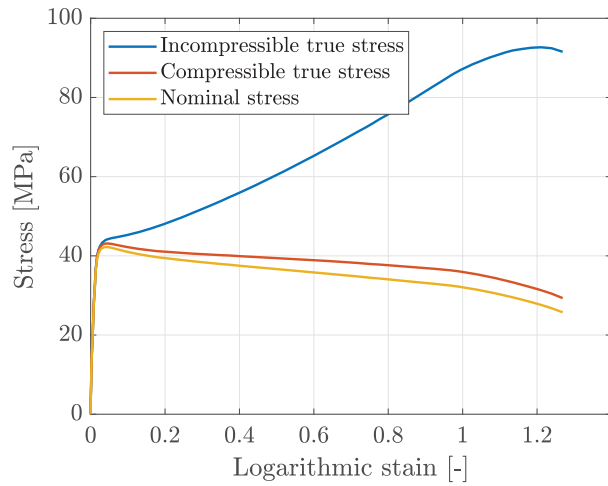
Location	B
\angle	0°
$\dot{\epsilon}_0$	$10^{-1.0} \text{ s}^{-1}$
T	-30 °C
Door trim no.	11
t_0	2.3 mm
w_0	7.04 mm
t_d	6 s
ϵ_f	1.27



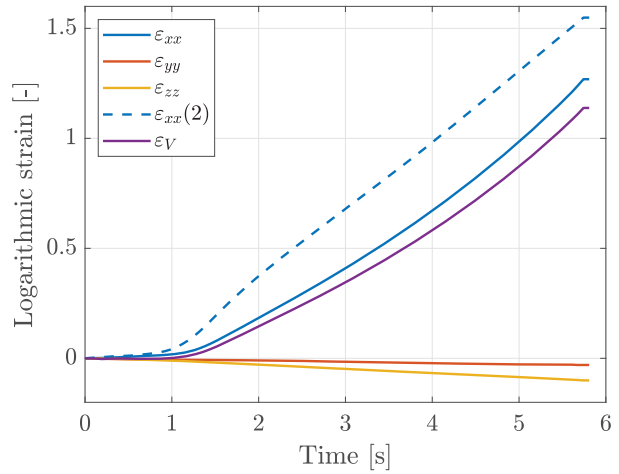
(a) Specimen



(b) Force - displacement



(c) Stress - logarithmic strain



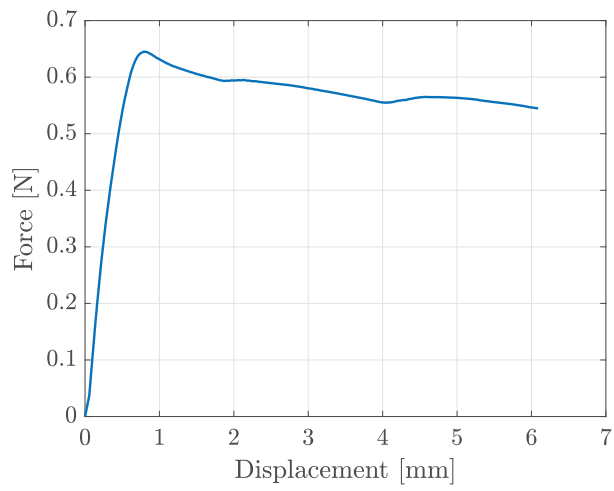
(d) Strain components - time

B.2.15 UT_B-2_00_L_-30

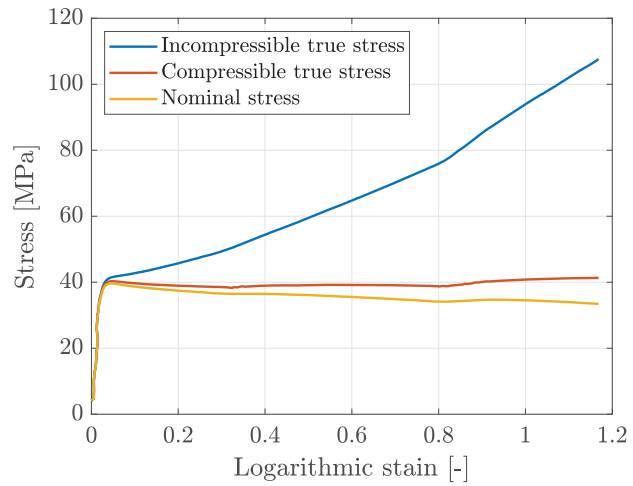
Location	B
\angle	0°
$\dot{\epsilon}_0$	$10^{-1.5} \text{ s}^{-1}$
T	-30 °C
Door trim no.	2
t_0	2.31 mm
w_0	7.05 mm
t_d	32 s
ϵ_f	1.17



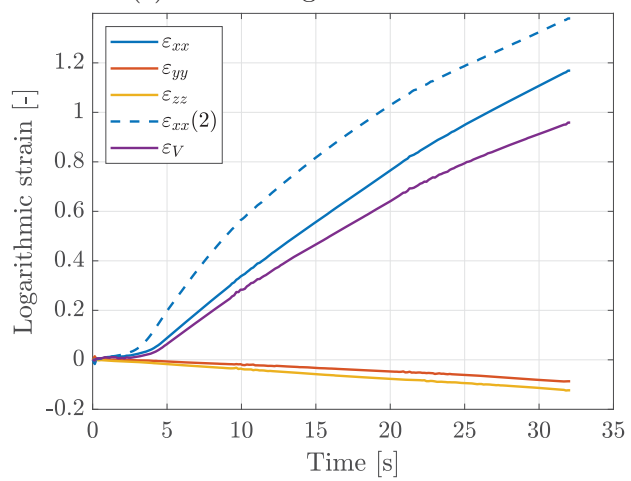
(a) Specimen



(b) Force - displacement



(c) Stress - logarithmic strain



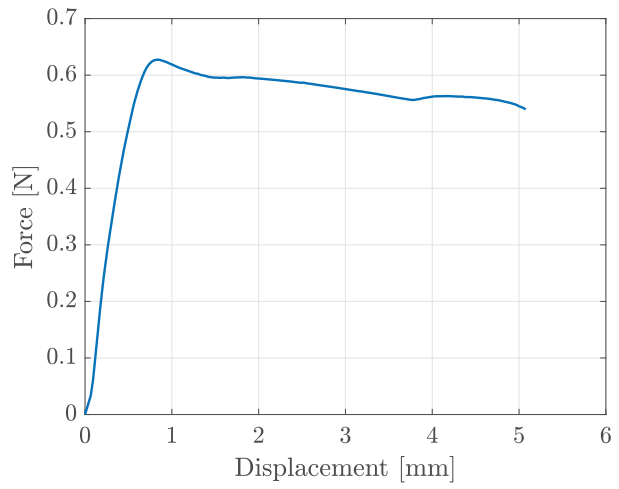
(d) Strain components - time

B.2.16 UT_B-2_45_L_-30

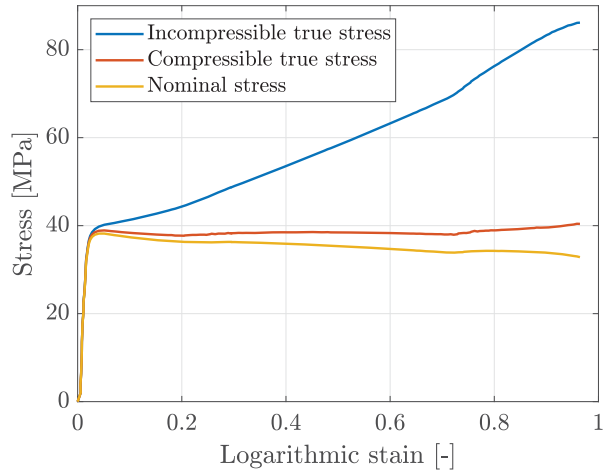
Location	B
\angle	45°
$\dot{\epsilon}_0$	$10^{-1.5} \text{ s}^{-1}$
T	-30 °C
Door trim no.	2
t_0	2.33 mm
w_0	7.05 mm
t_d	27 s
ϵ_f	0.96



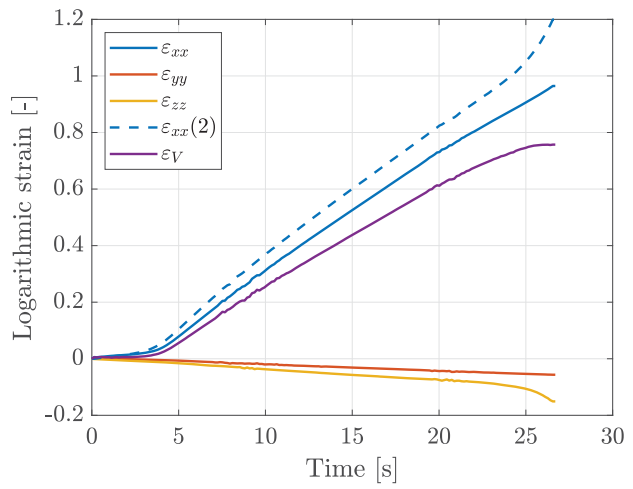
(a) Specimen



(b) Force - displacement



(c) Stress - logarithmic strain



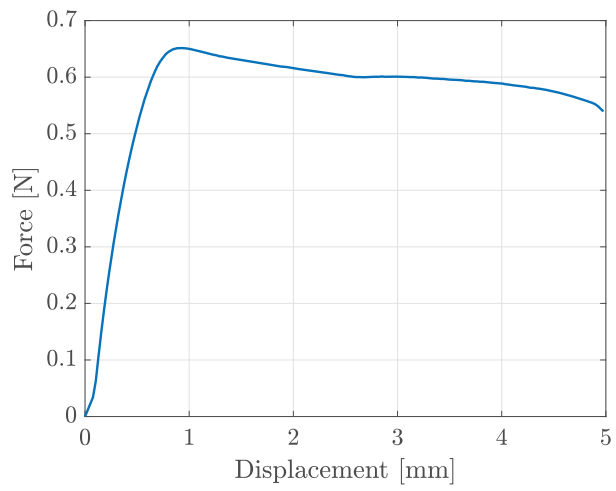
(d) Strain components - time

B.2.17 UT_B-2_90_L_-30

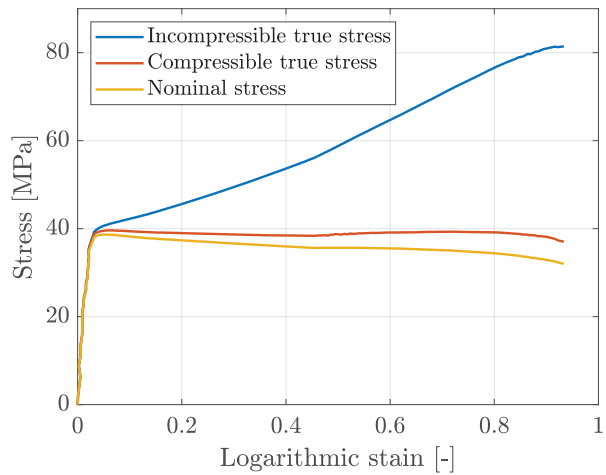
Location	B
\angle	90°
$\dot{\epsilon}_0$	$10^{-1.5} \text{ s}^{-1}$
T	-30 °C
Door trim no.	2
t_0	2.4 mm
w_0	7.02 mm
t_d	26 s
ϵ_f	0.93



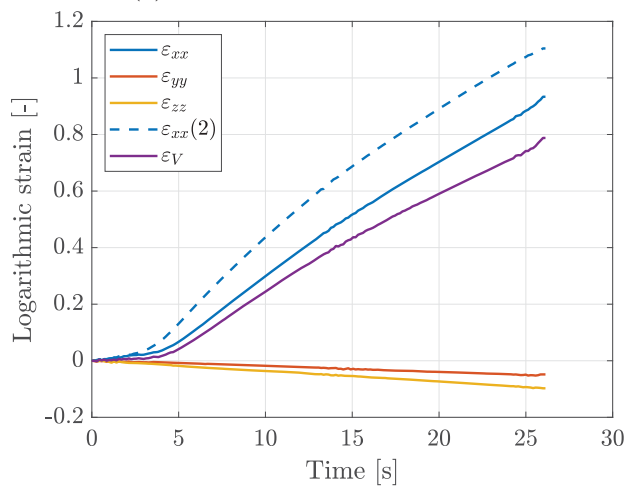
(a) Specimen



(b) Force - displacement



(c) Stress - logarithmic strain



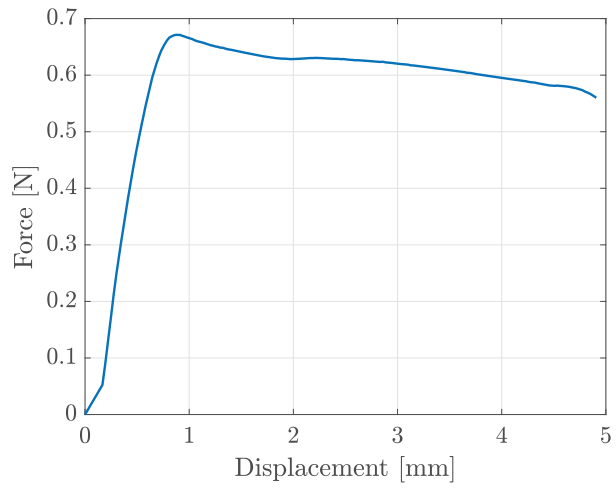
(d) Strain components - time

B.2.18 UT_CS-12_90_L_-30

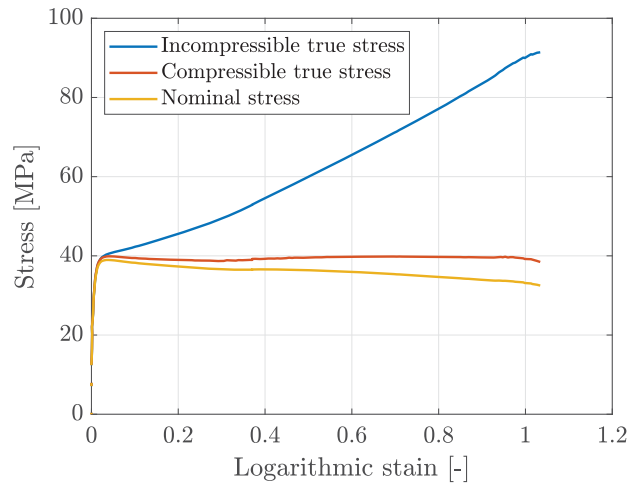
Location	CS
\angle	90°
$\dot{\epsilon}_0$	$10^{-1.5} \text{ s}^{-1}$
T	-30 °C
Door trim no.	12
t_0	2.45 mm
w_0	7.04 mm
t_d	25 s
ϵ_f	1.03



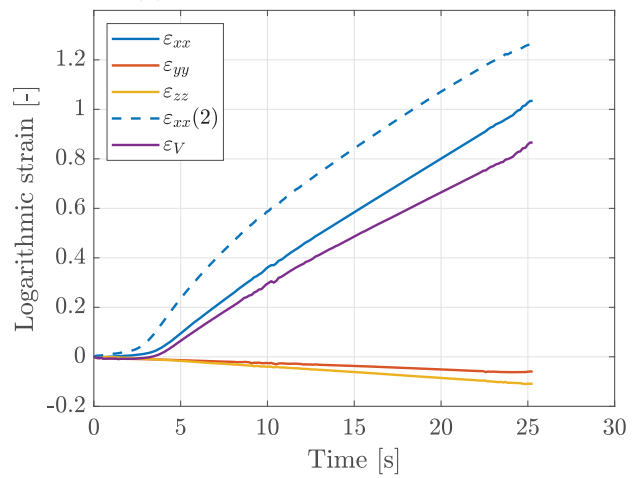
(a) Specimen



(b) Force - displacement



(c) Stress - logarithmic strain



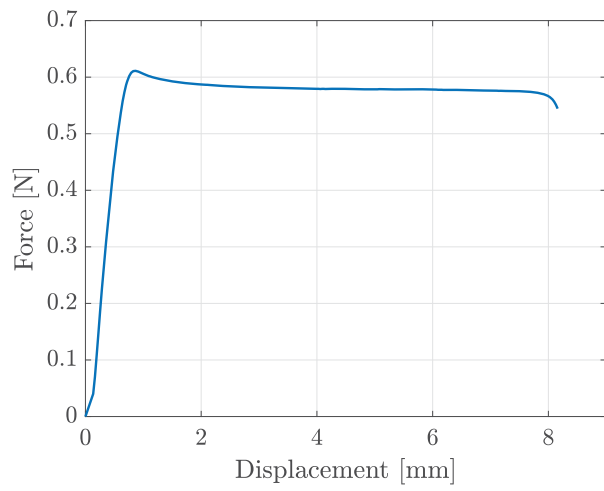
(d) Strain components - time

B.2.19 UT_CS-12_90_VL_-30

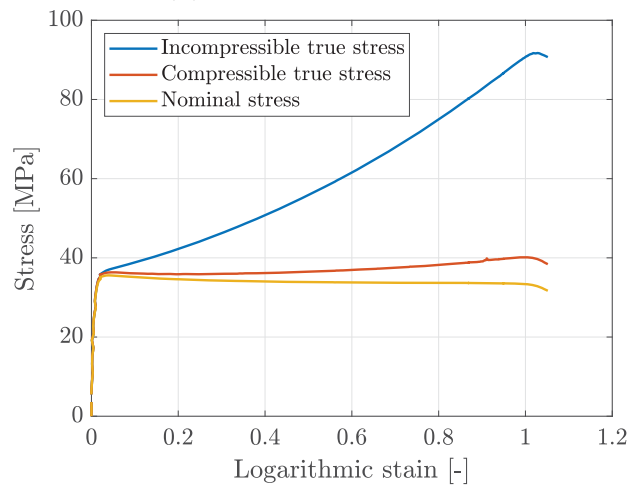
Location	CS
\angle	90°
$\dot{\epsilon}_0$	$10^{-2.0} \text{ s}^{-1}$
T	-30 °C
Door trim no.	12
t_0	2.44 mm
w_0	7.04 mm
t_d	135 s
ϵ_f	1.05



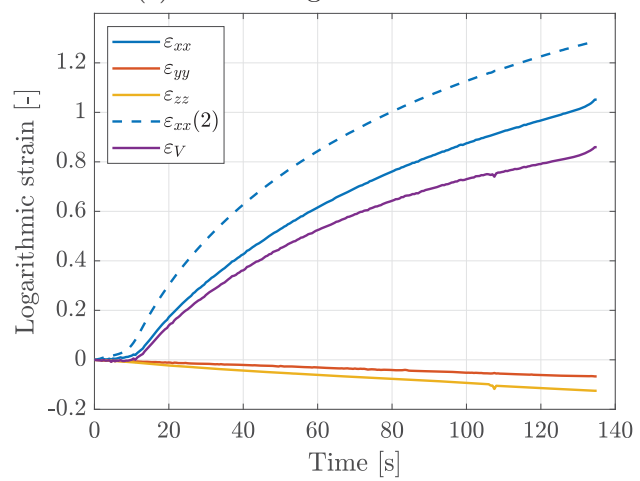
(a) Specimen



(b) Force - displacement



(c) Stress - logarithmic strain



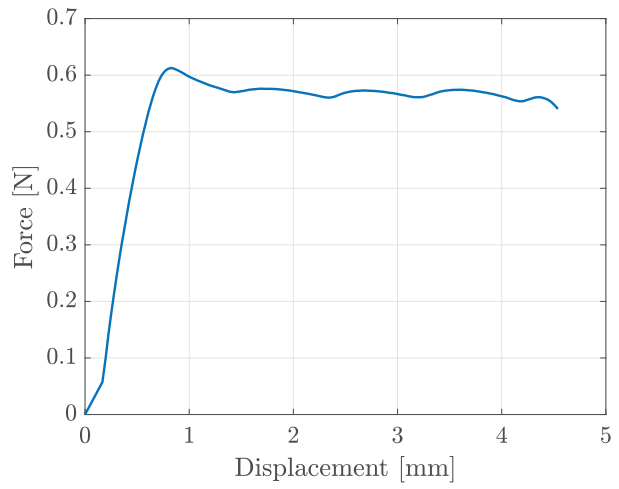
(d) Strain components - time

B.2.20 UT_CR-1_00_VL_-30

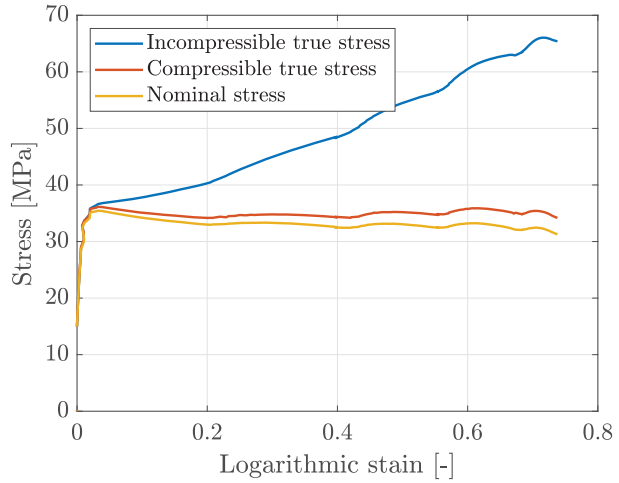
Location	CR
\angle	0°
$\dot{\epsilon}_0$	$10^{-2.0} \text{ s}^{-1}$
T	-30 °C
Door trim no.	1
t_0	2.44 mm
w_0	7.09 mm
t_d	74 s
ϵ_f	0.74



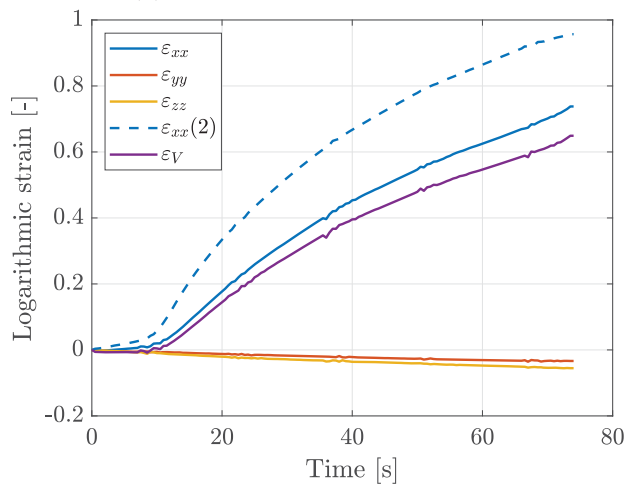
(a) Specimen



(b) Force - displacement



(c) Stress - logarithmic strain



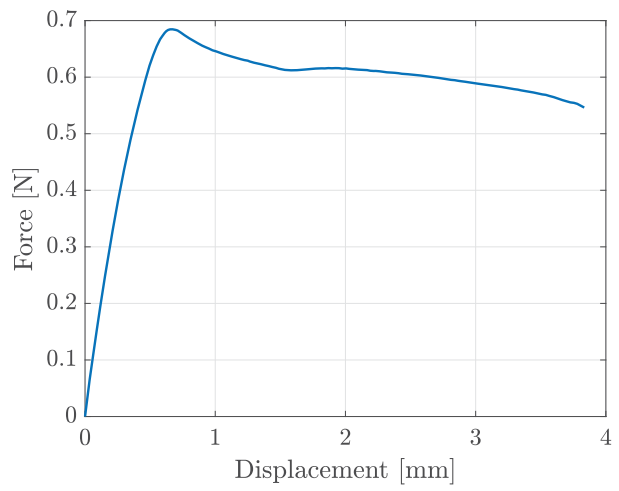
(d) Strain components - time

B.2.21 UT_CR-2_00_L_-30

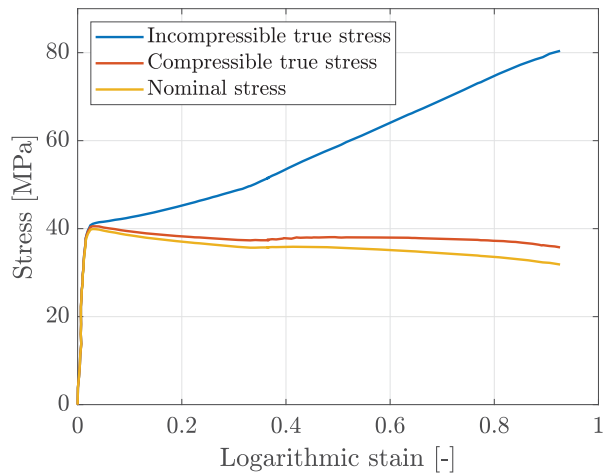
Location	CR
\angle	0°
$\dot{\epsilon}_0$	$10^{-1.5} \text{ s}^{-1}$
T	$-30 \text{ }^\circ\text{C}$
Door trim no.	2
t_0	2.43 mm
w_0	7.05 mm
t_d	20 s
ϵ_f	0.93



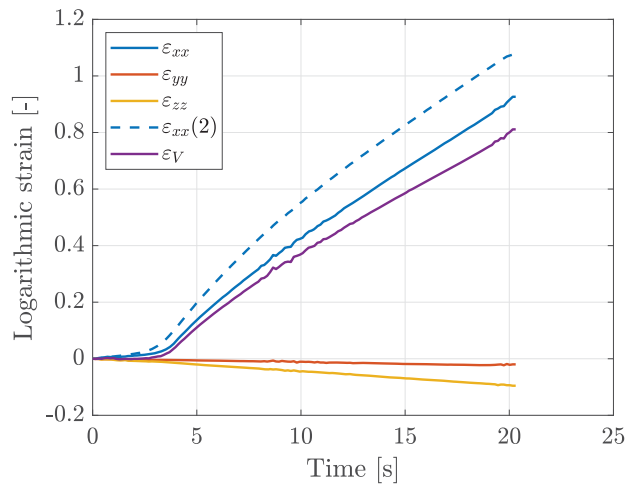
(a) Specimen



(b) Force - displacement



(c) Stress - logarithmic strain



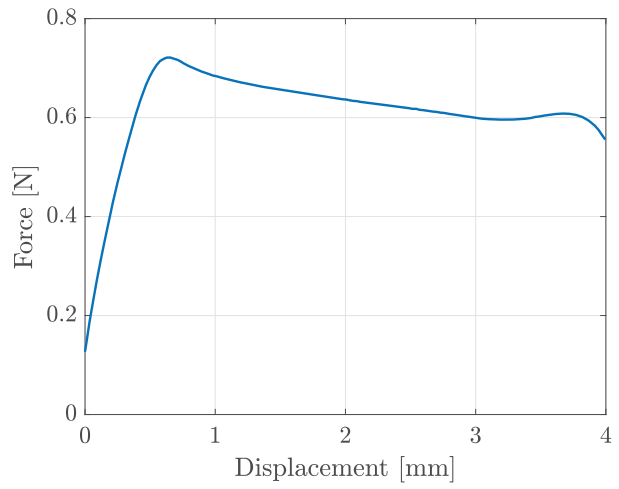
(d) Strain components - time

B.2.22 UT_CR-2_45_L_-30

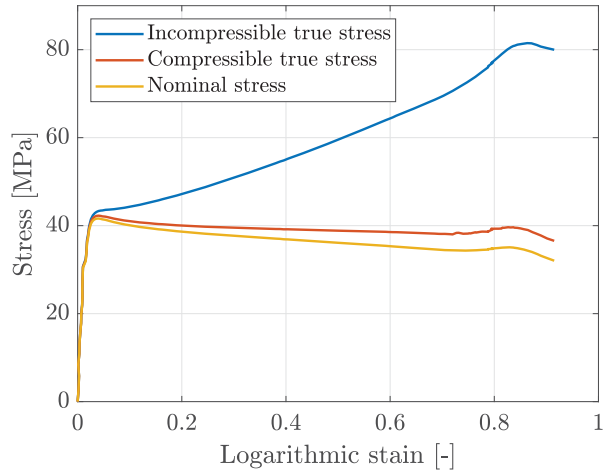
Location	CR
\angle	45°
$\dot{\epsilon}_0$	$10^{-1.5} \text{ s}^{-1}$
T	-30 °C
Door trim no.	2
t_0	2.46 mm
w_0	7.05 mm
t_d	22 s
ϵ_f	0.92



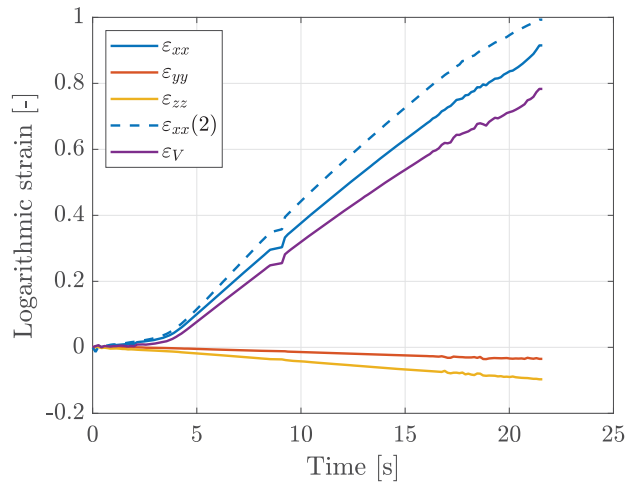
(a) Specimen



(b) Force - displacement



(c) Stress - logarithmic strain



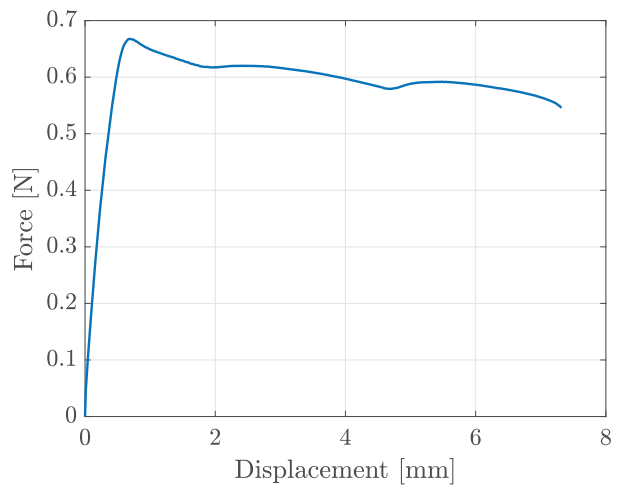
(d) Strain components - time

B.2.23 UT_CR-2_90_L_-30

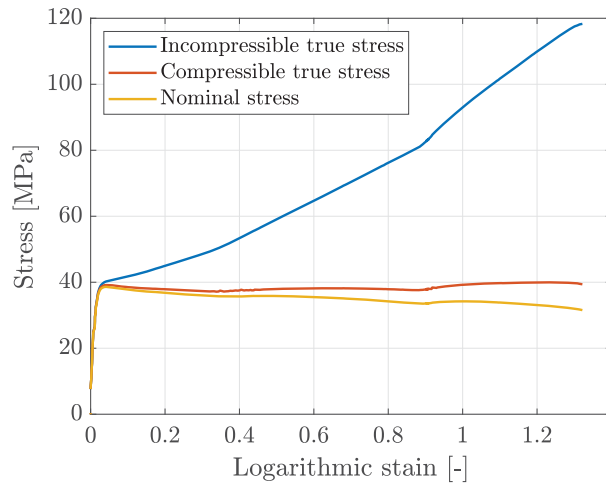
Location	CR
\angle	90°
$\dot{\epsilon}_0$	$10^{-1.5} \text{ s}^{-1}$
T	-30 °C
Door trim no.	2
t_0	2.45 mm
w_0	7.06 mm
t_d	39 s
ϵ_f	1.32



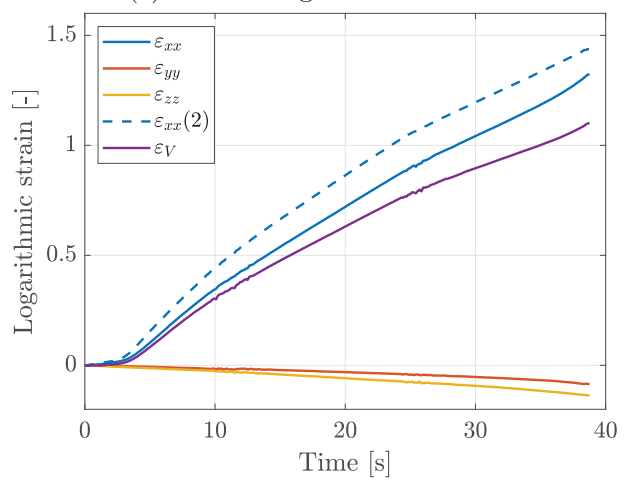
(a) Specimen



(b) Force - displacement



(c) Stress - logarithmic strain



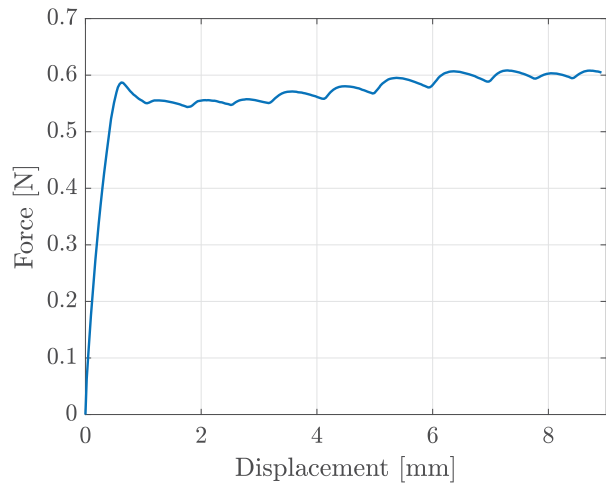
(d) Strain components - time

B.2.24 UT_CR-3_00_VL_-30

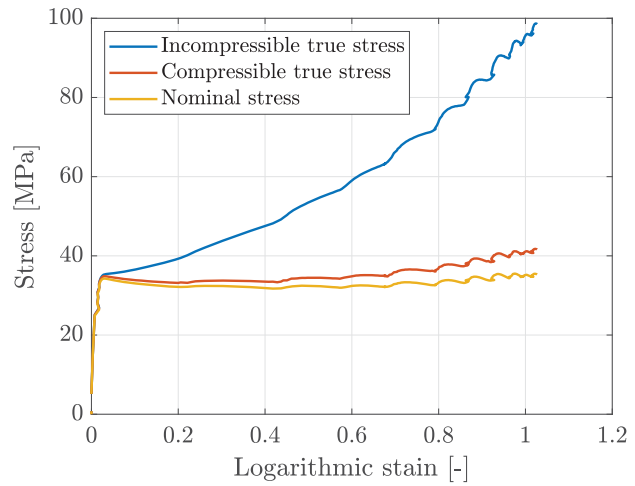
Location	CR
\angle	0°
$\dot{\epsilon}_0$	$10^{-2.0} \text{ s}^{-1}$
T	$-30 \text{ }^\circ\text{C}$
Door trim no.	3
t_0	2.43 mm
w_0	7.05 mm
t_d	150 s
ϵ_f	1.03



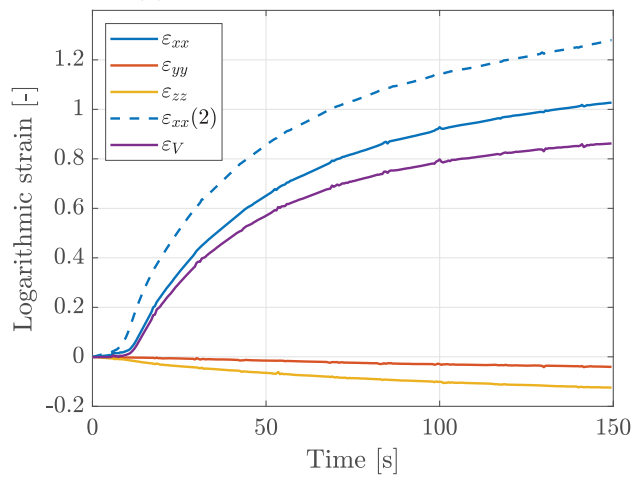
(a) Specimen



(b) Force - displacement



(c) Stress - logarithmic strain



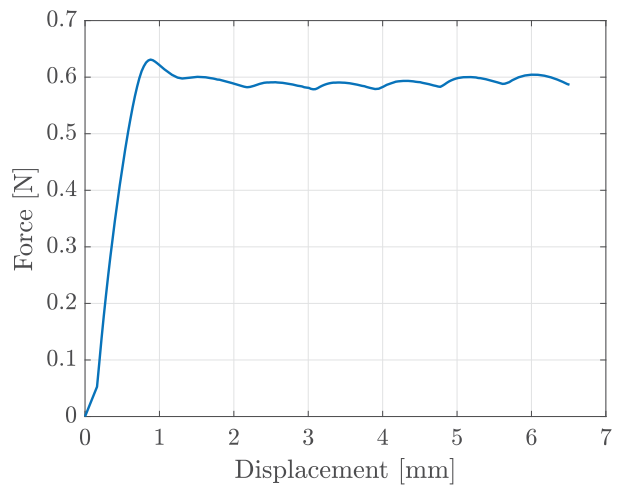
(d) Strain components - time

B.2.25 UT_CL-1_00_VL_-30

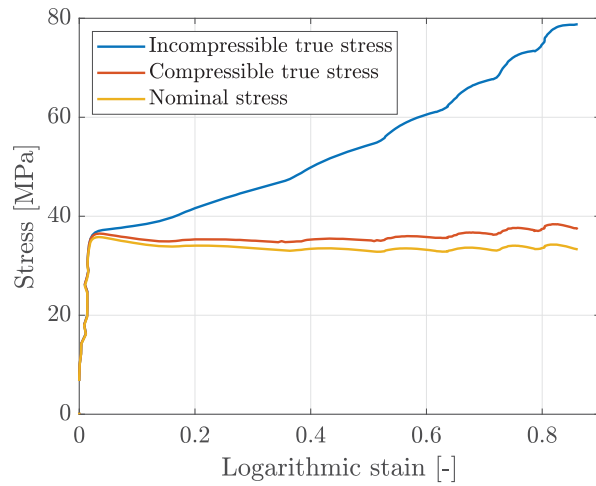
Location	CL
\angle	0°
$\dot{\epsilon}_0$	$10^{-2.0} \text{ s}^{-1}$
T	-30 °C
Door trim no.	1
t_0	2.5 mm
w_0	7.05 mm
t_d	107 s
ϵ_f	0.86



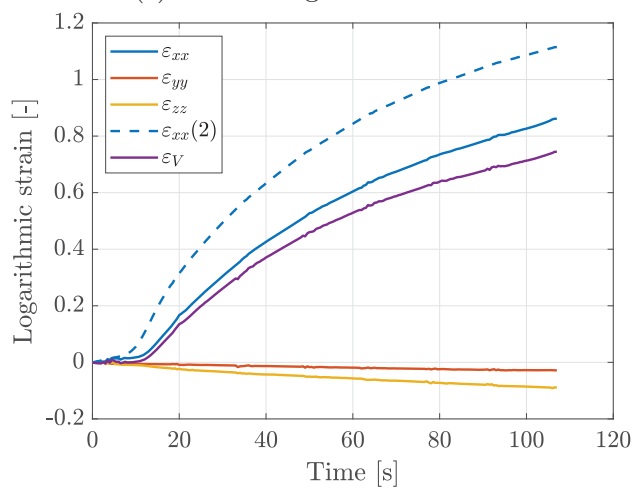
(a) Specimen



(b) Force - displacement



(c) Stress - logarithmic strain



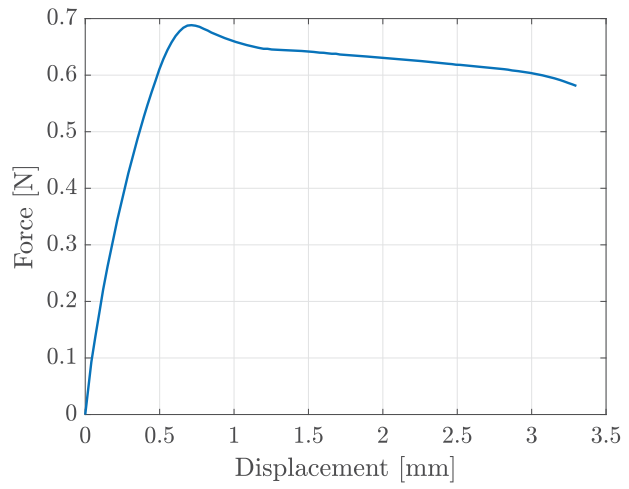
(d) Strain components - time

B.2.26 UT_CL-2_00_L_-30

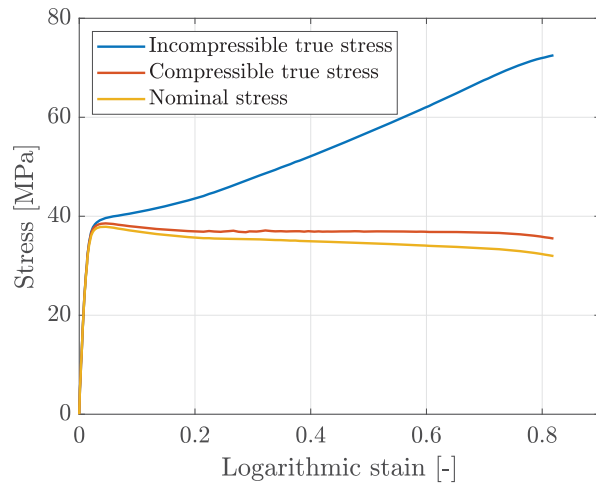
Location	CL
\angle	0°
$\dot{\epsilon}_0$	$10^{-1.5} \text{ s}^{-1}$
T	-30 °C
Door trim no.	2
t_0	2.6 mm
w_0	7 mm
t_d	17 s
ϵ_f	0.82



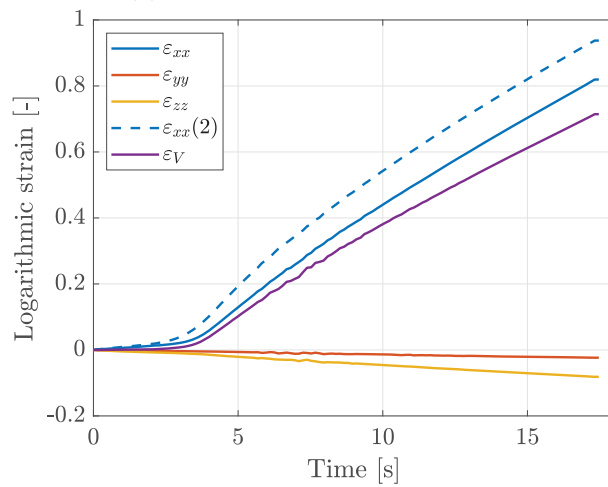
(a) Specimen



(b) Force - displacement



(c) Stress - logarithmic strain



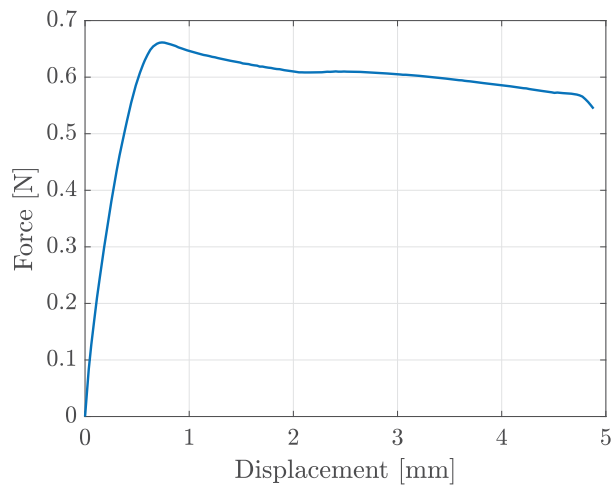
(d) Strain components - time

B.2.27 UT_CL-2_45_L_-30

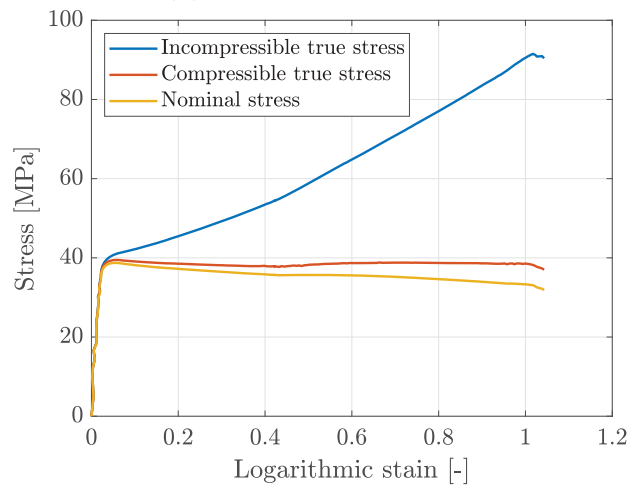
Location	CL
\angle	45°
$\dot{\epsilon}_0$	$10^{-1.5} \text{ s}^{-1}$
T	-30 °C
Door trim no.	2
t_0	2.43 mm
w_0	7.04 mm
t_d	26 s
ϵ_f	1.04



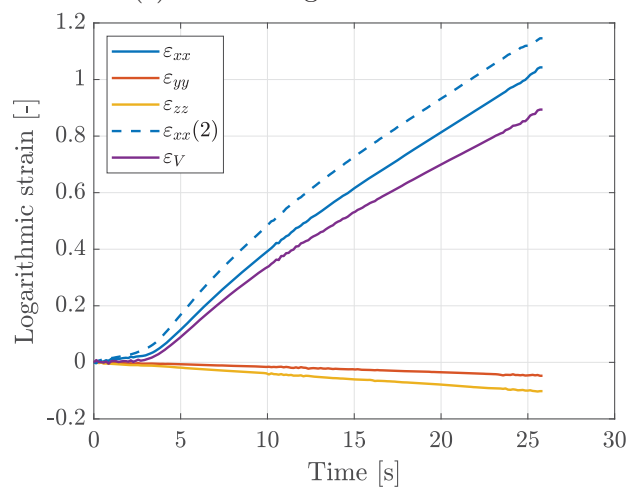
(a) Specimen



(b) Force - displacement



(c) Stress - logarithmic strain



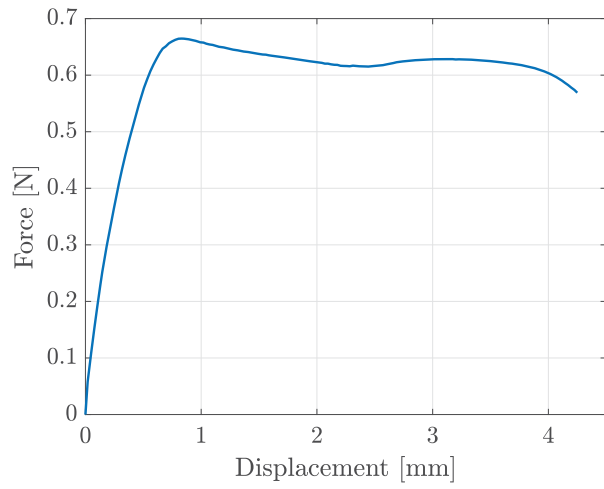
(d) Strain components - time

B.2.28 UT_CL-2_90_L_-30

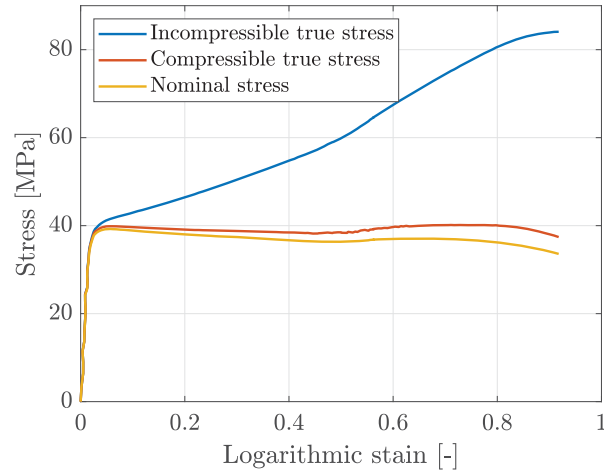
Location	CL
\angle	90°
$\dot{\epsilon}_0$	$10^{-1.5} \text{ s}^{-1}$
T	-30 °C
Door trim no.	2
t_0	2.41 mm
w_0	7.04 mm
t_d	23 s
ϵ_f	0.92



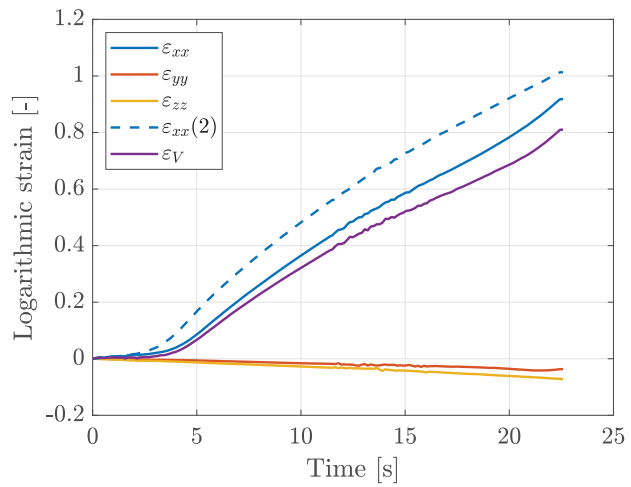
(a) Specimen



(b) Force - displacement



(c) Stress - logarithmic strain



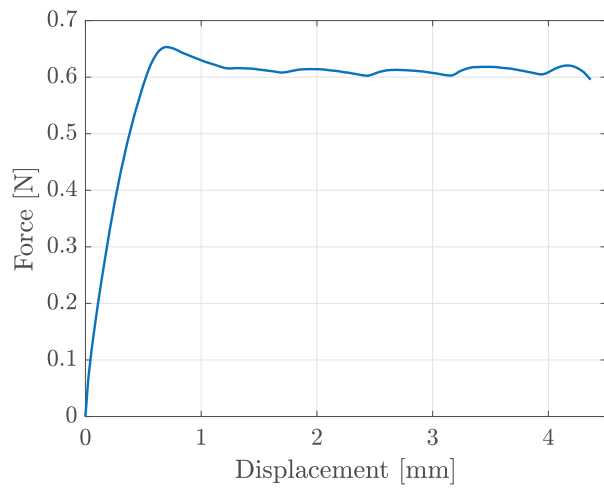
(d) Strain components - time

B.2.29 UT_CL-3_00_VL_-30

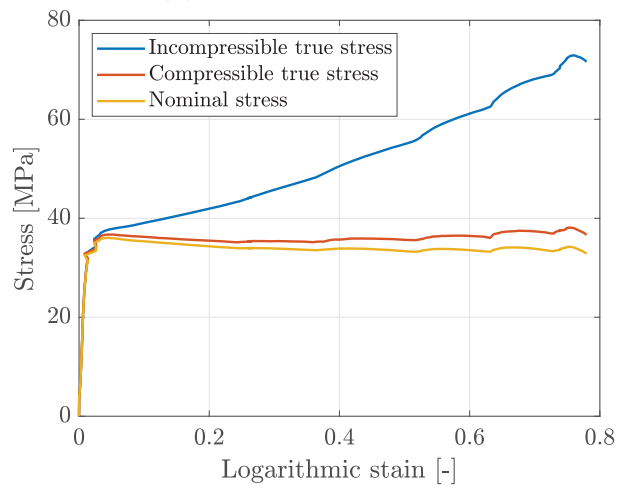
Location	CL
\angle	0°
$\dot{\epsilon}_0$	$10^{-2.0} \text{ s}^{-1}$
T	-30 °C
Door trim no.	3
t_0	2.59 mm
w_0	7 mm
t_d	74 s
ϵ_f	0.78



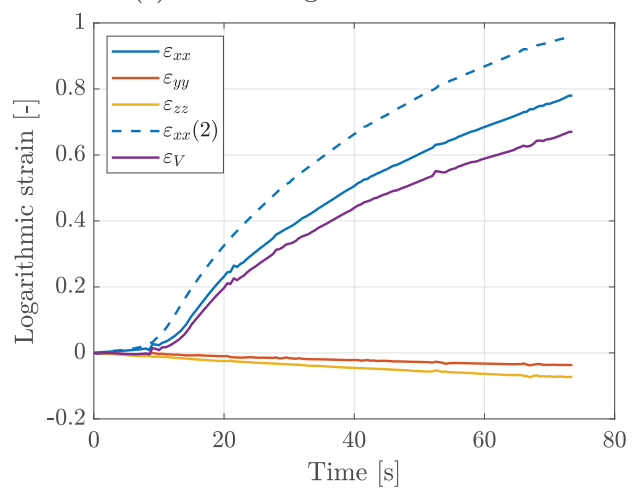
(a) Specimen



(b) Force - displacement



(c) Stress - logarithmic strain



(d) Strain components - time

Drop Tower Tests

In this appendix, the dimensionless force-displacement curves obtained for the door trim cutout specimens are given initially. Additionally, all successful tests conducted in the drop tower are archived. For each test specimen, the test specifics, dimensions and a picture of the deformed geometry is provided. In addition, two different graphs are plotted displaying the force-displacement and velocity-time curves. All recorded data is cut at fracture, but no filter is used. The correction factor is also applied to all results showed here.

The following abbreviations are used in this appendix:

T	Temperature
t_0	Initial specimen thickness
t_d	Test duration
v_i	Initial velocity
v_r	Residual velocity
E	Young's modulus
F	Force
a	Span radius
u	Displacement

C.1 Dimensionless results

In order to account for the slight variation in thickness that was found for the door trim cutout specimens, dimensionless force-displacement curves were plotted. The resulting curves are shown in Figure C.1.1, and are derived using an approach described by Daiyan et al. [54]. Here, F denotes the force, a corresponds to the span radius, E describes the Young's modulus, t is the plate thickness and u denotes the central displacement of the plate.

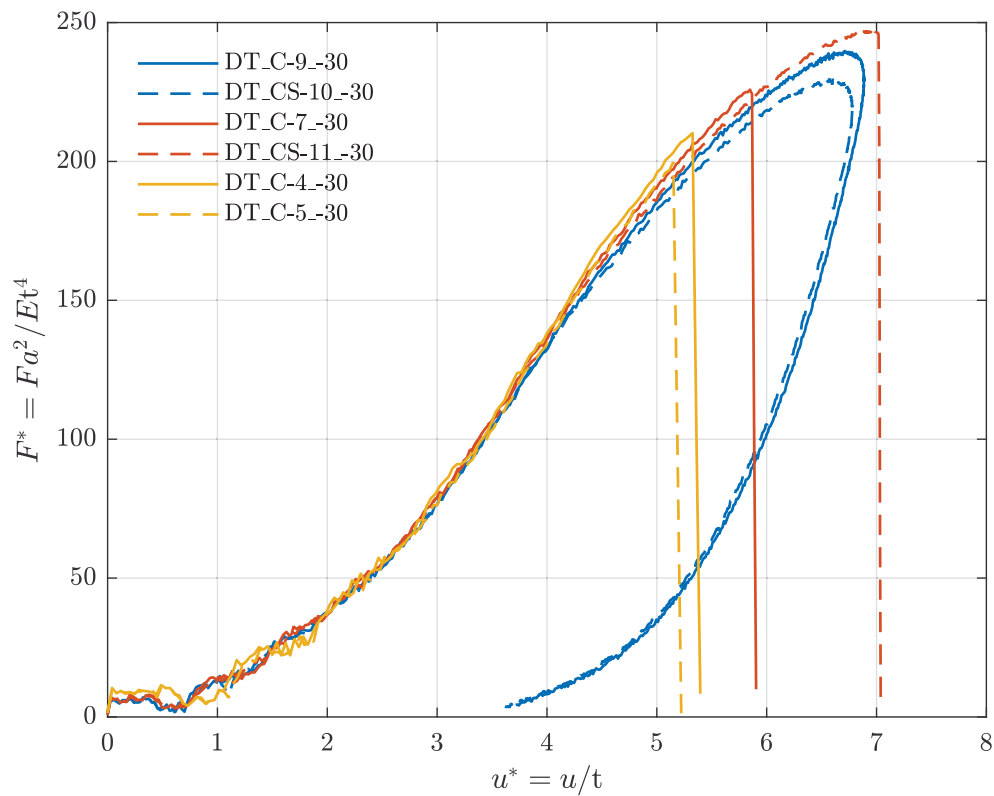


Figure C.1.1: Dimensionless force-displacement curve for door trim cutouts

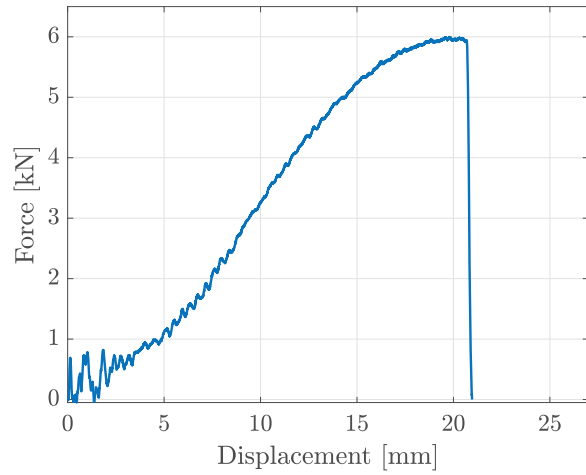
C.2 Material sample plates

C.2.1 DT_S_-30_07

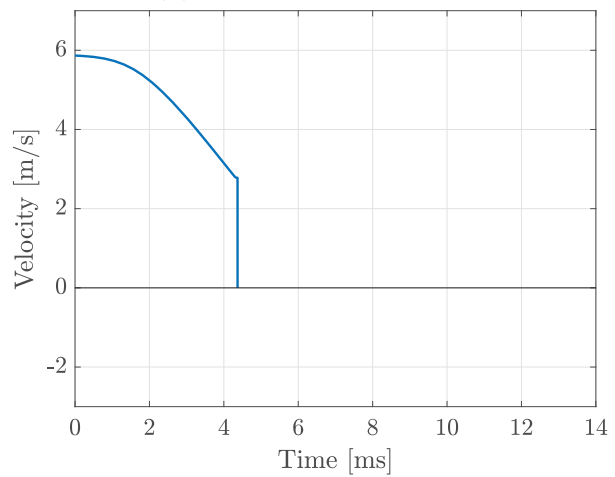
Material	S
T	-30 °C
Replicate	7
t_0	3.15 mm
t_d	4.4 ms
v_i	5.87 m/s
v_r	2.78 m/s



(a) Specimen



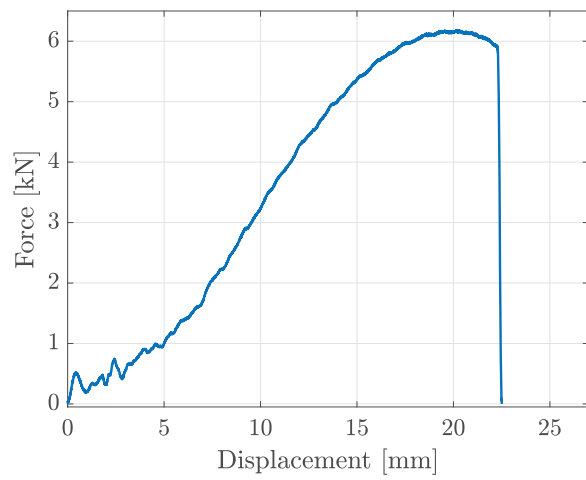
(b) Force - displacement



(c) Velocity - time

C.2.2 DT_S_-30_08

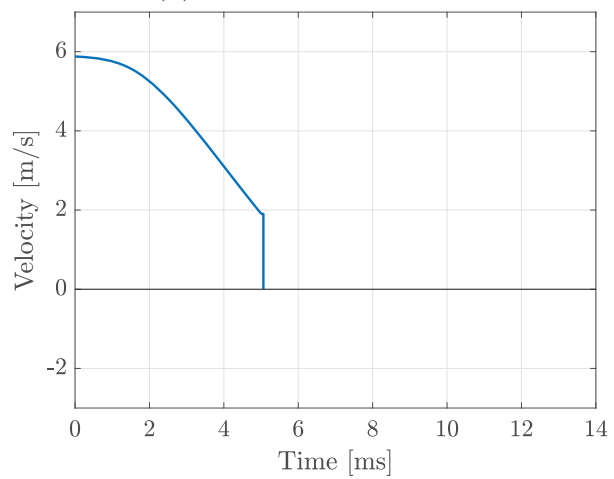
Material	S
T	-30 °C
Replicate	8
t_0	3.15 mm
t_d	5.1 ms
v_i	5.88 m/s
v_r	1.9 m/s



(b) Force - displacement



(a) Specimen



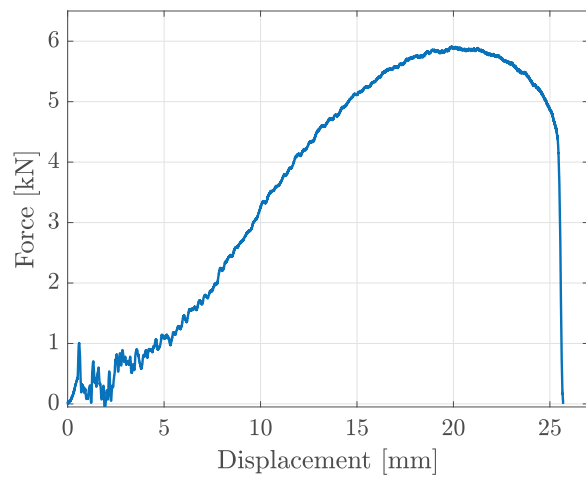
(c) Velocity - time

C.2.3 DT_S_-30_01

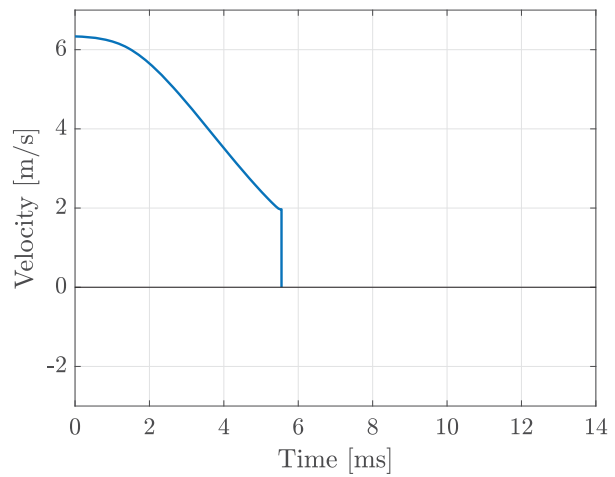
Material	S
T	-30 °C
Replicate	1
t_0	3.15 mm
t_d	5.6 ms
v_i	6.33 m/s
v_r	1.97 m/s



(a) Specimen



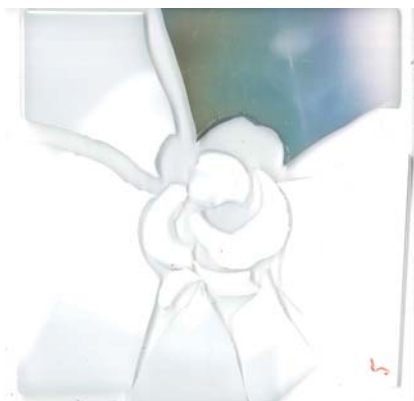
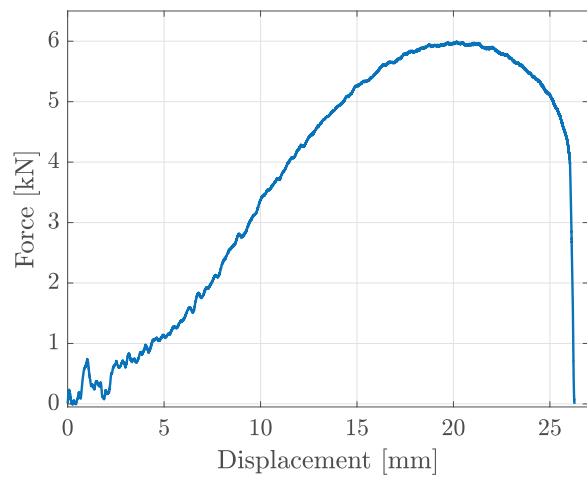
(b) Force - displacement



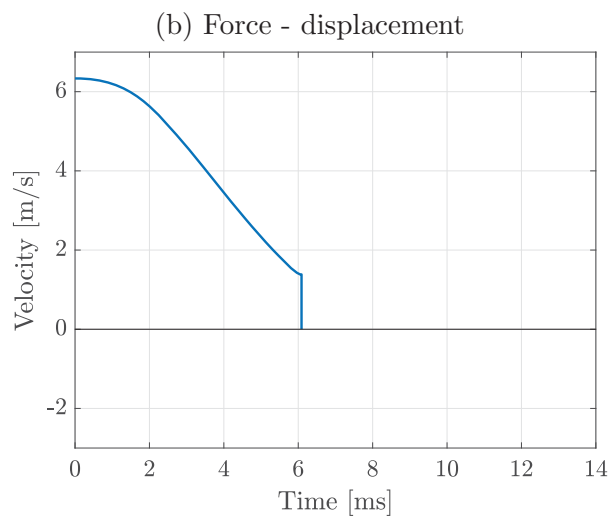
(c) Velocity - time

C.2.4 DT_S_-30_03

Material	S
T	-30 °C
Replicate	3
t_0	3.15 mm
t_d	6.1 ms
v_i	6.33 m/s
v_r	1.38 m/s



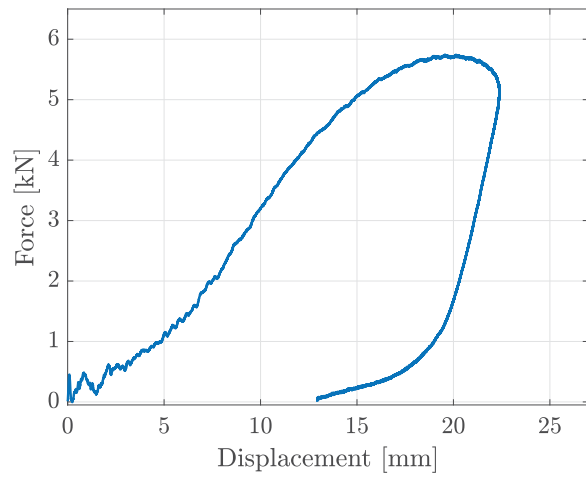
(a) Specimen



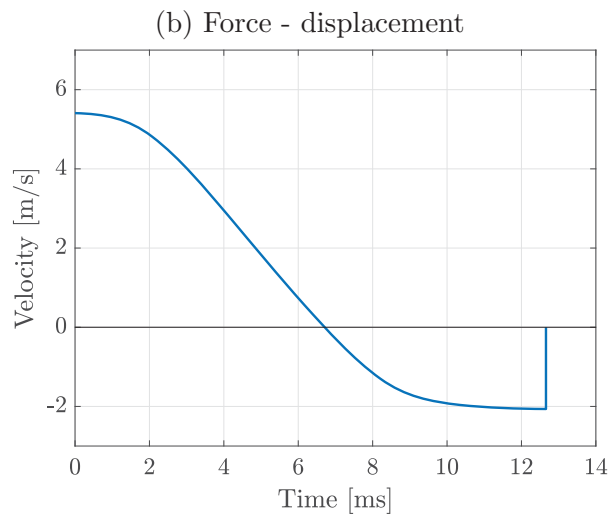
(c) Velocity - time

C.2.5 DT_S_-30_04

Material	S
T	-30 °C
Replicate	4
t_0	3.15 mm
t_d	12.7 ms
v_i	5.41 m/s
v_r	-2.06 m/s



(a) Specimen

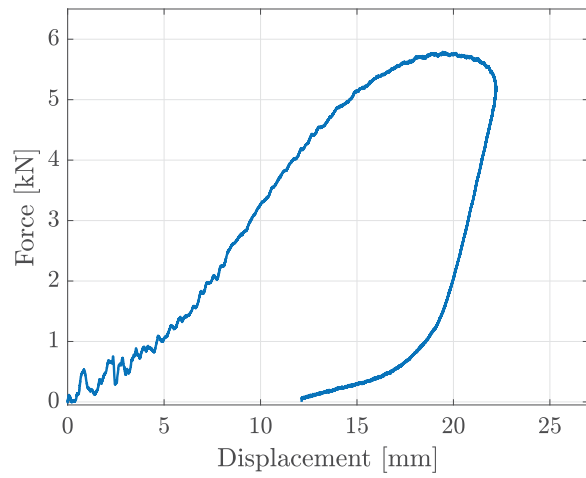


C.2.6 DT_S_-30_05

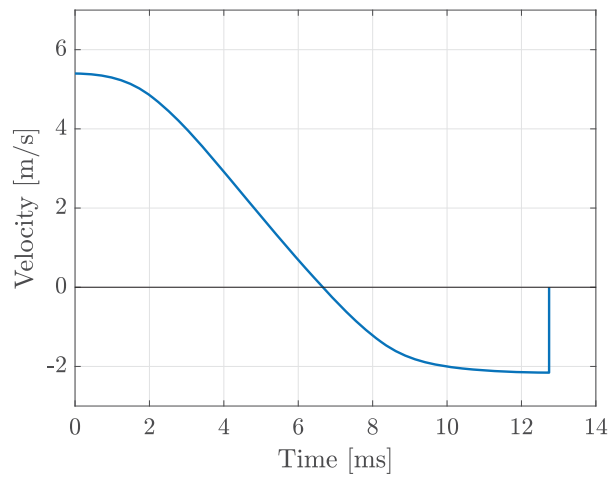
Material	S
T	-30 °C
Replicate	5
t_0	3.16 mm
t_d	12.7 ms
v_i	5.4 m/s
v_r	-2.16 m/s



(a) Specimen



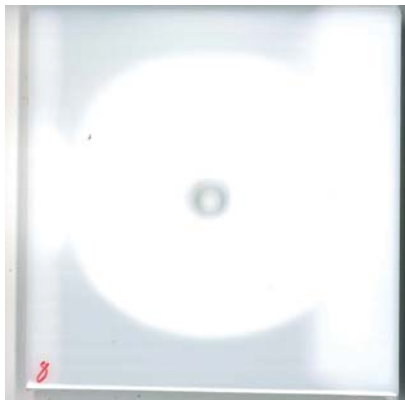
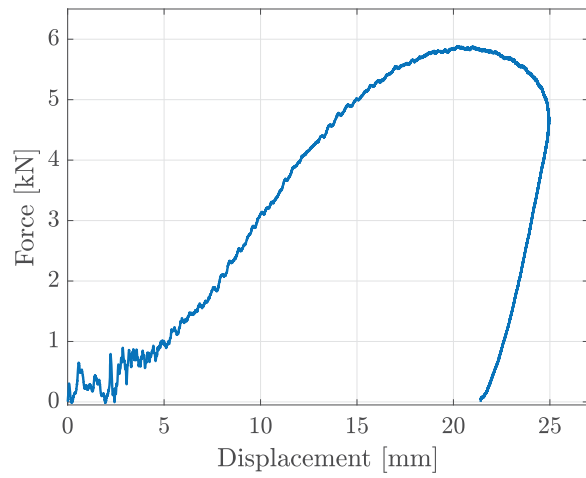
(b) Force - displacement



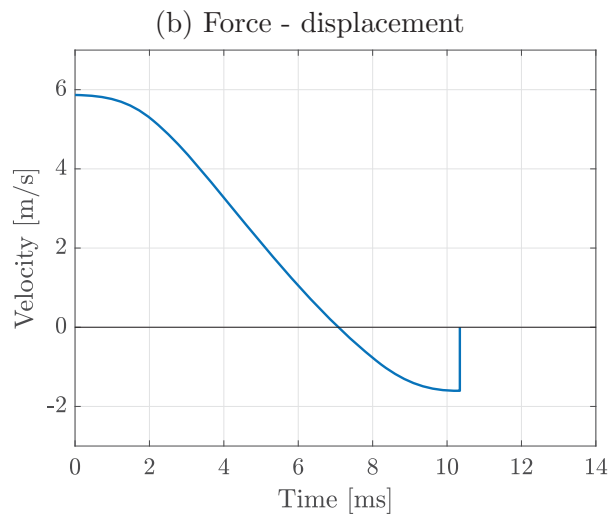
(c) Velocity - time

C.2.7 DT_S_-30_06

Material	S
T	-30 °C
Replicate	6
t_0	3.15 mm
t_d	10.3 ms
v_i	5.87 m/s
v_r	-1.6 m/s



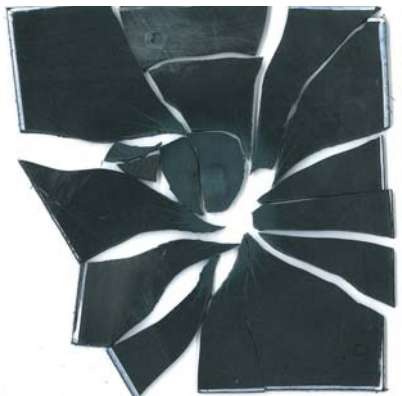
(a) Specimen



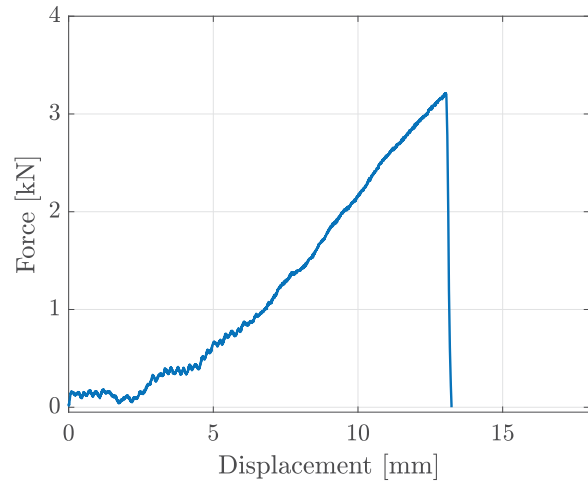
C.3 Door trim cutouts

C.3.1 DT_C-4_-30

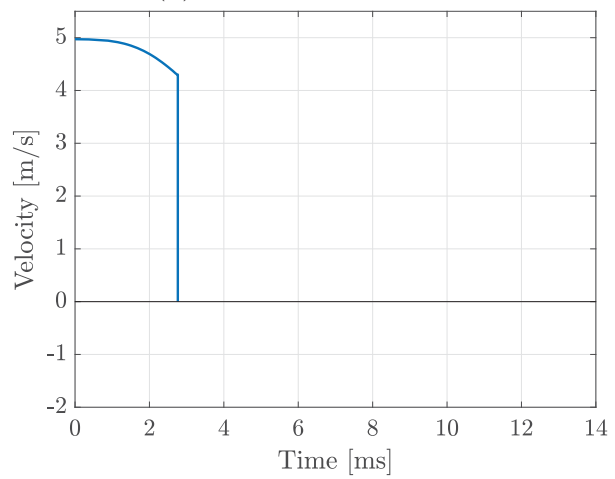
Location	C
T	-30 °C
Door trim no.	4
t_0	2.45 ms
t_d	2.8 ms
v_i	4.97 m/s
v_r	4.3 m/s



(a) Specimen



(b) Force - displacement



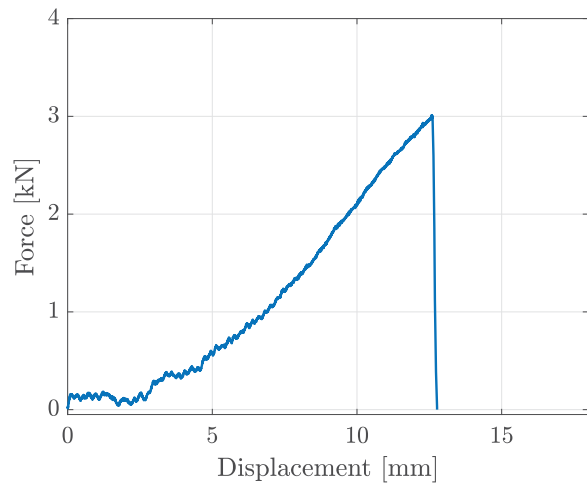
(c) Velocity - time

C.3.2 DT_C-5_-30

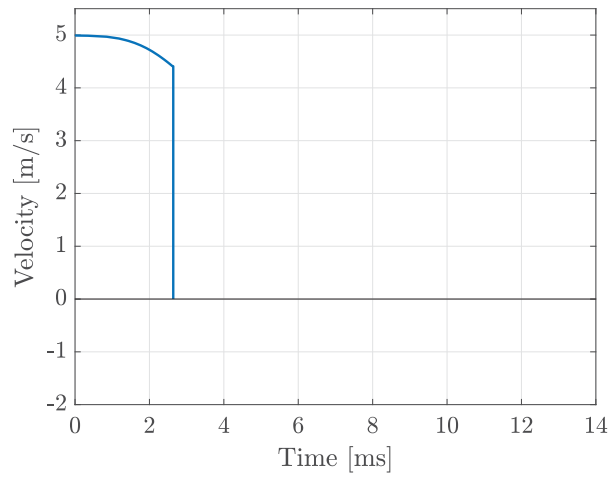
Location	C
T	-30 °C
Door trim no.	5
t_0	2.45 ms
t_d	2.6 ms
v_i	4.99 m/s
v_r	4.41 m/s



(a) Specimen



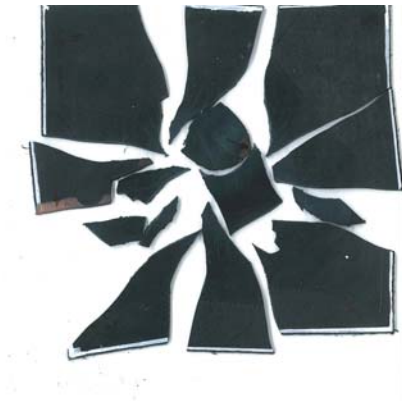
(b) Force - displacement



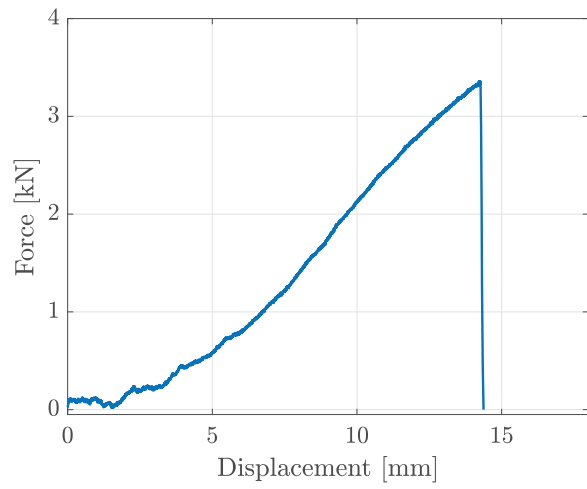
(c) Velocity - time

C.3.3 DT_C-7_-30

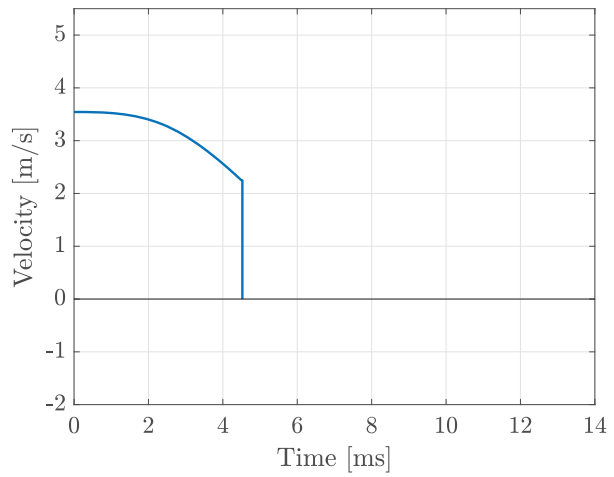
Location	C
T	-30 °C
Door trim no.	7
t_0	2.43 mm
t_d	4.5 ms
v_i	3.54 m/s
v_r	2.25 m/s



(a) Specimen



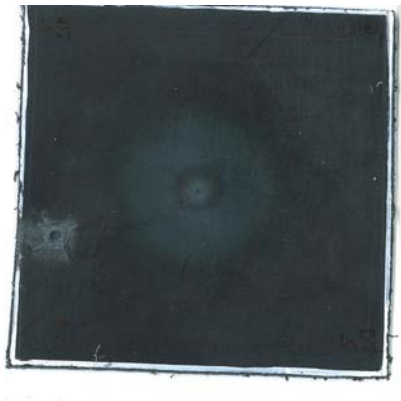
(b) Force - displacement



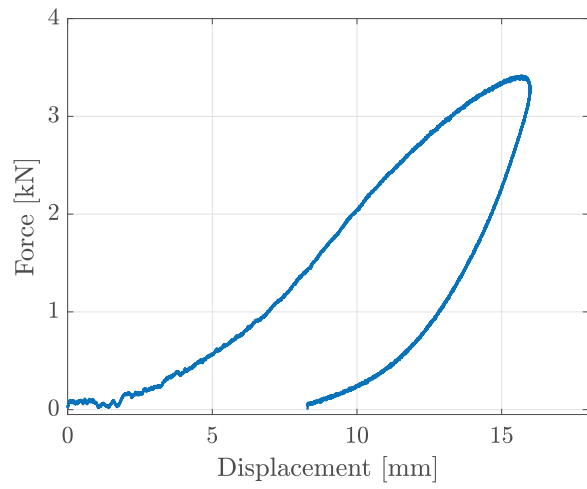
(c) Velocity - time

C.3.4 DT_C-8_-30

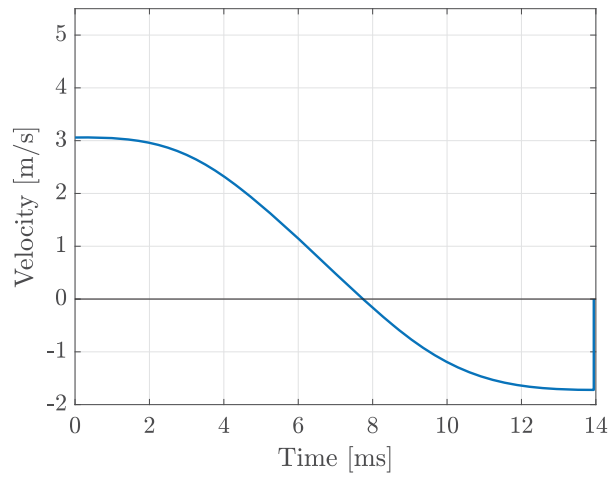
Location	C
T	-30 °C
Door trim no.	8
t_0	2.45 ms
t_d	13.9 ms
v_i	3.06 m/s
v_r	-1.72 m/s



(a) Specimen



(b) Force - displacement



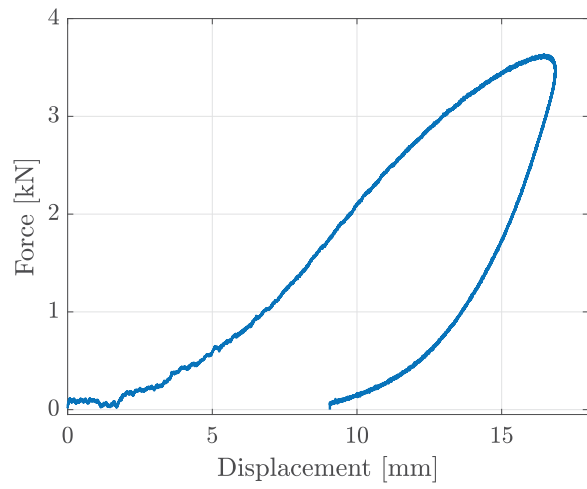
(c) Velocity - time

C.3.5 DT_C-9_-30

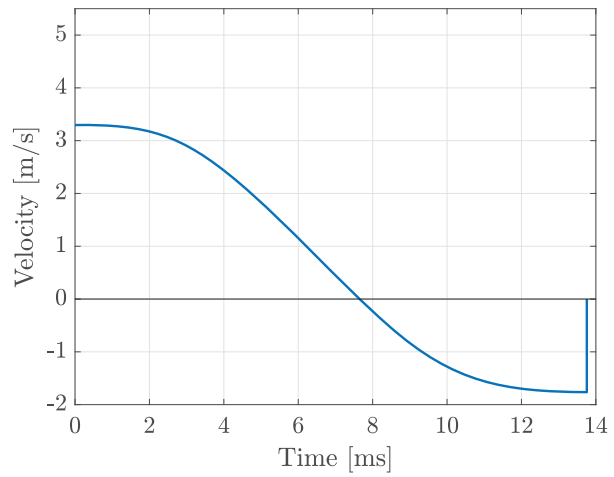
Location	C
T	-30 °C
Door trim no.	9
t_0	2.45 ms
t_d	13.8 ms
v_i	3.3 m/s
v_r	-1.76 m/s



(a) Specimen



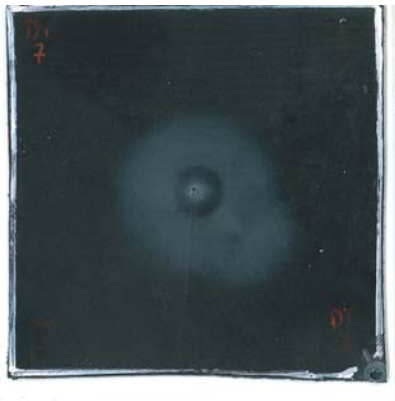
(b) Force - displacement



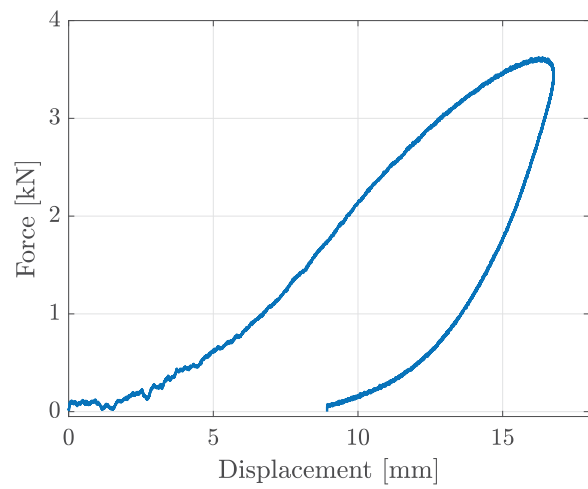
(c) Velocity - time

C.3.6 DT_CS-10_-30

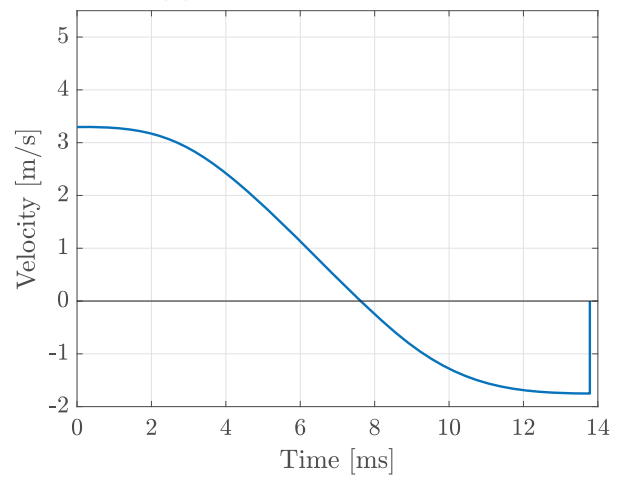
Location	CS
T	-30 °C
Door trim no.	10
t_0	2.47 mm
t_d	13.8 ms
v_i	3.3 m/s
v_r	-1.75 m/s



(a) Specimen



(b) Force - displacement



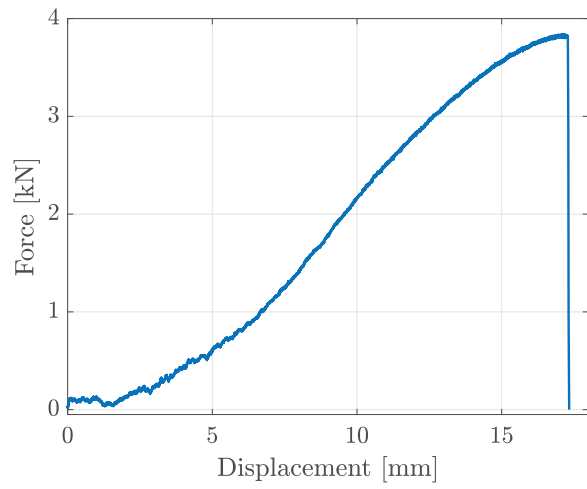
(c) Velocity - time

C.3.7 DT_CS-11_-30

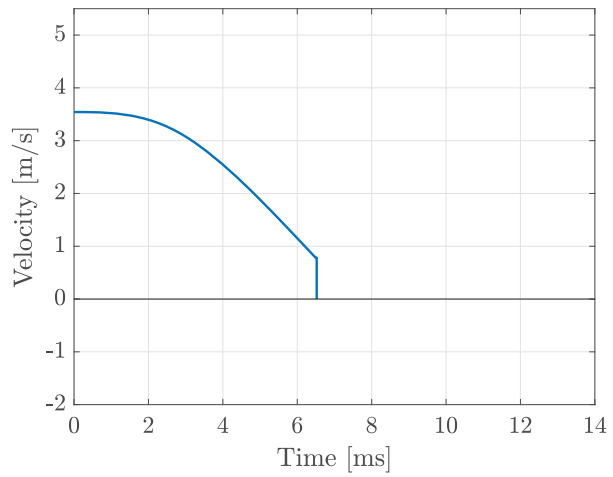
Location	CS
T	-30 °C
Door trim no.	11
t_0	2.46 mm
t_d	6.5 ms
v_i	3.54 m/s
v_r	0.78 m/s



(a) Specimen



(b) Force - displacement



(c) Velocity - time

Split-Hopkinson Tension Bar Tests

D.1 Strain and stress waves

For dynamic load conditions, the absorbed energy in the given component or specimen generally occurs via two distinct phases, i.e. the transient phase and the global mode phase, respectively [62]. The SHTB test rig is designed in such a way that the specimen normally fails before the global mode phase comes into play, i.e. before the boundaries are fully activated.

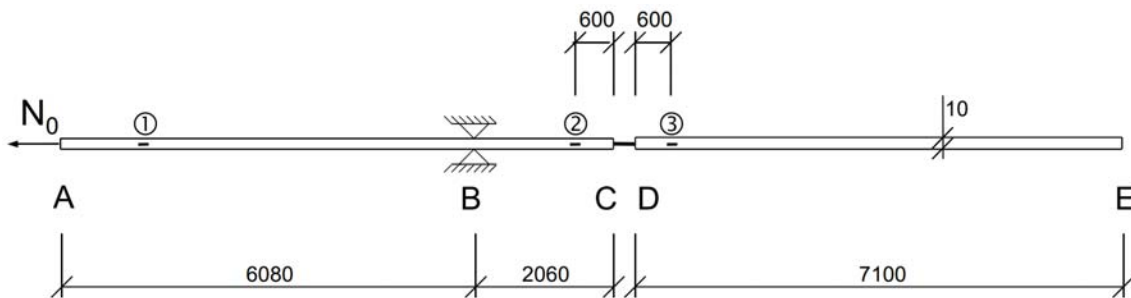


Figure D.1.1: Principal overview of the SHTB rig at SIMLab [55] [mm]

It is assumed that the wave propagation is fully elastic, which in the general case implies a three-dimensional problem involving dilatational, distortional and surface waves, respectively. However, the long and thin geometry of the SHTB simplifies the problem, and permits a one-dimensional treatment [57]. Due to the Poisson's ratio of the steel bars, lateral contraction and expansion is nonetheless expected during the experiment. Hence, the arising strains are not entirely uniaxial. The consecutive inertia effects due to this lateral straining are, however, negligible due to the small

diameter-length ratio of the bars. Ultimately, this means that the behaviour of the SHTB is assumed to be governed by the one-dimensional wave equation, of the form

$$\frac{\partial^2 u}{\partial t^2} = c^2 \frac{\partial^2 u}{\partial x^2}. \quad (\text{D.1})$$

Here, x is the coordinate along the length of the bar, t is the time, u is the longitudinal displacement of the bar and c is the material-specific velocity of the propagating wave, determined by

$$c = \sqrt{\frac{E}{\rho}}, \quad (\text{D.2})$$

where E and ρ denotes the Young's modulus and the density of the material, respectively.

Hence, the instant for which the clamping mechanism at point B is suddenly removed, an initial tensile strain wave, $\varepsilon_I(t)$, propagates through the incident bar from point B towards point C. This wave is partly reflected as, $\varepsilon_R(t)$, i.e. a wave travelling back to point B and A, because of the abrupt decrease in cross-sectional area and change in material associated with the tested specimen. Nevertheless, the initial wave is also partly transmitted as, $\varepsilon_T(t)$, i.e. a wave propagating into the specimen. When this transmitted wave has propagated through the specimen and reached point D, another division into a reflected and a transmitted wave occurs. Here, one part is transmitted into bar DE, while the other is reflected and travels back to point C where a new sequence of reflection and transmission takes place.

These successive sequences of transmission and reflection can rather easily be calculated by the method described by Clausen [57], as long as all components of the system behave elastically. In the general case, however, the specimen undergoes a considerable amount of plastic deformation before it ultimately fractures. The inelastic behaviour of the test specimen introduces the tangent stiffness, E_t , into Eq. (D.2) which is much smaller than the Young's modulus, E . Hence, the propagation velocity is significantly reduced, and the wave propagation within the system is changed.

Regardless of test specimen material, the strain wave transmitted into bar DE is reflected at point E and propagates back towards point D as a compression wave, i.e. activation of the boundary in the transmission bar. The strain wave returns as a compression wave because the boundary at point E is a free end. At free ends, there are no strains or stresses, which means that the reflected wave must be compression

for equilibrium to be fulfilled. However, when testing polymers, transmission of such compression reflected waves can often be neglected since the associated flow stresses and consecutive fracture stresses are low enough for fracture to occur during the loading inflicted by the first tensile wave.

The previously described strain waves correspond to equivalent stress waves, that are more intuitively comprehended. The release of stress waves within both the incident and the transmission bar of the SHTB rig is illustrated in Figure D.1.2. Initially, the stress corresponding to the stretching of portion AB of the incident bar, L_{AB} , at time $t = 0$ by the axial tensile force, N_{pre} , is called σ_{pre} . This initial state of loading corresponds to $\varepsilon_I(t)$ just before the clamping at point B is removed. Furthermore, when the clamping at point B is removed, the stress wave, incorporated as a rectangular pulse with intensity $\sigma_{pre}/2$, propagates through portion BC of the incident bar, L_{BC} , and reaches point C at time $t = L_{BC}/c_b$. Here, c_b represents the wave propagation velocity within the steel bars.

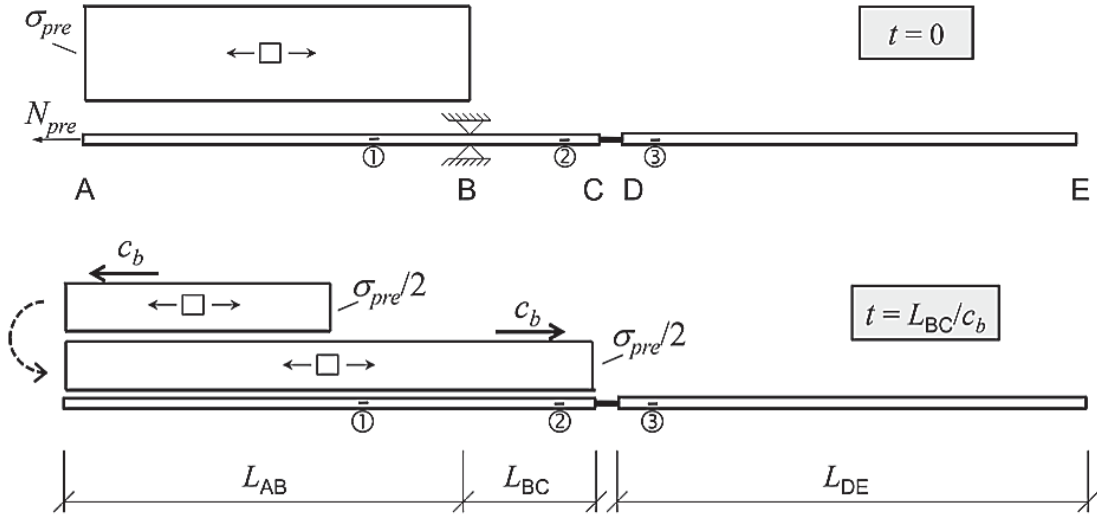


Figure D.1.2: Illustration of the release of stress waves during SHTB testing [55]

Using Eq. (D.2), the wave propagating velocity within the SHTB rig is found to be,

$$c_b = \sqrt{\frac{E_b}{\rho_b}} = \sqrt{\frac{210 \cdot 10^9 \text{ N/m}^2}{7850 \text{ kg/m}^3}} = 5172.2 \text{ m/s},$$

where E_b and ρ_b is the Young's modulus and density of the steel bars, respectively. The portion of σ_{pre} that had already propagated through L_{BC} to point C at time $t = L_{BC}/c_b$, i.e. $\sigma_{pre}/2$, has also been subtracted from L_{AB} . This is illustrated

in the lower part of Figure D.1.2. Following events of transmission and reflection of different portions of $\sigma_{pre}/2$ between the bars and the specimen will occur in the same manner as described for $\varepsilon_T(t)$ and $\varepsilon_R(t)$ earlier.

It should be noted that as long as the tested specimen is capable of transmitting such waves back and forth between the two bars, the sum of stress waves within the system will always correspond to the total stress, σ_{pre} . However, this is only true for elastic deformation where no energy is dissipated. Since the tested specimens experience high strain rates in the SHTB testing, plastic deformation is almost always obtained. Thus, if the specimen fractures or in any way experience plastic deformation, some internal energy is dissipated and the total stress within the system is obviously reduced. Additionally, subsequent to fracture, the incident- and transmission bar are no longer linked, preventing transmission of any strain or stress waves.

D.2 Door trim cutouts

In this appendix, all successful tests conducted in the SHTB are archived. For each test specimen, the test specifics, dimensions and a picture of the deformed geometry is provided. In addition, three different graphs are plotted displaying two stress measures, strain components and the strain rate. All recorded data is cut at fracture, but no filter is used.

The following abbreviations are used in this appendix:

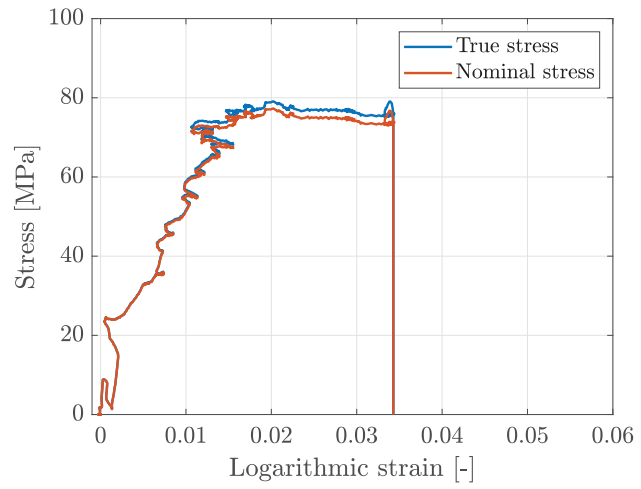
\angle	Test specimen orientation
$\dot{\varepsilon}_0$	Analytic strain rate
T	Temperature
\mathbf{t}_0	Initial gauge area thickness
\mathbf{w}_0	Initial gauge are width
t_d	Test duration
ε_f	Logarithmic fracture strain

D.2.1 SH_B-3_02

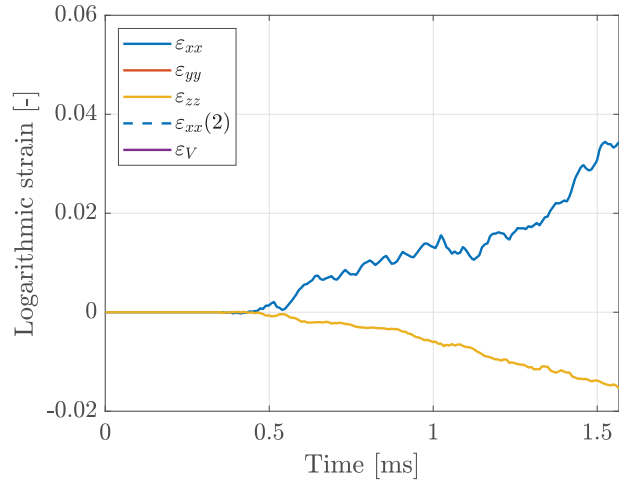
Location	B
\angle	0°
$\dot{\epsilon}_0$	37 s^{-1}
T	$-30 \text{ }^\circ\text{C}$
Door trim no.	3
Replicate	2
t_0	2.29 mm
w_0	7.02 mm
t_d	1.57 ms
ϵ_f	0.034



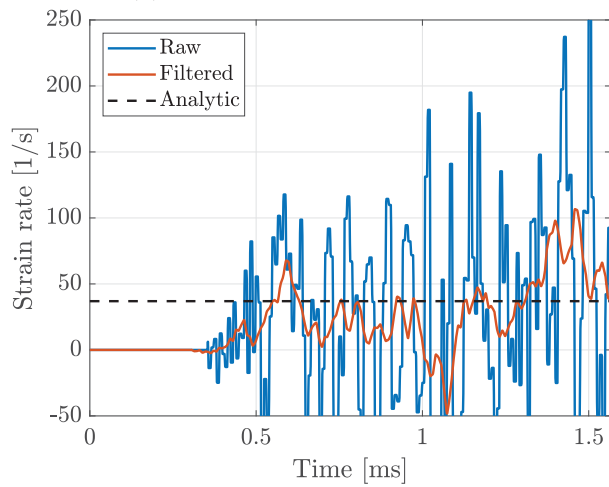
(a) Specimen



(b) Stress - logarithmic strain



(c) Strain components - time



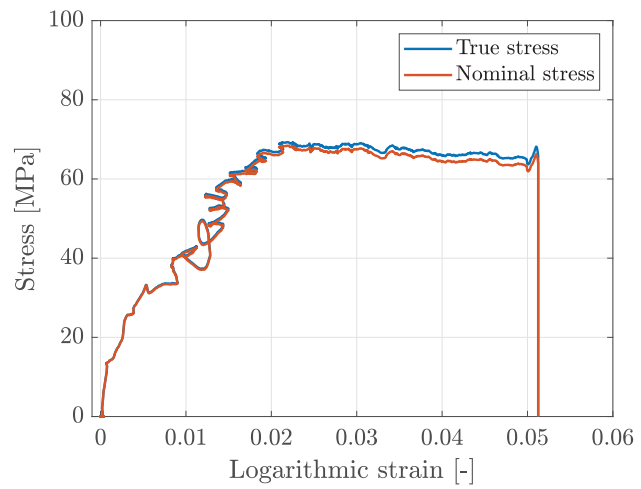
(d) Strain rate - time

D.2.2 SH_B-10_02

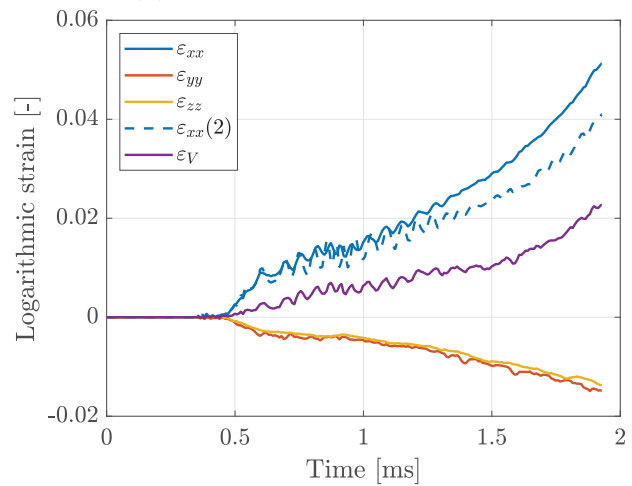
Location	B
\angle	0°
$\dot{\epsilon}_0$	34 s^{-1}
T	$-30 \text{ }^\circ\text{C}$
Door trim no.	10
Replicate	2
t_0	2.29 mm
w_0	7.02 mm
t_d	1.93 ms
ϵ_f	0.051



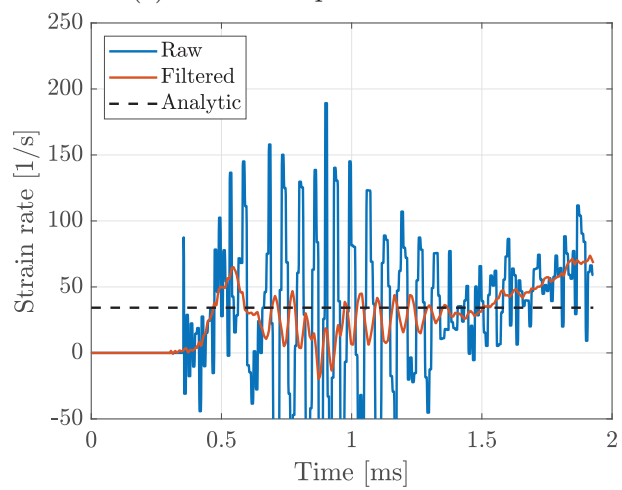
(a) Specimen



(b) Stress - logarithmic strain



(c) Strain components - time



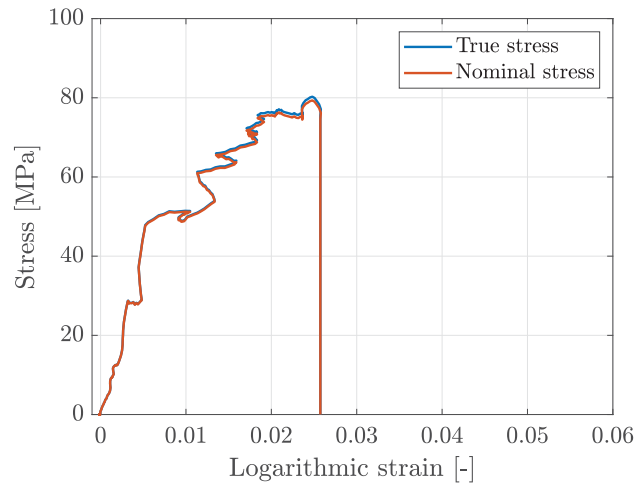
(d) Strain rate - time

D.2.3 SH_B-4_01

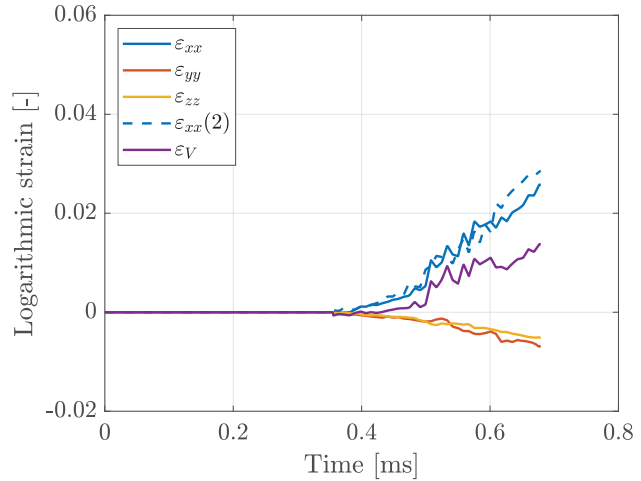
Location	B
\angle	0°
$\dot{\epsilon}_0$	157 s^{-1}
T	$-30 \text{ }^\circ\text{C}$
Door trim no.	4
Replicate	1
t_0	2.27 mm
w_0	7.01 mm
t_d	0.68 ms
ϵ_f	0.026



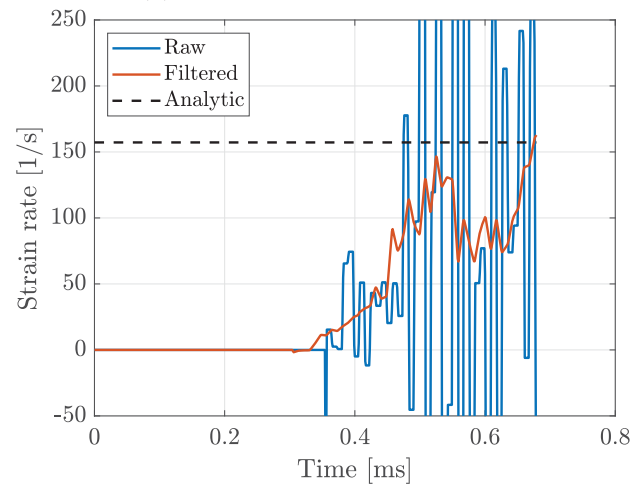
(a) Specimen



(b) Stress - logarithmic strain



(c) Strain components - time



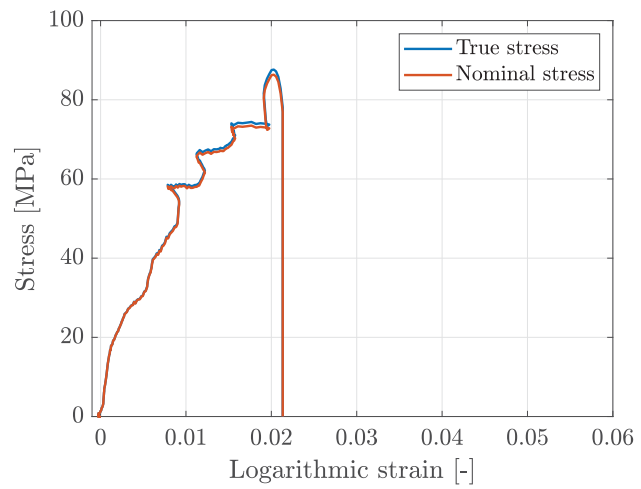
(d) Strain rate - time

D.2.4 SH_B-4_02

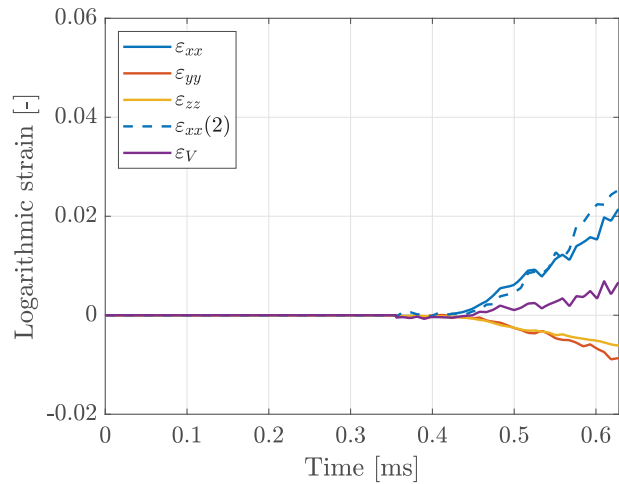
Location	B
\angle	0°
$\dot{\epsilon}_0$	152 s^{-1}
T	$-30 \text{ }^\circ\text{C}$
Door trim no.	4
Replicate	2
t_0	2.29 mm
w_0	7.01 mm
t_d	0.63 ms
ϵ_f	0.021



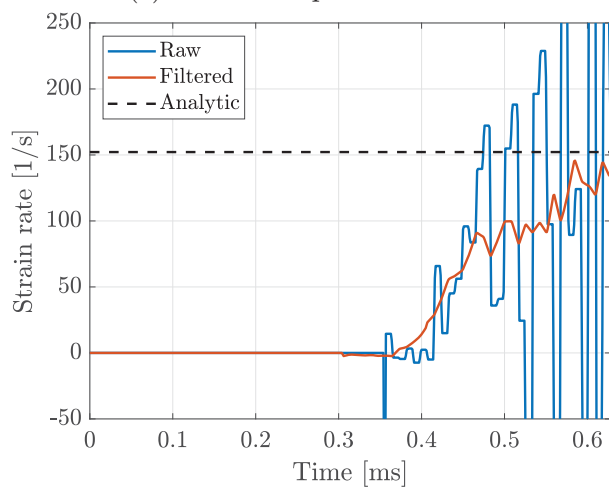
(a) Specimen



(b) Stress - logarithmic strain



(c) Strain components - time



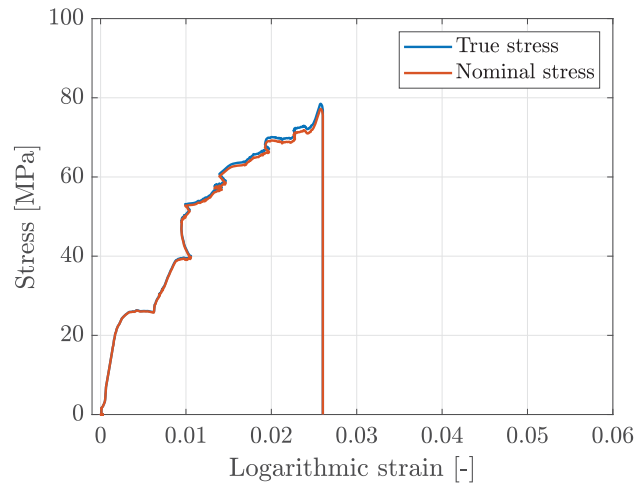
(d) Strain rate - time

D.2.5 SH_B-5_01

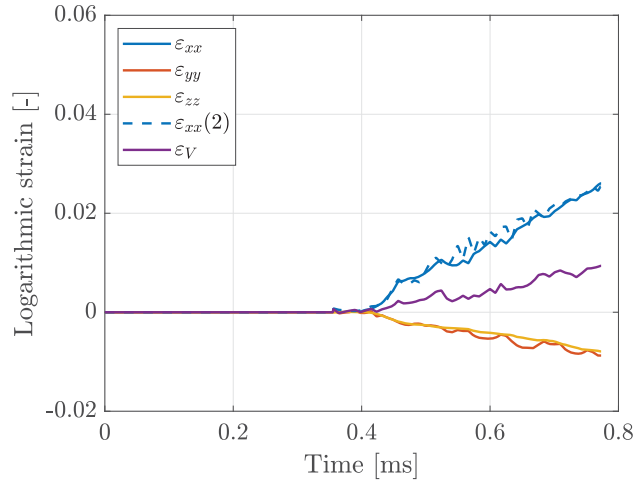
Location	B
\angle	0°
$\dot{\epsilon}_0$	101 s^{-1}
T	$-30 \text{ }^\circ\text{C}$
Door trim no.	5
Replicate	1
t_0	2.27 mm
w_0	7.02 mm
t_d	0.77 ms
ϵ_f	0.026



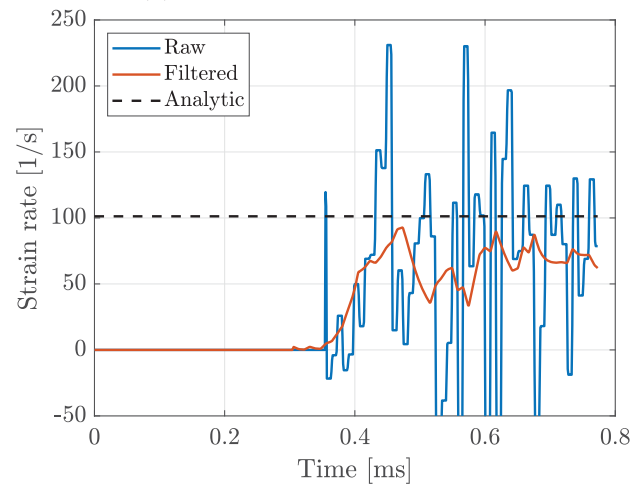
(a) Specimen



(b) Stress - logarithmic strain



(c) Strain components - time



(d) Strain rate - time

Component Tests

E.1 Door trims

In this appendix, the component drop tests conducted at TME are archived. For each door trim, the given number, production date and mould number are displayed. Note that the numbers given here do not correspond to the numbers given to the door trims used for specimen extraction at DSE. In addition, the drop heights tested for each respective door trim and the result in terms of fracture are given. A picture of both the front and back of most door trims are also provided.

The following abbreviations are used in this appendix:

F Fracture

NF No fracture

E.1.1 Door trim 3

Door trim	3
Production date	2018-02
Mould number	49862

	Test location		
	B	H	J
Drop height [mm]	1900	-	1900
Failure [NF/F]	F	-	F



(a) Front



(b) Back

E.1.2 Door trim 6

Door trim	6	Test location			
Production date	2018-02	B	H	J	
Mould number	49862	Drop height [mm]	1000	1900	500
		Failure [NF/F]	F	F	F



(a) Front

E.1.3 Door trim 7

Door trim	7
Production date	2017-09
Mould number	49862

	Test location		
	B	H	J
Drop height [mm]	500	1000	300
Failure [NF/F]	NF	NF	F



(a) Front



(b) Back

E.1.4 Door trim 8

Door trim	8
Production date	2015-10
Mould number	49862

	Test location		
	B	H	J
Drop height [mm]	750	1050	300
Failure [NF/F]	F	NF	NF



(a) Front



(b) Back

E.1.5 Door trim 9

Door trim	9
Production date	2017-03
Mould number	49862

	Test location		
	B	H	J
Drop height [mm]	650	1100	300
Failure [NF/F]	F	F	NF



(a) Front



(b) Back

E.1.6 Door trim 10

Door trim	10
Production date	2017-03
Mould number	49862

	Test location		
	B	H	J
Drop height [mm]	600	1050	300
Failure [NF/F]	F	NF	NF



(a) Front



(b) Back

E.1.7 Door trim 11

Door trim	11
Production date	2018-02
Mould number	49862

	Test location		
	B	H	J
Drop height [mm]	550	1100	350
Failure [NF/F]	NF	F	F



(a) Front



(b) Back

E.1.8 Door trim 12

Door trim	12
Production date	2018-02
Mould number	49862

	Test location		
	B	H	J
Drop height [mm]	600	1050	350
Failure [NF/F]	NF	F	F



(a) Front



(b) Back

E.1.9 Door trim 13

Door trim	13
Production date	2017-10
Mould number	49862

	Test location		
	B	H	J
Drop height [mm]	650	1100	300
Failure [NF/F]	F	NF	NF



(a) Back

E.1.10 Door trim 15

Door trim	15
Production date	2018-02
Mould number	49862

	Test location		
	B	H	J
Drop height [mm]	600	1100	350
Failure [NF/F]	NF	NF	NF



(a) Front



(b) Back

E.1.11 Door trim 16

Door trim	16
Production date	2018-02
Mould number	49862

	Test location		
	B	H	J
Drop height [mm]	600	1100	350
Failure [NF/F]	NF	NF	NF



(a) Front



(b) Back

E.1.12 Door trim 17

Door trim	17	Test location			
Production date	2017-11	B	H	J	
Mould number	49862	Drop height [mm]	600	1100	350
		Failure [NF/F]	NF	F	F

E.1.13 Door trim 18

Door trim	18
Production date	2017-10
Mould number	49862

	Test location		
	B	H	J
Drop height [mm]	600	1100	350
Failure [NF/F]	NF	NF	NF



(a) Back

E.1.14 Door trim 19

Door trim	19
Production date	2017-11
Mould number	49862

	Test location		
	B	H	J
Drop height [mm]	650	1150	400
Failure [NF/F]	NF	F	NF



(a) Front



(b) Back

E.1.15 Door trim 20

Door trim	20
Production date	2017-10
Mould number	49862

	Test location		
	B	H	J
Drop height [mm]	650	1150	400
Failure [NF/F]	NF	NF	NF



(a) Front



(b) Back

Material Cards

In this appendix, material cards used to define the parameters in the SIMLab polymer model are displayed. The appendix provides two versions, one for use in Abaqus/CAE and one for use in LS-DYNA.

F.1 Abaqus

```
*Material, name = SPM.S
*Density
  9.05e-10
*Include, input = depvar_SPM.inc
*User Material, constants = 28
**   EFLAG,      YFLAG,   RMAPFLAG,      FFLAG,      HFLAG
      1,         1,       5,             1,          1
**   VFLAG,      TFLAG,   DFLAG,      STFLAG,      E0
      1,         1,      -1,             0,        2696.47
**   NU,         SIGMAT,   ALPHA,      KSI,         BETA
      0.267,     32.785,    1.22,     0.01,       1.881
**   THETAR1,    QR1,      THETAR2,    QR2,         THETAR3
      253.499,   2.74298,    25.332,  -45.176696, -62.41689
**   QR3,        THETAMIN,  C,         PDOT0,       RHO
      -2.5583,   0,          0.3066,    1.0,         9.05e-10
**   CT,         DINIT,    DCRIT,
      1.925e+09, 0,          0.233,
```

F.2 LS-DYNA

```

$# LS-DYNA Keyword file created by LS-PrePost(R) V4.5.2
$#- 22Oct2017
$# Created on May-29-2018 (08:42:50)
*KEYWORD
*MAT_USER_DEFINED_MATERIAL_MODELS_TITLE
SPM_S
$      MID      RHO      MT      LMC      NHV      IORTHO
$#     mid      ro      mt      lmc      nhv      iortho
      1 9.05E-10      42      32      116      0
$      IBULK    ISHEAR    IVECT    IFAIL    IHTERM    IHYPER
$#     ibulk      ig      ivect      ifail      itherm      ihyper
      1      2      1      1      0      0
$      IEOS      LCMA      BULK      SHEAR
$#     ieos      lmca  unused      unused      p1      p2
      0      0      2452.1      1352.8
$      EFLAG    YFLAG  RMAPFLAG    FFLAG    HFLAG    VFLAG
$#     p3      p4      p5      p6      p7      p8
      1.0      1.0      5.0      1.0      1.0      1.0
$      TFLAG    DFLAG    STFLAG    E0      NU      SIGMAT
$#     p1      p2      p3      p4      p5      p6
      0.0      -1.0      0.0      2696.47      0.267      32.785
$      ALPHA    KSI      BETA    THETAR1    QR1      THETAR2
$#     p7      p8      p1      p2      p3      p4
      1.22      0.01      1.881      253.499      2.74298      25.332
$      QR2    THETAR3    QR3    THETAMIN    C      PDOT0
$#     p5      p6      p7      p8      p1      p2
      -45.1767 -62.41689 -2.5583      0.0      0.3066      1.0
$      DINIT    DCRIT
$#     p3      p4      p5      p6      p7      p8
      0.0      0.233      0.0      0.0      0.0      0.0
*END

```

Friction Coefficient Test

Introduction

To justify our initial choice of friction coefficient in the numerical representations, a brief experimental test was conducted. The objective of this test was to determine the static coefficient of friction acting between the material sample plates and support table used in the drop tower.

Theory

Friction is the force resisting relative movement when one surface is in contact with another. There are two types of friction, static and kinetic, associated with surfaces at rest and in motion, respectively. The static friction force is usually larger than its kinetic counterpart. These frictional forces can be related to the forces acting normal to the surface, through the following relations

$$f_s = \mu_s N, \quad \text{and} \quad f_k = \mu_k N, \quad (\text{G.1})$$

where f_s and f_k correspond to the static- and kinetic frictional forces, while μ_s and μ_k are the static- and kinetic coefficients of friction. The normal force is given by N .

This experiment relies on the static coefficient of friction being determined using an inclined plane and the test specimen. The idea was that the angle of the plane could be used to obtain the static coefficient of friction, acting between the two surfaces.

The following assumptions were made in this derivation:

- The only forces acting on the test specimen are the gravitational force and the friction between the two surfaces.
- The sum forces acting on the test specimen and inclined plane is zero just before the specimens starts to slide.
- Both the surface of the support table and the surface of the specimens are smooth.

A schematic drawing of the inclined plane is shown in Figure G.0.1 in addition to a free-body-diagram, describing the forces acting on the specimen. Note that a n-t coordinate system was utilised here, rotated according to an arbitrary angle of the inclined plane, θ .

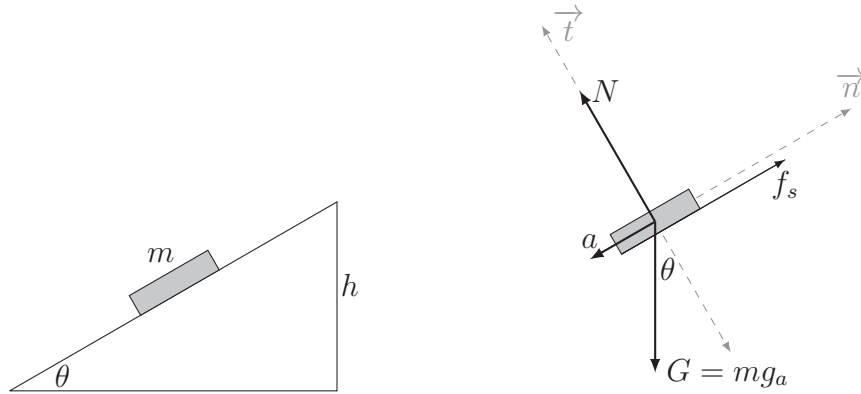


Figure G.0.1: Schematic drawing of inclined plane and free-body-diagram

Since the sum of forces acting on the specimen is assumed to be zero, Newton's first law can be utilised to express the equilibrium equations in both directions. Thus, in the n-direction, one obtain

$$\Sigma F_n = 0 : \quad N - G \cos \theta = 0 \quad (\text{G.2})$$

$$\Rightarrow N = mg_a \cos \theta \quad (\text{G.3})$$

where m is the mass of the specimen and g_a is the gravitational acceleration. A similar relation can be expressed from Newton's first law in the t-direction,

$$\Sigma F_t = 0 : \quad -f_s + mg_a \sin \theta = 0. \quad (\text{G.4})$$

The relation between the frictional- and normal force, expressed in Eq. (G.1), as well as the relation in Eq. (G.3) can now be substituted into the equation above. By solving with respect to the coefficient of friction, one obtain the following

$$-\mu_s N + mg_a \sin \theta = 0 \quad (\text{G.5})$$

$$-\mu_s (mg_a \cos \theta) + mg_a \sin \theta = 0 \quad (\text{G.6})$$

$$\mu_s = \frac{\sin \theta}{\cos \theta}. \quad (\text{G.7})$$

Hence, an expression relating the static coefficient of friction to the angle of the inclined plane is obtained. This implies that for an inclined plane of length, l , the height h , and subsequently the angle of the plate, can be increased until the plate starts to slide. At this critical angle, the static coefficient of friction can be found using this equation

$$\mu_s = \tan \theta = \frac{h}{\sqrt{l^2 - h^2}}. \quad (\text{G.8})$$

Procedure

The test setup used in this experiment, is shown in Figure G.0.2. To ensure an accurate determination of the coefficient of friction, the support table used in the drop tower impact test was removed from the drop tower and utilised as the plane. Its length of 399 mm was further measured, such that the height could be related to the angle. Care was taken such that any holes in the plate would not affect the results. A stand was used to hold one side of the plane, creating an angle. The inclined plane test involved decreasing the plan height until the sample plate no longer slipped, when placed on the plane. The height was measured using a ruler, and recorded for each test. Due to some differences in the two largest surfaces of the sample plates, they were tested separately.

Results and discussion

The results from the experimental test are summarised in Table G.0.1. The table shows the height of one end of the inclined plane, as well as the result in terms of slip (S) or no slip (NS). Since one test was conducted for each of the two surfaces of the specimens, the results are divided accordingly. The table shows that that



Figure G.0.2: Inclined plane test setup

the smoothest surface slipped at a smaller angle than the rough. This makes sense, since a rougher surface is likely to result in larger frictional forces between the two surfaces.

Table G.0.1: Test results

h [mm]	Surface	
	Smooth	Rough
150	S	S
131	S	S
124	S	S
120	S	S
118	S	NS
116	S	-
113	S	-
111	NS	-

There were mainly two uncertainties related to the experimental inclined plane test. Firstly, due to the smooth coating of the drop tower support table, some amount of suction was created between the two surfaces. This transpired into small inconsistencies with respect to whether the sample plate slipped or not. Secondly, because of the large mass of the support table, determination of exact heights was complicated. This meant that a highly accurate coefficient of friction could not be obtained in this experiment. The goal of such a simple procedure was, however, only to obtain a starting point for further investigation in the sensitivity study. Since the kinetic coefficient of friction was likely to act between the surfaces during the actual drop tower impact test, using the static coefficient of friction would overestimate

the friction forces.

The height causing the sample to slip and the approximate static coefficient of friction for the two different surfaces, are shown in Table G.0.2. The coefficients of friction were determined using the expression derived in Eq. (G.8). From the table, it is clear that the coefficients of friction for the two surfaces are relatively similar.

Table G.0.2: The resulting static coefficient of friction

Surface	h [mm]	μ_s [-]
Smooth	112	0.29
Rough	119	0.31

Conclusion

A simple experimental setup based on an inclined plane was used to obtain an initial estimate for static coefficient of friction acting between the surfaces in the drop tower. This would only serve as a defined parameter in the numerical representations, and was investigated further in a numerical sensitivity study. Due to the slight difference between the two surfaces of the material sample plates, somewhat different coefficients of friction were also found. Although some uncertainties are related to the validity of the results, these coefficient are sufficiently accurate for use in the numerical model.